Development of novel multimodal light-sheet fluorescence microscopes for in-vivo imaging of vertebrate organisms

Matteo Bernardello

PhD thesis supervised by:

Dr. Pablo Loza-Alvarez (Supervisor)

Dr. Emilio J. Gualda (Co-supervisor)

PhD in Photonics - ICFO - The Institute of Photonic Sciences – June 2022

Abstract

The observation of biological processes in their native environments is of critical importance for life science. While substantial information can be derived from the examination of in-vitro biological samples, in-vivo studies are necessary to reveal the complexity of the dynamics happening in real-time within a living organism. Between the possible biological model choices, vertebrates represent an important family due to the various characteristics they share with the human organism. The development of an embryo, the effect of a drug, the interaction between the immune system and pathogens, and the cellular machinery activities are all examples of highly-relevant applications requiring in-vivo observations on broadly used vertebrate models such as the zebrafish and the mouse.

To perform such observations, appropriate devices have been devised. Fluorescence microscopy is one of the main approaches through which specific sample structures can be detected and registered in high-contrast images. Through micro-injections or transgenic lines, a living specimen can express fluorescence and can be imaged through such microscopes. Various fluorescence microscopy techniques have been developed, such as Widefield Microscopy (WM) and Laser Scanning Confocal Microscopy (LSCM). In WM the entire sample is visualized in a single 2D image, therefore losing the depth information, while LSCM can recover the 3D information of the sample but with inherent limitations, such as phototoxicity and limited imaging speed.

In the last two decades, Light-Sheet Fluorescence Microscopy (LSFM) emerged as a technique providing fast and 3D imaging, while minimizing collateral damages to the specimen. However, due to the particular configuration of the microscope's components, LSFM setups are normally optimized for a single application. Also, sample management is not trivial, as controlling the specimen positioning and keeping it alive for a long time within the microscope needs dedicated environmental conditioning.

In this thesis, I aimed at advancing the imaging flexibility of LSFM, with particular attention to sample management. The conjugation of these aspects enabled novel observations and applications on living vertebrate samples.

In Chapter 1, a brief review of the concepts employed within this thesis is presented, also pointing to the main challenges that the thesis aims to solve.

In Chapter 2, a new design for multimodal LSFM is presented, which enables performing different experiments with the same instrument. Particularly, high-throughput studies would benefit from this imaging paradigm, conjugating the need for fast and reproducible mounting of multiple samples with the opportunity to image them in 3D. Additionally, from this design, a transportable setup has also been implemented.

With these systems, I studied the dynamics of the yolk's microtubule network of zebrafish embryos, describing novel features and underlining the importance of live imaging to have a whole view of the sample's peculiarities. This is described in Chapter 3.

Further applications on challenging live samples have been implemented, monitoring the macrophage recruitment in zebrafish and the development of mouse embryos. For these applications, described in Chapter 4, I devised specific mounting protocols for the samples, keeping them alive during the imaging sessions.

In Chapter 5, an additional LSFM system is described, which allows for recording the sub-cellular machinery in a living vertebrate sample, while avoiding its damage thanks to the devised sample mounting. Through this, single-molecule microscopy (SMM) studies, normally performed on cultured cells, can be extended to the nuclei of living zebrafish embryos, which better recapitulate the native environment where biological processes take place.

Finally, Chapter 6 recapitulates the conclusions, the impacts, future integrations, and experimental procedures that would be enabled by the work resumed in this thesis.

Resumen

La observación de los procesos biológicos en su entorno es de vital importancia para las ciencias de la vida. Si bien se puede derivar información sustancial desde muestras biológicas in-vitro, los estudios in-vivo son necesarios para revelar la complejidad de la dinámica que ocurre, en tiempo real, dentro de un organismo vivo. Entre las posibles elecciones de modelos biológicos, los vertebrados representan una familia importante debido a las diversas características que comparten con el organismo humano. El desarrollo de un embrión, la interacción entre el sistema inmunitario y los patógenos, el efecto de un fármaco y las actividades celulares son ejemplos de aplicaciones que requieren observaciones in-vivo en modelos de vertebrados, como el pez cebra y el ratón.

La microscopía de fluorescencia es uno de los principales métodos mediante los cuales se pueden grabar imágenes, de alto contraste, de estructuras biológicas específicas. Utilizando microinyecciones o líneas transgénicas, es posible inducir una expresión de proteínas fluorescentes en la muestra y entonces puede ser observada a través de dichos microscopios. Existen varias técnicas de microscopía de fluorescencia, entre ellas las más utilizadas son la microscopía “widefield” (WM) y la microscopía “confocal” (LSCM). En WM, una sola imagen en 2D representa el volumen entero de la muestra, por lo cual la información de profundidad se pierde. Por otro lado, LSCM puede recuperar la información en 3D con algunas limitaciones como la fototoxicidad y una velocidad de generación de las imágenes limitada.

En las últimas dos décadas, la microscopía de fluorescencia de hoja de luz (LSFM) surgió como técnica que ofrece imágenes de manera rápidas y en 3D, y que al mismo tiempo minimiza los daños colaterales de la muestra. Sin embargo, debido a la geometría de los componentes del microscopio, las configuraciones de LSFM normalmente se optimizan para una sola aplicación. Además, la gestión de las muestras no es trivial, ya que controlar su posición y mantenerlas vivas durante largos periodos de tiempo dentro del microscopio requiere una atención específica.

En esta tesis, me propuse mejorar la versatilidad que LSFM puede ofrecer, con especial atención a la gestión de muestras vivas. La conjugación de estos aspectos permitió nuevas observaciones y nuevas aplicaciones en vertebrados vivos.

En el Capítulo 1, se presenta un breve resumen de los conceptos empleados dentro de esta tesis, señalando también los principales desafíos que la tesis pretende resolver.

En el Capítulo 2, se presenta un nuevo diseño para un LSFM multimodal, que permite realizar diferentes experimentos con el mismo instrumento. Los estudios de High-Throughput se beneficiarían de este diseño, ya que conjuga la necesidad de un montaje rápido y reproducible de varias muestras con las ventajas de LSFM. Además, a partir de este diseño, también se ha desarrollado un otro microscopio LSFM transportable.

Con estos sistemas, se estudió la dinámica de la red de microtúbulos en embriones de pez cebra, describiendo características nuevas y acentuando la importancia de los experimentos in-vivo para obtener una visión completa de la muestra. Esto se describe en el Capítulo 3.

Para realizar otras aplicaciones, como la observación de la dinámica de macrófagos en el pez cebra y del desarrollo de embriones de ratón, descritas en el Capítulo 4, se establecieron protocolos de montaje específicos para las muestras, manteniéndolas vivas durante las sesiones experimentales.

En el Capítulo 5, se describe otro sistema LSFM, que permite extender los estudios de microscopía de moléculas individuales (SMM), normalmente realizados en cultivos de células, a núcleos de embriones de pez cebra vivos, que recrean mejor el entorno natural de los procesos biológicos.

Finalmente, el Capítulo 6 recapitula las conclusiones, los impactos, las integraciones futuras y los procedimientos experimentales que esta tesis permite.

Table of contents

List of Figures

List of Tables

List of Acronyms

AOTF	acousto-optic tunable filter
BFP	Back Focal Plane
dpf	days post-fertilization
DSLM	Digital Scanned Laser Light-Sheet Fluorescence Microscopy
eMTN	external microtubule network
eYSN	external Yolk Syncytial Nuclei
FoV	Field of View
GFP	Green Fluorescent Protein
GR	Glucocorticoid Receptor
HILO	Highly Inclined and Laminated Optical sheet microscopy
hpf	hours post-fertilization
hpi	hours post-infection
HT	High-Throughput
iMTN	internal microtubule network
iSPIM	inverted Selective Plane Illumination Microscopy
iYSN	internal Yolk Syncytial Nuclei
LLSFM	Lattice Light-Sheet Fluorescence Microscopy
lmpa	low melting point agarose
LS	Light-Sheet
LSCM	Laser Scanning Confocal Microscopy
LSFM	Light-Sheet Fluorescence Microscopy
LSFSMM	Light-Sheet Fluorescence Single Molecule Microscopy
MOW	Microtubule Organizational Wave
MPR	Multiwell Plate Reader
MSD	Mean Square Displacement

MT	microtubule
OPFOS	Orthogonal-Plane Fluorescence Optical Sectioning microscopy
PTU	1-phenyl 2-thiourea
SMM	Single Molecule Microscopy
SMLM	Single Molecule Localization Microscopy
SPIM	Selective Plane Illumination Microscopy
TIRF	Total Internal Reflection Fluorescence microscopy
WM	Widefield Microscopy
YCL	Yolk Cytoplasmatic Layer
YFP	Yellow Fluorescent Protein
YSN	Yolk Syncytial Nuclei

Chapter 1: Introduction and Thesis objectives

1.1 Introduction

The curiosity that drove humans to examine the surrounding world also led them to thrive to understand themselves, generating the most fundamental questions: how is life generated? What are the components of our body? How do they communicate between them? How can we control them? The quest for these answers generated huge philosophical discussions and an immense amount of knowledge, condensed within the "life science" term. Life science concerns the study of the principles underlying living organisms, and nowadays it is subdivided into various fields. With the advent of modern science, the previous conclusions derived from philosophical and theological theories have been revolutionized by the scientific method. Since its adoption, experimental researches in the most diversified fields include a fundamental step: observation.

In life science, the needed observations have been achieved also through animal and human corpse dissections, in the quest for the various components of our body. Apparatus, organs, and tissues have been identified, but new methods needed to be adopted to allow the searching for the ultimate building block of life. The early advances in the optical field came to help the life scientist. The design and construction of lenses and their adoption by Robert Hooke enabled the first visualizations in 1665 of what we now know to be a fundamental block for life: the cell [1]. Robert Hooke visualized the walls of dead cells of cork, therefore not being able to visualize their internal components. A few years later, Anton van Leeuwenhoek would use his simple microscope to firstly visualize live organisms [1]. Optical microscopy has since then become essential for the inspection of the living tissues, revealing the various components of the cells and their complexity. Many technological advances enabled optical microscopy to see the details of life, reaching uncountable progress for the biological field.

1.2 Fluorescence Microscopy

The incredible and fascinating complexity of cells has requested the need for selective visualization of the inner constituents, to be able to clearly distinguish them, understanding their morphology and their interactions. This requirement fostered the development of one of the most successful optical microscopy techniques: fluorescence microscopy [2].

Fluorescence microscopy achieves adding to the imaging process the spectral dimension, by tagging biological constituents with a fluorescent indicator, normally a protein or a dye [1,2]. This component is designed to couple with the biological structure of interest and, upon illumination with a characteristic wavelength (normally in the visible range), its electrons absorb the delivered energy and enter the excited state [2]. Subsequently, as the electrons decay toward the ground state, the fluorescent indicator releases energy in the form of light emission, at a greater wavelength with respect to the excitation one [2]. Finally, the electrons are ready for another excitation-emission cycle, as shown by the Jablonski diagram in Fig. 1.1.

The fluorescent indicator, therefore, permits highlighting one or more specific biological features of the sample, normally the presence of particular proteins, from the immense variety of constituents present within the biological material. The results are high-contrast images of the selected biological components [1]. The isolation, usage, and further development of the first green fluorescent protein (GFP) has been a ground-breaking advance in life science, which deserved the researchers Osamu Shimomura, Martin Chalfie, and Roger Y. Tsien the Nobel prize in Chemistry in 2008 [3]. Fluorescent tagging is now used in a variety of experimental combinations, and it can be induced in in-vitro (through specific processes such as immune-staining) and in-vivo studies (mainly through mRNA injections or the generation of a transgenic fluorescent line) [4–6].

Particularly, in-vivo studies refer to the analysis of the biological features within their natural environment, i.e. the living organism. In-vivo studies can elucidate

aspects such as the immune system dynamics during bacterial infection, the dynamics of single molecules, or how an entire organism forms from a single cell, just to name a few examples that could not be answered from only fixed samples or from isolated cell cultures. The ability to image through fluorescence microscopy in-vivo processes is, therefore, an essential tool for a variety of fields, such as developmental biology, drug screenings, biophysics, neuroscience, immunology, and many others.

However, it is also a complex application: when it comes to imaging a specific living sample, many factors have to be considered [7,8]. Although ideally one would like to record the smallest structures and their fastest dynamics for the whole duration of the process, the obtainable imaging parameters are tightly connected, and so a trade-off exists when it comes to imaging living fluorescent samples. To produce a series of images over time from which relevant information can be extracted, the signal-to-noise ratio (SNR) has to be high enough to be able to distinguish the feature of interest from the background. The SNR depends on the so-called photon budget, i.e. the number of emitted photons coming from a fluorophore for a given time, and detectable at the microscope [9,10]. In turn, this parameter is connected to other characteristics of the fluorescent tag: the quantum yield and the photobleaching rate [9,10]. The first is an efficiency measure of how many photons the fluorophore is going to emit with respect to the number of absorbed photons. The latter refers to the permanent loss of the fluorescent molecule of the capability to emit new photons, due to trapped electrons in the so-called triplet state, and puts an end to the excitation-emission cycles [8–10]. While increasing the excitation energy delivered to the fluorophores will increase the number of emitted photons as well, it will also increase the possibility for photobleaching, which inevitably causes the degradation of the SNR over time.

As said, live imaging experiments need to consider the sample health as one of the key parameters, being the aim of the session the recording of a dynamic process ideally in its original and unperturbed form. Unfortunately, visible light can be absorbed by organic molecules naturally present within the cells, such as porphyrins and flavins [11]. Through this absorption process and subsequent reaction with oxygen, these molecules degrade generating reactive oxygen species (ROS) [11,12]. ROS are also generated as a product of the normal functioning of cells, as they can act as signalling molecules in different physiological processes [8]. However, an excessive amount of these products, which include superoxide radicals, hydroxyl radicals, and hydrogen peroxide [11], can result toxic to the biological environment and interfere with the physiological conditions of the sample. As an example, a high concentration of ROS molecules can trigger the cell to exit the cell cycle or produce DNA and mitochondrial damages, or inactivation of enzymes, and with time it will lead to the cell's apoptosis [8,11]. These damaging effects are always induced when illuminating the sample and their effect on the biological environment is directly proportional to the excitation power. Besides the direct absorption of light by molecules naturally present in the cell, ROS can be generated also by the introduced fluorophores. When they are excited, fluorophores can become degraded as a result of a reaction with oxygen [11], exiting the excitation-emission cycles and causing the previously mentioned photobleaching. During this photobleaching, ROS can be generated which then interfere with the biological environment as previously explained [11]. Thus, photobleaching and phototoxicity are two different but related major constrictions in fluorescence microscopy that can limit the duration of an experiment due to insufficient SNR or due to an unhealthy sample [11]. As consequence, while illuminating the sample with high excitation energies will increase the SNR, it will also accelerate the photobleaching and phototoxicity processes.

Another option to increase the SNR of the images is to adopt a longer exposure time to permit the collection of more photons. Nevertheless, this is at the expense of the temporal resolution, i.e. the minimum time interval between the production of two images. Besides that, the bigger the volumetric FoV, i.e. the portion of the sample that fits within the images both in the lateral and depth directions, the longer the acquisition time will be for the selected volume and consequently the temporal resolution will worsen. The lateral FoV furthermore is defined by the overall magnification of the system which in turn, in combination with the characteristics of the microscope's objectives and detectors, can influence the overall spatial resolution of the system, i.e. the minimum distance at which two points within the sample can be distinguished between each other at the generated image.

Additionally, a physic limitation exists for the spatial resolution, described by Ernst Karl Abbe in 1873 and named the diffraction limit [1]. When imaging a single point through a lens, due to the wave nature of the light, diffraction occurs. This results in the enlarging of the image produced by the point forming a pattern known as the Airy disk and limiting the spatial resolution. The diameter of the Airy disk is correlated to the wavelength (λ) of the emitted light and the numerical aperture (NA) of the lens employed. The minimum Airy disk diameter practicably obtainable results in around 250 nm, which is still too large for the correct visualization of many sub-cellular features. Some fluorescence microscopy techniques (see [13] for a complete review) bypass this constriction and obtain so-called super-resolution images, but their spatial resolution is highly dependent on the excitation power and the achievable SNR. In these cases, high-energy illumination schemes or long exposure times are used, which highly limit the usage of such techniques for in-vivo applications.

When imaging live samples it is essential to find a trade-off between the mentioned imaging constraints. Their interdependency and the examined considerations make it very challenging to obtain the best of one of the parameters without having to

sacrifice the others: often it is the biological application itself that will dictate the best trade-off. These dependences and the resulting live imaging factors trade-off, also known as “pyramid of frustration” [8], is resumed in Fig. 1.1B.

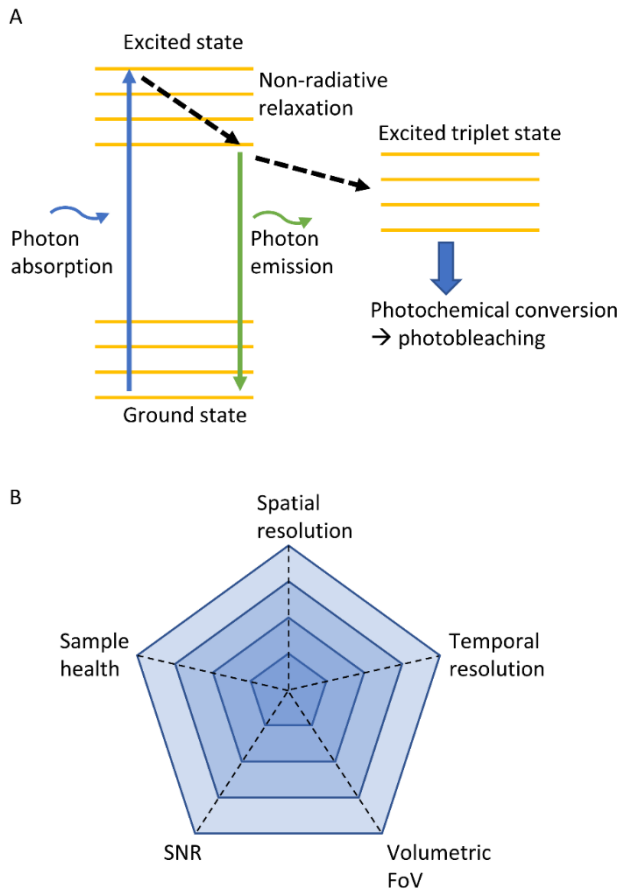

Figure 1.1: Principles of fluorescence microscopy. (A) Jablonsky diagram for the energetic transitions underlying fluorescence emission. The incident photon is absorbed (in blue) delivering the needed energy for the excitation of the electrons from the ground state towards the excited state. The decay of the electrons back to the ground state release the energy in radiative form (in green) which is the emitted fluorescence. Trapped electrons in the triplet state give rise to photobleaching. (B) The live imaging trade-off. The principal microscopy parameters correspond to the vertexes of a polygon. Achieving the maximum of one of the parameters will be at the expense of the others.

Despite this restriction in the imaging parameters’ choice, the adoption of fluorescent microscopy and the achievements in fluorescent tagging techniques have led to countless advances in the understanding of how biological structures form, work, and interact with each other. Likewise, the development of various

microscopy techniques based on the fluorescence principle allowed reaching novel performances and applications [14].

One of the simplest fluorescence microscopy configurations is Widefield Microscopy (WM). In WM the whole sample is illuminated and the same objective is used to collect the emitted fluorescence, which is then projected onto a camera chip, converting a volumetric sample into a 2D image [2,14] (Fig. 1.2A). Although simple and fast, the imaging process of WM can only in a limited depth recover the position in depth of the imaged structures, and not accurately. Moreover, the collected photons are generated not only from the fluorophores at the objective's focal plane but also from the below and above sections, which inevitably induce blurring and the presence of high background intensity in the resulting images [2,14].

To overcome these problems, Laser Scanning Confocal Microscopy (LSCM, or simply "confocal microscopy") has been developed. In LSCM, the sample is illuminated with a focused beam of excitation light [2,14,15]. This produces the excitation of fluorophores in an extended part of the sample's volume as well but, thanks to a pinhole positioned in the detection path, only the fluorescence generated at the focal point is allowed to pass, reaching the point-detector (photomultiplier). Instead, the photons emitted by the fluorophores positioned above or below the objective's focal plane are filtered out and do not participate in the formation of the image [2,14] (Fig. 1.2B). This approach produces huge impacts on the final images. Firstly, the background intensity is highly reduced, increasing the contrast and ultimately the spatial resolution of the system. Secondly, by rejecting the out-of-focus light, only the portion of the sample at the focal plane is imaged: by displacing the sample in the depth direction, various sections can be acquired and, by stacking them together, the entire volume can be reconstructed in 3D. Therefore, confocal microscopy enables the so-called optical sectioning, i.e. the capability of retrieving the precise depth information from the volumetric images.

Confocal microscopy however still suffers from some limitations. The illumination and detection processes are done through a point-by-point raster-scanning approach, i.e. only the image of one point of the focal plane is retrieved for each exposure time, which makes confocal microscopy relatively slow compared to other techniques. Moreover, as the illumination is performed through a highly focused cone of light, it is prone to scattering and absorption events within the sample, limiting the achievable penetration depth. Besides that, extended portions of the sample are illuminated multiple times during the volume acquisition. Consequently, photobleaching and phototoxicity effects might occur, posing a substantial limit to the duration of the imaging session, either due to the decay of the SNR or due to toxicity induced to the specimen.

The principles underlying WM and LSCM are depicted in Fig. 1.2.

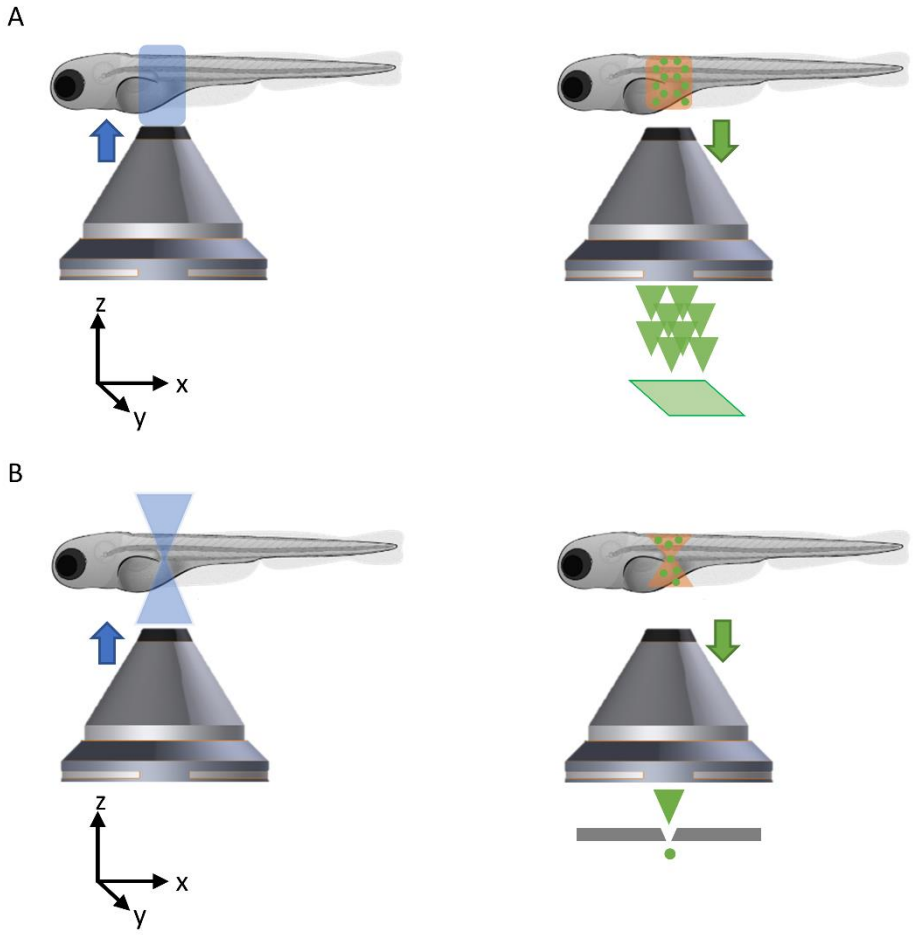

Figure 1.2: Widefield and confocal microscopy working principles. (A) In WM a large portion of the sample is illuminated (left panel) and all the fluorophores within that volume are excited (right panel). The collected photons from the entire volume are projected on a single image, losing the depth information. (B) in LSCM, a highly focused beam illuminates the sample (left panel). Although all the fluorophores within the illuminated volume are collected (left panel), only the photons coming from the detection focal volume are contributing to the final image. Blue indicates the illumination radiation, green indicates the fluorophore emission, and orange indicates the potentially photobleached areas. x and y represent the lateral directions, z represents the depth direction. Note that (B) is representative for the LSCM imaging of only a single point. During the acquisition of a plane (volume), the excitation and relative photobleaching extends also in the lateral (depth) directions and therefore it could be more intense than in the WM case.

1.3 Light-Sheet Fluorescence Microscopy

In the last decades, a novel approach has been developed that solves many of these aspects, namely Light-Sheet Fluorescence Microscopy (LSFM). In its canonical implementation, LSFM uses two different objectives placed perpendicularly to each

other, one dedicated to the illumination of the sample and the other one dedicated to the collection of the emitted photons.

Through the optical elements present in the illumination path, a plane of light (called light sheet, LS) is generated and delivered to the specimen by the illumination objective. In this way, the excited fluorophores are all laying on the same plane (defined by the coordinates x and y), which is made to correspond with the focal plane of the detection objective. This objective will collect the emitted light from the whole illuminated slice of the sample. No pinhole is here necessary, because all the photons are coming from the same in-focus plane. They are therefore projected onto the chip of a camera (a plane-detector), which can discriminate the position of the fluorophores in the lateral directions, producing an image of the entire excited plane. By translating the sample in the depth (defined by the z coordinate) direction, i.e. across the LS, and repeating the process, the various slices of the specimen are illuminated and imaged leading to the volumetric acquisition. This set of images is called “z-stack”.

This microscopy configuration enables several advantages over the previously mentioned techniques. Firstly, it is much more energetically efficient with respect to confocal microscopy: as no pinhole is present here, all the fluorescence collected by the detection objective can contribute to the final image. In turn, this efficiency permits to lower the power needed at the illumination, contributing to lower the photobleaching and phototoxicity effects. Secondly, as only the slice of the sample to be imaged is illuminated, LSFM offers intrinsic optical sectioning capability, low background, and it avoids illuminating multiple times the same regions, further limiting photobleaching and phototoxicity. Thirdly, the low divergence of the LS limits the scattering within the sample, achieving to excite deeper structures within the sample with respect to confocal microscopy. Finally, as an entire slice of the specimen is imaged during the same exposure time and the image is projected on a camera sensor, LSFM results in a fast volumetric microscopy technique. Additionally,

modern scientific cameras offer higher quantum efficiencies (between 80% to 95%) than point detectors (between 40 to 60%) such as the PMT or APD used in LSCM, therefore increasing the overall SNR of the images generated by LSFM.

Altogether, these advantages have made LSFM an optimal tool mainly for developmental biology, enabling the recording of large developing samples and their inner structure for hours, without significant photobleaching and phototoxicity effects. The working principle of LSFM is resumed in Fig. 1.3.

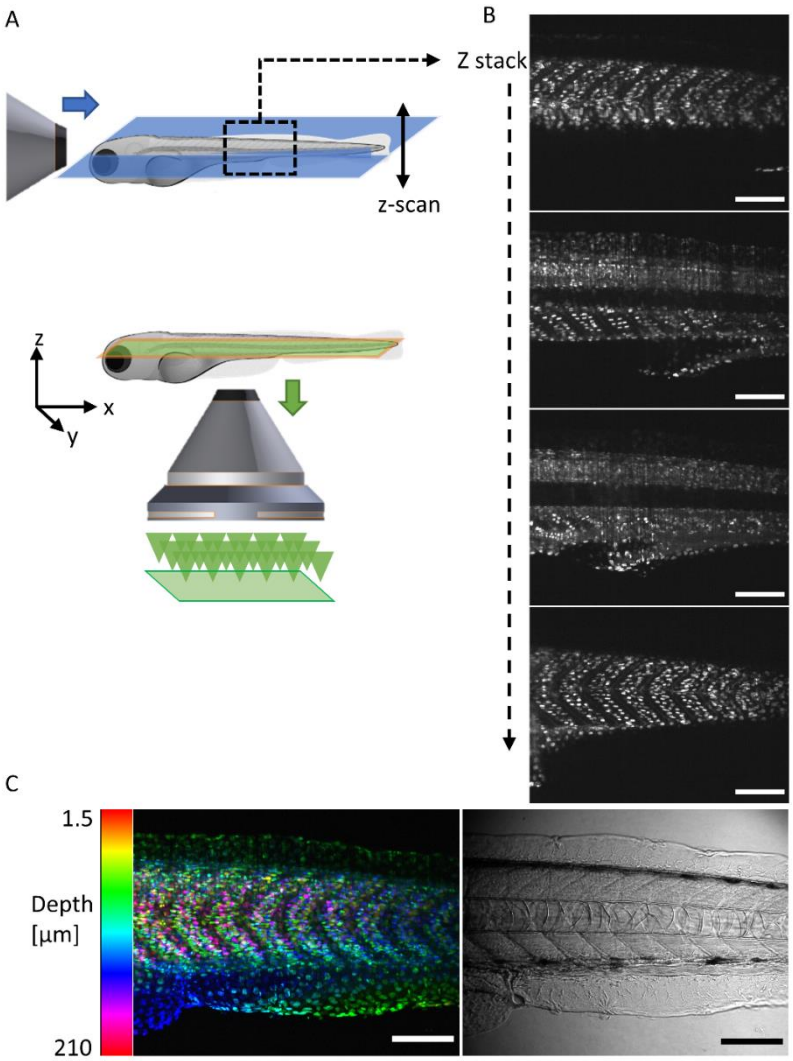

Figure 1.3: LSFM working principle. (A) In LSFM a light sheet is used to illuminate a section of the sample (upper panel). All the photons coming from the excited plane are collected and contribute to the final

image (lower panel). Blue indicates the illumination radiation, green indicates the fluorophore emission, and orange indicates the potentially photobleached areas. x and y represent the lateral directions, z represents the depth direction. Note that only the slice currently under investigation is illuminated. (B) By translating the sample across the LS, a set of images is obtained (the z-stack) in which each image is depicting a section of the sample in depth. (C) The z-stack can be used to reconstruct in 3D the sample, or to obtain a global view of the structure of interest through a maximum intensity projection (left panel, in which the depth is color-coded). On the right panel a bright field image of the sample, for comparison. The sample here is a 3dpf (day-post-fertilization) zebrafish in which all nuclei are tagged with the mCherry fluorophore (H2A:mCherry). Scale bars 200 µm.

As explained above, one of the main characteristics of LSFM is the de-coupling of the illumination from the detection optical path. This produces consequences also in the determination of the Point Spread Function (PSF) of the system. The PSF is the diffraction pattern in 3D produced by an infinitesimal point source, when imaging it through an optical system. As already mentioned, this is due to the wave nature of the light, and it is a measure of the quality of the produced images. From the 3D shape of the PSF, which mainly depends on the objective specification (but also on the quality of the subsequent optical elements), the lateral (i.e. in the xy plane) and depth (i.e. along the z direction) resolutions can be calculated.

In confocal microscopy, a single objective is used, which dictate the single PSF from which both the lateral and axial resolutions are obtained. In LSFM instead, the use of two (usually) different objectives permits to separate, until a certain degree, the lateral from the depth resolution. In fact, the optical lateral (or transversal) resolution is determined basically by the numerical aperture (NA) of the detection objective, as in WM. A common criterion to determine it, which is here used for the definition of transversal resolution in a LSFM system, is given by the Rayleigh criterion [16], which assume the resolution of the system to be the radius of the Airy disk laying on the middle plane of the 3D PSF of the detection objective:

$$R_T = \frac{0.61\,\lambda_{em}}{NA_{Det}}$$

Here, R_T is the transversal resolution, λ_{em} is the emission wavelength of the fluorescent indicator, and NA_{Det} is the NA of the detection objective. Note that this formula provides the lateral resolution of the LSFM microscope only if the full optical

power given by the detection objective can be actually used. This means that the following tube lens should be selected so that the overall magnification, coupled with the pixel size of the camera chip, permits to satisfy the Nyquist criterion. If this is not satisfied, the above formula gives the resolving power of the used detection objective alone, and the lateral resolution of the overall system is given by [16]:

$$R_T = 2\frac{px_{size}}{M}$$

where px_{size} is the dimension of the (square) pixel of the camera chip, and M is the magnification of the detection arm. In the simplest case (an objective followed by a tube lens) M is equal to the ratio between the focal lengths of the tube lens and the objective.

The axial resolution instead is formally given by the product of the illumination and detection PSFs [17]. Practically however, it is assumed that the axial resolution of the LSFM system is equal to the light sheet thickness, which depends on the focusing power of the illumination objective(s), and therefore defines as well the optical sectioning capability [16]. When using Gaussian beams for the illumination, which is the most common practice, a relationship exists between the thickness of the focused beam at its waist, and the Rayleigh range, i.e. the distance along the propagation axis at which the diameter of the beam increases by a $\sqrt{2}$ factor in respect to its waist diameter. In particular:

$$R_{axial} = D_{beam} = 2\frac{n\lambda_{ex}}{\pi NA_{ill}}$$

where R_{axial} indicates the axial resolution, D_{beam} the diameter of the beam at its waist, n the medium refractive index, λ_{ex} the excitation wavelength, and NA_{ill} the NA of the illumination objective. The Rayleigh range z_r is derived as [16]:

$$z_r = \frac{\pi\,(D_{beam}/2)^2}{\lambda_{ex}}$$

Therefore, the smaller the waist diameter D_{beam} (i.e. more focused the beam), the shorter the Rayleigh range z_r (i.e. the more diverging is the beam). Consequently, a highly focused Gaussian LS will provide high sectioning capability at its waist, but the length over which it can be considered uniform will be short. This is of extreme importance, as a highly diverging LS will illuminate also portions of the sample far from the focal plane of the detection objective, delivering blurred images and losing the excitation selectivity.

Thus, a compromise must be accepted between the axial resolution of the system (and its optical sectioning capability) and the usable length of the LS, i.e. the portion in which its thickness can be considered constant. This last parameter, determined as the double of the Rayleigh length, defines the illumination field of view along the propagation direction (FoV_x). The height of the LS instead defines the illumination field of view along the other lateral direction (FoV_y). The intersection between the total illumination FoV (FOV_{ill}) and the FoV determined by the magnification of the detection arm (FOV_{det}) gives the overall FoV, in which a sample is uniformly illuminated and detectable by the system. See also Fig. 1.4A.

1.3.1 LSFM: State of the art

The first implementation of a LSFM-like instrument, called “ultramicroscopy”, has been described by Siedentopf and Zsigmondy in 1903 [18,19]. They used a slit aperture in order to illuminate gold particles with sunlight, and observed them through a perpendicular optical path. A similar concept was then developed in the 1990s by Voie et al. to image cleared and fluorescently stained guineapig cochlea through the so-called Orthogonal Plane Fluorescence Optical Sectioning (OPFOS) [20,21]. Although the OPFOS implementation already contained the key elements and concepts of modern LSFM, only after the Science article published by Huisken et al. [22], which applied the technology to the in-vivo imaging, the advantages offered by LSFM have awaken an increased interest.

From 2004, a fluorescence microscopy revolution initiated, which led to the development of various LSFM versions in a continuous quest for improvement in illumination and detection strategies.

1.3.1.1 LSFM: Illumination strategies

As explained above, LSFM relies on the illumination of a single slice of the specimen through a light sheet. Therefore, the quality of the LS is of outmost importance and it can be evaluated through three different parameters: its thickness (D_{beam}), its capability to penetrate the sample, and the portion of uniform illumination (FoV_x). An ideal LS is therefore thin, long, and insensitive to scattering events within the sample. In practice however this is not achievable, but many efforts have been made in order to increase the illumination quality, and again the final application will dictate the best illumination strategy.

The first LSFM implementations used solely a cylindrical lens [20,21,23]. A collimated laser beam passing through this kind of lens would be focused only in one direction, creating the needed plane of light. Of course, the numerical aperture (NA) of conventional cylindrical lenses is limited and therefore the produced LS would be generally thick.

Although this might be enough for the imaging of samples of the order of centimeters and millimeters in size (such as fixed mouse brains), in which a larger FoV is preferred over the sectioning capability, it poses a fundamental limit to applications in which the sectioning of smaller samples (having a size of hundreds of micrometers or smaller) is needed. Adding an objective in the illumination path will permit the use of its higher focusing capability to create a thinner (but shorter) LS (Fig. 1.4B). The LSFM configurations that use a cylindrical lens for the generation of this “static” LS are usually referred to as SPIM (Selective Plane Illumination Microscopy), from the work of Huisken et al. [22] (Fig. 1.4B).

The static LS, however, being mono-directional, can be blocked by strongly absorbing sample structures which do not permit to illuminate properly the

following portion of the specimen. This is known as “shadowing effect” and it can create stripes of high and low contrast levels in the images. Moreover, the LS illuminating large samples (in the order of hundreds of micrometers and above) can be subject to absorption, scattering, and refraction effects from the specimen itself. This results in a proper illumination of only the first portion of the sample, while the subsequent parts result weakly excited, or not illuminated at all.

A possible solution to these problematics has been proposed by the Multidirectional SPIM (mSPIM) [24], in which a pivoting mirror is introduced in the illumination path, conjugate with the front focal plane (FFP) of the illumination objective. In this way, the LS is pivoting around a point located in the sample, enabling to illuminate areas that would be otherwise shadowed by previous structures. Besides this, the illumination arm is duplicated (implemented also in the same year in [25]) so that the specimen can be excited from both sides alternatively. This approach generates two images, one for each side of the sample, which will be digitally fused together. In doing so, the effective FoV is doubled, permitting the *in toto* visualization of big samples.

Another approach for LSFM is called Digital Scanned Laser Light-Sheet Fluorescence Microscopy (DSLM) [26], and it generates a “virtual” LS (Fig. 1.4C). Here, a laser scanner (usually a galvanometric mirror) in the illumination path is conjugated to the back focal plane (BFP) of the illumination objective. This configuration converts the angular displacement introduced to a collimated laser beam by the scanner into a lateral displacement over the xy plane of the beam focused by the objective. Hence no cylindrical lens is used and the “virtual” LS is produced by fast scanning the beam (Fig. 1.4C). This results in a more flexible LS, compatible with further excitation and detection strategies. Still, as the original implementations of both SPIM and DSLM are based on Gaussian beams, they suffer from the above-mentioned compromise between sectioning ability and achievable FoV.

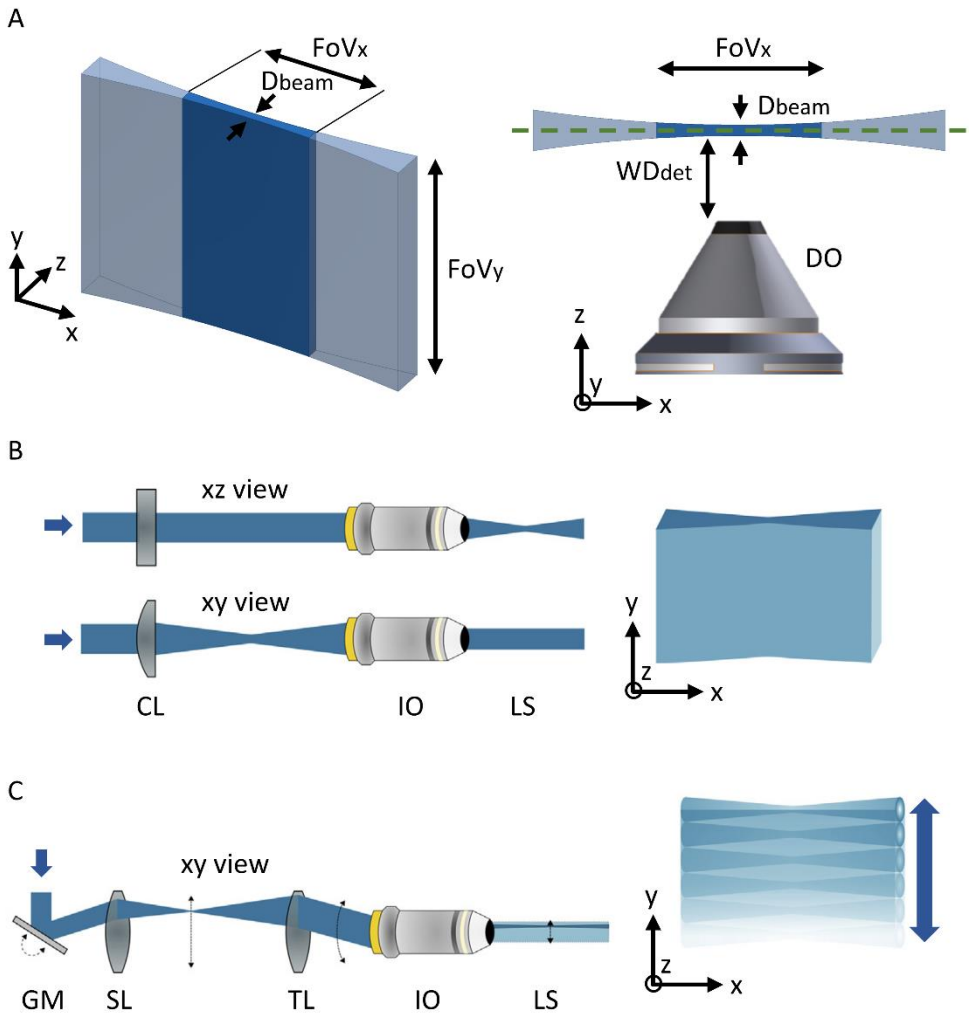

Figure 1.4: LSFM parameters and first implementations. (A) Side (left panel) and top (right panel) views of a Gaussian light sheet (LS). The illumination Field of View (FoV_{ill}) is defined by its height (FoV_y) and width (FoV_x). The thickness of the LS is defined by the diameter at its waist (D_{beam}). The region of the LS considered uniform is highlighted in dark blue. The detection objective (DO) is placed at its working distance (WD_{det}) from the LS, so that the entire illuminated plane results in focus. (B) The working principle for the SPIM configuration, in which a cylindrical lens (CL) generates the "static" LS. (C) The working principle for the DSLM configuration. The scan lens (SL), the tube lens (TL), and the illumination objective (IO) convert the angular offset introduced by the galvanometric mirror (GM) into a lateral movement on the sample plane, generating a "virtual" LS. Figures B and C are adapted from Kromm et al. [15]

The possibility offered by DSLM to create a LS through the translation of a single focused beam has been instrumental to the development of alternative illumination strategies.

Firstly, to increase the achievable penetration depth, two-photon-based LSFM systems have been implemented [28,29]. Being the illumination wavelength in the near-infrared spectrum, this excitation allows imaging deeper into the sample, being less prone to scattering events with respect to the conventional one-photon excitation. However, the excitation relies on the two-photons absorption effect, which limits the achievable FoV in the propagating direction.

Subsequently, Bessel beams have been used to generate the virtual LS through DSLM, also combined with two-photon excitation [30,31]. Bessel beams do not follow the above described Gaussian propagation, being (mathematically) invariant along the propagation direction. This means that their use in LSFM permits the generation of long and thin virtual LS, effectively increasing the achievable illumination FoV. On the other hand, Bessel beams present side lobes concentric to the "principal" beam, which can excite fluorophores far from the detection focal plane and thus deliver burred images, especially in applications in which the subcellular optical sectioning is desired.

Following approaches have used multiple non-interacting Bessel beams at the same time, i.e. not following the classical DSLM principle in which a single beam (Gaussian or Bessel) is scanned along the y direction to form the virtual LS. In this way, and utilizing the principles of Structured Illumination Microscopy (SIM, [32]) the 3D resolution could be enhanced [33].

Following that, further developments considered the interaction of the array of Bessel beams delivered at the xy plane and the modulation of their distance to generate different periodic interference patterns. The result of this method is called Lattice Light Sheet (LLS) [34,35]. Two main modalities have been individualized: the

SIM mode, which delivers super-resolution images by stepping the LLS in the lateral direction, and the dithered mode, in which the LLS is oscillated along the y direction to produce a time-averaged sub-micrometer LS [34]. Lattice LSFM (LLSFM) has offered unprecedented optical sectioning capability over long FoVs, especially useful for sub-cellular imaging.

1.3.1.2 LSFM: Detection strategies

On the detection side, several developments have been dedicated to increasing the speed of the volumetric acquisition. Classical LSFM systems use a mechanical scanner to translate the specimen across the LS, in order to illuminate its various slices and to keep the illumination and detection planes coincident. While effective, the mechanical scan might be too slow for certain applications.

One solution has been implemented in [36], in which the sample is kept fixed and the illumination and detection optics are translated along the z-direction. Here the detection and the illumination optics (implemented through optical fiber) are connected together so that the distance between the collection objective and the illuminating LS is maintained fixed. The apparatus is mounted on a piezo scanner, that can move the optics along the z direction producing the z-scan of the sample, which remains static. In this way, the speed of the volumetric scanning is given by the velocity of the piezo scanner, which is much faster than the motors usually used for sample translation. Nevertheless, this approach needs to move a heavy part of the microscope in order to maintain the relative position between illumination and detection planes.

An alternative but similar approach is to de-couple the illumination and detection optics. Here the LS is moved sequentially along the z-direction by conjugating a galvanometric mirror to the BFP of the illumination objective, similarly to what was implemented in DSLM (but in the z direction). On the detection side, however, the focal plane of the objective must follow the displacement along z of the illumination LS (Fig. 1.5A). This is obtained again by a piezoelectric stage, but it would be

connected solely to the detection objective, translating it along the z direction synchronously with the LS scanning and enabling its refocusing [34,37].

An all-optical approach for increasing the acquisition velocity has been presented in [38]. The illumination LS would be translated along z through a galvanometric mirror, as mentioned previously. To enable the refocusing, an electrically tunable lens (ETL) is inserted in the collection path, conjugated with the BFP of the detection objective (Fig. 1.5B). The ETL is a device formed by a liquid crystal lens whose curvature varies with the applied voltage. As the focal length of a lens is a function of its curvature, by modulating the applied voltage one can vary the focal length of the ETL, and therefore controlling it digitally. In their implementation, Fahrbach et al. [38] used the modulation of the focal length of the ETL introduced in the LSFM detection path to change the position of the focal plane of the collection objective, synchronizing it with the oscillation in z of the exciting LS and enabling to record the zebrafish beating heart.

Although effective, a faster method has been implemented in [39]. Here, as previously, the sample can be maintained in a fixed position and the LS is translated along z to perform the volumetric scan. However, the detection focal plane is not displaced to follow the LS. Instead, wavefront-coding (WFC) techniques are implemented to extend the Depth of Field (DoF) of the detection objective. This is obtained by placing a cubic phase mask conjugated to the exit pupil of the detection objective through a deformable mirror (Fig. 1.5C). This phase mask reduces the sensitivity to defocus of the objective, extending its DoF [39]. As a result, the illuminating LS can be placed anywhere within this extended DoF and the resulting images will all present the same quality. It should be noted that the produced images result distorted by the introduced aberration, but as they all show the same (known) distortion independently from their corresponding position in depth, this can computationally be compensated for through deconvolution. Therefore, through this approach, the volumetric imaging speed is no more dictated by the velocity of

the refocusing of the detection focal plane, but by the speed of the scanning LS (that can reach the KHz regime) and the framerate of the camera.

To increase the image contrast instead, a “confocal slit” approach has been developed [40], which makes use of the reading modality of the sCMOS camera. The camera chip, formed by the various pixels, can detect the incident photons in two main modalities. The first one is the “global shutter”, in which the whole chip is active at the same time (the exposure time) and all the incident light is converted in electrons, and therefore in the final digital signal forming the image intensity. The second mode is called “rolling shutter” and it activates the rows of the camera chip with a subsequent order, i.e. at a certain time, only a selected number of rows of the chip are active and ready to convert the incident photons into electrons. In this way, a digital slit is generated, which translates through the whole chip, and its width can be electronically controlled. By conjugating the translation of the digital slit with the translation of the focused beam on the sample plane in the DSLM scheme, this approach can reject a big portion of the photons generated by the scattering of the beam within the sample, that would otherwise contribute in the blurring of the final image (Fig. 1.5D).

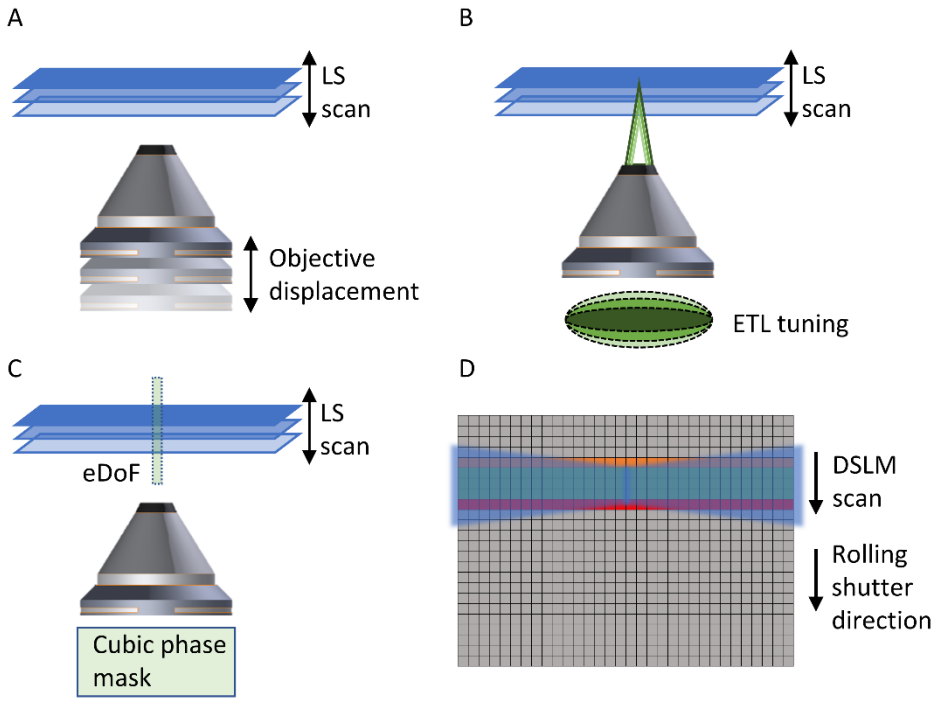

Figure 1.5: LSFM detection strategies. (A-C) When scanning the LS in the z-direction, the illuminated plane must be kept in focus. This can be accomplished by translating the detection objective in z as well (A), or by the use of an ETL for remote focussing (B), or by extending the objective's DoF (C). (D) Through the rolling shutter modality of the camera, a digital slit of active pixels (green) can be generated. This is translated along the chip, synchronized with the beam-DSLM scanning to avoid the conversion of incident photons generated by the scattering of the beam within the sample, that are projected in the inactive pixels (grey). Orange indicates the rows in read-out phase, red indicates the rows that are going to start the exposure.

Additional information from the collected photons are coming from their spectra. The emitted wavelength is of course depending on the fluorescent marker used, which in turn is conjugated to a particular feature of interest of the sample under observation. It is common to have specimens showing two different fluorescent markers, or channels, that become instrumental in studying the interactions between two biological structures.

The recording of multiple channels can be implemented either sequentially, by changing the excitation laser and emission filter according, or simultaneously, either through the insertion of a dichroic mirror in the detection path and the use of two cameras or through similar commercial solutions [41].

Alternatively, interesting solutions that can be applied on samples showing up to five different channels have been developed by conjugating hyper-spectral imaging with LSFM [42]. A DSLM scheme is used to profit from its single-line excitation. An additional de-scanning mirror in the detection path is used to project the collected photons coming from the currently illuminated line on the sample plane toward a diffracting unit. In here, a grating mirror will spatially separate the spectral information across the rows of the camera chip. This results in the generation of a 2D image containing the whole spectra (and therefore all the channels simultaneously) for each single line excited in the specimen plane. On the recorded data a linear unmixing algorithm [42,43] is applied, which can determine and deconvolve the spectra of each of the fluorophores used finally retrieving the separation of the various channels.

1.3.1.3 LSFM: Objective configurations

As mentioned before, the first LSFM configurations use two optical elements placed perpendicularly between each other [22,26] (Fig. 1.6A). However, especially when the aim is to image the whole volume of big samples such as embryos, only the first part of the specimen can be efficiently illuminated, due to the absorption and scattering events that limit the penetration depth of the LS. On the collection side as well, only the portion of the specimen facing the detection objective can be properly imaged. Again, absorption and scattering events happen within the sample also for the emitted photons. While the photons generated closer to the detection objective can be collected without being heavily scattered, photons coming from the opposite side diffuse and deviate while traveling toward the objective, losing their spatial information and leading to blurred images. The magnitude of these problematics is of course proportional to the sample thickness and transparency.

Therefore, solutions have been implemented firstly by adding a second illumination arm [24,25] (Fig. 1.6B), and subsequently by adding also an additional detection objective [44,45] (Fig. 1.6C). In this way, the four quadrants of the sample volume

can be efficiently illuminated and imaged. In a particular implementation, all four objectives work (sequentially) as both illumination and detection optics, in order to speed up the volumetric acquisition and obtain isotropic resolution [46]. Similar results can be obtained also by setups using only two objectives but implementing a sample rotation, which permits to expose sequentially the various sides of the sample to the objectives.

When collecting multiple views, either through multiple illumination/detection objectives or through sample rotation, each of the generated datasets will exhibit a degradation on the opposite side of the current illuminator. Therefore, those views must be fused into a single dataset through a dedicated algorithm as implemented in [47] and in [48]. In the latter, fluorescent beads are inserted into the sample's embedding medium, working as fiducial markers. The unique beads constellations so generated identify the single beads over the different views, so that the orientation of the sample can be retrieved by the dedicated processing software. The dataset generated from the acquired multiple views fused through these algorithms [47,48] therefore presents isotropic resolution in the three spatial dimensions and uniformity of the image quality, properties extremely valuable when imaging relatively large samples.

When instead imaging small samples such as cells, which are usually cultured in petri dishes horizontally positioned, the objectives can be placed at 45° with respect to the optical table, such as in iSPIM and diSPIM, in both the upright and inverted (or "open-top") versions [37,49,50] (Fig. 1.6D-E).

For certain subcellular applications, a very thin LS conjugated with a high-resolution power (NA>1.0) is desirable, but this requires having high NAs at both the illumination and detection optics. The physical size of such objectives and the particular need of maintaining (at least) two objectives perpendicularly between each other for the implementation of an LSFM scheme, makes this task mechanically impossible. Fortunately, researchers have developed alternative systems, which

relax the need for orthogonality between the objective, by using additional optical elements.

It is the case for example of Reflective LSFM (RLSFM), which positions a medium-high NA objective, used for the illumination, facing the detection objective (Fig. 1.6F). The produced LS is then deviated at 90° through a micro-reflective surface in order to coincide with the focal plane of a high NA (up to 1.4) detection objective [51–53].

Another approach instead, called single-objective SPIM (soSPIM), only requires a single high-NA objective while maintaining the orthogonality between illumination and detection. In this case, the illuminating LS is generated on the side of the high-NA objective and again reflected at 90° through a micro-mirror, to illuminate the focal plane [54–56] (Fig. 1.6G). Finally, a more sophisticated method also requires a single objective but implements an oblique illumination (Oblique Plane Microscopy, OPM) [57–59]. The LS is again delivered from the side of the optics and it scans obliquely the sample (Fig. 1.6H).

Further configurations have been also devised for specific applications, such as for increasing the imaging throughput, and they will be discussed as well in the related chapters.

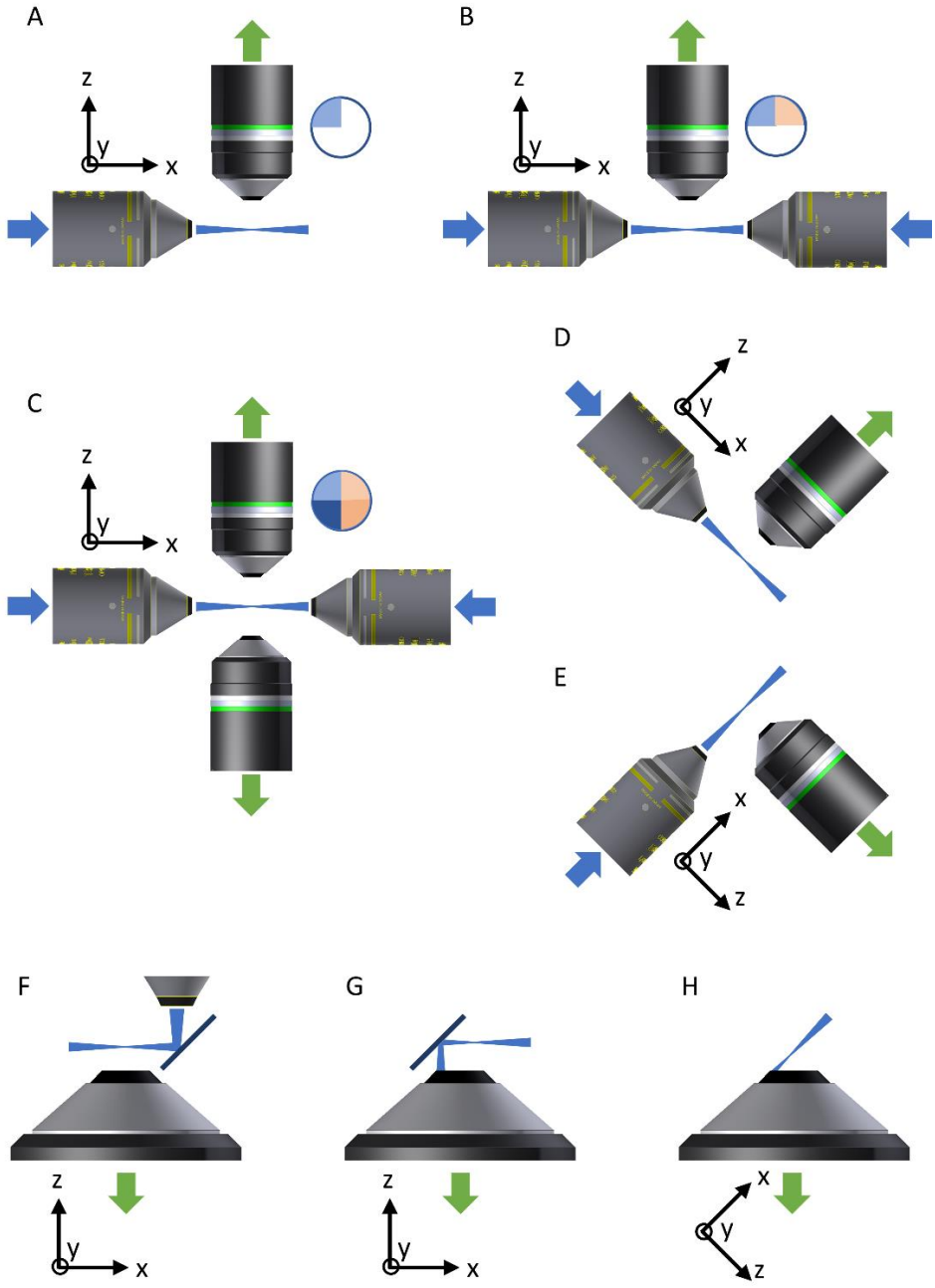

Figure 1.6: LSFM objective configurations. (A) The classical configuration with two objectives applied on big samples permits to obtain a sharp image only over one quarter of the volume. Configurations with two illumination objectives (B) illuminate the sample more efficiently and the use of two detection objectives (C) permits to increase the portion of the volume efficiently illuminated and detected. (D-E) iSPIM configuration in the upright and inverted versions enable the use of classical horizontal sample supports. (F-H) Configurations bypassing the need for orthogonality between two objectives permits to use higher NAs in the collection path, such as RLSFM (F), soSPIM (G), and OPM (H).

1.3.1.4 LSFM: Sample mounting

A critical aspect in LSFM concerns the insertion of the sample into the microscope. In conventional techniques like WM and LSCM the sample is usually positioned on a horizontal support such as petri-dish, multi-well plates, or sandwiched between a glass slide and a coverslip: this means that the specimen can be visualized only from a single side, and within a limited depth.

In LSFM instead, due to the orthogonality of the illumination and detection optical paths, the sample needs to be inserted within the focal planes of both objectives. Additional degrees of freedom are also needed for the movement of the sample in order to perform the translations to acquire a z-stack, and eventually rotation or lateral displacements. Moreover, the imaging medium is also playing a relevant role, as the use of a specific media depends on the sample characteristics and could have an impact on the choice of the objectives, and therefore on the overall performances. Finally, as LSFM is a technique aiming at volumetric acquisition, the 3D structure of the sample must be maintained, and also, in the case of in-vivo imaging, the viability of the sample should be preserved without interfering with its natural development.

To answer those needs, imaging chambers have been designed and developed. In various cases, imaging chambers are constituted by a cubic container in which two (or more) objectives can be inserted and sealed (Fig. 1.7A). In this way, the chamber can retain a water-based imaging medium, often used for the imaging of developing embryos. Different applications will require different flexibility in the sample viability or movements, and therefore custom-designed chambers are often implemented to be adapted to the specific use.

The sample can be then embedded within an optical clear element that maintains it steady during the images' acquisition. This can subsequently be connected to a translational/rotational stage to enable the needed movements. Different choices can be made for the optical clear component, but the classical ones are low melting

point agarose (lmpa) solutions. Lmpa solutions melt at around 70° and solidify (depending on the concentration) at room temperature. When imaging live samples, the lmpa solution can be prepared with the water-based medium identified for the correct sample development, which results also ideal for the use of water-dipping objectives. Typically, the sample is dropped into the liquid lmpa solution and then aspired into a glass capillary through a plunger. Once the lmpa solution solidifies (typically within 5 to 10 minutes, depending on the lmpa concentration), an agarose cylinder containing the specimen can be partially extruded from the glass capillary (Fig. 1.7B). The agarose cylinder is then inserted in the imaging chamber and the glass capillary is connected to the translational stages.

Eventually, when low (about 0.1 to 0.5%) lmpa concentrations are used, the agarose cylinder is not stiff enough to maintain its connection to the glass capillary. In these cases, it is possible to insert the sample and the lmpa solution within a Fluorinated Ethylene Propylene (FEP) support (Fig. 1.7C). FEP is an inert material similar to Teflon, and it presents a refractive index similar to water's one (n_{FEP}≈1.33). FEP can be produced in tubes, which helps in the mounting within the LSFM imaging chamber. In this way, no extrusion is necessary and the imaging is done through the FEP tube that, in principle, should not introduce important distortions thanks to its refractive index.

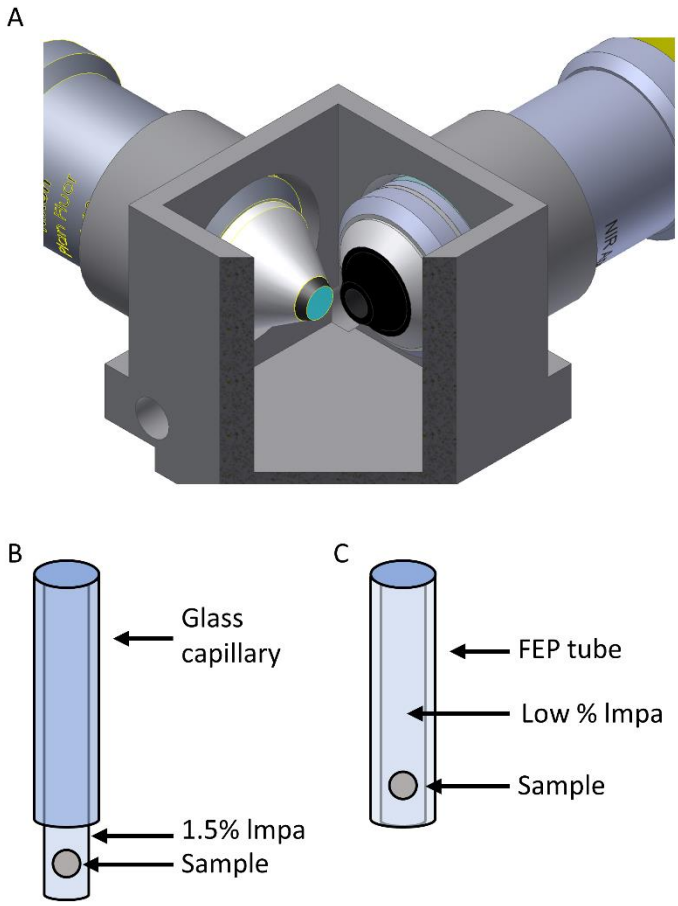

Figure 1.7: Inserting the sample into the microscope. (A) An example of an imaging chamber in which the two objectives can be inserted and sealed (cut view to ease visualization of the objectives' disposition). The chamber can then be filled in the water-based medium in which the sample can be maintained. The sample can be embedded in a high percentage lmpa gel extruded from a glass capillary (B), or within a low percentage lmpa gel supported by an FEP tube (C). The sample with its support will be inserted within the imaging chamber, between the objectives.

Precautions have however to be considered when using these mounting media. The stiffness of solidified lmpa solution is proportional to the percentage of lmpa content. This means that stiff lmpa cylinders used to embed a living specimen might constrict it and interfere with its natural biophysical processes. Similarly, a FEP tube might introduce unwanted aberration due to its cylindrical shape, or excessive wall thickness. Again, the specific application would dictate the property of the available mounting medium and imaging chamber. These and other evaluations have to be

considered when designing LSFM experiments, especially when the aim is to monitor biological processes happening in the living samples.

1.3.1.5 LSFM: Data handling

As said, the assets offered by LSFM opened up the possibility of collecting the information in 3D from multiple views, multiple channels, with high temporal and spatial resolutions, over big FoVs, and for a prolonged time. This opportunity is of course tempting for life scientists, but it also has the disadvantage of resulting in a huge quantity of data generated. Single LSFM experiments can easily pass the TB size, therefore far exceeding the usual data output of e.g. confocal microscopy, and therefore significant challenges arise when it comes to visualizing, processing, and analyzing the images.

To mitigate these effects, block-wise file formats have been developed, which permit to load only the portion of data needed for the current task, at the needed resolution. These formats, such as HDF5, N5, ZARR, and “Keller lab block” therefore permit to accelerate the visualization, annotation, and processing of the data [60].

1.4 Thesis objectives and methodology

As illustrated above, LSFM presents unique properties. It is intrinsically fast, being a plane-based approach, and it delivers low-background images thanks to an efficient excitation/collection scheme. In addition, this efficiency results in low photobleaching and phototoxicity regimes, therefore enabling the imaging of light-sensitive samples. Finally, LSFM presents increased penetration depth and intrinsic optical sectioning capability. These are key features when the aim is the in-vivo imaging: they allow to substantially improve the available temporal resolutions and durations of the imaging sessions of a biological specimen, with respect to LSCM. Moreover, LSFM makes possible the 3D description of thick samples.

However, the use of LSFM is still limited between biologists. This can be related to the fact that it is a relatively new technique, that it generates a large amount of data

needing high computational power, and that the setup itself is highly dependent on the specific application and sample. Also, in the context of large populations of samples, the unique capabilities of LSFM in terms of speed, resolution, and optical sectioning are not yet fully exploited to answer biological challenges. High-throughput (HT) approaches for imaging and analysis are still limited in LSFM, also due to the high specificity of the sample mounting procedure to the specimen itself. Additionally, the possibility of having high resolution and good optical sectioning is not yet translated into improving some particular applications. As an example, single-molecule microscopy (SMM) experiments would benefit from the integration with LSFM.

My PhD project, carried out at the Super-Resolution Light Microscopy and Nanoscopy Facility (SLN) at ICFO, aims to contribute to the overcoming of the above-mentioned limitations and explore specific novel applications for LSFM. Particularly, I focused on in-vivo imaging. In-vivo imaging is key to understanding how an organism develops from a single cell, how an external pathogen interacts with the organism, and how the cellular machinery works, besides many other biological questions.

To contribute to these research fields, I firstly developed an LSFM setup adaptable to multiple biological experiments. This was based on a modular design with components that can be interchanged, a fluidic mounting approach, and a high degree of automation. This design led toward a flexible platform enabling long-term imaging, high-speed volumetric imaging, and the capability to image several specimens in sequence to permit experiments with enhanced throughput.

Therefore, through a single platform multiple experimental designs can be performed, increasing the flexibility and usability of the setup. From this, an additional compact state-of-the-art LSFM system has been extracted, optimized for long-term imaging. In this case, the microscope follows a double illumination/double detection scheme to permit the imaging of the whole sample.

Finally, the implementation of a third LSFM system enables optical sectioning at the subcellular level and simple sample mounting of living embryos. In particular, using an iSPIM configuration, this setup enables to control the position and rotation of relatively big samples such as zebrafish embryos, and maintain them alive for long imaging sessions. This would enable the combination of SMM and LSFM, opening up new experimental possibilities that could correlate micro and macro biological processes happening in the living samples.

In-vivo imaging is also challenging: delicate samples must be maintained alive and within an environment as close as possible to the natural one. When needed, these conditions must be maintained for a long time, up to days. Therefore, within the PhD project, efforts have been made to design imaging chambers specifically adapted to LSFM configuration enabling on one side the needed environmental conditions for preserving the sample healthy, and on the other side for having a simple insertion mechanism.

Being part of the Marie Skłodowska-Curie "ImageInLife" EU project (grant agreement No. 721537), I profited from a highly interdisciplinary network including universities and companies from the biology, microscopy, image analysis, and mathematical modelling fields. This led me to the unique possibility to directly test the setups resulting from my project to specific biological questions through the foreseen collaborations and secondments. Moreover, other biological studies targeted within SLN group have been object of study through LSFM. Thus, my PhD thesis goes beyond the pure development of the setups, as I actively interact in many applications to answer specific biological questions. These are described in the following chapters.

1.4.1 The biological samples

During my PhD project, I applied the above-mentioned microscopy concepts to explore how they could contribute to various biological questions in the fields of

early embryogenesis, regenerative and immune system features, and in the quest for the imaging of intranuclear single-molecule dynamics in living samples.

1.4.1.1 The zebrafish model

Especially, I used zebrafish (*Danio Rerio*) as the main biological model. Zebrafish is a tropical fish originally found in south-east Asia, and its use in research has begun in the 1960s. Nowadays it is a common biological model used by many labs in different research fields (Fig. 1.8A), as it presents various advantages with respect to other animal species. Firstly, the zebrafish is a vertebrate, which makes it more similar to human with respect to other non-vertebrate models. It presents tissues and organs (such as the brain, muscles, eyes, and many others) with common features to the human counterpart. The sequencing of its genome found that in zebrafish orthologs for about 70% of human genes exist. Furthermore, in zebrafish exist orthologs for approximately 84% of the genes associated with human disease [61].

Zebrafish are also small, making easier and cheaper the breeding and the setting up of large zebrafish facilities, with respect to other animal models such as mouse or rabbit. In developmental biology, zebrafish are of utmost importance because embryos are fertilized and develop outside the body of the mother, resulting therefore easily accessible. Moreover, a single couple can produce hundreds of embryos, enabling studies on large populations such as pharmacological screenings [62]. Embryos are almost transparent and develop in a few hours (Fig. 1.8B), making them a perfect candidate for microscopy studies in early morphogenesis. Additionally, zebrafish are highly genetically tractable, which led to the development of a huge quantity of transgenic lines expressing different phenotypes and fluorescently labeled proteins, and they become adults relatively fast (2-3 months), which makes it easier to create and maintain a determined transgenic line.

Thanks to all these advantages, the use of zebrafish has been exponential in the biological community over the past years, and this model is nowadays a useful platform to compare, repeat and validate results between different labs.

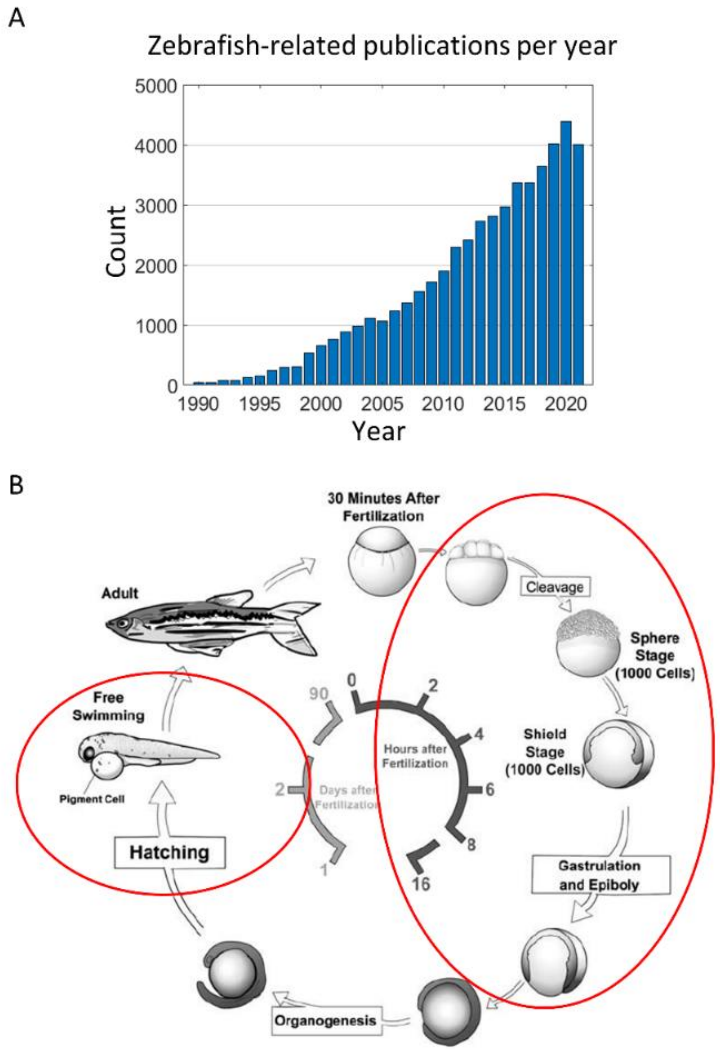

Figure 1.8: The zebrafish as animal model. (A) Graph showing the continuous growing of the interest in the usage of zebrafish as animal model over the years, visualized through the number of publications having the term "zebrafish" in the title (data source: https://pubmed.ncbi.nlm.nih.gov/). (B) schematic representation of the life-cycle of zebrafish. Highlighted are the stages at which the setups described in this thesis have been applied. Image adapted from [51].

Experiments involving zebrafish were carried in compliance with protocols approved by ICFO and by Comissió d'Experimentació Animal, Direcció General de Polítiques Ambientals i Medi Natural of the Departament de Territori i Sostenibilitat, Generalitat de Catalunya (Spain). "Neural activity recording in zebrafish larvae" (Expedient: FUE-2019-01161091; ID: PD8GZTVV7; Project: 10716). Experiments

involving zebrafish carried out at the University of Montpellier were approved by the local ethical committee.

1.4.1.2 The mouse model

As an additional biological model, the mouse embryo has also been an object of my investigation. Being a mammal, the mouse is much more similar to human, and it is nowadays by far the most extensively studied mammal. The restriction on the study of human embryos makes those samples interesting to understand certain stages of mammalian development. Thanks to the complete genome sequencing, we now know that about 95% of the genes in the mouse do have an analogous form in humans as well. The mouse is relatively small, easy to keep, and it reproduces rapidly: following the three weeks of the gestation period, up to ten offspring are born. Moreover, mice can mate also with relatives and, in this way, exemplars that are very genetically similar can be produced, helping researchers to avoid conclusions that might be due to the genetic difference within a population and to obtain comparable results.

All experiments involving mouse embryos performed at ICFO described in this thesis were carried in compliance with protocols approved by the Comissió d'Experimentació Animal, Direcció General de Polítiques Ambientals i Medi Natural of the Departament de Territori i Sostenibilitat, Generalitat de Catalunya (Spain). "In vivo visualization of pre implantation process during mouse development through light-sheet fluorescence microscopy" (Expedient: FUE-2019-01190993; ID: XM5VTQ9BN; Project: 10758).

1.5 Summary of the results

While in the literature emphasis is given mainly to the optical performances of the LSFM system in terms of illumination and detection strategies, the incubation chambers, the environmental control, and the displacing possibility of the sample are of crucial importance to enable in-vivo applications as well as novel applications for LSFM. Especially in its conjunction with the developmental biology, the imaging

chamber have to provide optical access and mimic the native environmental conditions to allow long-term imaging of developing organisms, whose features and shape are constantly varying. In this thesis, strategies and incubation chambers have been developed to enable novel applications of LSFM in different fields, with different samples, and at different spatial-temporal scales.

Firstly, an LSFM setup that enable various experimental designs has been developed, and it is described in the second chapter. The platform uses a modular approach and different optical paths so that it can be easily and rapidly modified to adapt to the sample under observation and to the wanted experimental design. This implementation therefore enables long-term imaging, high-speed volumetric imaging, and the possibility to easily insert samples in sequence, to enhance the throughput and ease the visualization of various specimens. One of the main features is a microfluidic-based sample mounting approach, which does not need any agarose for the insertion of the specimen into the microscope. Moreover, a dedicated imaging chamber permits additional automation and flexibility in the imaging procedure. From this setup, an additional LSFM system has been extracted. This is a compact and transportable light-sheet microscope optimized for long-term imaging and for multi-view acquisition, similarly to the MuViSPIM setup [44]. Its imaging chamber has been designed specifically to accept delicate samples such as living embryos, integrating temperature and pH control of the immersion medium besides being autoclavable. These two setups have been used for specific biological applications in developmental and immune-system biology.

In the third chapter, I will discuss the use of the previously described platforms on the study of particular processes during the first hours of development of the zebrafish (*Danio rerio*). Firstly, the organization and dynamics of the microtubule network of the yolk cell of the zebrafish embryo is analyzed, showing a particular feature previously not fully described, that I called MOW (Microtubule Organizational Wave), and a previously unreported set of microtubules, that I

named Internal Microtubule Network (iMTN). Secondly, in a subsequent temporal window of the zebrafish development called epiboly, a particular organization of the yolk microtubules is visualized and analyzed on various samples, profiting from the enhanced throughput capability of the setup respect to the classical LSFM systems.

In the fourth chapter, the use of the setups for two collaborations carried within the ImageInLife network are described. Firstly, the macrophage recruitment in the zebrafish embryo has been imaged in two scenarios: during wound healing, and during bacterial infection. This was done in collaboration with the "Cytokines, Evolution and Onset of Immunity" lab (University of Montpellier, France), and performed partly at ICFO and partly during my secondment at the University of Montpellier, thanks to the transportation and installation of the MuViSPIM setup in the local imaging facility.

Through a second project, the visualization of pre-implantation mouse embryos is discussed. While zebrafish embryos naturally develop outside from the mother's body, mouse embryos develop within the utero. Registering their development is therefore particular challenging, as they are much more sensitive to temperature and pH in comparison to the zebrafish. Thus, the imaging chamber has to mimic the intra-utero environmental conditions. Mouse embryos are of great interest, as the understanding of their development could shed light on the development of human embryos, being both species mammals. This was done in collaboration with the Mammalian Embryo and Stem Cell Groups (University of Cambridge, UK).

Having realized how important the sample environmental control is, I translated this knowledge to explore fields at different spatial scales, in which the in-vivo vertebrate imaging is normally not considered. Single-molecule microscopy (SMM) permits to obtain information about the dynamics of proteins, and it is usually performed within cultured cells. However, the conjugation of SMM and LSFM can be instrumental to study the protein behaviour in their native environment, i.e. the living organism. In the fifth chapter I describe the work done in this area, that

permitted to study the glucocorticoid receptor (GR) dynamics within the nuclei in living zebrafish embryos, enabling in-vivo LSFSMM (Light-Sheet Fluorescence Single-Molecule Microscopy). This was the result of a collaboration with the Schaaf Lab (Institute of Biology, Leiden University, The Netherlands), carried out both at ICFO and during my secondment at Leiden University.

The results of this thesis have led to four scientific publications [64–67] and an additional manuscript currently in preparation [68].

1.6 References

1. A. J. M. Wollman, R. Nudd, E. G. Hedlund, and M. C. Leake, "From Animaculum to single molecules: 300 years of the light microscope.," Open Biol. **5**(4), 150019 (2015).

2. M. J. Sanderson, I. Smith, I. Parker, and M. D. Bootman, "Fluorescence microscopy.," Cold Spring Harb. Protoc. **2014**(10), pdb.top071795 (2014).

3. "The Nobel Prize in Chemistry 2008," https://www.nobelprize.org/prizes/chemistry/2008/summary/.

4. F. Progatzky, M. J. Dallman, and C. Lo Celso, "From seeing to believing: labelling strategies for in vivo cell-tracking experiments," Interface Focus **3**(3), 20130001 (2013).

5. J. K. Heppert, D. J. Dickinson, A. M. Pani, C. D. Higgins, A. Steward, J. Ahringer, J. R. Kuhn, and B. Goldstein, "Comparative assessment of fluorescent proteins for in vivo imaging in an animal model system.," Mol. Biol. Cell **27**(22), 3385–3394 (2016).

6. S. Chapman, K. J. Oparka, and A. G. Roberts, "New tools for in vivo fluorescence tagging.," Curr. Opin. Plant Biol. **8**(6), 565–573 (2005).

7. P. J. Keller, "Imaging morphogenesis: technological advances and biological insights.," Science **340**(6137), 1234168 (2013).

8. P. P. Laissue, R. A. Alghamdi, P. Tomancak, E. G. Reynaud, and H. Shroff, "Assessing phototoxicity in live fluorescence imaging," Nat. Methods **14**(7), 657–661 (2017).

9. Q. Zheng and L. D. Lavis, "Development of photostable fluorophores for molecular imaging.," Curr. Opin. Chem. Biol. **39**, 32–38 (2017).

10. C. Teng-Leong, "How poor photon budget can ruin your experiments and your AIC proposal," https://www.aicjanelia.org/post/poor-photon-budget.

11. J. Icha, M. Weber, J. C. Waters, and C. Norden, "Phototoxicity in live fluorescence microscopy, and how to avoid it.," Bioessays **39**(8), (2017).

12. H. Schneckenburger, P. Weber, M. Wagner, S. Schickinger, V. Richter, T. Bruns, W. S. L. Strauss, and R. Wittig, "Light exposure and cell viability in fluorescence microscopy.," J. Microsc. **245**(3), 311–318 (2012).

13. Y. M. Sigal, R. Zhou, and X. Zhuang, "Visualizing and discovering cellular structures with super-resolution microscopy.," Science **361**(6405), 880–887 (2018).

14. C. A. Combs and H. Shroff, "Fluorescence Microscopy: A Concise Guide to

Current Imaging Methods.," Curr. Protoc. Neurosci. **79**, 2.1.1-2.1.25 (2017).

15. C. L. Gregg and J. T. Butcher, "Quantitative in vivo imaging of embryonic development: opportunities and challenges.," Differentiation. **84**(1), 149–162 (2012).

16. O. E. Olarte, J. Andilla, E. J. Gualda, and P. Loza-Alvarez, "Light-sheet microscopy: a tutorial," Adv. Opt. Photonics **10**(1), 111–179 (2018).

17. R. M. Power and J. Huisken, "A guide to light-sheet fluorescence microscopy for multiscale imaging.," Nat. Methods **14**(4), 360–373 (2017).

18. H. Siedentopf and R. Zsigmondy, "Uber Sichtbarmachung und Größenbestimmung ultramikoskopischer Teilchen, mit besonderer Anwendung auf Goldrubingläser," Ann. Phys. **315**(1), 1–39 (1902).

19. P. A. Santi, "Light sheet fluorescence microscopy: a review.," J. Histochem. Cytochem. Off. J. Histochem. Soc. **59**(2), 129–138 (2011).

20. A. H. Voie, D. H. Burns, and F. A. Spelman, "Orthogonal-plane fluorescence optical sectioning: three-dimensional imaging of macroscopic biological specimens.," J. Microsc. **170**(Pt 3), 229–236 (1993).

21. A. H. Voie and F. A. Spelman, "Three-dimensional reconstruction of the cochlea from two-dimensional images of optical sections.," Comput. Med. imaging Graph. Off. J. Comput. Med. Imaging Soc. **19**(5), 377–384 (1995).

22. J. Huisken, J. Swoger, F. Del Bene, J. Wittbrodt, and E. H. K. Stelzer, "Optical sectioning deep inside live embryos by selective plane illumination microscopy.," Science **305**(5686), 1007–1009 (2004).

23. J. Huisken and D. Y. R. Stainier, "Selective plane illumination microscopy techniques in developmental biology.," Development **136**(12), 1963–1975 (2009).

24. J. Huisken and D. Y. R. Stainier, "Even fluorescence excitation by multidirectional selective plane illumination microscopy (mSPIM).," Opt. Lett. **32**(17), 2608–2610 (2007).

25. H.-U. Dodt, U. Leischner, A. Schierloh, N. Jährling, C. P. Mauch, K. Deininger, J. M. Deussing, M. Eder, W. Zieglgänsberger, and K. Becker, "Ultramicroscopy: three-dimensional visualization of neuronal networks in the whole mouse brain," Nat. Methods **4**(4), 331–336 (2007).

26. P. J. Keller, A. D. Schmidt, J. Wittbrodt, and E. H. K. Stelzer, "Reconstruction of zebrafish early embryonic development by scanned light sheet microscopy.," Science **322**(5904), 1065–1069 (2008).

27. D. Kromm, T. Thumberger, and J. Wittbrodt, "Chapter 5 - An eye on light-sheet microscopy," in *The Zebrafish*, H. W. Detrich, M. Westerfield, and L. I. Zon, eds., Methods in Cell Biology (Academic Press, 2016), **133**, pp. 105–123.

28. J. Palero, S. I. C. O. Santos, D. Artigas, and P. Loza-Alvarez, "A simple scanless two-photon fluorescence microscope using selective plane illumination," Opt. Express **18**(8), 8491–8498 (2010).

29. T. V Truong, W. Supatto, D. S. Koos, J. M. Choi, and S. E. Fraser, "Deep and fast live imaging with two-photon scanned light-sheet microscopy," Nat. Methods **8**(9), 757–760 (2011).

30. O. E. Olarte, J. Licea-Rodriguez, J. A. Palero, E. J. Gualda, D. Artigas, J. Mayer, J. Swoger, J. Sharpe, I. Rocha-Mendoza, R. Rangel-Rojo, and P. Loza-Alvarez, "Image formation by linear and nonlinear digital scanned light-sheet fluorescence microscopy with Gaussian and Bessel beam profiles," Biomed. Opt. Express **3**(7), 1492–1505 (2012).

31. T. A. Planchon, L. Gao, D. E. Milkie, M. W. Davidson, J. A. Galbraith, C. G. Galbraith, and E. Betzig, "Rapid three-dimensional isotropic imaging of living cells using Bessel beam plane illumination," Nat. Methods **8**(5), 417–423 (2011).

32. C. J. R. Sheppard, "Structured illumination microscopy and image scanning microscopy: a review and comparison of imaging properties," Philos. Trans. R. Soc. A Math. Phys. Eng. Sci. **379**(2199), 20200154 (2021).

33. L. Gao, L. Shao, C. D. Higgins, J. S. Poulton, M. Peifer, M. W. Davidson, X. Wu, B. Goldstein, and E. Betzig, "Noninvasive imaging beyond the diffraction limit of 3D dynamics in thickly fluorescent specimens.," Cell **151**(6), 1370–1385 (2012).

34. B.-C. Chen, W. R. Legant, K. Wang, L. Shao, D. E. Milkie, M. W. Davidson, C. Janetopoulos, X. S. Wu, J. A. 3rd Hammer, Z. Liu, B. P. English, Y. Mimori-Kiyosue, D. P. Romero, A. T. Ritter, J. Lippincott-Schwartz, L. Fritz-Laylin, R. D. Mullins, D. M. Mitchell, J. N. Bembenek, A.-C. Reymann, R. Böhme, S. W. Grill, J. T. Wang, G. Seydoux, U. S. Tulu, D. P. Kiehart, and E. Betzig, "Lattice light-sheet microscopy: imaging molecules to embryos at high spatiotemporal resolution.," Science **346**(6208), 1257998 (2014).

35. E. Betzig, "Excitation strategies for optical lattice microscopy," Opt. Express **13**(8), 3021–3036 (2005).

36. T. F. Holekamp, D. Turaga, and T. E. Holy, "Fast three-dimensional fluorescence imaging of activity in neural populations by objective-coupled planar illumination microscopy.," Neuron **57**(5), 661–672 (2008).

37. Y. Wu, A. Ghitani, R. Christensen, A. Santella, Z. Du, G. Rondeau, Z. Bao, D. Colón-Ramos, and H. Shroff, "Inverted selective plane illumination microscopy (iSPIM) enables coupled cell identity lineaging and neurodevelopmental imaging in Caenorhabditis elegans.," Proc. Natl. Acad. Sci. U. S. A. **108**(43), 17708–17713 (2011).

38. F. O. Fahrbach, F. F. Voigt, B. Schmid, F. Helmchen, and J. Huisken, "Rapid 3D light-sheet microscopy with a tunable lens," Opt. Express **21**(18), 21010–21026 (2013).

39. O. E. Olarte, J. Andilla, D. Artigas, and P. Loza-Alvarez, "Decoupled illumination detection in light sheet microscopy for fast volumetric imaging," Optica **2**(8), 702–705 (2015).

40. E. Baumgart and U. Kubitscheck, "Scanned light sheet microscopy with confocal slit detection," Opt. Express **20**(19), 21805–21814 (2012).

41. R. Jorand, G. Le Corre, J. Andilla, A. Maandhui, C. Frongia, V. Lobjois, B. Ducommun, and C. Lorenzo, "Deep and Clear Optical Imaging of Thick Inhomogeneous Samples," PLoS One **7**(4), e35795 (2012).

42. W. Jahr, B. Schmid, C. Schmied, F. O. Fahrbach, and J. Huisken, "Hyperspectral light sheet microscopy," Nat. Commun. **6**(1), 7990 (2015).

43. M. E. Dickinson, G. Bearman, S. Tille, R. Lansford, and S. E. Fraser, "Multi-spectral imaging and linear unmixing add a whole new dimension to laser scanning fluorescence microscopy.," Biotechniques **31**(6), 1272,1274-1276,1278 (2001).

44. U. Krzic, S. Gunther, T. E. Saunders, S. J. Streichan, and L. Hufnagel, "Multiview light-sheet microscope for rapid in toto imaging.," Nat. Methods **9**(7), 730–733 (2012).

45. R. Tomer, K. Khairy, F. Amat, and P. J. Keller, "Quantitative high-speed imaging of entire developing embryos with simultaneous multiview light-sheet microscopy.," Nat. Methods **9**(7), 755–763 (2012).

46. R. K. Chhetri, F. Amat, Y. Wan, B. Höckendorf, W. C. Lemon, and P. J. Keller, "Whole-animal functional and developmental imaging with isotropic spatial resolution.," Nat. Methods **12**(12), 1171–1178 (2015).

47. J. Swoger, P. Verveer, K. Greger, J. Huisken, and E. H. K. Stelzer, "Multi-view image fusion improves resolution in three-dimensional microscopy.," Opt. Express **15**(13), 8029–8042 (2007).

48. S. Preibisch, S. Saalfeld, J. Schindelin, and P. Tomancak, "Software for bead-based registration of selective plane illumination microscopy data.," Nat.

Methods **7**(6), 418–419 (2010).

49. A. Kumar, Y. Wu, R. Christensen, P. Chandris, W. Gandler, E. McCreedy, A. Bokinsky, D. A. Colón-Ramos, Z. Bao, M. McAuliffe, G. Rondeau, and H. Shroff, "Dual-view plane illumination microscopy for rapid and spatially isotropic imaging.," Nat. Protoc. **9**(11), 2555–2573 (2014).

50. A. K. Glaser, N. P. Reder, Y. Chen, C. Yin, L. Wei, S. Kang, L. A. Barner, W. Xie, E. F. McCarty, C. Mao, A. R. Halpern, C. R. Stoltzfus, J. S. Daniels, M. Y. Gerner, P. R. Nicovich, J. C. Vaughan, L. D. True, and J. T. C. Liu, "Multi-immersion open-top light-sheet microscope for high-throughput imaging of cleared tissues.," Nat. Commun. **10**(1), 2781 (2019).

51. J. C. M. Gebhardt, D. M. Suter, R. Roy, Z. W. Zhao, A. R. Chapman, S. Basu, T. Maniatis, and X. S. Xie, "Single-molecule imaging of transcription factor binding to DNA in live mammalian cells.," Nat. Methods **10**(5), 421–426 (2013).

52. M. Reisser, A. Palmer, A. P. Popp, C. Jahn, G. Weidinger, and J. C. M. Gebhardt, "Single-molecule imaging correlates decreasing nuclear volume with increasing TF-chromatin associations during zebrafish development.," Nat. Commun. **9**(1), 5218 (2018).

53. F. Greiss, M. Deligiannaki, C. Jung, U. Gaul, and D. Braun, "Single-Molecule Imaging in Living Drosophila Embryos with Reflected Light-Sheet Microscopy.," Biophys. J. **110**(4), 939–946 (2016).

54. E. Zagato, T. Brans, S. Verstuyft, D. van Thourhout, J. Missinne, G. van Steenberge, J. Demeester, S. De Smedt, K. Remaut, K. Neyts, and K. Braeckmans, "Microfabricated devices for single objective single plane illumination microscopy (SoSPIM).," Opt. Express **25**(3), 1732–1745 (2017).

55. M. B. M. Meddens, S. Liu, P. S. Finnegan, T. L. Edwards, C. D. James, and K. A. Lidke, "Single objective light-sheet microscopy for high-speed whole-cell 3D super-resolution.," Biomed. Opt. Express **7**(6), 2219–2236 (2016).

56. R. Galland, G. Grenci, A. Aravind, V. Viasnoff, V. Studer, and J.-B. Sibarita, "3D high- and super-resolution imaging using single-objective SPIM.," Nat. Methods **12**(7), 641–644 (2015).

57. S. Kumar, D. Wilding, M. B. Sikkel, A. R. Lyon, K. T. MacLeod, and C. Dunsby, "High-speed 2D and 3D fluorescence microscopy of cardiac myocytes.," Opt. Express **19**(15), 13839–13847 (2011).

58. C. Dunsby, "Optically sectioned imaging by oblique plane microscopy," Opt. Express **16**(25), 20306–20316 (2008).

59. M. B. Bouchard, V. Voleti, C. S. Mendes, C. Lacefield, W. B. Grueber, R. S. Mann, R. M. Bruno, and E. M. C. Hillman, "Swept confocally-aligned planar excitation (SCAPE) microscopy for high speed volumetric imaging of behaving organisms.," Nat. Photonics **9**(2), 113–119 (2015).

60. E. H. K. Stelzer, F. Strobl, B.-J. Chang, F. Preusser, S. Preibisch, K. McDole, and R. Fiolka, "Light sheet fluorescence microscopy," Nat. Rev. Methods Prim. **1**(1), 73 (2021).

61. K. Howe, M. D. Clark, C. F. Torroja, J. Torrance, C. Berthelot, M. Muffato, J. E. Collins, S. Humphray, K. McLaren, L. Matthews, S. McLaren, I. Sealy, M. Caccamo, C. Churcher, C. Scott, J. C. Barrett, R. Koch, G.-J. Rauch, S. White, W. Chow, B. Kilian, L. T. Quintais, J. A. Guerra-Assunção, Y. Zhou, Y. Gu, J. Yen, J.-H. Vogel, T. Eyre, S. Redmond, R. Banerjee, J. Chi, B. Fu, E. Langley, S. F. Maguire, G. K. Laird, D. Lloyd, E. Kenyon, S. Donaldson, H. Sehra, J. Almeida-King, J. Loveland, S. Trevanion, M. Jones, M. Quail, D. Willey, A. Hunt, J. Burton, S. Sims, K. McLay, B. Plumb, J. Davis, C. Clee, K. Oliver, R. Clark, C. Riddle, D. Elliott, G. Threadgold, G. Harden, D. Ware, S. Begum, B. Mortimore, G. Kerry, P. Heath, B. Phillimore, A. Tracey, N. Corby, M. Dunn, C. Johnson, J. Wood, S. Clark, S. Pelan, G. Griffiths, M. Smith, R. Glithero, P. Howden, N. Barker, C. Lloyd, C. Stevens, J. Harley, K. Holt, G. Panagiotidis, J. Lovell, H. Beasley, C. Henderson, D. Gordon, K. Auger, D. Wright, J. Collins, C. Raisen, L. Dyer, K. Leung, L. Robertson, K. Ambridge, D. Leongamornlert, S. McGuire, R. Gilderthorp, C. Griffiths, D. Manthravadi, S. Nichol, G. Barker, S. Whitehead, M. Kay, J. Brown, C. Murnane, E. Gray, M. Humphries, N. Sycamore, D. Barker, D. Saunders, J. Wallis, A. Babbage, S. Hammond, M. Mashreghi-Mohammadi, L. Barr, S. Martin, P. Wray, A. Ellington, N. Matthews, M. Ellwood, R. Woodmansey, G. Clark, J. D. Cooper, A. Tromans, D. Grafham, C. Skuce, R. Pandian, R. Andrews, E. Harrison, A. Kimberley, J. Garnett, N. Fosker, R. Hall, P. Garner, D. Kelly, C. Bird, S. Palmer, I. Gehring, A. Berger, C. M. Dooley, Z. Ersan-Ürün, C. Eser, H. Geiger, M. Geisler, L. Karotki, A. Kirn, J. Konantz, M. Konantz, M. Oberländer, S. Rudolph-Geiger, M. Teucke, C. Lanz, G. Raddatz, K. Osoegawa, B. Zhu, A. Rapp, S. Widaa, C. Langford, F. Yang, S. C. Schuster, N. P. Carter, J. Harrow, Z. Ning, J. Herrero, S. M. J. Searle, A. Enright, R. Geisler, R. H. A. Plasterk, C. Lee, M. Westerfield, P. J. de Jong, L. I. Zon, J. H. Postlethwait, C. Nüsslein-Volhard, T. J. P. Hubbard, H. R. Crollius, J. Rogers, and D. L. Stemple, "The zebrafish reference genome sequence and its relationship to the human genome," Nature **496**(7446), 498–503 (2013).

62. C. A. MacRae and R. T. Peterson, "Zebrafish as tools for drug discovery," Nat. Rev. Drug Discov. **14**(10), 721–731 (2015).

63. A. D'Costa and I. T. Shepherd, "Zebrafish Development and Genetics: Introducing Undergraduates to Developmental Biology and Genetics in a

Large Introductory Laboratory Class," Zebrafish **6**(2), 169–177 (2009).

64. M. Bernardello, M. Marsal, E. J. Gualda, and P. Loza-Alvarez, "Light-sheet fluorescence microscopy for the in vivo study of microtubule dynamics in the zebrafish embryo," Biomed. Opt. Express **12**(10), 6237–6254 (2021).

65. M. Bernardello, E. J. Gualda, and P. Loza-Alvarez, "Modular multimodal platform for classical and high throughput light sheet microscopy.," Sci. Rep. **12**(1), 1969 (2022).

66. M. Bernardello, R. J. Gora, P. Van Hage, G. Castro-Olvera, E. J. Gualda, M. J. M. Schaaf, and P. Loza-Alvarez, "Analysis of intracellular protein dynamics in living zebrafish embryos using light-sheet fluorescence single-molecule microscopy.," Biomed. Opt. Express **12**(10), 6205–6227 (2021).

67. M. Marsal, M. Bernardello, E. J. Gualda, and P. Loza-Alvarez, "Multiple asters organize the yolk microtubule network during dclk2-GFP zebrafish epiboly," Sci. Rep. **12**(1), 4072 (2022).

68. T. Sipka, S. Tairi, M. Bernardello, E. J. Gualda, P. Loza-Alvarez, A. Blanc-Potard, G. Lutfalla, and M. Nguyen-Chi, "Dynamics of macrophage polarization during Salmonella Typhimurium infection in zebrafish," (n.d.).

Chapter 2: Solutions for multimodal LSFM in-vivo imaging

This chapter contains content entirely reproduced or adapted from the article [1]: Bernardello, M., Gualda, E.J. & Loza-Alvarez, P. Modular multimodal platform for classical and high throughput light-sheet microscopy. Sci Rep 12, 1969 (2022). https://doi.org/10.1038/s41598-022-05940-2

2.1 Abstract

Light-Sheet Fluorescence Microscopy (LSFM) has become an important tool for biological and biomedical research. Although several illumination and detection strategies have been developed, the sample mounting still represents a cumbersome procedure as this is highly dependent on the type of sample and often this might be time-consuming. This prevents the use of LSFM in other promising applications in which a fast and straightforward sample-mounting procedure and imaging are essential. These include the high-throughput research fields, e.g. in drug screenings and toxicology studies. Here a new imaging paradigm for LSFM is described, which exploits modularity to offer multimodal imaging and straightforward sample mounting strategy, enhancing the flexibility and throughput of the system. Through its implementation, the sample can be imaged either as in any classical configuration, as it flows through the light-sheet using a fluidic approach, or a combination of both. Its ability to image a variety of samples, from zebrafish embryos and larvae to 3D complex cell cultures is also evaluated.

2.2 Introduction

Since its development, Light-Sheet Fluorescence Microscopy (LSFM) has gained much interest in the biological and biomedical community. As stated in the introductory chapter, in LSFM images are generated through a plane-based strategy in which only a single slice of the sample is excited per exposure time, and the emitted photons are collected perpendicularly, forming an image. This procedure is then repeated for each plane of the sample's volume, leading to optical sectioning and 3D reconstruction capabilities [2]. LSFM provides low induced photodamage, fast acquisition rates, and resolution comparable to traditional confocal microscopy. These advantages made it a necessary tool for the biological and biomedical community, which consequently led researchers to develop several LSFM configurations, each adapted to solve particular experimental needs [3].

The main efforts for improvements on LSFM technologies were made to achieve higher spatial resolution [4,5], to increase even more its acquisition speed [6,7], and to image the *in-toto* volume of the specimen [8–10]. Still, a conventional LSFM platform remains restricted in its imaging throughput capability, mostly because of tedious and time-consuming protocols for optical alignment and sample mounting that are normally embedded in a semi-rigid medium.

This constraint limits the usage of LSFM in highly relevant fields such as high-throughput (HT) studies and drug screenings, in which a high number of samples must be analyzed to cover all possible variables and to provide statistical significance. For this reason, in the last years, there have been attempts to increase the imaging throughput of LSFM setups for specific applications. While initial solutions aimed at introducing more samples in the embedding medium [11,12], various subsequent designs pointed to conserving the well-established approach in biology in using multiwell plates. To use those plates, LSFM researchers either adapted the illumination-collection strategy to a single objective or modified the multiwell plate itself to provide the needed orthogonality between excitation and detection planes [13–16].

Other approaches have been presented that aim at merging LSFM to flow-cytometry-like technologies [17,18]. Here, the main principle is to use microfluidic circuits to flow the sample in a controlled way through a static light sheet. In this case, the different optical sections are captured as the sample goes through the light sheet. This LSFM modality has been used to visualize small samples such as fluorescent particles, phytoplankton, and single cells [19–21]. Further evolutions have resulted in compact single microfluidic chips containing also the illumination optics. Such systems have been demonstrated by imaging fixed spheroids and fixed *Drosophila* embryos [22–24]. Additionally, a fluidic-based LSFM system, based on the use of Fluorinated Ethylene Propylene (FEP, n_{FEP} = 1.33) tubes has also been

developed. In this case, the FEP tube is used to flow big samples such as 3D cell aggregates, zebrafish embryos, and zebrafish larvae in an HT fashion [25].

Although effectively increasing the imaging throughput capabilities of LSFM, all these fluidic approaches, however, suffer some drawbacks. Firstly, the acquisition is limited to one or two channels, as the specimen passes only once through the light sheet. Secondly, due to the inner aperture of the fluidic channel, the sample crosses the light sheet with a random angular offset, preventing some features of interest to be efficiently imaged. This is especially important in the case of highly scattering samples such as spheroid, embryos, and larvae, in which it might be interesting to visualize specific structures or organs. To image fluorescent neutrophils in live zebrafish larvae, a fluidic circuit was used in which the samples were stopped in the detection field of view (FoV) [26]. Still, no rotation control of the specimen was implemented, and the use of glass capillaries would inevitably generate refractive index mismatches in both the illumination and detection paths, limiting also the resolution power. For the various fluidic approaches listed above, the random positioning of the sample within the fluidic channel makes it difficult to repeat the imaging of the same specimen over time, e.g. in order to visualize in a time-lapse fashion how a particular feature evolves, with an enhanced throughput approach.

Furthermore, while biological and biomedical researchers need to deal regularly with the ability to perform complex experiments, and image different types of samples at different spatial-temporal scales, most of the LSFM setups are designed for a specific application. It would be therefore beneficial for the biological community to rely on a single imaging platform that could perform various experiments, ranging from 3D time-lapse movies of a single specimen over several hours to 3D volume renderings of many samples.

Here the optical design of a flexible LSFM imaging system called Flexi-SPIM (Flexi-Selective Plane Illumination Microscope) is presented. The setup is capable to be adapted to a large variety of experimental needs, allowing full sample control

positioning and fast, multi-channel, *in-toto,* and *in-vivo* imaging with HT capabilities. Moreover, an additional transportable setup similar to the MuViSPIM implementation [10] optimized for long-term imaging of living delicate samples is described in detail.

2.3 Flexi-SPIM: Modularity of the system

The Flexi-SPIM contains illumination, sample mounting, and detection modules. This modularity permits easy modification of the overall imaging procedure of the system, enabling several radically different experiments on various samples.

2.3.1 Illumination module

The illumination module can generate the light sheet through a cylindrical lens (configuration normally referred to as SPIM [2]) or through the combination of two galvanometric mirrors and lenses to scan the focused beam along one direction (i.e. Digitally Scanned Laser Light Microscopy or DSLM [27]). With this design, the light-sheet (LS) can be generated either vertically or horizontally, by either rotating the cylindrical lens or by manually removing the cylindrical lens and electronically controlling the two galvanometric mirrors, keeping one static.

In addition, dual side illumination is implemented by a duplicated illumination arm, producing a second light sheet that enables a more homogeneous sample excitation [28]. The two co-planar LSs can be generated either sequentially or simultaneously. The first case is ideal for imaging thick and scattering samples in which an important degradation of the LS occurs, preventing the optimal illumination and imaging at the other end of the sample. With this scheme, each side of the sample can be sequentially illuminated and imaged, and computationally fused after removing the respective blurred image. The double simultaneous illumination scheme can be used on transparent specimens in which the LS degradation can be neglected. The switch between simultaneous and sequential double illumination can be electronically controlled through the use of shutters positioned within both illumination arms.

In the DSLM mode, the manual modulation of an iris aperture placed close to the back focal aperture (BFP) of each of the illumination objectives enables reducing the illumination NA, which in turn elongates the available illumination FoV at the expense of an increased LS thickness. This allows adapting the imaging conditions according to the user's needs: a full open iris will enable better optical sectioning capabilities, while a smaller aperture can provide larger FOV. For a detailed explication on the illumination module's components, see Appendix A, section A.1.

By using an illumination objective of NA= 0.13 and by varying the iris aperture from 4 mm to fully open, I characterized the variation in the illumination beam's profile derived (see Appendix A) and measured the LS thickness. These were: 8.95 µm (R1, iris aperture diameter = 4 mm), 6.89 µm (R2, iris aperture diameter = 7 mm), 6.48 µm (R3, iris aperture diameter = 10 mm), 5.33 µm (R4, iris aperture diameter = 13 mm), 5.17 µm (R5, iris aperture diameter = fully open), being R1 to R5 the identification of the selected iris aperture, from the smallest to the largest (see also Appendix A, section A.2 for the measurement procedure). Following the Gaussian beam properties, the theoretical illumination FoVs resulted to vary from approximately 258 to 86 µm, in good agreement with the measured values. These values are valid for the single illumination scheme, and therefore by using the double illumination modality they can be increased by a factor of 2, yielding illumination FoVs from 172 to 516 µm. Consequently, the available FoVs are capable of image samples of different sizes. As an example, considering the zebrafish model organism, it is possible to visualize its heart (about 100 to 150 µm), its brain (about 400-500 µm), and even the eggs (about 700 µm).

2.3.2 Detection module

The design for the detection module makes use of three different objectives. Two of them are located parallel to the optical table and are used when the LS is generated in the vertical direction. The other one, located perpendicular to the

optical table and above the sample holder, is used when the LS is generated in the horizontal direction (Fig. 2.1A).

This allows collecting the fluorescence through multiple optical paths that finally converge at the camera chip to form the image. The three optical paths merge into a Path Selector (PS) module whose elements can be switched as follows: 1) A knife-edge prism to enable simultaneous double-side lateral detection (Fig. 2.1B), using the two horizontally positioned objectives (vertical LS). The prism optically divides the camera chip between the two views, each for each side of the specimen; 2) A motorized mirror to enable sequential double side detection (Fig. 2.1C) for the same couple of objectives (vertical LS). The rotating mirror allows using the full camera chip for each of the collecting arms. 3) Finally, no elements are introduced in the PS, resulting in conventional single side detection (Fig. 2.1D). This uses the vertically positioned objective and sets the LS to the horizontal position.

The multiple detection scheme allows to fully exploit the flexibility offered by the illumination module and the different sample mounting systems here presented while maintaining a single final optical path. Notice also that such scheme is compatible with any eventual supplementary detection add-ons (e.g. filters, remote focusing elements, adaptive optics, phase masks, etc.). For a detailed explication on the detection module's components, see Appendix A, section A.3.

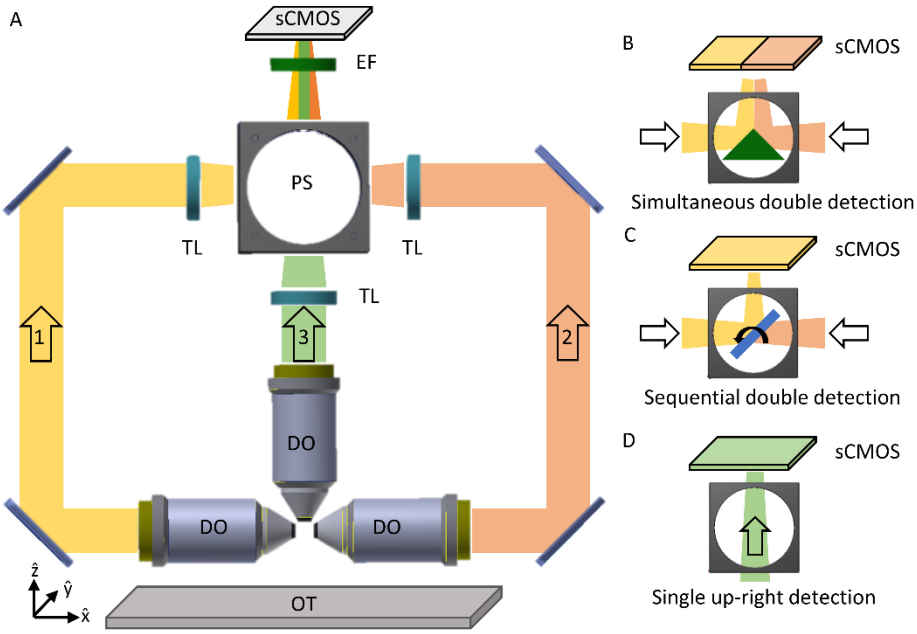

Figure 2.1: Detection scheme enabling the collection of emitted photons through three different paths. (A) DO = detection objective, TL = tube lens, PS = path selector, EF = emission filter. The coordinate system is indicated with respect to the horizontal optical table (OT). (B-D) The elements included in the PS are switchable and permit obtaining (B) simultaneous double, (C) sequential double, or (D) single detection schemes. All the optical paths converge after the path selector to reach the sCMOS camera chip. The FoV determined by the camera chip can be either optically split (B) between the views or used as a full (C, D). Image reproduced from [1].

The final resolution obtained from the optical system depends on the actual objectives and tube lenses used. The design enables using tube lenses having the same focal length (200 mm) for the three paths, obtaining the same magnification/resolution in all the views. Otherwise, the lateral paths enable also the insertion of different tube lenses (180 mm). The tested detection objectives ranged from 0.3 NA to 0.5 NA which, in combination with the tube lens and camera specifics, achieve theoretical lateral resolutions from 1.07 µm to about 0.64 µm, i.e. adaptable to various experimental needs. Practically, I measured the lateral resolutions obtained to be of about 1.2 µm and 0.88 µm respectively, which permit the imaging at the cellular level of entire organisms (see also Appendix A, section A.4 for the resolution characterization).

2.3.3 Sample scanning and mounting modules

One of the key features of the platform is the different possibilities for the sample mounting, which is a critical factor in LSFM as it can limit or boost the performance of the entire system. To provide flexible, fast, and easy-to-use sample loading capabilities, three different interchangeable sample mounting approaches were designed (Fig. 2.2).

The first scanning option reflects what is normally considered a classical approach, in which the sample (usually embedded in agarose forming an optically clear cylinder) is placed to cross the LS, enabling a double side illumination/detection [10] scheme (Fig. 2.2B). Volume scanning is achieved through the sample's displacement with rotation possibilities.

The second scanning approach makes use of a fluidic circuit to mount the specimen. The circuit is based on a Fluorinated Ethylene Propylene (FEP) tube. FEP is a material that presents a refractive index of about 1.33, hence an excellent match for water-based imaging medium, allowing the use of water-dipping objective and minimizing optical aberrations [29]. The fluidic circuit crosses the water-filled imaging chamber at 45° (Fig. 2.2C) and it is connected to a flow controller [25]. Once the sample is loaded into the circuit, it can be displaced at a constant flow rate. This approach permits to use of the continuous sample flow as the mean for volume scanning across a static vertical light-sheet.

The third mounting approach uses the fluidic circuit only to position the sample in the light sheet region. Once it is there, the sample's flow is stopped and the specimen can then be scanned across the LS (in this case set to the horizontal position). This is done either mechanically, translating the full chamber with the FEP tube containing the specimen, or optically, through the LS displacement mediated by one galvanometric mirror in synchrony with the movement of the collection objective using a piezo scanner [30] (Fig. 2.2D). In addition, the FEP tube can be rotated along its longitudinal axis, enabling it to better expose a particular feature

of the sample, that otherwise would be hidden by the specimen itself, toward the detection objective (e.g. to image the heart or the brain of the zebrafish). Notice that this mounting scheme would also enable remote focusing using an electrically tunable lens or other wavefront coding strategies [6,7].

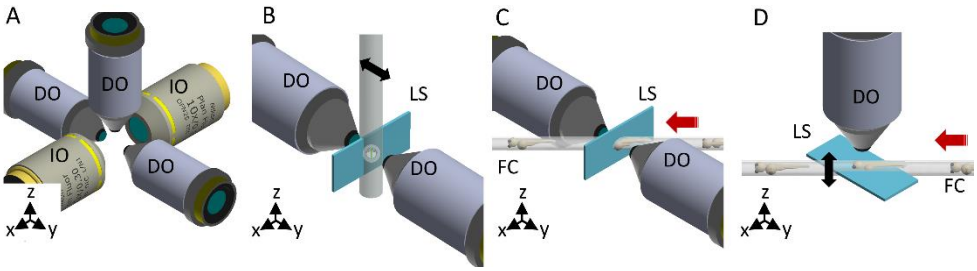

Figure 2.2: Sample scanning strategies. (A) The objectives' configuration enabling multiple illumination/detection schemes. (B) Through the first mounting option, the sample is embedded within a cylinder perpendicular to the optical table. The black arrow indicates the scanning direction. (C) The second approach uses the flow of the samples to scan them through the light sheet. The red arrow indicates the flow direction. (D) Through the third approach, the sample flow (red arrow) is used to position the sample in the objective's FoV of the DO. The scanning of the specimen is obtained instead in the vertical direction (black arrow), either mechanically or optically. IO = illumination objective, DO = detection objective, LS = light sheet, FC = fluidic circuit. Image reproduced from [1].

Importantly, and opposite to traditional mounting schemes, the use of fluidic methods allows to consecutively load different samples. Therefore, specimens can be mounted and imaged in their own culture media, helping in maintaining adequate physiological conditions. After imaging, these samples can be placed back in the culture medium or incubator for future inspections without any further protocols (such as the removal of solid agarose). This approach, therefore, increases both the sample throughput and the subsequent specimen viability. In addition, by stopping the sample under the objectives' FoV, the third method allows easy sample loading and imaging of the developing specimen and their selected features for long periods of time. It, therefore, combines the advantages of the two previously described approaches. See also Appendix A, section A.5 for a description of the sample scanning module's components.

2.4 Flexi-SPIM: Multi-modality of the system.

Through the combination of the modules illustrated above, three different imaging modalities are resulting, each of them with particular advantages. The imaging modalities are here called *Classic* LSFM, *Flow* LSFM, and *Hybrid* LSFM. While the first configuration is ideal for long-term imaging, the second allows increasing the throughput of the system. Finally, the third configuration can be used for both long-term imaging and enhanced throughput, also assuring the repeatability of the imaging session. Therefore, through the implementation of a single optical setup, called Flexi-SPIM, a variety of experiments can be performed, as explained below.

2.4.1 Classic LSFM

The *Classic LSFM* follows the traditional design of SPIM or DLSM setups, and makes use of two illumination objectives and two detection objectives, allowing a dual side excitation/collection scheme. The four objectives lay on the horizontal plane, around a custom-designed imaging chamber. While the detection is implemented through water-dipping objectives, sealed within the chamber, the excitation vertical LS is generated by the two air-based objectives, passing through two coverslips glued to the chamber.

2.4.1.1 The long-term imaging chamber

To enable long-term imaging, I designed a dedicated LSFM chamber. The structure, after various 3D printed prototypes in Polylactic Acid (PLA), was then 3D printed in medical-grade stainless steel (316L, from Materialise Manufacturing Services, Fig. 2.3A-B) to assure the autoclavability. The chamber permits the integration of two detection objectives within the imaging medium compartment, while two windows covered with glass coverslips provide optical access for the illumination through the LS generated by the two air objectives (Fig. 2.3A). The alignment of the four objectives between them and with the center of the chamber is facilitated by rods (cage rods, from Thorlabs) that are mounted on each of the objective mounts and for which apposite tunnels have been designed in the chamber (Fig. 2.3C). In this way, the alignment in the lateral directions is assured for each of the objectives,

while the depth position can be adjusted through the stage included in each of the objective mounts. This also helps the insertion of the sample, which only needs to be placed in the center of the chamber to be visible in the field of view of the four objectives. Being the chamber filled with an aqueous medium (such as PBS or E3, depending on the application), a sealing system for the detection objectives has been devised. Firstly, an O-ring is placed on the tip of the objective, and then the entire body is covered with a rubber cylinder. The objective is then inserted into the medium compartment through the dedicated tunnel implemented in the design of the chamber and to which a second rubber tube was previously glued. Once the objective has been positioned at approximately the needed working distance from the center of the compartment, a second O-ring is placed over its body, until touching the chamber. Once here, the second rubber cylinder is applied to cover the compartment's tunnel and the entire body of the objective. Thanks to this flexible rubber cylinder, the objective can still be moved in the depth direction without losing the sealing with the chamber, and therefore avoiding leaks (Fig. 2.3C).

The 3D scanning of the specimen is performed through the mechanical translation of the sample through the static vertical LS, by means of a linear stepper motor stage. An additional stepper motor rotational stage is also included, to enable the rotation of the sample with respect to its vertical axis (Fig. 2.3D).

To provide the needed environmental conditions for the development of samples such as zebrafish embryos (which naturally develop at approx. 28°), I also integrated into the chamber a heating system that permits to increase the temperature of the imaging medium with respect to the room temperature (normally at approx. 22°). This was implemented by a heating element (power resistor of 12 Ω) placed on an aluminum plate attached to the bottom of the imaging chamber. To the same aluminum plate, a temperature sensor (PT100) was also attached. These two devices were then connected to a Proportional–Integral–Derivative (PID) controller (E5CN-H, Omron), which maintains the temperature of the plate, and therefore of

the imaging chamber, constant. Being the heater placed at the exterior of the chamber, its temperature is not the same as the temperature of the medium, and therefore a second temperature sensor and logger (NTC thermistor sensor TSP-TH, and logger TSP01, Thorlabs) is immersed into it, monitoring and storing the evolution of its temperature over time (Fig. 2.3E).

Finally, to image delicate mammalian samples such as mouse embryos, the environmental control needs to deal also with the pH of the imaging medium. This is done by adding a continuous flow of CO_2 into the medium compartment (see also the chapter dedicated to mouse embryo imaging). Thanks to this environmental control, it is possible to maintain the necessary conditions for imaging delicate live specimens during prolonged time periods: I tested it on E4.5 mouse embryos for up to 8 hours, and for zebrafish embryos at different developmental stages for up to 24 hours (see Chapter 4, section 4.4 for the experimental procedure on mouse embryos).

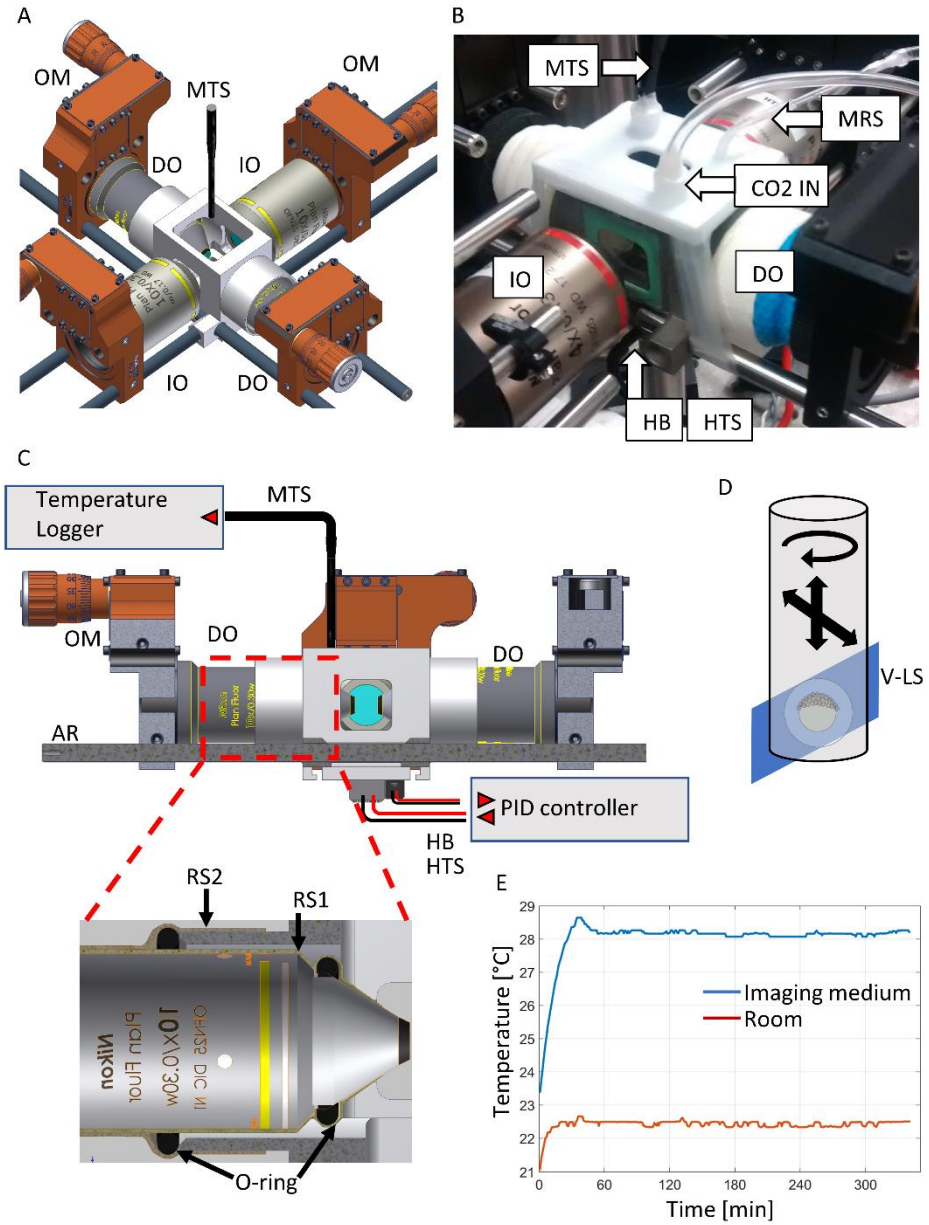

Figure 2.3: The long-term imaging chamber. (A) Schematic of the chamber and the integration of the four objectives. (B) Photo of the actual 316L steel imaging chamber, with the two air illumination objectives (IO) and the two sealed water detection objectives (DO). (C) Section view of the chamber showing the alignment between chamber and objectives through rods (AR), and the sealing of the detection objectives. (D) Exemplification of the sample mounting and scanning system. The sample's position can be controlled in 3D and rotated along its vertical axis. V-LS=Vertical light-sheet. OM=objective mount, MTS=medium temperature sensor, MRS=refilling system, CO2 IN= CO2 inlet, HB=heater block, HTS=heater temperature sensor, RS=rubber sealing. (E) Example over 6 hours of the imaging medium's temperature maintained constant at 28°.

2.4.1.2 Applications

As the system provides a double detection scheme, by inserting in the path selector of the collection module the knife-edge prism mirror (Fig. 2.4A) it is possible to combine the frontal and back views of the sample during the same exposure time. Alternatively, when the knife-edge prism is substituted by the mirror mounted on a stepper motor (Fig. 2.4B), it is possible to use the full FoV of the camera for each of the detection objectives, and thus use objectives with higher magnification or numerical apertures. In such a case, the sample would be displaced through the LS and the alternate selection of the front and back views can be used for visualizing the front/back of the sample.

One of the main applications of this configuration (Fig. 2.4A-B) involves developmental biology. Particularly, in the lab it has been used for recording multicolor images of fixed specimens (Fig. 2.4C) and time-lapse videos of living samples such as the development of zebrafish embryos through nuclei, actin, or microtubule staining, from cleavage stages to gastrulation and beyond, obtaining the 3D structure of the entire sample volume (Fig. 2.4D). Through the prism mirror and by using a sequential double side illumination and a double side lateral detection scheme (with Nikon 10x, 0.3NA objectives) it is possible to record both half-volumes of the embryo simultaneously on the same camera chip (2048 x 2048 pixels) (Fig. 2.4D and Video A.1). The images obtained from both sides are then fused on a single dataset using fusing algorithms [31] (Video A.2) are also possible (Video A.3).

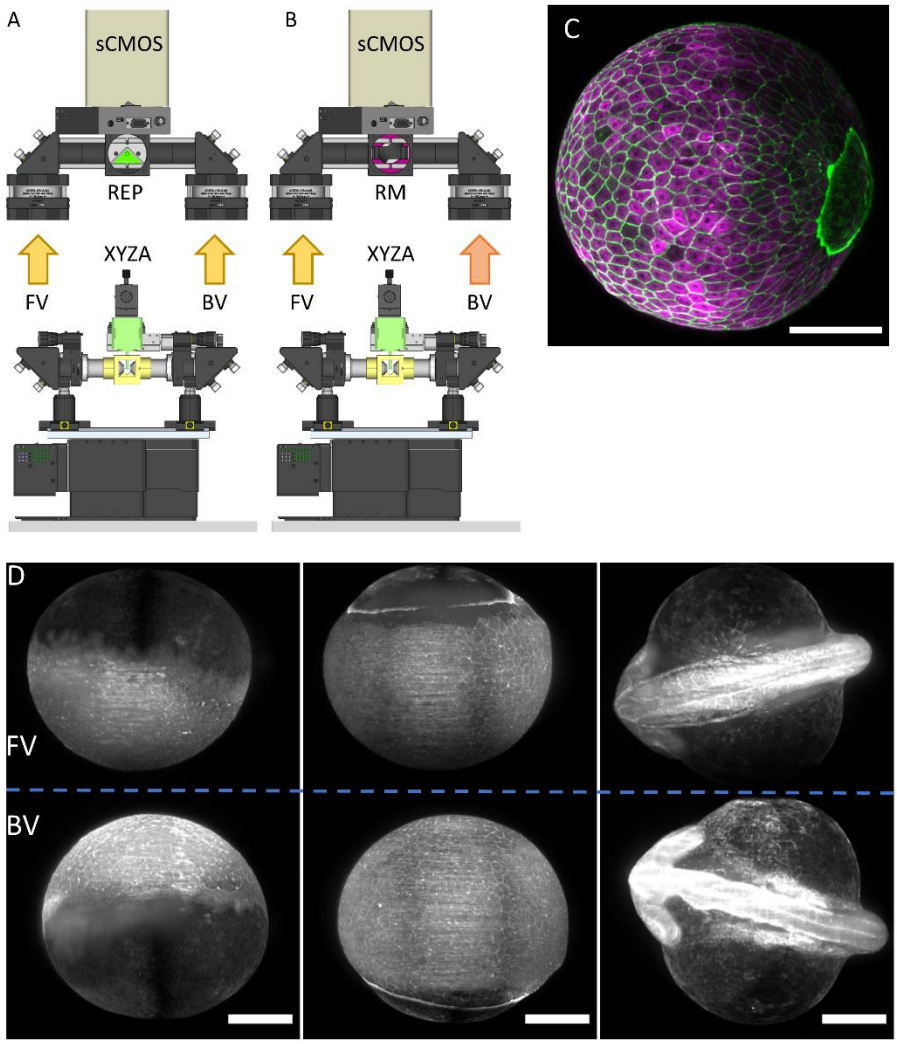

Figure 2.4: Application examples for the Classic LSFM configuration. (A-B) The setup implementation in the Classic LSFM modality, for (A) simultaneous and (B) alternate double side detection (FV: front view, BV: back view), using an sCMOS scientific camera (sCMOS). The path selector is a right-edge prism (REP) in (A) and a rotating mirror (RM) in (B). (C) Maximum intensity projection of a fixed zebrafish embryo at 90% epiboly, labeling actin (green) and tubulin (magenta), showing multicolor capability and achieving homogenous excitation thanks to the double illumination scheme. Scale bar 200 µm. (D) Maximum intensity projections from three time points of a time-lapse movie recording an unconstrained developing zebrafish embryo (actin-GFP) from blastula to segmentation stages. The REP was used to register the front (top) and back (bottom) views onto the same camera chip, at the same time. A double illumination scheme was used for excitation. Scale bars 200 µm. Image adapted from [1].

2.4.2 Flow LSFM

2.4.2.1 The fluidic imaging chamber

Substituting the previous imaging chamber with a custom-designed 3D printed cuvette crossed by an FEP tube, one can switch from the classical modality to the so-called *Flow LSFM* mode (Fig. 2.5A-B).

As previously, four objectives laying on the horizontal plane are employed: two air objectives for the illumination through a vertical LS, and two water objectives sealed within the chamber, for the emission collection. In order to assure the optical access and at the same time intersect all objectives' foci, the FEP tube crosses the chamber on the horizontal plane at 45° with respect to the light sheet. As explained above, the sample is loaded into the FEP tube using a syringe pump which allows the control of the position and flow speed of the specimen. This also allows programming capabilities of protocols for sample unloading and retrieving it again if necessary. While the sample is continuously flowing through the vertical LS (Fig. 2.5C), the two detection objectives retrieve the views of its 3D structure. Both views are then projected onto the camera chip at the same time through the knife-edge prism mirror.

2.4.2.2 Applications

The *Flow LSFM* modality enables whole-sample high-throughput screens possibilities, thanks to the easiness and fast sample loading, resulting in an effective high-resolution 3D imaging flow-cytometer system.

For thick and scattering samples, the double side illumination enables a homogeneous excitation of the fluorophores while the double simultaneous detection scheme permits retrieving features that would be otherwise hidden by the sample volume itself, as shown in Fig. 2.5D. The same principles can be used to reconstruct the entire volume in 3D of much bigger samples such as entire and elongated zebrafish embryos (Fig. 2.5E-F) that would not fit in the FoV of conventional LSFM schemes. Moreover, for thin and transparent samples the record

of multichannel images could be done by inserting two different emission filters in the two detection paths. In this case, the knife-edge prism would permit the recording of the two channels on the same camera chip.

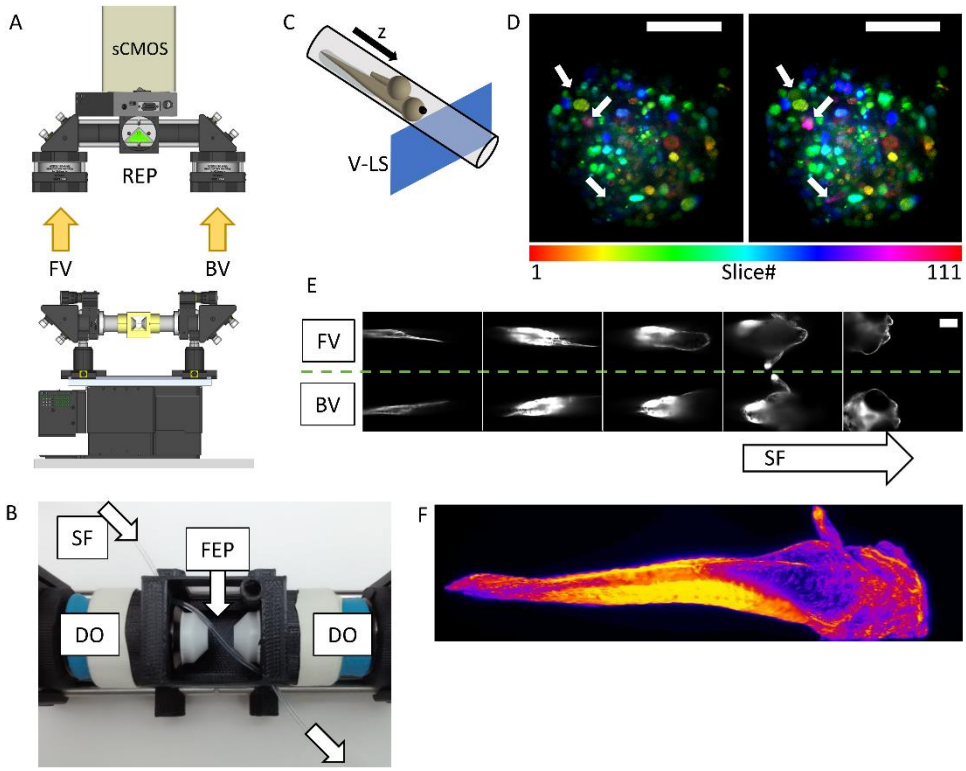

Figure 2.5: Implementation and application of the Flow LSFM mode. (A) The setup implementation in the Flow LSFM modality with a double simultaneous detection scheme. (B) The imaging chamber embedding two sealed water detection objectives (DO) and an FEP tube crossing it at 45°. SF= sample flow. (C) Exemplification of the sample mounting and scanning system. The sample flows within the FEP tube through a vertical light-sheet. (D) Depth-colored maximum intensity projection of a fixed tissue spheroid expressing a histone H2B fluorescent nuclear reporter protein (mCherry), obtained through single (left) and double (right) side detection scheme. The fusion of two views (on the right) reveals nuclei that would be otherwise missed through single side detection (see white arrows). Scale bars 100 µm. (E) Series of images during the flow of a Fli-GFP zebrafish embryo through the system. The front view (FV) and the back view (BV) are simultaneously registered on the same camera chip. Scale bar 100 µm. (F) 3D reconstruction view of the same zebrafish showed in (E). Color scale represents signal intensity (Fire LUT in Fiji). Image reproduced from [1].

2.4.3 Hybrid LSFM

Using the same sample loading approach through the FEP tube, removing the knife-edge prism mirror, and setting the light sheet to horizontal, one can convert the detection path to a single upright detection scheme. This is part of the so-called

Hybrid LSFM mode, in which samples are loaded and brought within the field of view of the camera using the syringe pump (fluidic loading) but imaged in a classical way.

2.4.3.1 The Hybrid LSFM imaging procedure

In this case, the fluidic circuit is composed of three consecutively connected FEP tubes within a third 3D printed imaging chamber: the “loading tube” in which the sample is loaded, the “imaging tube” that crosses the chamber, and the “aspiring tube” that is connected to the pump (Fig. 2.6A-B). The two air objectives generate the horizontal LS, while a single vertical water-objective is dipping within the medium compartment of the chamber, for the collection of the emitted photons (Fig. 2.6C).

The imaging proceeds as follows: the sample and medium are inserted into the “loading tube”, and aspired by the syringe pump towards the “imaging tube” until reaching the field of view of the detection objective. Once here, the specimen is automatically detected, and its flow is stopped. At this point, two stepper motors integrated into the imaging chamber can rotate the “imaging tube”, rotating also the sample. This enables to align the specimen in the desired direction and to expose a particular feature of interest toward the detection objective.

The sample’s volume can now be scanned in two ways. The first possibility consists of translating the entire imaging chamber in the vertical direction through a vertical stage across a static horizontal light sheet(s) illuminating the focal plane of the detection objective. The second option consists of the refocusing of the detection objective through a piezo element, which is in turn synchronized with the galvanometric scanner in the illumination path [30]. In that case, the sample remains static while the light-sheet(s) moves synchronously with the detection objective’s focal plane. This approach allowed to reach acquisition rates of 0.5 and 1 volume/second (typically 1 volume is made of 100 optical sections, varying the z-step size depending on the sample thickness).

Moreover, a LED integrated into the chamber allows obtaining bright-field images. These are critical for the detection of the passage of the specimen, stopping it under the objective's FoV, and adjusting the specimen orientation.

2.4.3.2 The Hybrid LSFM imaging chamber

One of the main advantages given by the *Hybrid LSFM* configuration is the straightforward sample mounting through an FEP-based fluidic circuit. To profit the most from this modality, the imaging chamber should: (i) maintain firm the FEP tube during the scanning, to avoid sample's movements during imaging; (ii) contain the imaging medium needed for the water-dipping detection objective, which provides index matching with the FEP tube; (iii) permit the rotation along the longitudinal axis of the sample; (iv) provide the system with quasi-brightfield imaging capability.

To accomplish these tasks, I designed and 3D printed a custom imaging chamber and additional components that permit sample rotation and water-sealing. The 3D-printed PLA model is the core part. It gives the structure to the entire HT chamber, it contains the imaging medium (water-based), and it prevents eventual medium leaks. A channel crosses the entire structure along its longitudinal axis, through which the "imaging tube" is positioned. The PLA model features an almost-symmetric geometry: the central compartment contains the medium, and the detection objective is placed on its top. The lateral walls are windows, glued with 22x22mm coverslips, to permit the light-sheet to enter the medium compartment and illuminate the imaging tube.

Under this unit, the model offers a cavity for the insertion of a blue LED, which provides the illumination for the brightfield imaging. This LED is assured to the chamber's center thanks to a 3D printed part, complementary to the void cavity. Light is delivered to the water-compartment thanks to a circular coverslip, glued with a 2-components glue (UHU Endfest), illuminating the FoV of the detection objective.

Right outside the water compartment and following the longitudinal channel, two small void cubicles contain grease (High Vacuum Grease, DOW CORNING) which prevents the medium from leaking and helps the rotation of the imaging tube within the channel. At the opposite sides of the model, two vertical panels offer the possibility to attach and screw two stepper motors (L4118S1404-M6X1 - NEMA 17, Nanotec Electronic GmbH & Co. KG). These motors offer a threaded (M6x1) hollow shaft and are driven by an Arduino-based controller, which gives the user the possibility to digitally control them (see Appendix A, section A.6 for the complete description of the Arduino controller). A custom-designed and internally machined part, called “RotationScrew”, is screwed to the rotator shaft of each stepper. The imaging tube is fixed to it. An additional custom-designed part, called “MotorConnector”, is connected through 4x M3 screws to the motors’ body. The MotorConnector offers a central cavity where two O-rings (sized 3x3 and 4x3) and one bearing ball (623ZZ, ID=3mm, OD=10mm) are glued with the 2-components UHU Schnellfest glue. In the 3mm diameter remaining void cylinder, the tip of the “RotationScrew” is inserted. Both the MotorConnector and the RotationScrew feature a channel (ID 1.6mm) along the longitudinal direction.

Finally, the FEP tube, carefully cut into three different parts (loading, imaging, and aspiring, Fig. 2.6A) is inserted in the central channel of the system. The first tip of the loading tube is reserved for the insertion of the sample. The other end is inserted in the left-sided MotorConnector for a length of 5mm, and fixed with the two retaining screws. This position corresponds to the interface between loading and imaging tubes. Symmetrically, the first end of the aspiring tube is fixed with retaining screws in the right-sided MotorConnector, and the other end is connected to the syringe pump. Between them, the imaging tube is present. It is fixed on both sides with retaining screws into the two RotationScrew components. From each RotationScrew, the imaging tube exceeds for a length of 10mm. The two tips of the

imaging tube are in direct contact, inside the MotorConnector, with the loading and aspiring tubes.

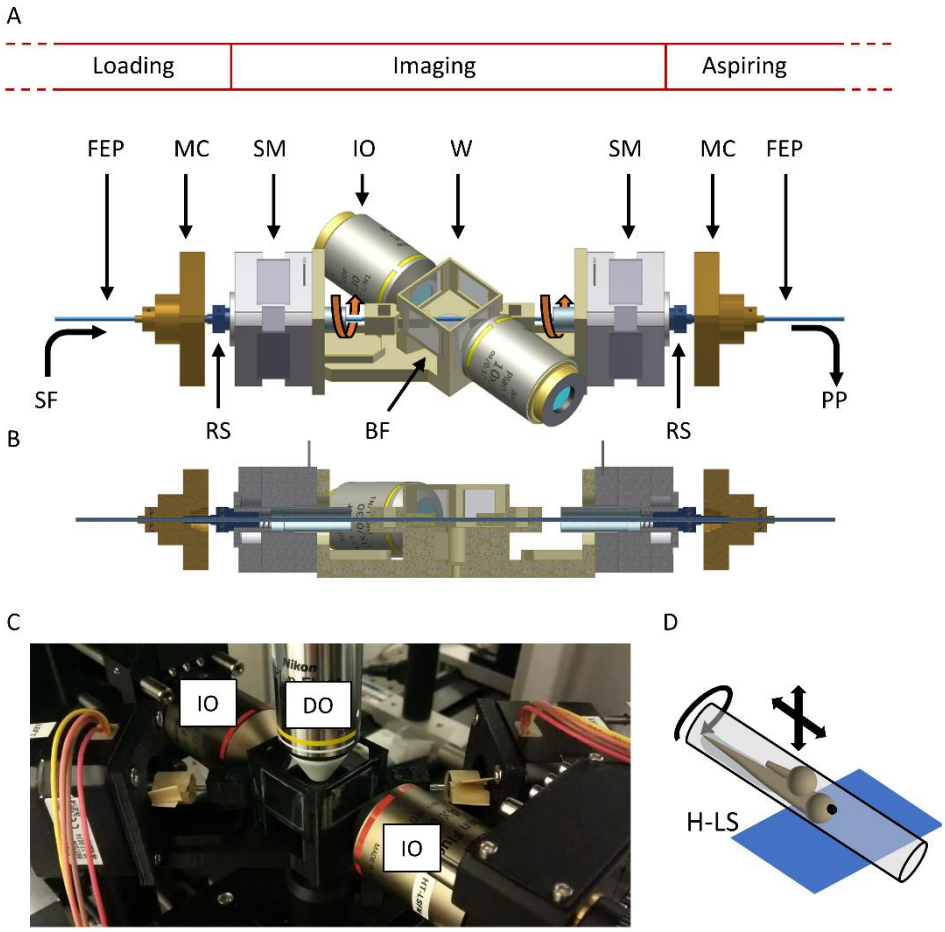

Figure 2.6: The Hybrid LSFM imaging chamber. (A) Schematic of the imaging chamber and its components. The fluidic circuit is divided into three FEP tubes (loading-, imaging-, aspiring-tube) SF= sample flow, MC= Motor Connector, RS= Rotational screw, SM= stepper motor, W=water compartment, PP= programmable pump (not shown), BF= bright field compartment, IO= illumination objective, DO= detection objective. (B) Lateral section view of the chamber, to ease visualization of the FEP-tubes circuits crossing the entire structure along the longitudinal axis. (C) The actual chamber integrated into the microscope. (D) Exemplification of the sample mounting and scanning system. The sample can be displaced in longitudinal and depth directions and can be rotated along the longitudinal axis of the imaging tube. Image adapted from [1].

2.4.3.3 Applications

The *Hybrid LSFM* approach and its implementation in the setup (Fig. 2.7A-B) present several advantages.

Compared with agarose-based C*lassic LSFM*, the loading of samples is extremely facilitated as it is based on the use of the syringe pump and the FEP tubes, increasing at the same time the throughput capabilities of the system in a natural way.

Secondly, compared to the *Flow LSFM* mode, it easily allows multicolor and repeatable imaging of a large population of samples. Although the detection makes use of a single objective, the designed imaging chamber allows rotating the sample (Fig. 2.7C-D) in order to obtain multi-view recording or to expose a specific part of interest of the sample toward the objective. This is particularly useful for heart, head, caudal fin, or brain imaging of zebrafish larvae (Fig. 2.7E-G), which views might be hindered from a non-controlled orientation of the specimen. It also enables the imaging of long samples, such as entire zebrafish larvae that exceed the available field of view, by stitching (Fig. 2.7H). In that case, the syringe pump performs the translation to the next sample's section to be imaged.

Finally, the *Hybrid LSFM* mode allows to perform 3D time-lapse movies in different conditions, such as 3D multicolor dual side illuminated movies of the macrophage movement in zebrafish head and fin (Fig. 2.7D, and Video A.5 and Video A.6); neuron activity in the full zebrafish brain at 0.5 volumes/second (50 planes) (Fig. 2.7E and Video A.7), or alternate dual side illumination multicolor imaging of zebrafish embryo development (Fig. 2.7I).

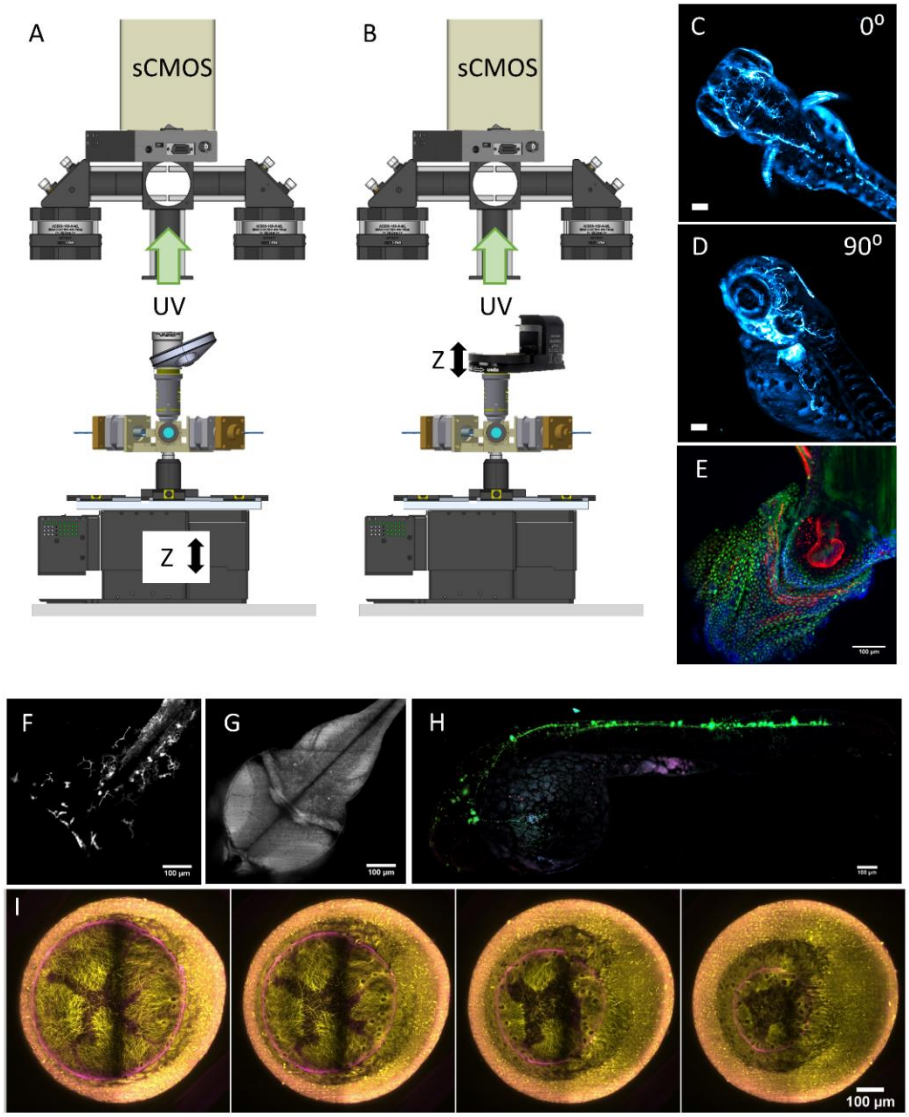

Figure 2.7: Setup implementation in the Hybrid LSFM modality with upright detection scheme and examples. The scanning in the depth (z) direction can be performed either (A) through a vertical stage moving the entire chamber or (B) through the displacement of the detection objective with a piezo-element synchronized with galvanometric scanning of the light sheet. UV= upper view. (C-D) The imaging chamber enables the rotation of the sample around the longitudinal axis of the FEP tube. (E) The system allowed high-throughput imaging of the zebrafish heart in a single imaging session (18 samples. The showed image was processed through a background correction method to decrease yolk's auto-fluorescence). Full set of images in Appendix A, Fig. A.7. The use of piezo focus control (B) allows fast imaging of macrophage migration in the caudal fin (F) as well as zebrafish brain's neural activity using calcium indicators (G). More information is in Videos 5, 6, and 7. Samples can also be moved in a controlled and stepwise manner along the tube, providing multichannel high-resolution whole larvae imaging by stitching (H). (I) Long-term multicolor time-lapse movies of zebrafish embryo development are also achieved. Scale bars: 100 µm. Image adapted from [1].

The new capabilities offered by the *Hybrid LFSM* mode (facilitated sample loading, 3D multicolor stack recording, and automated sample positioning) were used to perform volumetric HT imaging in a single day of ~100 of complex 3D-3 culture models [32] including a co-culture of tumor cell spheroids of non-small cell lung carcinoma, cancer-associated fibroblasts and a monocytic cell line (THP-1) on alginate capsules (Appendix A, Fig. A.6), or tens of three-colour fixed and immunostained zebrafish embryos (Appendix A, Fig. A.7). Additionally, more complex experiments in which the imaging of various samples can be repeated before and after a defined interaction (e.g. to obtain a control image [33], or the addition of a drug) are now possible, thanks to the easiness of the sample's loading and unloading procedures that maintain sample's viability.

Note that in the Hybrid LSFM, as in the Flow LSFM, the medium that fills the FEP tube can be the medium that best fits the experimental need (e.g. culturing media for organoids, or E3 medium for zebrafish, or medium with the addition of drugs for chemical interaction experiments).

2.4.3.4 Automatic sample loading

An additional add-on for the Flexi-SPIM platform is a 3D printed multiwell plate reader (MPR) system, which accepts common 96-multiwell plates and is connected to the distal tip of the FEP "loading tube" (as explained in Appendix A, Section A.7).

The MPR aims to move the tip of the loading tube over the plate containing multiple samples and insert it into the desired well. Once the tip is within the well, the syringe pump will aspire the specimen transporting it toward the FoV. The combination of the MPR, the motorized imaging chamber, and the *Hybrid LSFM* approach, permits not only the full automation of the sample loading, imaging, and sorting procedures of multiple samples but also the definition of automated drug delivery to the specimen directly in the multiwell plate. This is also thanks to the automation of communications between all the devices through an in-house implemented

LabVIEW-based program (see also Appendix A, section A.9 for the hardware and software used as computing center of the setup).

2.5 Flexi-SPIM: Discussion and potential impact

A summary of the main features of the different acquisition modes available within the Flexi-SPIM setup is shown in Table 1.

Acquisition mode	Dual side illumination	Dual side detection	Light sheet orientation	Multi-colour	Sample rotation	Mounting	Optimized for	Drawbacks
Classic LSFM	YES	YES	Vertical	YES	YES	One by one (agarose)	3D Time-lapse, multicolour imaging	Low throughtput
Flow LSFM	YES	YES	Vertical	Possible	NO	Multiple samples within FEP tube	Low resolution, increased throughput	Single colour on thick samples
Hybrid LSFM	YES	NO	Horizontal	YES	YES	Multiple samples within FEP tube	High resolution, increased throughput, multicolour imaging, stitching.	Single side detection

Table 1: Summary of the different acquisition modes available within the Flexi-SPIM setup.

Biological and biomedical research often need to deal with complex specimens whose development, functions, or drug-induced effects are not trivial to understand. LSFM offers unprecedented high x, y, and z resolution and optical sectioning capabilities along with low photobleaching rates and high-speed imaging.

However, the big variety of experiments needed to fully understand the biological complexity spans over different spatial and temporal scales and it often involves the statistical evaluation of many specimens. This diversity could not, until now, be practically addressed by using the current imaging approaches. The LSFM here described has a straightforward and automated sample mounting scheme that is capable to perform long-term imaging as well as high-throughput screens. Being

based on the LSFM concept, it contains all its inherent advantages. Furthermore, this can be used in a wide range of applications, going from developmental to functional imaging, to high-throughput screenings.

Three different highly automatized acquisition modes are combined on a single machine: *i*) *Classic LSFM*, with mechanical sample scanning and sample rotation, *ii*) *Flow LSFM* with fluidic scanning of the sample using specialized syringe pumps, and *iii*) *Hybrid LSFM*, which combines fluidic loading of samples and high-speed volume's scanning.

The performance of the Flexi-SPIM platform and its ability to carry out imaging of large populations were evaluated in a variety of samples (Appendix A, Fig. A.6 and Fig. A.7), from zebrafish embryos and larvae to 3D complex cell cultures, with high resolution, and minimal photo-bleaching. The achieved throughput will depend on the specific application and samples since the main limitation comes from the loading process. The highest throughput is achieved on the complex 3D culture imaging experiment, where several (around 10 to 20) samples are loaded at once and imaged sequentially in the *Hybrid LSFM*. For this experiment, we considered 12 distinct types of 3D cell cultures with a total of 110 specimens imaged in 5 hours, which leads to a throughput of about 20 samples per hour. When imaging zebrafish, each specimen needs to be loaded individually. The entire imaging process (loading the sample, positioning it within the FoV, rotating it to face the feature of interest, acquiring a 3D-3colour stack, and discarding a fish) took around 10-12 minutes, so the throughput was limited to 5 to 6 fish per hour.

The demonstrated system results in a robust and flexible multimodal light-sheet microscopy-based compact platform. The three different modalities could be interchanged in a few minutes and the re-alignment is extremely straightforward as changing from vertical to horizontal light sheets can be easily done thanks to the electronically controllable galvanometric mirrors. An open-source approach using custom-made Arduino-based electronics is used to control the shutters, LEDs, and

rotational motors. Importantly, an advanced sample loading system that enables extending the throughput capabilities of the previous configuration of LSFM is also described. In addition to that, the modular detection scheme, which uses a single camera, is key for allowing multiple imaging modalities. Finally, in addition to the double-sided illumination/detection scheme, the system possesses an additional detection channel (three in total) that is used in the *Hybrid LSFM* configuration.

Samples mounted through the fluidic-based loading system can be easily imaged using water dipping objectives, as in an upright microscope. This approach allows the straightforward interchange of objectives (from 10x 0.3NA to 40x 0.8NA). From the practical point of view, examples of a rich variety of experiments and applications (from time-lapse movies to high-throughput screens and 3D volume renders) were shown, all of them recorded with the same microscope.

Although the use of syringe-based loading for *Flow LSFM* and *Hybrid LSFM* modes is useful, some precautions need to be taken. Due to its fragility, the loading of zebrafish embryos on the first day of development is advisable to use a manual protocol, i.e. pipetting them into a loading pool and pulling them at low suction speeds. For harder samples, such as zebrafish embryos (from 2dpf), complex 3D-cultures, or organoids, the multiwell plate loading system can be alternatively used. Moreover, although the rotation of the sample is possible, it may slip and not perfectly follow the FEP tube rotation. For that reason, for the *Classic LSFM,* multi-view fusion algorithms can be easily implemented. The idea behind sample rotation in *Hybrid LSFM* mode is not to fulfill this requirement but to rotate the area of interest of the embryo (heart, brain, eye, etc.) towards the detection objective.

2.6 The transportable MuViSPIM

From the design of the Flexi-SPIM setup, I implemented an additional LSFM system in the MuViSPIM configuration [10]. This setup implements the *Classic LSFM* modality described above, i.e. with a double illumination/detection scheme. As described above and in the following chapters, its main application has been the

long-term imaging of delicate living embryos, featuring the same imaging chamber in 316L steel and environmental control setup explained in the previous section. The system was mounted on an optical breadboard, and the complete optical setup fits in a volume of about 60x60x60 cm^3 (Fig. 2.8).

The illumination delivery section (Fig. 2.8A) develops on the horizontal plane and it combines two laser lines (488 nm and 561 nm, Cobolt) for the excitation of broadly used fluorophores such as GFP, RFP, mCherry. After a 50:50 beam splitter divides the radiation between the two illumination arms, the cylindrical lens and the two excitation objectives (Nikon 4x 0.13 NA air) deliver the vertical light sheets within the chamber. A shutter inserted in each arm, implemented through a servo motor, enables to block the beam so that simultaneous or alternate illumination can be implemented. The shutters and the lasers are controlled by an Arduino board, which communicates with the controlling workstation in which the main software runs.

As for the Flexi-SPIM, the detection path (Fig. 2.8B) develops in the vertical direction and the views coming from the two collection objectives are projected either simultaneously or alternatively to the single camera chip by a right-edge prism or by a rotating mirror, respectively. In each detection arm, a tube lens having a focal length of 200 mm is mounted. However, these can be easily removed and the user can install a 300 mm tube lens if additional magnification is needed (e.g. Nyquist criterium would otherwise not be satisfied), without alignment operations. Finally, the sample mounting system is the same as described in the *Classic LSFM* mode of the Flexi-SPIM setup (Fig. 2.8C).

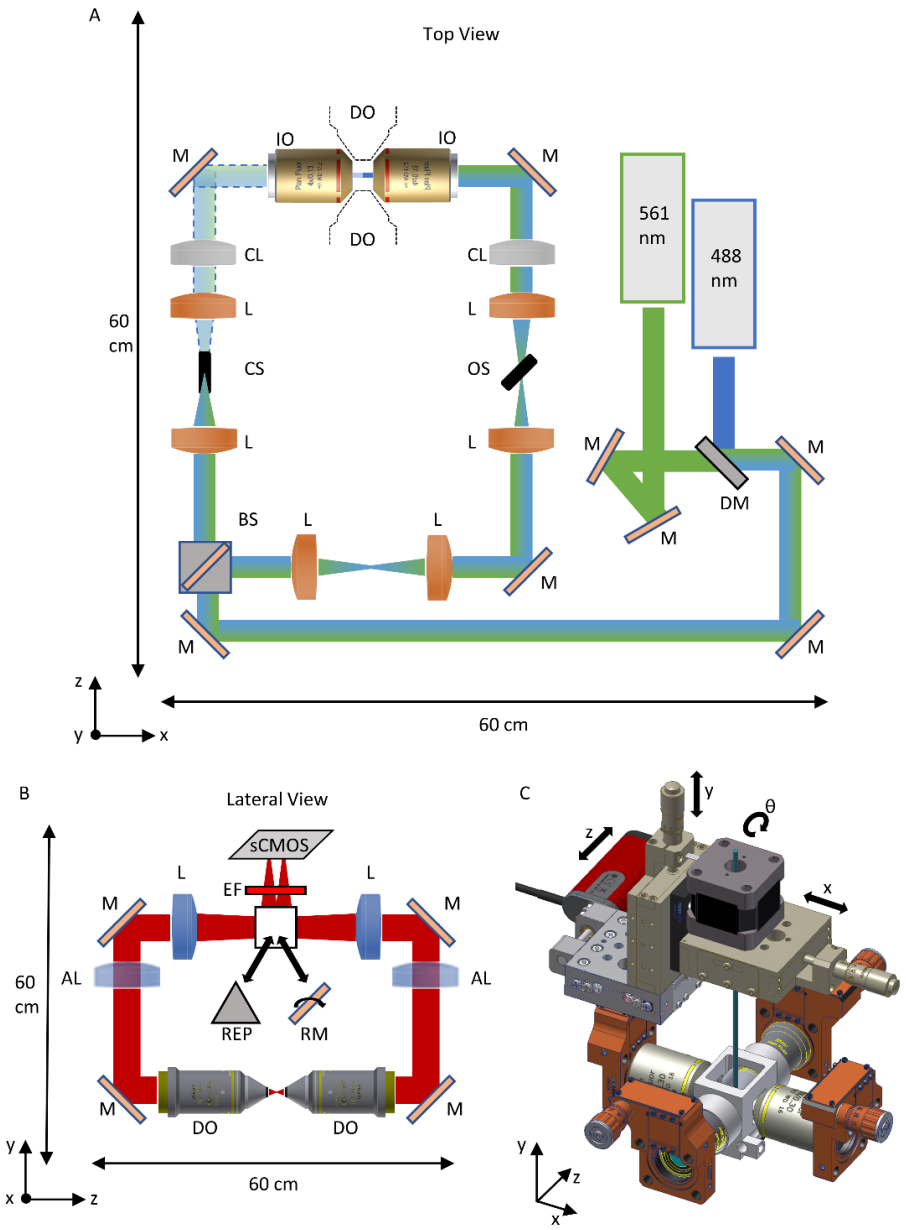

Figure 2.8: Modules' schematic of the MuViSPIM setup. (A) The illumination section is implemented on the horizontal plane and provides a double-illumination scheme. (B) The double-sided detection module develops in the vertical plane, combining the two views through either a right-edge prism (RP) or a rotating mirror (RM). The tube lens (L) normally used provides a focal length of 200mm, but it can be substituted by an alternative lens (AL) of 300 mm in focal length. (C) The sample module uses a high-precision motor for the scanning of the sample along z, two stages for the sample positioning in xy, and a stepper motor for sample rotation. The sample is connected to the stages through a glass capillary, and positioned in the middle of the chamber, at the foci of all objectives. M= mirror, DM= dichroic mirror, BS= beam splitter, OS= open shutter, CS= closed shutter, CL=cylindrical lens, IO= illumination objective, DO= detection objective, EF= emission filter.

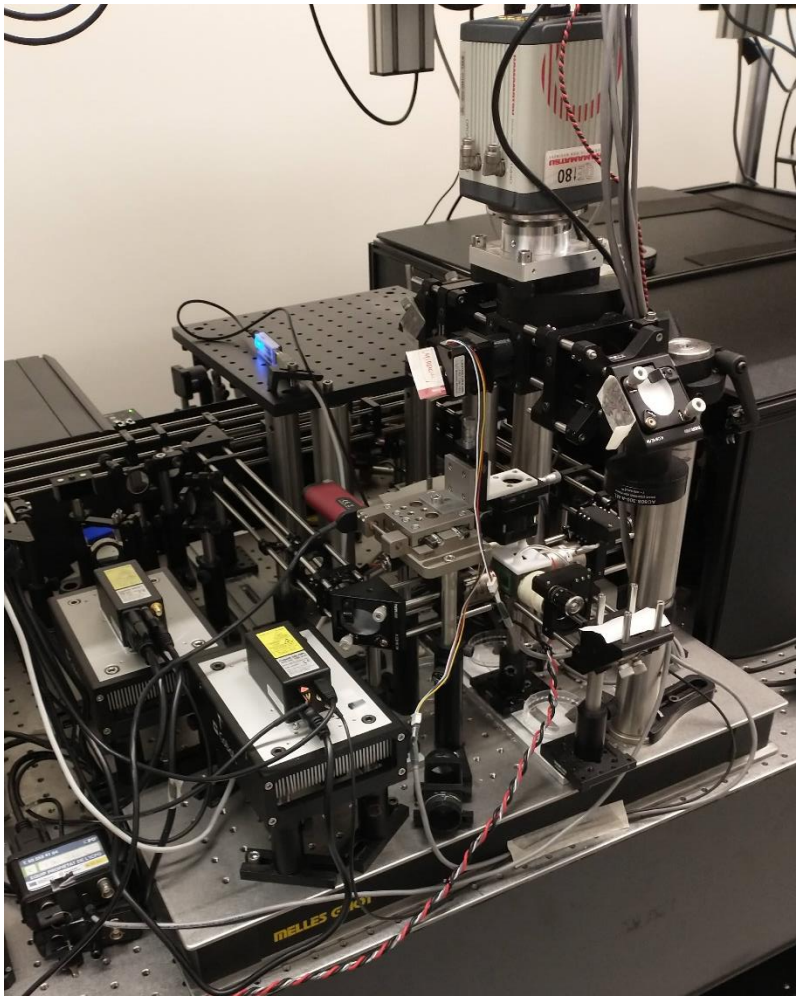

Figure 2.9: Photo of the MuViSPIM setup.

To completely automate the setup for long imaging sessions, all components are connected to a workstation that acts as a computing center. This is connected directly to some instruments, such as the camera, the filter wheel, and the sample stage. Moreover, it communicates with an Arduino controller which in turn controls lasers, shutters, and stepper motors (Fig. 2.10).

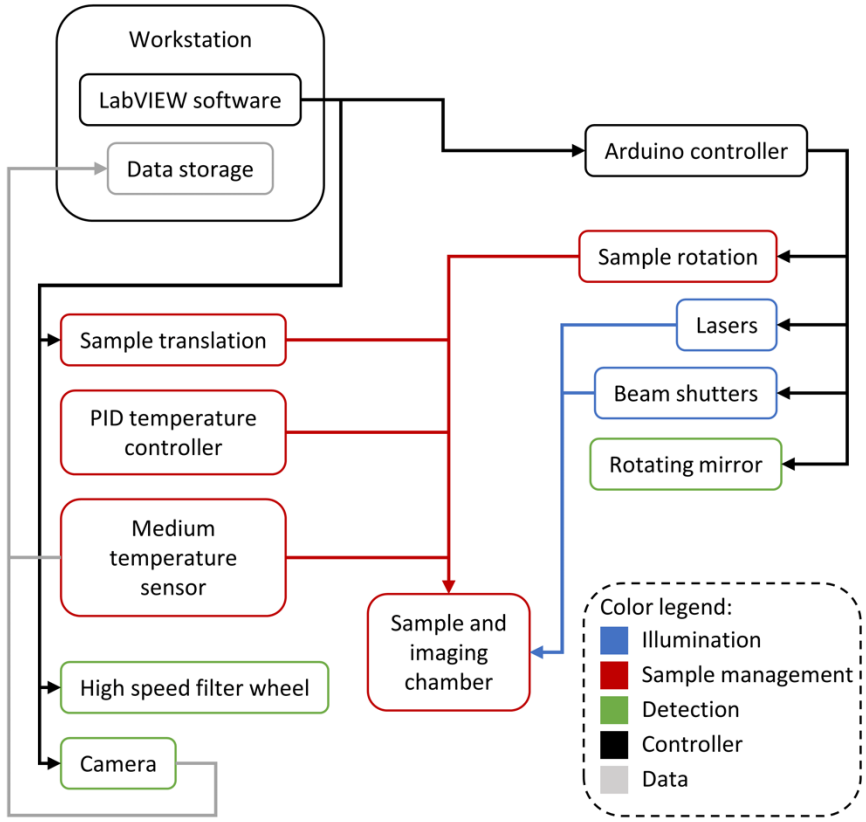

Figure 2.10: Schematic of principle for the implemented MuViSPIM setup. The whole setup is controlled by a LabVIEW software running on the workstation. Some components are directly controlled by the workstation, while others are managed by the Arduino board. Arrows indicate data flows and connections between the components.

In addition, I coded the controlling software through LabVIEW (National Instruments) to generate a user-friendly graphical interface (Fig. 2.11), so that also non-experts in microscopy could access the setup and define their own imaging needs using the implemented hardware. The software makes use of the "object-oriented" paradigm, which helps the reading of the software and importantly enables to easily maintain it operational if e.g. a specific component is substituted with another model. In that case, the programmer will need to modify only the class specific to that component, while no modification will be needed for the rest of the software.

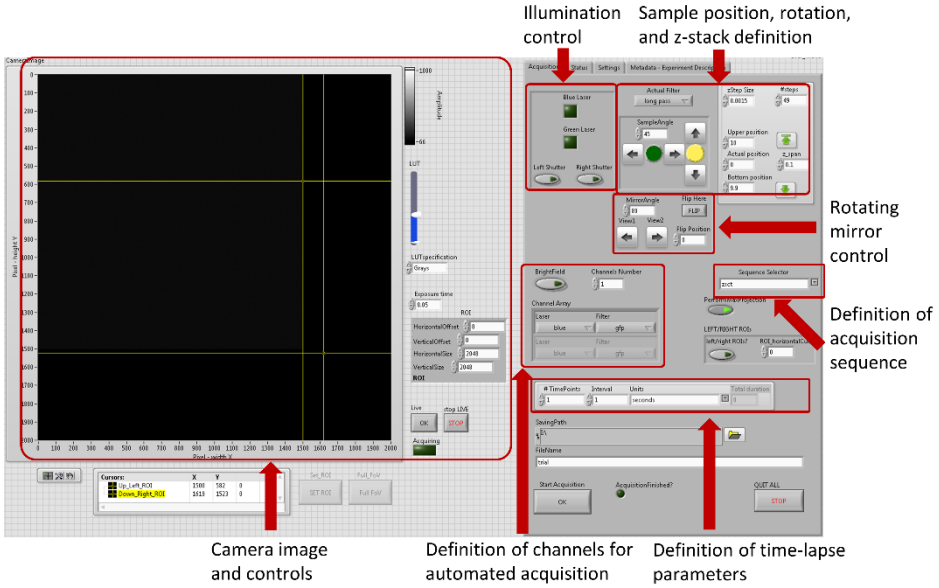

Figure 2.11: The graphical interface for the MuViSPIM microscope's software and its main components. Through this, the user can control all the devices of the microscope in "live" mode, and set all needed parameters for the launch of automated volume acquisitions over time.

The resulting system is a compact, easy-to-align, and easy-to-use microscope. It was used for some of the applications described in the following chapters, and it was also transported and installed in the imaging facility of the University of Montpellier (France) for one month (see Chapter 4). There it has been used in the context of a collaboration and also made available to external users for trials on their own samples.

2.7 Future perspectives

The modularity of the Flexi-SPIM setup also permits other functionalities to be easily implemented. On the illumination side Bessel, Airy, or 2-photon excitation can be easily added through the DLSM version [34,35], to achieve larger FOV and help in the imaging of thicker and highly scattering samples.

On the detection module, an additional port could also be used to introduce optical manipulation capabilities such as photoactivation or laser ablation. In this way, repeatable LSFM imaging and sample manipulation of a large population would be

possible, in high throughput and fully-automatic approach. This would potentially boost research e.g. in the field of regeneration studies.

Finally, the combination of the high-throughput capability with remote focusing or wavefront coding techniques for fast volumetric imaging could also be implemented [6,7]. The openness of the system will allow performing these improvements and the conjugation to new modules that further extend the platform's capabilities.

2.8 Additional information

Additional information on the various components of the setups, characterization procedures, and videos links and descriptions can be found in Appendix A and in [1].

2.9 References

1. M. Bernardello, E. J. Gualda, and P. Loza-Alvarez, "Modular multimodal platform for classical and high throughput light sheet microscopy.," Sci. Rep. **12**(1), 1969 (2022).

2. J. Huisken, J. Swoger, F. Del Bene, J. Wittbrodt, and E. H. K. Stelzer, "Optical sectioning deep inside live embryos by selective plane illumination microscopy.," Science **305**(5686), 1007–1009 (2004).

3. O. E. Olarte, J. Andilla, E. J. Gualda, and P. Loza-Alvarez, "Light-sheet microscopy: a tutorial," Adv. Opt. Photonics **10**(1), 111–179 (2018).

4. B.-C. Chen, W. R. Legant, K. Wang, L. Shao, D. E. Milkie, M. W. Davidson, C. Janetopoulos, X. S. Wu, J. A. 3rd Hammer, Z. Liu, B. P. English, Y. Mimori-Kiyosue, D. P. Romero, A. T. Ritter, J. Lippincott-Schwartz, L. Fritz-Laylin, R. D. Mullins, D. M. Mitchell, J. N. Bembenek, A.-C. Reymann, R. Böhme, S. W. Grill, J. T. Wang, G. Seydoux, U. S. Tulu, D. P. Kiehart, and E. Betzig, "Lattice light-sheet microscopy: imaging molecules to embryos at high spatiotemporal resolution.," Science **346**(6208), 1257998 (2014).

5. R. Galland, G. Grenci, A. Aravind, V. Viasnoff, V. Studer, and J.-B. Sibarita, "3D high- and super-resolution imaging using single-objective SPIM.," Nat. Methods **12**(7), 641–644 (2015).

6. O. E. Olarte, J. Andilla, D. Artigas, and P. Loza-Alvarez, "Decoupled illumination detection in light sheet microscopy for fast volumetric imaging," Optica **2**(8), 702–705 (2015).

7. F. O. Fahrbach, F. F. Voigt, B. Schmid, F. Helmchen, and J. Huisken, "Rapid 3D light-sheet microscopy with a tunable lens," Opt. Express **21**(18), 21010–21026 (2013).

8. R. Tomer, K. Khairy, F. Amat, and P. J. Keller, "Quantitative high-speed imaging of entire developing embryos with simultaneous multiview light-sheet microscopy.," Nat. Methods **9**(7), 755–763 (2012).

9. B. Schmid, G. Shah, N. Scherf, M. Weber, K. Thierbach, C. P. Campos, I. Roeder, P. Aanstad, and J. Huisken, "High-speed panoramic light-sheet microscopy reveals global endodermal cell dynamics.," Nat. Commun. **4**, 2207 (2013).

10. U. Krzic, S. Gunther, T. E. Saunders, S. J. Streichan, and L. Hufnagel, "Multiview light-sheet microscope for rapid in toto imaging.," Nat. Methods **9**(7), 730–733 (2012).

11. F. Pampaloni, B.-J. Chang, and E. H. K. Stelzer, "Light sheet-based fluorescence microscopy (LSFM) for the quantitative imaging of cells and

tissues.," Cell Tissue Res. **360**(1), 129–141 (2015).

12. B. Patra, Y.-S. Peng, C.-C. Peng, W.-H. Liao, Y.-A. Chen, K.-H. Lin, Y.-C. Tung, and C.-H. Lee, "Migration and vascular lumen formation of endothelial cells in cancer cell spheroids of various sizes.," Biomicrofluidics **8**(5), 52109 (2014).

13. C. Dunsby, "Optically sectioned imaging by oblique plane microscopy," Opt. Express **16**(25), 20306–20316 (2008).

14. A. K. Glaser, N. P. Reder, Y. Chen, C. Yin, L. Wei, S. Kang, L. A. Barner, W. Xie, E. F. McCarty, C. Mao, A. R. Halpern, C. R. Stoltzfus, J. S. Daniels, M. Y. Gerner, P. R. Nicovich, J. C. Vaughan, L. D. True, and J. T. C. Liu, "Multi-immersion open-top light-sheet microscope for high-throughput imaging of cleared tissues.," Nat. Commun. **10**(1), 2781 (2019).

15. B. Eismann, T. G. Krieger, J. Beneke, R. Bulkescher, L. Adam, H. Erfle, C. Herrmann, R. Eils, and C. Conrad, "Automated 3D light-sheet screening with high spatiotemporal resolution reveals mitotic phenotypes.," J. Cell Sci. **133**(11), (2020).

16. A. Beghin, G. Grenci, H. Rajendiran, T. Delaire, S. B. Mohamad Raffi, D. Blanc, R. de Mets, H. T. Ong, V. Acharya, G. Sahini, V. Racine, R. Galland, J.-B. Sibarita, and V. Viasnoff, "High content 3D imaging method for quantitative characterization of organoid development and phenotype," bioRxiv 2021.03.26.437121 (2021).

17. E. J. Gualda, H. Pereira, G. G. Martins, R. Gardner, and N. Moreno, "Three-dimensional imaging flow cytometry through light-sheet fluorescence microscopy.," Cytometry. A **91**(2), 144–151 (2017).

18. P. Paiè, R. Martínez Vázquez, R. Osellame, F. Bragheri, and A. Bassi, "Microfluidic Based Optical Microscopes on Chip," Cytom. Part A **93**(10), 987–996 (2018).

19. J. Wu, J. Li, and R. K. Y. Chan, "A light sheet based high throughput 3D-imaging flow cytometer for phytoplankton analysis.," Opt. Express **21**(12), 14474–14480 (2013).

20. H. Jiang, T. Zhu, H. Zhang, J. Nie, Z. Guan, C.-M. Ho, S. Liu, and P. Fei, "Droplet-based light-sheet fluorescence microscopy for high-throughput sample preparation, 3-D imaging and quantitative analysis on a chip.," Lab Chip **17**(13), 2193–2197 (2017).

21. T. Miura, H. Mikami, A. Isozaki, T. Ito, Y. Ozeki, and K. Goda, "On-chip light-sheet fluorescence imaging flow cytometry at a high flow speed of 1 m/s," Biomed. Opt. Express **9**(7), 3424–3433 (2018).

22. P. Paiè, F. Bragheri, A. Bassi, and R. Osellame, "Selective plane illumination microscopy on a chip.," Lab Chip **16**(9), 1556–1560 (2016).

23. F. Sala, M. Castriotta, P. Paiè, A. Farina, S. D'Annunzio, A. Zippo, R. Osellame, F. Bragheri, and A. Bassi, "High-throughput 3D imaging of single cells with light-sheet fluorescence microscopy on chip," Biomed. Opt. Express **11**(8), 4397–4407 (2020).

24. R. Memeo, P. Paiè, F. Sala, M. Castriotta, C. Guercio, T. Vaccari, R. Osellame, A. Bassi, and F. Bragheri, "Automatic imaging of Drosophila embryos with light sheet fluorescence microscopy on chip.," J. Biophotonics **14**(3), e202000396 (2021).

25. E. J. Gualda, H. Pereira, T. Vale, M. F. Estrada, C. Brito, and N. Moreno, "SPIM-fluid: open source light-sheet based platform for high-throughput imaging.," Biomed. Opt. Express **6**(11), 4447–4456 (2015).

26. S. L. Logan, C. Dudley, R. P. Baker, M. J. Taormina, E. A. Hay, and R. Parthasarathy, "Automated high-throughput light-sheet fluorescence microscopy of larval zebrafish," PLoS One **13**(11), e0198705 (2018).

27. P. J. Keller, A. D. Schmidt, J. Wittbrodt, and E. H. K. Stelzer, "Reconstruction of zebrafish early embryonic development by scanned light sheet microscopy.," Science **322**(5904), 1065–1069 (2008).

28. J. Huisken and D. Y. R. Stainier, "Even fluorescence excitation by multidirectional selective plane illumination microscopy (mSPIM).," Opt. Lett. **32**(17), 2608–2610 (2007).

29. A. Kaufmann, M. Mickoleit, M. Weber, and J. Huisken, "Multilayer mounting enables long-term imaging of zebrafish development in a light sheet microscope.," Development **139**(17), 3242–3247 (2012).

30. M. B. Ahrens, M. B. Orger, D. N. Robson, J. M. Li, and P. J. Keller, "Whole-brain functional imaging at cellular resolution using light-sheet microscopy.," Nat. Methods **10**(5), 413–420 (2013).

31. S. Preibisch, S. Saalfeld, J. Schindelin, and P. Tomancak, "Software for bead-based registration of selective plane illumination microscopy data.," Nat. Methods **7**(6), 418–419 (2010).

32. S. P. Rebelo, C. Pinto, T. R. Martins, N. Harrer, M. F. Estrada, P. Loza-Alvarez, J. Cabeçadas, P. M. Alves, E. J. Gualda, W. Sommergruber, and C. Brito, "3D-3-culture: A tool to unveil macrophage plasticity in the tumour microenvironment.," Biomaterials **163**, 185–197 (2018).

33. A. L. Cartaxo, J. Almeida, E. J. Gualda, M. Marsal, P. Loza-Alvarez, C. Brito,

and I. A. Isidro, "A computational diffusion model to study antibody transport within reconstructed tumor microenvironments.," BMC Bioinformatics **21**(1), 529 (2020).

34. J. Palero, S. I. C. O. Santos, D. Artigas, and P. Loza-Alvarez, "A simple scanless two-photon fluorescence microscope using selective plane illumination," Opt. Express **18**(8), 8491–8498 (2010).

35. O. E. Olarte, J. Licea-Rodriguez, J. A. Palero, E. J. Gualda, D. Artigas, J. Mayer, J. Swoger, J. Sharpe, I. Rocha-Mendoza, R. Rangel-Rojo, and P. Loza-Alvarez, "Image formation by linear and nonlinear digital scanned light-sheet fluorescence microscopy with Gaussian and Bessel beam profiles," Biomed. Opt. Express **3**(7), 1492–1505 (2012).

Chapter 3: Yolk’s microtubule dynamics in the early zebrafish embryo

This chapter contains content entirely reproduced or adapted from the article [1]: M. Bernardello, M. Marsal, E. J. Gualda, and P. Loza-Alvarez, "Light-sheet fluorescence microscopy for the in vivo study of microtubule dynamics in the zebrafish embryo," Biomed. Opt. Express 12, 6237-6254 (2021).

3.1 Abstract

During its first hours of development, the zebrafish embryo presents a large microtubule array in the yolk region, essential for its development. Despite of its size and dynamic behavior, this network has been studied only in limited field of views or in fixed samples. Light Sheet Fluorescence Microscopy can provide the imaging of the entire yolk microtubule (MT) network in-vivo. This application has allowed us to develop a novel image analysis from which we clearly observe a cyclical re-arrangement of the entire MT network in synchrony with blastoderm mitotic waves. These dynamics also affect a previously unreported microtubule array deep within the yolk, here described. These findings provide a new vision of the zebrafish yolk microtubules arrangement, and offers novel insights in the interaction between mitotic events and microtubules reorganization. The results here described are also resumed in [1].

3.2 Introduction

During the first hours of embryonic development, microtubules (MT) can be found ubiquitously along the zebrafish (*Danio rerio*) embryo. In the blastoderm, siting at the animal pole, MT are mainly responsible for cell divisions and are highly condensed during mitosis in the mitotic spindles. In the yolk cell, an initially a-nuclear lipid sphere of roughly 700 µm in diameter [2], MTs are also present and account for transport of molecules essential for early development [3–6].

The current view for the MTs organization in the yolk cell describes a network of parallel MTs that emerge from the marginal blastomeres, extend towards the vegetal pole and are located at the superficial region of the yolk cell, in the Yolk Cytoplasmic Layer (YCL) [4,7–10]. Reaching the 512-cell stage, a syncytium forms in the yolk, called Yolk Syncytial Layer (YSL) [2], containing the Yolk Syncytial Nuclei (YSN) [9], which derive from the collapse of the marginal cells and the release of their content into the yolk mass. YCL MTs are believed to be associated with the most vegetally located external YSN (eYSN) once the YSL has been formed.

These parallel MT arrays have been studied mainly for their role in the mechanism of epiboly, i.e. the developmental process characterized by the thinning and spreading of the blastoderm around the yolk, coordinating the mechanisms that lead blastomeres and eYSN from the animal pole toward the vegetal pole [7]. The parallel MT arrays have been proved to be necessary for the correct migration of the eYSN toward the vegetal pole [8], through associated motor proteins [10].

Besides that, the presence of a MTs mesh in the internal YSL (iYSL) between the internal YSN (iYSN) and eYSN, has also been described [7–9]. However, little is known about the organization and changes that the yolk MT network presents at cleavage and blastula stages. In this temporal window it is assumed that the parallel arrays are associated to the marginal blastomeres [8], but no extensive data is available to describe how this network is maintained and eventually re-organized over a long period of time until the initiation of epiboly. Most studies are conducted by fixing embryos at various time points, hiding the potential transient dynamics. Live-imaging has also been performed using confocal microscopy [4,8,11,12].

This method however, provides limited field of views (FoV), has poor penetration capabilities and has the potential to induce unwanted phototoxic effects. Therefore, these approaches (use of fixed embryos, visualization of small field of views, or use of confocal microscopy) are far from providing an accurate and complete description of the dynamic nature of the MT network over the full yolk sphere. The study of this MT network in its full complexity would provide the basis for the description of its role before the initiation of epiboly, and it would offer an in-vivo model for the study of MT dynamics and its organization in a scale that largely encompasses the size of ordinary cells.

In many biological systems signals need to travel across the cellular environment. Although this could be achieved at small scales through molecule diffusion, the mechanism would not be efficient at large scales [13], i.e. where signals need to induce spatial-temporal coordination over distances of hundreds of micrometers. In

such large-scale environments many examples of wave-like patterns can be found. Wave-like patterns consist in the cascade of a particular event that appears to cross the system. The events are synchronized between them in such a way that it is possible to visualize a travelling wavefront. Examples of wave-like patterns include the bulk actin wave in zebrafish oocytes [14], calcium waves [15,16], and mitotic waves in zebrafish [2,17,18], in Xenopus embryos [19], and in Xenopus egg extracts [20].

Light Sheet Fluorescence Microscopy (LSFM) [21], provides an efficient way for in-vivo imaging of large samples and at high resolutions [22]. In fact, in zebrafish development, LSFM has been extensively and successfully used to observe nuclei movements and to describe cells' fate in the entire embryo or of specific germ layers [17,23–25]. Through the custom-made LSFM setups developed along this thesis (namely the Flexi-SPIM in the *Hybrid-LSFM* mode, and the MuViSPIM, see Chapter 2 and Appendix B, Fig. B.1) it was possible to observe the dynamical changes in the structure of the zebrafish external YCL MT network (eMTN).

The two used LSFM configurations, based respectively on agarose [21] and fluidic [26,27] sample mounting methods, enable to image living zebrafish embryos within their native chorion. This possibility is of exceptional importance for a correct live imaging session, as it avoids the mechanical constrictions that conventional agarose medium, such as the ones used in confocal microscopy, could exert on the sample development. Moreover, the sample orientation can be easily adjusted thanks to the motorized rotational stage. This imaging flexibility is not possible in conventional confocal microscopes, and it provides a clear advantage for the study over a prolonged time of living organisms. In addition, the temperature at which the embryos develop can be controlled and maintained constant for the whole experiment.

This study focuses on the MT network dynamic nature over the entire yolk. Along the present work, I will show and characterize a particular feature, firstly indicated

in [12] in a limited spatial-temporal window, but to my knowledge not yet described in its full dimensions: Microtubule Organizational Waves (MOW) that cross the yolk cell. Here I present the MOW as a new wave-like pattern. Besides its visualization, I also correlate it with other macro-events happening in the embryo, such as a constriction and relaxation of the blastoderm margin and the cells' division cycles. In addition, I also provide a set of dedicated tools for the image quantification of this phenomenon, considering the spherical shape of the embryo.

Moreover, I give evidence of the presence of another set of MTs present deep into the yolk, the internal MT network (iMTN), and show how it is affected by the MOWs' passage. Previous work based on embryos' fixation and immunostaining could not conclude on the eventual existence of the iMTN [8] and only now, thanks to the penetration depth provided by in-vivo LSFM, this new MT network can be rigorously investigated.

Taken together, these results permit to provide a more complete vision of the MT networks populating the zebrafish yolk cell in the cleavage and blastula stages, both in their morphology and their dynamics. In turn, the zebrafish yolk MT networks emerges as an in-vivo model to test different hypotheses on microtubule-based nucleation and on the interaction between mitotic waves, centrosomes, and MT branches [28].

In addition, a particular microtubule aster arrangement arises in the embryos of the TG(XlEef1a1:dclk2-GFP) transgenic line during the epiboly stage, which is here also characterized.

The methodology, based on LSFM and a novel image analysis procedure, has the potential to further investigate new and already approached problems in various temporal windows. Examples might extend from a complete description of large scale transport of molecules and organelles to an all-embryo global view on the MT-based epiboly movements. Moreover, these can be quantitatively assessed in

various early zebrafish development mutants showing alterations in MT organization.

3.3 Results

3.3.1 LSFM permits the visualization of the MTs re-arrangement in the whole embryo

Thanks to the big FoV (maximum 1300 µm x 1300 µm) of the custom-build LSFM systems described in Chapter 2, it has been possible to follow the development of whole zebrafish embryos at high spatial (ranging from 0.60 µm to 1.45µm) and time resolution (ranging from 0.3 to 1 volumes/minute). In order to visualize MT dynamics, the MT reporter transgenic line TG(XlEef1a1:dclk2-GFP) [11] (noted as dclk2-GFP) was employed. In addition, as MT spindles are a key component during mitosis, the dclk2-GFP line also provides useful information about their spatial (e.g., orientation of the divisions) and temporal behavior (e.g., synchronization between them and other events).

From the collected images it is particularly evident how the concentration of microtubules changes during the division cycle of both blastomeres and YSNs. This is because during metaphase the spindles produce a higher fluorescence signal that then rapidly decreases until interphase, providing a measure of the cell cycle timing. By following the mean intensity profile of the entire blastoderm over time (Fig. 3.1A), it was possible to account for the different cell cycles stages. In fact, this mean intensity value follows alternatively peaks and valleys, which correspond to the meta- and inter- phases of the cell cycle respectively (Fig. 3.1B). This analysis provides a means of staging the embryo under observation, which can be later used for additional analysis. The correspondence between intensity peaks and valleys with the mitosis events remains valid also when smaller regions are analyzed. Therefore, it allows to follow up locally the timing of the division cycles of single cells or YSN.

The dclk2-GFP line provides not only the visualization of the MT spindles during the division cycles of the blastomeres and YSN, but also of the MT network in the yolk. Through the custom-made LSFM setups, I mesoscopically analyzed the in-vivo dynamics of the eMTN during cleavage, blastula, and gastrula stages over the entire yolk cell. As the eMTN is located in the YCL, it can be visualized through the maximum intensity projection of the acquired 3D stacks (Fig. 3.1A).

We observed that the MT network periodically and progressively undergoes a reorganization process over time (Video B.1), forming what I called Microtubule Organizational Waves (MOWs). These subsequent wave-like patterns consist of variations in MTs density, either due to cyclical polymerization and de-polymerization [12] or bundling and unbundling events. The measure of the mean intensity over a determined region of interest (ROI) correlates with a measure of the density of the microtubules present in the same region (Fig. 3.1C). Therefore, the drop of the mean intensity, from a higher value (dense network and low bundling levels of microtubules) to a lower value (sparser network), correlates with the passage of the MOW wavefront in that region. Several MOWs can be visualized sequentially in a given ROI between cleavage and blastula stages, before the initiation of epiboly. They appear to originate from the blastoderm margin and advance, in a belt-like fashion, towards the vegetal pole, where they concentrically close (Fig. 3.1D-F). A closer look reveals that before the passage of the MOW the MT network appears to be diffused and disorganized, without a clear and precise orientation (Fig. 3.1G). At the passage of the MOW, the involved microtubules appear to be re-organized in well-defined and thicker bundles (Fig. 3.1H). Shortly after, they become again diffused (Fig. 3.1I) and the following MOW will repeat the bundling process.

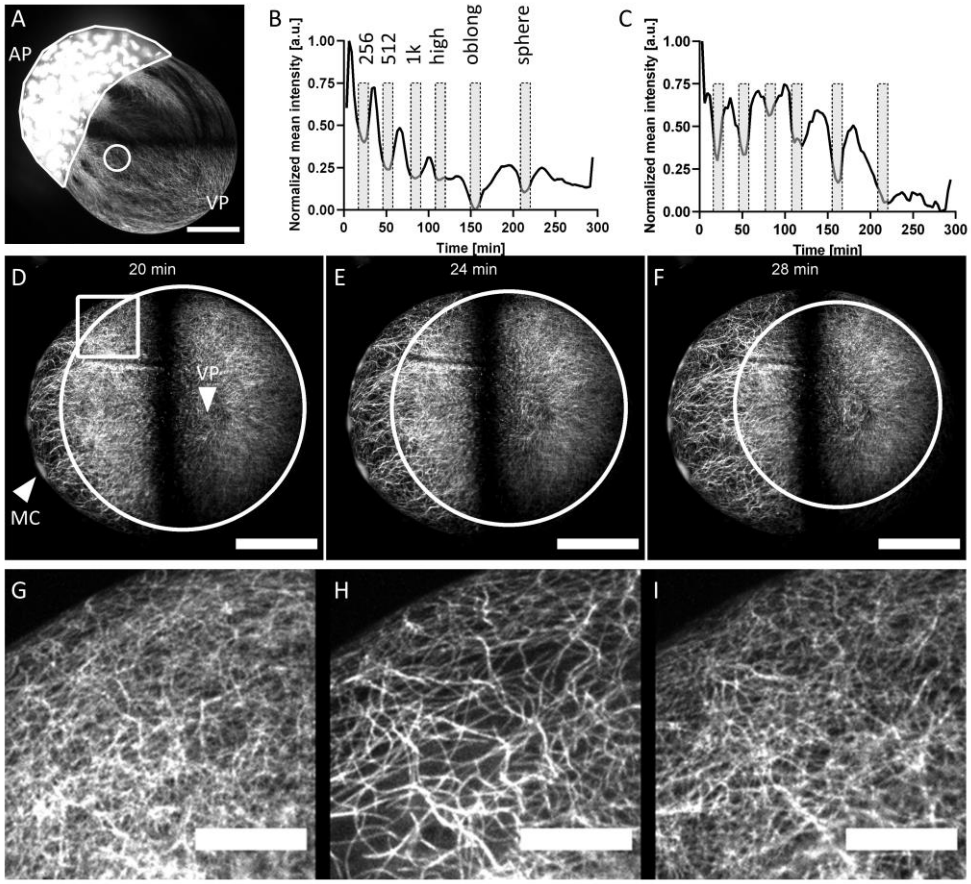

Figure 3.1: LSFM permits to see the microtubule re-arrangement in the whole embryo. (A) dclk2-GFP embryo during synchronous mitosis events of the blastomeres. Lateral view, AP=animal pole, VP= vegetal pole, scale bar 200µm. (B) Normalized mean intensity profile over time of the blastoderm region as highlighted in (A). The overlaid bars indicate the subsequent developmental stages of the embryo, from 256-cell to sphere stage. (C) The obtained graph for the normalized mean intensity over time on the yolk surface (circular ROI in (A)). Overlaid bars highlight drops of intensity corresponding to MOW passages. (D-F) Three frames (maximum intensity projection) from time-lapse LSFM imaging of the same embryo. The white circumferences indicate the wavefront of the same MOW that is advancing over the eMTN of a dclk2-GFP embryo at cleavage stage, vegetal view. During this time, the wavefront travels toward the vegetal pole of the embryo (the travelling is indicated by the reducing size of the overlapped circumference). See also Video B.1. MC= marginal cell, scale bar 200 µm. Central black region is due to the LS bending caused by the curvature of the sample. (G-I) Zoom in at the square region highlighted in (D), visualizing the eMTN (G) before (diffuse network), (H) during (sparser MTs), and (I) shortly after (re-diffused network) the MOW passage. Scale bars 50 µm. Image reproduced from [1].

3.3.2 Temporal concurrence of mitosis and MOWs

It is accepted that the microtubules at the YCL emerge from microtubule organizing centers (MTOCs) associated with the marginal cells (or eYSN, when formed) [7,8]. From this work, it also appears that the dividing blastomeres potentially also induce the division of the connected MT branch, giving rise to two sub-branches (see Appendix B, Fig. B.2). As previously described, MOWs pass across the yolk from the blastoderm margin to the vegetal pole (see also Video B.2). Therefore, the temporal concomitance between the MOWs initiation and the division of the blastomeres/eYSN generating the microtubule branch was examined. Interestingly, the MOWs appear to be synchronized with the division cycle of the blastomeres/eYSN (Fig. 3.2A-C). Moreover, the re-organizational process of the microtubules in the yolk cell (Fig. 3.2D-F) appears to be also synchronized with cyclic embryo macro-scale shape changes, such as constriction at the blastoderm margin, followed by expansion periods (Fig. 3.2G-I).

In order to demonstrate the temporal concomitance between MOWs initiation and the division cycle of the blastoderm cells I recorded, for all the time points, the mean intensity of the closest to the YSL part of a yolk's microtubule branch and the mean intensity of the cell (or eYSN) that appear to generate that branch (through the FIJI plugin "Manual Tracking with Trackmate" [29], see Appendix B, section B.2 for the complete description of the analysis procedure). For cells and eYSN analysis, a peak in the mean intensity corresponds to a mitotic event (Fig. 3.2J). Over the microtubule branch, a drop in the mean intensity corresponds to a MOW passage (Fig. 3.2K). The periodic constriction and expansion of the blastoderm margin was also detected (Fig. 3.2L). The analysis confirms a temporal correlation of these three events, which would suggest that they are closely related. In particular, while the blastoderm margin contractions are temporally concomitant with the blastomeres' divisions, the MOW initiations follow with a slightly delayed timing.

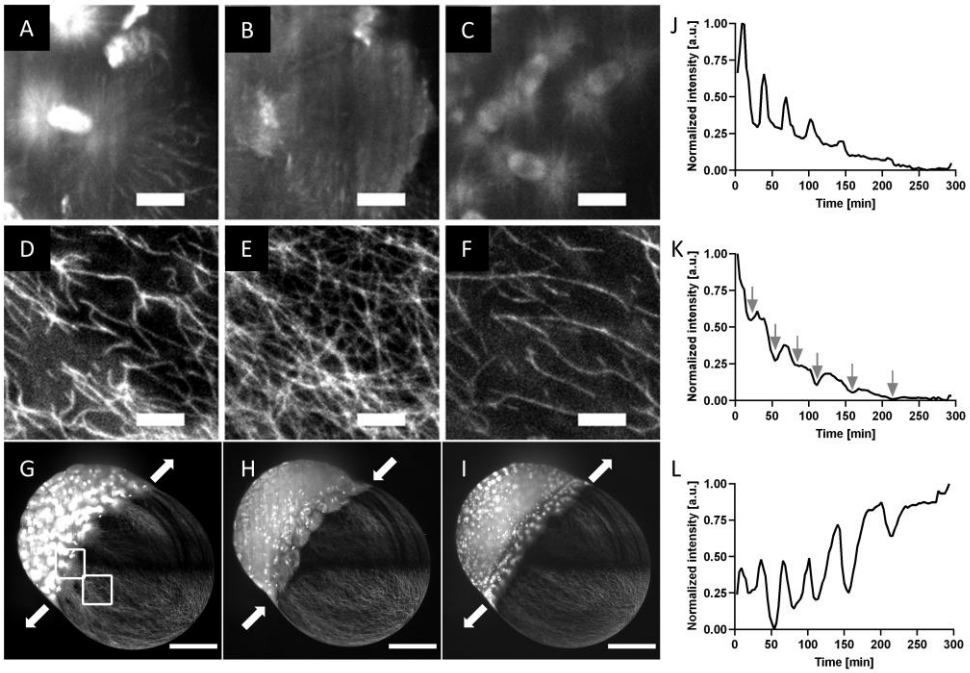

Figure 3.2: Temporal concurrence of mitosis and MOWs. (A-C) Visualization of blastomere/eYSN cycle phases (relative ROI indicated in panel (G)) through microtubules' labelling: (A) metaphase, (B) interphase, (C) metaphase (at minutes 9, 24, 102). Scale bars 25 µm. (D-F) Visualization of MOWs passages in the subsequent yolk region (relative ROI indicated in panel (G)). The MT network is (D) highly oriented and sparse, then (E) re-diffuses, and again (F) sparse (at minutes 15, 27, 108). Scale bars 25 µm. (G-H) The same dclk2-GFP embryo from a lateral view at three different timepoints (at minutes 9, 24, 102), scale bars 200 µm. Animal pole at top left, vegetal pole at bottom right. Arrows indicate expansion (pointing outward in A and C) and contraction (pointing inward in B) of the blastoderm margin. (J) Normalized mean intensity graph visualizing blastomeres/YSNs cycles (metaphases are peaks, interphases are valleys, graph obtained from the local analysis). (K) Normalized mean intensity graph visualizing the periodic MOWs passage (arrows) over the yolk region (graph obtained from the local analysis). (L) The periodic blastoderm contractions (valleys) and expansions (peaks). Blastoderm margin expansion and nuclei metaphase appear to be synchronized, MOW passage follows after few minutes. See Appendix B, sections B.2 and B.3 for details on how the graphs were retrieved. See also Video B.2. Image reproduced from [1].

3.3.3 MOWs depend on the cell/eYSN divisions

One of the major events that occurs prior to gastrulation is the fact that the eYSNs become post-mitotic, coinciding with the beginning of epiboly [30]. Given the low photobleaching and phototoxicity properties of LSFM setups, the development of our embryos throughout all the embryonic developmental stages can be imaged, from cleavage to beyond epiboly (see Video B.3). This allows to examine when the last MOW takes place, in order to correlate the origin of the MOWs with the

divisions of blastomeres or eYSN. From visual inspections, no MOW is emerging during gastrulation. To further investigate it, I detected the time points of last divisions of the eYSNs (see also Appendix B, section B.5 for the complete description of the analysis procedure) and compared them with the last MOW's initiation timing. Nuclei are visible as non-fluorescence spots over a bright (microtubules) background (Fig. 3.3A), except when the division takes place, i.e. when the mitotic spindles increase the fluorescent signal (Fig. 3.3B). MT density variations defining the MOW initiation (Fig. 3.3C-D) are retrieved, and the comparison of the obtained graphs (Fig. 3.3E-F) supported our hypothesis (i.e. the last MOW's initiation is temporally correlated with the last division of eYSNs) in five out of six examined embryos.

In order to gain further evidences of the dependence of the MOWs initiation on the blastomeres/eYSN divisions, I sought to interfere with the periodicities of their division's cycles. A simple but effective method is given by the sensitivity of the embryo to the temperature. It is well established that the division timing of the blastoderm is influenced by the temperature of the medium in which the embryo is immersed: higher temperatures will accelerate the processes, while lower temperatures will consistently delay the division cycles [2]. Through the LSFM imaging chamber, the temperature of the imaging medium in which the embryos are immersed can be controlled, and permitted to follow embryos' development at three different temperatures: 22, 26.5, and 31 degrees Celsius. On the retrieved images, I tracked the YSN and the relative branch mean intensities over time to detect the time points in which (1) the mitosis events and (2) the MOW initiation occurs.

Finally, periodicities, defined as the time elapsed between one event and its immediately precedent occurrence, were calculated for both MOWs and mitosis. Fig. 3.3H shows how temperature affects, as expected, the division periodicity of the blastomeres or eYSN's mitosis (33.79 ± 12.79 min at 22 degrees, N=21; 22.77 ± 5.32

min at 26.5 degrees, N=11; 19.38 ± 7.05 min at 31 degrees, N=12; means ± standard deviations). It can also be observed how the periodicities of the MOW's initiation change according (35.56±11.32min at 22 degrees, N=17; 22.17±5.94 min at 26.5 degrees, N=12; 18.53±6.25 min at 31 degrees, N=17; means ± standard deviations). Importantly, no statistically significant difference was observed between mitosis' periodicities and MOWs' initiation periodicities relative to the same experimental condition, which confirms our hypothesis that MOWs' initiations closely follow mitosis events in their variation due to temperature. See also Appendix B, section B.7 for the statistical analysis procedure.

Besides demonstrating that the interference with the mitosis cycle also affects MOW's initiations timing, from the experiments we can also infer that there is a one-to-one relationship between every division (cell or eYSN) and MOW's initiation. This correspondence is independent of stage and temperature. This is easily visualized by plotting the exact timing for each event, highlighting how the correspondence between each mitosis and MOW initiation is consistent throughout the analyzed embryos (Fig. 3.3G). In our analysis, this hypothesis was confirmed in 55 cases out of 63 (Fig. 3.3I). The remaining 8 hypothetical [mitosis-MOW] couples were lacking either the mitosis event or the MOW initiation event. This could be explained due to the presence of biological outliers (4 cases) or due to technical imaging issues, in which the cells were out of the FoV or their hypothetical division happened before the start of the imaging, and therefore the hypothesis outcome could not be verified (4 cases). The association between the two events can also be visualized through the graph depicted in Fig. 3.3J, showing a strong positive correlation (Pearson correlation coefficient $r=0.86$, $R^2=0.74$, $p<0.001$) between the detected number of MOW initiation and detected mitosis, for the different embryos.

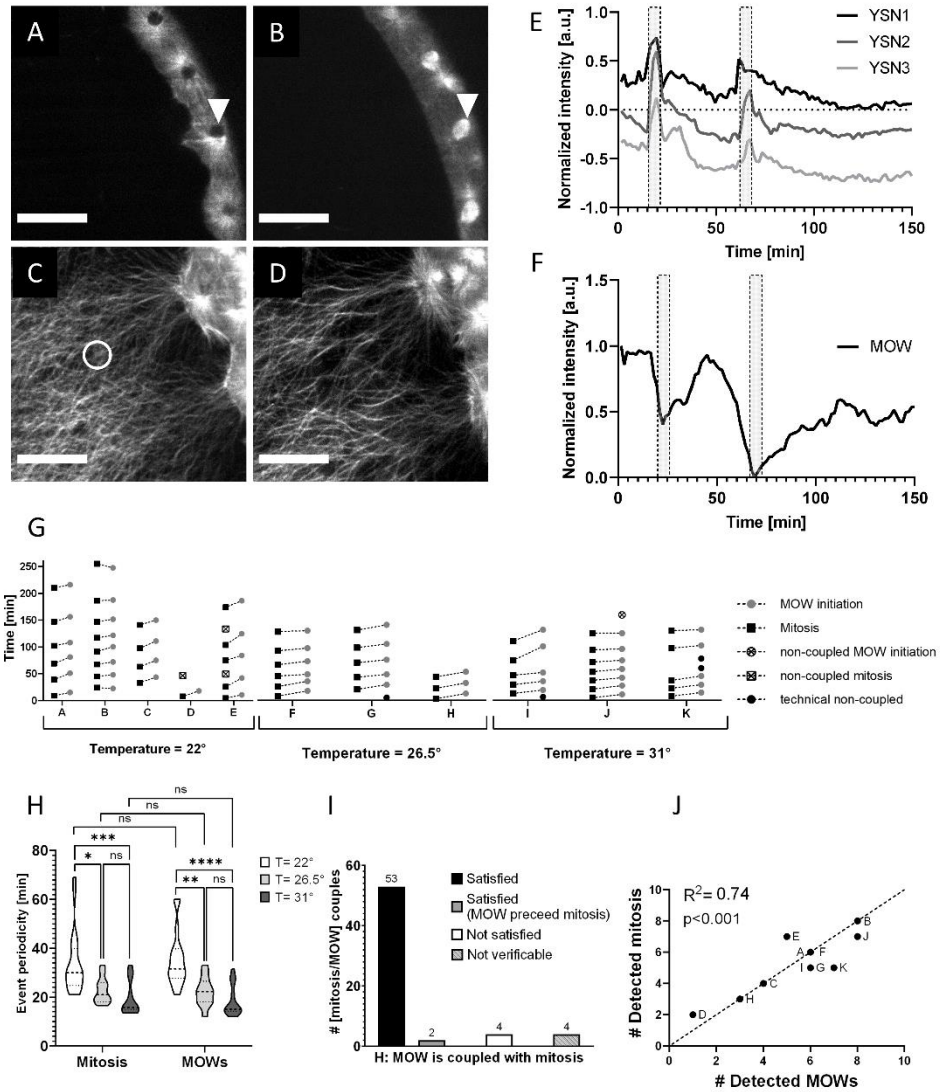

*Figure 3.3: MOWs depend on the cell/eYSN divisions. (A-B) Internal slices from the 3D stack showing the YSN (white arrow) before (A) and during (B) a mitotic event. (C-D) Maximum intensity projection for the same area in (A-B), showing the MT network emerging from the YSN, before (denser network, C) and after (sparser network, D) the YSN mitotic event. Scale bars 50 µm. (E) Normalized mean intensity profiles of three YSN tracked through the 3D stack over time, recording their last two divisions (overlaid bars). For better visualization, an incremental offset is applied to avoid graphs' overlapping. (F) Normalized mean intensity profile from a 19µm ROI (white circumference in (C)) over the MT branch from the maximum intensity projection over time. The retrieved graph records the last two MOWs' initiations (overlaid bars), corresponding to the YSN divisions in (E). (G) Time points at which mitosis (squares) and MOWs' initiations (circles) happens, for embryos at different temperatures. Each letter identifies one embryo. (H) Violin plots resuming the effect of experimental temperature on periodicities of mitosis (left part) and MOWs' initiations (right part). p-values: ns= p>0.05, *= p<0.05, **= p<0.01, ***= p<0.001, ****= p<0.0001. (I) Overview on the 63 analysed [mitosis/MOW initiation] coupled events and their outcome to the hypothesis "MOW initiation coupled with mitosis". (J) Correlation*

graph between the number of detected MOW initiation and of detected cell/YSN divisions from each embryo (letters). Dotted line represents identity line. Image reproduced from [1].

3.3.4 MOWs' global visualization and analysis

Having observed the MOWs' propagation from the blastoderm margin towards the vegetal pole, I developed a dedicated image analysis tool to characterize it (see also Appendix B, section B.4 for the complete description of the analysis procedure).

This tool for global MOW analysis models the yolk as a sphere and it defines, over the spherical surface, meridians (the set of points having the same azimuth angle) and parallels (the set of points having the same elevation angle), as shown in Fig. 3.4A. By back-projecting the calculated coordinates onto the 2D image, the mean intensity over time of a 50 µm ROI travelling over the meridians (Fig. 3.4B) can be measured. From these values, and considering its spherical shape, a kymograph of the evolution of the microtubule dynamics over the whole imaged yolk's surface along specific meridians is produced from blastoderm margin to the vegetal pole (Fig. 3.4C). The connections of the intensity valleys between subsequent points of the same meridian identify the presence of various MOWs, and prove their propagation over the yolk's surface. In this way, the speed of the different waves can also be measured in degree/min along each meridian, i.e., for different MT branches. Applying this tool to embryos developing at different temperatures, I have measured the MOWs' propagation speeds over the yolk sphere to vary from 2.45±0.59 degrees/min to 4.70±1.50 degree/min which correspond to linear speeds ranging from 14.42±3.47 µm/min to 26.27±8.38 µm/min (means ± standard deviations, see also Appendix B, section B.4 for calculation details).

MOWs however, are not the only wave-like events happening in the embryo. In the first stages of development the cells forming the blastoderm divide synchronously but subsequently, as the embryo develops, the cells' divisions lose this synchronicity becoming "metasynchronous". Cells closer to the animal pole divide first and marginal cells afterwards, producing a wave-like pattern [2,17,18]. Modelling the blastoderm as a hemisphere in the same way, the above-mentioned analysis can be

repeated highlighting the propagation of the mitotic wave along the meridians defined over the blastoderm (Fig. 3.4D). This analysis also shows that MOWs' initiations are slightly delayed with respect to the blastomeres/eYSN divisions (Fig. 3.4E), which would agree with our hypothesis that the divisions could be the trigger of the MOW phenomena.

Through the same tool, the mean intensity kymograph can also be constructed also along the parallels of both the yolk and blastoderm hemispheres (Fig. 3.4F), which provides a way to visualize MOWs' and mitotic waves' wavefronts and to analyze their symmetry with respect to the animal-vegetal (AV) axis (Fig. 3.4G-H).

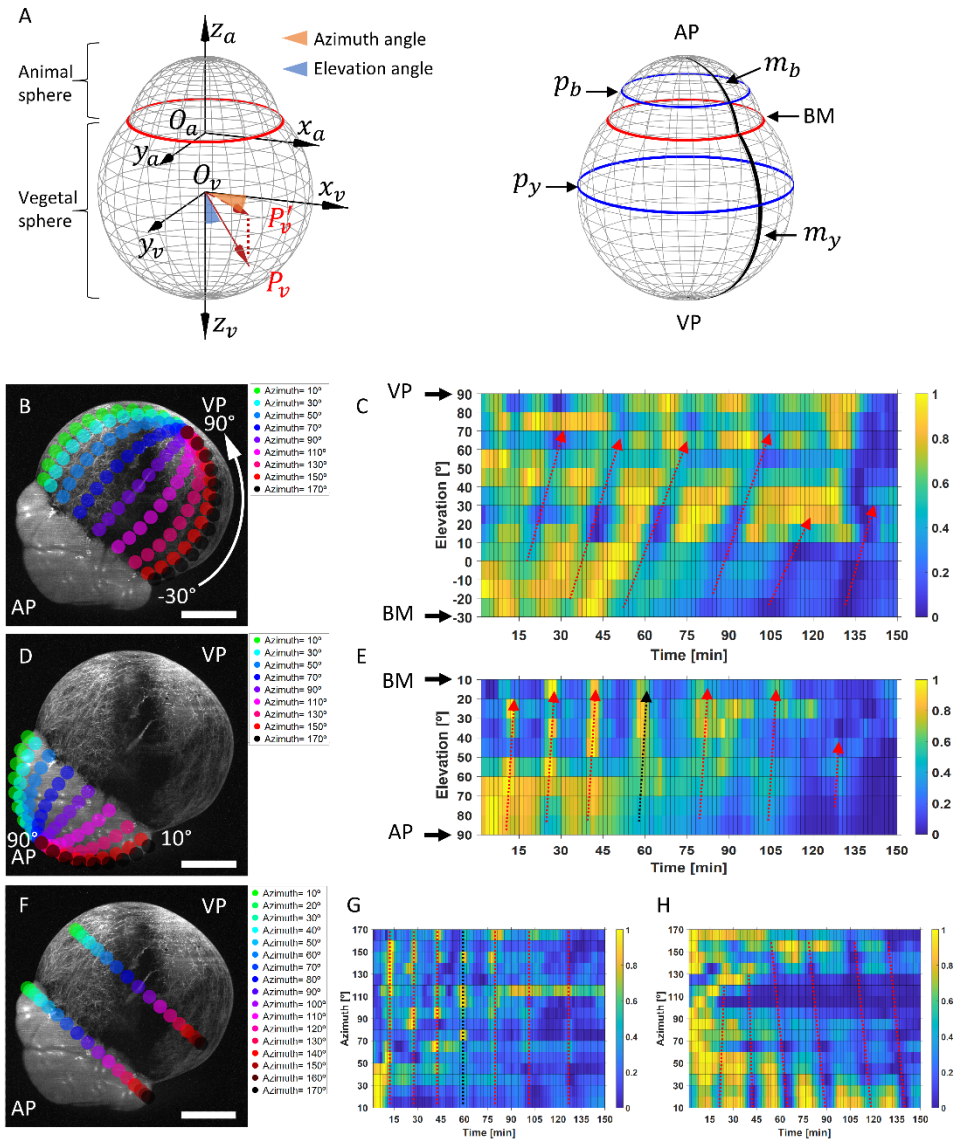

Figure 3.4: MOWs' global visualization and analysis. (A) Left panel: representation of the coordinates system and spherical coordinate convention of the double-hemisphere 3D model for the zebrafish embryo. Pv is a general point over the spherical yolk surface, and P'v its projection on the xy plane. Right panel: exemplification of meridians (black) and parallels (blue) on the blastoderm (mb, pb) and yolk sphere (my, py). In both panels, the red circumference represents the blastoderm margin. AP= animal pole, VP= vegetal pole, BM= blastoderm margin. (B) Maximum intensity projection of LSFM imaging of a dclk2-GFP embryo, lateral view, and some of the paths followed to adapt the analysis to the spherical yolk shape. Scale bar 200 µm. (C) Normalized mean intensity kymograph relative to a single meridian of the yolk sphere, over time. Intensity drops (red arrows) reveal MOWs' passage from BM to VP. Speed calculation is performed through slope measurement (elevation angle/time). (D) Some of the paths followed to perform the analysis over the blastoderm hemisphere. Scale bar 200 µm. (E) Normalized mean intensity kymograph relative to a single meridian of the blastoderm hemisphere, over

time. Intensity peaks (arrows) reveal the mitotic wave passage from AP to BM. From comparison of (C) and (E) is shown how MOWs follow in time the mitosis but also, in this particular embryo, the presence of an outlier as one mitosis (black arrow in E) is not followed by any MOW. (F) Over the maximum intensity projection of the same embryo (scale bar 200 µm), the analysis along parallels is performed. This produces the normalized mean intensity kymographs relative to blastoderm (G) and yolk (H), showing the wavefronts (dotted lines) of the mitotic waves (G, black dotted line indicates the outlier) and MOWs (H). The mid-band shadow, which is due to the LS degradation from the embryonic sphere, can affect the analysis only for certain parallels/meridians. Image reproduced from [1].

3.3.5 A novel MT network is present deep inside the yolk

LSFM greatly improves the penetration in depth respect to confocal microscopy, providing a unique opportunity to study the morphology and dynamics of the inner part of the zebrafish yolk. Despite the current view, which refers only to the MTs mesh around the iYSN and to the MTs branches in the external YCL (the eMTN) [4,7–9], we found that an intricate network of MTs is also present deep inside the yolk. To our knowledge, this internal MTs network (iMTN) was not previously reported. With LSFM we proceeded then to describe in detail its morphology and its dynamics, correlating it with the MOWs passages and the eYSN mitosis.

The iMTN appears to be uniformly present in the whole yolk and its presence was consistently observed in all the LSFM examined embryos. From a 3D vegetal view of a blastula embryo, we digitally removed the YCL and the related MTs network to visualize how this network spans the yolk until at least a depth of 350 µm from the vegetal pole (Fig. 3.5A). As visualized in Fig. 3.5B as maximum intensity projection of a 40 µm range, the internal MT network appears to be uniformly distributed also in the lateral direction. We found that several MTs form circular-like patterns, most probably surrounding the lipid granules, which are known to fill the yolk [2,18]. Additionally, several MTs are connected to the MT network present in the YCL and between them (Fig. 3.5C). More intriguingly, clear connections were found between the eYSN associated centrosomes with microtubules directed towards the interior part of the yolk, which we believe to be part of the iMTN (Fig. 3.5E-I, Video B.4, and Video B.5).

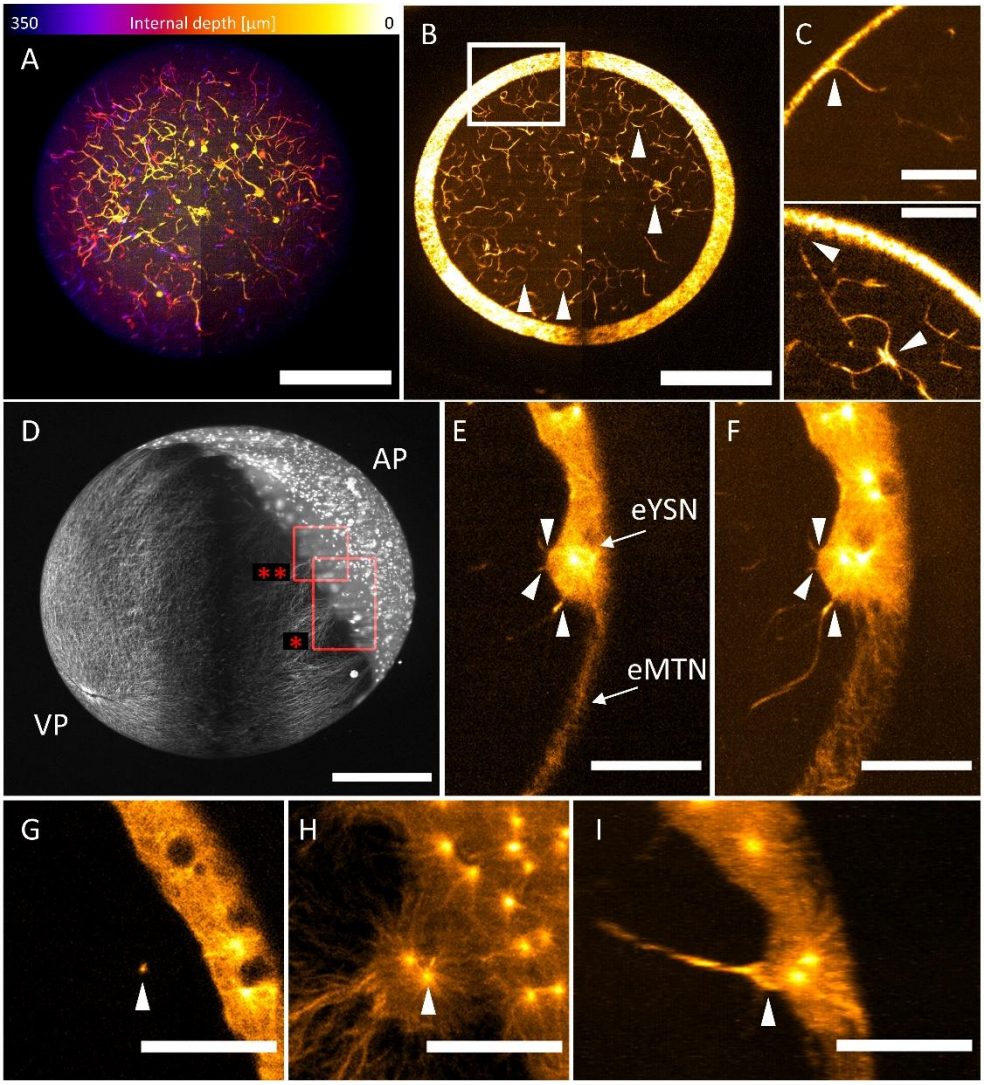

*Figure 3.5: Internal MT network morphology. (A) Depth-coded projection of a z-stack in which the information relative to the outer YCL was digitally removed. The internal microtubule network and its extension within the yolk is visible. Visualized depths range between 0 µm (white) and 350 µm (blue). Vegetal view, left and right images of the embryo are stitched together, scale bar 200 µm. (B) Maximum intensity projection over a 40 µm range of a yolk section. The internal MTs forms circular patterns (white arrows) and also are connected to the external yolk MTs (eMTN) network. Vegetal view, left and right images of the embryo are stitched together, scale bar 200 µm. (C) Zoom (single slices) on the yolk surface, showing clear connections between the internal and external MT networks (white arrows, upper and lower panel), and interconnections between internal MTs (white arrow, lower panel). Scale bars 50 µm. (D) Embryo at sphere stage, lateral view. AP= animal pole, VP= vegetal pole, scale bar 200 µm. (E) zoom into the ROI indicated by * in (D), single slice, showing connection of internal MTs to an eYSN (white arrows). eMTN= external MT network, scale bar 50 µm. (F) Maximum intensity projection over a 20 µm range of the same ROI showing also the extension toward the internal portion of the yolk of the MT connected to an eYSN. Scale bar 50 µm. See also Video B.5. (G) zoom into the ROI indicated by ** in (D), single slice, showing an internal MT bundle (white arrow) extending perpendicular to the*

image plane. (H) Maximum intensity projection showing the end point of that internal MT bundle, coinciding with a centriole (white arrow) associated to an eYSN. (I) An XZ re-slice view of the same ROI showing the connection of the same MT bundle and its extension toward the interior of the yolk. Scale bars 50 µm. See also Video B.4. All figures relative to dclk2-GFP embryos, and ImageJ's Orange HOT lookup table was used to ease iMTN visualization. Image reproduced from [1].

To verify the presence of the iMTN on wild-type (WT) embryos, we fixed and immunostained them with an anti-β-tubulin antibody [31,32] (see also Appendix B, section B.8 for the immunostaining procedure description), and imaged them with the same LSFM setups. Although the fixation step in the immunostaining protocol enhances the autofluorescence of the yolk, specific tubulin signal is detected in its internal part (see Appendix B, Fig. B.3), which would come from the microtubules associated to the iMTN below the YCL and surrounding the lipid granules. The use of non-fixed samples, the enhanced quantum efficiency of the sCMOS sensors and the extended penetration depth provided by the LSFM technique give us the power to detect the weak signal coming from the iMTN, normally hidden in previous studies. Therefore, this work adds a new MTs set to the zebrafish embryonic model.

This newly found network inside the yolk is present during the whole early embryonic development: we visualized it in non-fertilized eggs, and at cleavage (Appendix B, Fig. B.4), blastula, and epiboly (Fig. 3.6A, Video B.6) stages. In studying the dynamics of this MT network, we investigated how its links to the eMTN are affected from a MOW travelling in the YCL. We found that at the MOW passage, connections between the iMTN and the eMTN are lost and that new connections are formed afterwards (Fig. 3.6B-D, Video B.7, and Appendix B, Fig. B.4). A similar dynamic was also found at the connection between the iMTN and the eYSN during the nuclei divisions: the link is temporarily lost at mitosis, and re-established shortly after with the nuclei resulting from the division (Fig. 3.6E-G, Video B.4 and Video B.5).

The evidences found on the morphology and dynamic characteristics of this iMTN, and its connection with the MOW phenomena, provide therefore a novel view on

the description of the MT networks populating the yolk cell in the zebrafish's early embryonic development, as depicted in Fig. 3.6H.

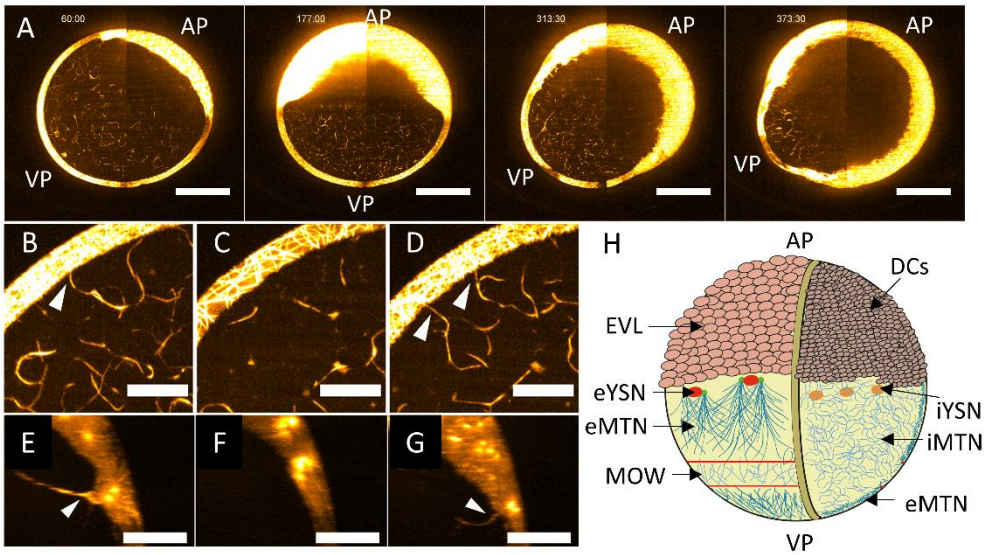

Figure 3.6: Internal MT network dynamics. (A) Time series visualizing a maximum intensity projection over a 30 µm of a developing embryo from (left to right) blastula, 50%, 70%, and 90% epiboly. The iMTN is visible in all these stages. AP= animal pole, VP= vegetal pole. Left and right images of the embryo are stitched together, scale bars 200 µm. See also Video B.6. (B-D) Time series visualizing through maximum intensity projection over 26 µm the dynamics of iMTN-eMTN connections upon MOW passage. Before MOW passage the connection is clearly visible (white arrow, B), during MOW passage the connection is lost (C), and is re-established after MOW passage (white arrows, D). Scale bars 50 µm. See also Video B.7. Single slice images relative to the same frame of (B) and (D) are visible in Appendix B, Fig. B.5. (E-G) Time series visualizing the XZ re-slice dynamics of iMTN-eYSN connection upon eYSN mitosis. Before the eYSN division the connection is present (E), during the division the connection is lost (F), and re-established after the division is completed (G). Scale bars 50 µm. All figures relative to dclk2-GFP embryos, and Orange HOT lookup table was used to ease iMTN visualization. (H) Updated model for the MT networks populating the zebrafish yolk between 512-cell and sphere stages. On the left side, the eMTN associated to the eYSN is subject to the MOW travelling toward the VP, exemplified as a belt of low-density MT. On the right side, the section view of the embryo is illustrated. The iMTN is present within the whole yolk cell. EVL= enveloping layer, DCs= deep cells. Representation not in scale. Image reproduced from [1].

3.3.6 YCL asters form during dclk2-GFP zebrafish epiboly

Besides the dynamics described above in cleavage and blastula stages [2], another interesting morphological feature of the yolk's microtubules network has been found in the dclk2-GFP zebrafish line during the process of epiboly, and resumed in [33]. In particular, various patterns from which microtubules bundles appear to

nucleate, which we called YCL asters, formed in the eMTN of many of the observed embryos.

We defined YCL asters as 3D large patterns of radially oriented microtubules that appear at middle-stage epiboly in the dclk2-GFP line embryos. They divide the eMTN into different and distinguishable compartments and remain visible until the blastoderm completely covers them during its epibolic migration toward the vegetal pole (Fig. 3.7A). Thanks to the 3D scanning capability of LSFM, we could image the internal structure of the asters, showing their half-sphere shape (Fig. 3.7B). We also found that these structures are compatible with the development, i.e. the embryos can complete the epiboly process. During epiboly, YCL asters appear to be absorbed below the blastoderm as it advances toward the vegetal pole (see also [33] for the complete dynamics). After the first days of development, these embryos become adults and fertile, and pass this particular phenotype also to the next generation.

Moreover, we noticed that their number was variable between the embryos, finding that embryos generated from the same female conserved similar numbers of YCL asters. Interestingly, the disposition of the YCL asters around the yolk does not appear to be random but instead, they tend to group at one or more spherical latitudes, forming different concentric rings. This has been studied through the image analysis tool I specifically developed in FIJI and MATLAB. Through these scripts, the researcher can annotate in the 3D z-stack the positions in the embryos of the center, the vegetal pole, and the various YCL asters. After modeling the yolk as a sphere, the spherical coordinates of the various YCL asters can be recovered, from which the division of the YCL asters' disposition can be better visualized and analyzed (Fig. 3.7C). The software code is available upon request to the author of this thesis or to the supervisor.

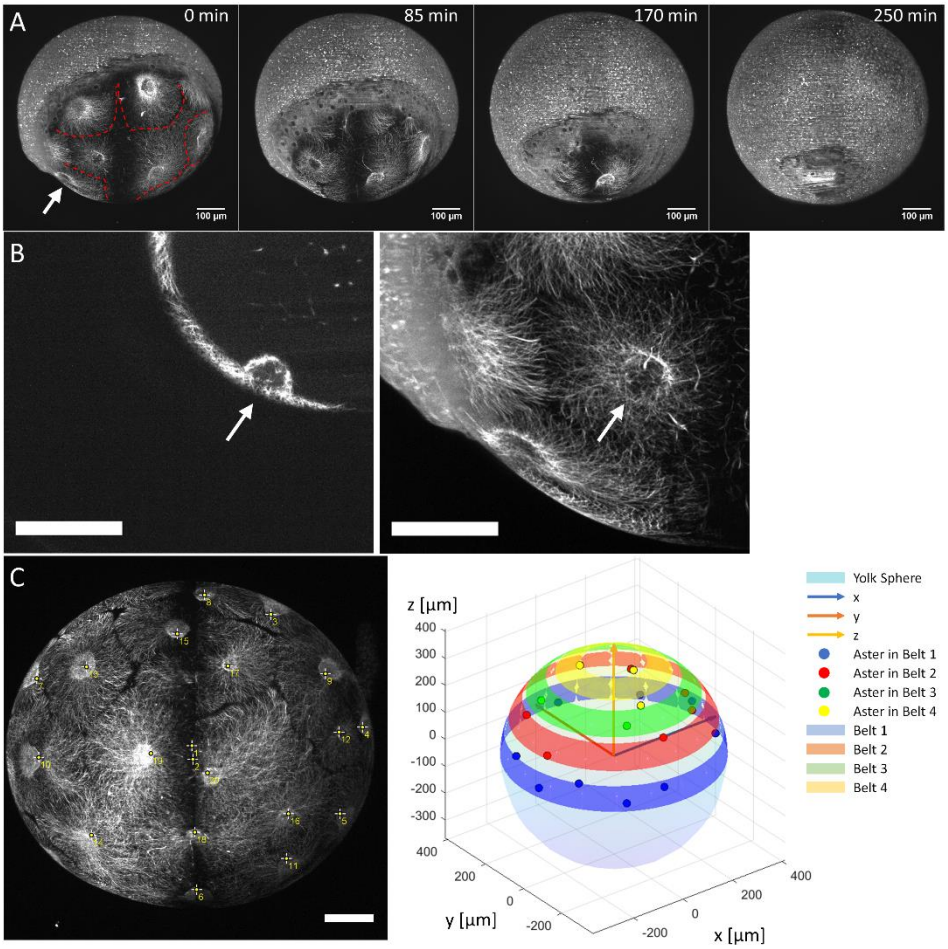

Figure 3.7: YCL asters forms in dclk2-GFP zebrafish embryos. (A) Time series showing the epiboly evolution on a dclk2-GFP embryo presenting several YCL asters. On the left panel, the different network compartments (red dotted lines) are highlighted and in the center of each compartment, a YCL aster is present (white arrow). The presence of the YCL asters did not interrupt the epiboly. Scale bars 100 µm. (B) Single LSFM slice showing the internal structure of a YCL aster and its hemispherical shape (left, white arrow). On the right, the maximum intensity projection shows the entire YCL aster (white arrow). Scale bars 100 µm. (C) A vegetal view of a dclk2-GFP embryo (left) shows many YCL craters, each of them annotated through the custom-made FIJI script (available upon request). From these annotations, their position on the sphere modeling the yolk is retrieved (right panel), and it visualizes how YCL asters forms in concentric rings around the animal-vegetal axis (aligned with the z-axis). Scale bar 100 µm. Image adapted from [33].

We, therefore, tried to visualize YCL asters in wild-type embryos as well. To do that, we profited from the throughput enhancement provided by the Flexi-SPIM setup, to screen and image in 3D various samples (Fig. 3.8). We fixed and performed immunostaining against ß-tubulin on both wild-type and dclk2-GFP embryos. ß-

tubulin is one of the key components of microtubules filaments and therefore the resulting images would highlight the microtubule dispositions. In dclk2-GFP we could confirm that ß-tubulin immunostaining overlapped to the dclk2-GFP signal, as expected, and therefore also highlighted the YCL asters (Fig. 3.8A). In wild-type embryos however, although ß-tubulin immunostaining enabled the microtubules' visualization, we never found YCL asters (Fig. 3.8B). This lets us conclude that YCL asters are a particular feature of the transgenic dclk2-GFP line.

To gain further insight on this, additional experiments were conducted and consisted of mRNA microinjection on one-cell stage wild-type embryos of the construct coding for either dclk or DCX (paralog gene doublecourtin) proteins, which would then result overexpressed. These experiments led to the formation of YCL asters in wild-type embryos, therefore further suggesting that the protein overexpression, induced through either microinjection or the transgenic line, is the cause for YCL formation.

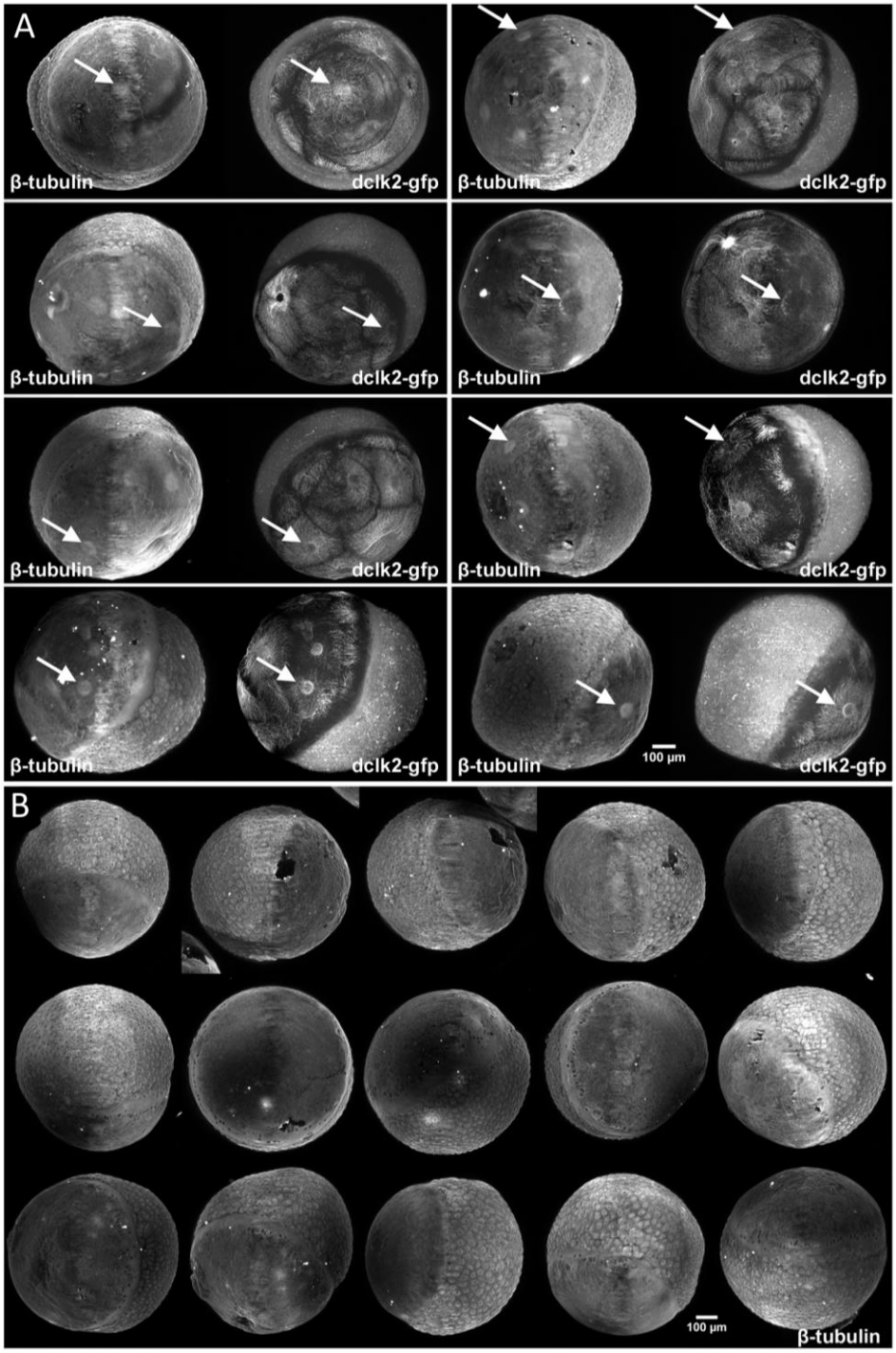

Figure 3.8: dclk2-GFP and wild-type embryos screening through Flexi-SPIM. (A) 8 different dclk2-GFP embryos were fixed and immunostained against ß-tubulin. The ß-tubulin and dclk2 channels of single embryos are shown on the left side and right side of each panel, respectively. YCL asters are visible in

both channels (white arrows). (B) 15 different wild-type embryos were fixed and immunostained against ß-tubulin. No YCL aster has been found. Scale bars 100 µm. Image adapted from [33].

The described YCL asters are characteristic of the dclk2-GFP transgenic line but these patterns do not interfere with the successful development of the embryos. Therefore, this animal model emerges as an interesting in-vivo platform for further studies on microtubules asters interactions and large microtubules networks' organization and dynamics.

3.4 Discussion

Previous works have shown the presence of two sets of MTs network in the zebrafish yolk cell: (1) a MTs mesh surrounding the iYSN and (2) a vegetally oriented MTs array in the YCL [7–9]. The latter MTs array, here called eMTN, is associated with the marginal blastomeres and subsequently to the eYSN [8], and it has been particularly studied during the epibolic process due to its important connection with the eYSN migration [10]. However, prior to the epiboly stage, the network has been mainly investigated either on fixed samples [4,8] or through restricted field of views [11,12,34], or in limited time windows [11].

In this work I developed experimental setups and workflows to effectively visualize and analyze the yolk MTs structures. With this we can contribute to fill the current lack of in-vivo studies on the MTs arrays during cleavage, blastula and epiboly stages and reveal important morphologies and dynamics which were, to our knowledge, until now hidden. LSFM emerges as the ideal tool for this particular application providing unprecedented penetration depth, high signal to noise ratios, large FoVs, and limited photobleaching [22]. These capabilities permit the study of MTs in the whole embryo for extended time windows. The correct development of the sample is also ensured by the possibility of controlling the temperature of the imaging environment and the absence of sample mounting medium's mechanical constrictions, as the zebrafish develops inside its own chorion.

The results show that the MT networks filling the zebrafish yolk in the early embryonic development present more complex characteristics than previously thought. Through this work I provide an important update on the current view [4,7–9] on the yolk's MT populations, schematically represented in Fig. 3.6H. The eMTN, located at the YCL, is associated with marginal blastomeres or, as the YSL forms, with the eYSN. Corresponding to each mitotic wave that involves the MT branch-associated nuclei, a MOW is initiated and travels over the YCL from the blastoderm margin to the vegetal pole, and it re-organizes the eMTN in thicker and sparser bundles. MOWs appear to travel in a belt-like fashion concentrically closing at the vegetal pole.

Moreover, an intricated iMTN is present in the whole inner part of the yolk, and it presents clear connections with the eMTN. These links are lost upon the passage of a MOW and new connections are re-established shortly after. In addition, the iMTN also appear connected to eYSN. This means that eYSN are associated not only with the AV parallel MTs array, as already known, but also to the iMTN. Upon eYSN mitosis, the connection is lost and re-established shortly after as well. Therefore, we found that the view describing a microtubule mesh in the iYSL [7–9] is partial in both space and time. Thanks to the intrinsic capabilities of LSFM, we in fact demonstrate that a MT mesh extends in the whole inner yolk, and that it is present not only when the YSL forms, but in the whole embryonic development from non-fertilized eggs until at least the end of epiboly.

The MOWs described here may correspond to what Chen et al. observed and defined as a "microtubule turnover" [12]. Nevertheless, the description provided in their work of the phenomena has been done in a limited region of the MT network, in restricted time windows and focused on the examination of Dachsous1b interactions with Aurora B and Ttc28 proteins [12], providing a complementary molecular study on YCL MTs. The approach here described goes instead towards the mesoscopic description of the MOW phenomena, revealing the dynamics of the

entire eMTN and defining this wave-like pattern over extended time windows. We provide evidence demonstrating a strong dependence between the mitotic cycles of the blastoderm (and when formed, of the YSN) with the MOWs' initiations. We hypothesize that MOWs are necessary to re-organize the eMTN after each blastomere/eYSN division to connect the extremely long MTs branches to the newly generated centrosomes, and thus to allow the following epibolic eYSN migration along the so organized network.

With the combination of large FoVs and extended time windows, the global analysis permits to visualize the mitotic waves [2,17,18] in the blastoderm, and how the MOWs, after being initiated, propagate towards the vegetal pole. This dedicated image-analysis tool enables as well the evaluation of their speed along the meridians of the yolk sphere. The MOWs' velocity values calculated in this work, although depending on the developmental temperature and on the current developmental stage, fit within the order of magnitude of the propagation speeds of other wave-patterns already observed in zebrafish embryos, such as bulk actin polymerization waves (ranging from approx. 20 to 70 µm/min [14]) and mitotic waves (ranging from approx. 10 to 65 µm/min [17,18]). Thus, this analysis allows to have an automatic tool for a global view of the wave-like processes until the end of blastula stages, considering the entire embryo dynamics and shape.

This analysis is of particular interest for the application on the yolk's MTs, as described in this work, and also in MT mutant phenotypes [3], that would permit a global approach to their study during extended time windows. Moreover, it could help the examination also of other spherical-based dynamics in zebrafish such as the mitotic waves [2,17,18] and calcium waves [15,35], both in mutant embryos and in their wild-type counterparts. In addition, the same tool can be used also in investigating other spherical organisms (e.g. Xenopus embryos). Besides that, the analysis along the parallels provides a way to understand eventual bias of the wave patterns with respect to the dorsal-ventral axis.

Although the nature of the MOW wave-like pattern remains unclear, due to the large size of the yolk and the relative fast propagation of the MOWs, the chemical wave model could be a possible explanation. In [20] the authors demonstrated that a Cdk1 activation wave is responsible for the visualized nuclear envelopes' dynamics synchronization *in vitro*. Such a wave is an example of "chemical wave" [13,28] (also called "trigger wave" [36]), and accounts for the propagation of the event in consideration through its subsequent activations on the neighboring areas, allowing the signal to advance. A link to support that MOWs are indeed chemical waves can be found in [28], in which is proposed that a chemical wave could account for large MT aster's growth, and that the centrosome could act as wave initiation site.

Moreover, Ishihara et al. speculate about possible cross talks between mitotic and microtubule chemical waves for large cells organization [28]. The yolk MTs emanated from blastomeres and eYSN centrosomes of the zebrafish embryo could be a model to study these hypotheses in-vivo, using the tools proposed in this work. Further studies are needed to understand how such intricated and large MT networks (both the eMTN and the iMTN) are nucleated and capable to extend in a large volume like the yolk cell. Ishihara et al. propose that MT nucleation can be stimulated from existing MTs far away from centrosomes by pre-existing MTs [28]. This hypothesis would explain the fact that MTs belonging to large asters do not appear to decrease in density with the increase of the distance from the centrosome, which would be expected if all MTs minus end were connected to it. The large microtubules branches of the zebrafish eMTN, together with its dynamics here described, and the connections to the iMTN found in this work could be a model to test this hypothesis in-vivo, also considering recent findings on non-centrosomal MT organizing centers [10].

I believe that the observation of the cyclic MOW process and the visualization of the iMTN have a critical importance in the complete description of the microtubule networks of the yolk. It shows the necessity to visualize and analyze the microtubule

networks in live samples and with a relatively large FoV, both characteristics enabled by LSFM. Therefore, we consider that the characterization of the networks' organization cannot be solely performed in a "static" way, but it must also be described in its dynamic dimension. In fact, the analysis of the microtubules in fixed samples could bring misleading conclusions about their actual arrangement as in the moment of the fixation is probably not known if the MOW has already given its effect or not, but more importantly because we showed that the network is not a static organization. Concluding, this study permits providing a novel insight on yolk's MT morphology and dynamics, and offers a basis to LSFM methodologies for studying new and already approached aspects of the yolk MT networks.

3.5 Future perspectives

The work described above characterizes the MOW as a global wave pattern happening in the early stage of zebrafish development. However, there is room for further investigation on the MOW's function and its interaction with the mitotic waves.

First, the nature of the pattern, either chemical- or phase- wave should be understood. While chemical waves are propagating due to subsequent activations of signals in the neighboring areas, phase waves are patterns formed by events that are delayed between them: their succession appears as a traveling wavefront, but they are independent. A method to distinguish the two typologies of waves is to introduce a physical barrier in the pattern's path [13]. This barrier would block the signal from traveling, i.e. blocking a chemical wave, while it would not block the phase wave, being the affected regions only synchronized between them, without a triggering.

Second, the interaction between mitotic waves and MOWs should be investigated. Although in this work I did interfere with the mitotic waves by manipulating the temperature and therefore changing the cell cycle duration, another possibility would be to block the mitosis and check what happens to the MOWs. During my

investigation, I did try to do so using dinaciclib, a drug that inhibits Cdk1 activity and thus interferes with the cell cycle, as performed in [14]. Unfortunately, I could not draw any conclusion from these experiments, as the use of dinaciclib (at various doses) also destroyed the eMTN, i.e. the object of the study (see Appendix B, Fig. B.5). Therefore, a different way to block the cell cycle should be found. Similarly, blocking the MOWs without affecting the mitosis would clarify the MOW's role for the correct development of the embryo.

Third, MOWs are global waves as they propagate through the whole eMTN. However, as the eMTN is formed by different branches, it would be interesting to understand if the re-bundling phenomena forming the MOW propagates along a branch independently from the other branches that form the network. In [19] the authors applied a temperature gradient to developing frog embryos. In this way, the cell cycle of one half of the embryo was slowed down by the low temperature, while in the other half the cell cycle was accelerated by the high temperature. Showing this, the authors concluded that the mitotic waves in the frog embryos are indeed phase-waves, as the development of the two halves happened independently [19]. A similar experiment could be implemented for the zebrafish embryo as well. Besides clarifying the nature of the mitotic waves, it would also test if the MOW happening in the branches of one half of the embryo is independent by the MOW propagating along the branches of the other half, or if a kind of cross-talking between the branches exists.

Finally, further studies on the iMTN are needed. As an example, the nucleation points of such a large network should be investigated. LSFM surely could help in this, with the coupling of microtubule-organizing centers labeling. In this work, I showed that some microtubules directed toward the inner yolk are connected to the eYSN, and in particular they appear to be connected to their centrioles. Being the iMTN large, it is unlike that the whole network is nucleated by the eYSN. Therefore, the involvement of the iYSN and possibly non-centrosomal microtubules organizing

center should be investigated. An ideal approach could be to cut the animal cap in embryos fixed after the YSL is formed, and isolate the entire yolk. This would provide better optical access through LSFM to the region just below the blastoderm.

3.6 Additional information

Additional information on the various components of the setups, algorithm of the developed software, characterization procedures, Supplementary Figures, and Supplementary Videos links on MOWs can be found in Appendix B and in [1]. The results on YCL asters are resumed in [33]. The software code is available upon request to the author of this thesis or to the supervisor.

3.7 References

1. M. Bernardello, M. Marsal, E. J. Gualda, and P. Loza-Alvarez, "Light-sheet fluorescence microscopy for the in vivo study of microtubule dynamics in the zebrafish embryo," Biomed. Opt. Express **12**(10), 6237–6254 (2021).

2. C. B. Kimmel, W. W. Ballard, S. R. Kimmel, B. Ullmann, and T. F. Schilling, "Stages of embryonic development of the zebrafish.," Dev. Dyn. an Off. Publ. Am. Assoc. Anat. **203**(3), 253–310 (1995).

3. N. Li-Villarreal, M. M. Forbes, A. J. Loza, J. Chen, T. Ma, K. Helde, C. B. Moens, J. Shin, A. Sawada, A. E. Hindes, J. Dubrulle, A. F. Schier, G. D. Longmore, F. L. Marlow, and L. Solnica-Krezel, "Dachsous1b cadherin regulates actin and microtubule cytoskeleton during early zebrafish embryogenesis.," Development **142**(15), 2704–2718 (2015).

4. S. Jesuthasan and U. Stähle, "Dynamic microtubules and specification of the zebrafish embryonic axis.," Curr. Biol. **7**(1), 31–42 (1997).

5. A. V Gore and K. Sampath, "Localization of transcripts of the zebrafish morphogen Squint is dependent on egg activation and the microtubule cytoskeleton.," Mech. Dev. **112**(1–2), 153–156 (2002).

6. R. Fuentes and J. Fernández, "Ooplasmic segregation in the zebrafish zygote and early embryo: pattern of ooplasmic movements and transport pathways.," Dev. Dyn. an Off. Publ. Am. Assoc. Anat. **239**(8), 2172–2189 (2010).

7. A. E. E. Bruce, "Zebrafish epiboly: Spreading thin over the yolk.," Dev. Dyn. an Off. Publ. Am. Assoc. Anat. **245**(3), 244–258 (2016).

8. L. Solnica-Krezel and W. Driever, "Microtubule arrays of the zebrafish yolk cell: organization and function during epiboly.," Development **120**(9), 2443–2455 (1994).

9. S. E. Lepage and A. E. E. Bruce, "Zebrafish epiboly: mechanics and mechanisms.," Int. J. Dev. Biol. **54**(8–9), 1213–1228 (2010).

10. Z. Fei, K. Bae, S. E. Parent, H. Wan, K. Goodwin, U. Theisen, G. Tanentzapf, and A. E. E. Bruce, "A cargo model of yolk syncytial nuclear migration during zebrafish epiboly.," Development **146**(1), (2019).

11. L. D. Tran, H. Hino, H. Quach, S. Lim, A. Shindo, Y. Mimori-Kiyosue, M. Mione, N. Ueno, C. Winkler, M. Hibi, and K. Sampath, "Dynamic microtubules at the vegetal cortex predict the embryonic axis in zebrafish.," Development **139**(19), 3644–3652 (2012).

12. J. Chen, G. D. Castelvecchi, N. Li-Villarreal, B. Raught, A. M. Krezel, H.

McNeill, and L. Solnica-Krezel, "Atypical Cadherin Dachsous1b Interacts with Ttc28 and Aurora B to Control Microtubule Dynamics in Embryonic Cleavages.," Dev. Cell **45**(3), 376-391.e5 (2018).

13. V. E. Deneke and S. Di Talia, "Chemical waves in cell and developmental biology.," J. Cell Biol. **217**(4), 1193–1204 (2018).

14. S. Shamipour, R. Kardos, S.-L. Xue, B. Hof, E. Hannezo, and C.-P. Heisenberg, "Bulk Actin Dynamics Drive Phase Segregation in Zebrafish Oocytes.," Cell **177**(6), 1463-1479.e18 (2019).

15. S. E. Webb and A. L. Miller, "Ca2+ signaling and early embryonic patterning during the blastula and gastrula periods of zebrafish and Xenopus development.," Biochim. Biophys. Acta **1763**(11), 1192–1208 (2006).

16. E. Gilland, A. L. Miller, E. Karplus, R. Baker, and S. E. Webb, "Imaging of multicellular large-scale rhythmic calcium waves during zebrafish gastrulation.," Proc. Natl. Acad. Sci. U. S. A. **96**(1), 157–161 (1999).

17. P. J. Keller, A. D. Schmidt, J. Wittbrodt, and E. H. K. Stelzer, "Reconstruction of zebrafish early embryonic development by scanned light sheet microscopy.," Science **322**(5904), 1065–1069 (2008).

18. N. Olivier, M. A. Luengo-Oroz, L. Duloquin, E. Faure, T. Savy, I. Veilleux, X. Solinas, D. Débarre, P. Bourgine, A. Santos, N. Peyriéras, and E. Beaurepaire, "Cell lineage reconstruction of early zebrafish embryos using label-free nonlinear microscopy.," Science **329**(5994), 967–971 (2010).

19. G. A. Anderson, L. Gelens, J. C. Baker, and J. E. J. Ferrell, "Desynchronizing Embryonic Cell Division Waves Reveals the Robustness of Xenopus laevis Development.," Cell Rep. **21**(1), 37–46 (2017).

20. J. B. Chang and J. E. J. Ferrell, "Mitotic trigger waves and the spatial coordination of the Xenopus cell cycle.," Nature **500**(7464), 603–607 (2013).

21. J. Huisken, J. Swoger, F. Del Bene, J. Wittbrodt, and E. H. K. Stelzer, "Optical sectioning deep inside live embryos by selective plane illumination microscopy.," Science **305**(5686), 1007–1009 (2004).

22. O. E. Olarte, J. Andilla, E. J. Gualda, and P. Loza-Alvarez, "Light-sheet microscopy: a tutorial," Adv. Opt. Photonics **10**(1), 111–179 (2018).

23. J. Huisken and D. Y. R. Stainier, "Selective plane illumination microscopy techniques in developmental biology.," Development **136**(12), 1963–1975 (2009).

24. B. Schmid, G. Shah, N. Scherf, M. Weber, K. Thierbach, C. P. Campos, I.

Roeder, P. Aanstad, and J. Huisken, "High-speed panoramic light-sheet microscopy reveals global endodermal cell dynamics.," Nat. Commun. **4**, 2207 (2013).

25. G. Shah, K. Thierbach, B. Schmid, J. Waschke, A. Reade, M. Hlawitschka, I. Roeder, N. Scherf, and J. Huisken, "Multi-scale imaging and analysis identify pan-embryo cell dynamics of germlayer formation in zebrafish.," Nat. Commun. **10**(1), 5753 (2019).

26. E. J. Gualda, H. Pereira, T. Vale, M. F. Estrada, C. Brito, and N. Moreno, "SPIM-fluid: open source light-sheet based platform for high-throughput imaging.," Biomed. Opt. Express **6**(11), 4447–4456 (2015).

27. M. Bernardello, E. J. Gualda, and P. Loza-Alvarez, "Modular multimodal platform for classical and high throughput light sheet microscopy.," Sci. Rep. **12**(1), 1969 (2022).

28. K. Ishihara, P. A. Nguyen, M. Wühr, A. C. Groen, C. M. Field, and T. J. Mitchison, "Organization of early frog embryos by chemical waves emanating from centrosomes.," Philos. Trans. R. Soc. London. Ser. B, Biol. Sci. **369**(1650), (2014).

29. J.-Y. Tinevez, N. Perry, J. Schindelin, G. M. Hoopes, G. D. Reynolds, E. Laplantine, S. Y. Bednarek, S. L. Shorte, and K. W. Eliceiri, "TrackMate: An open and extensible platform for single-particle tracking.," Methods **115**, 80–90 (2017).

30. L. Carvalho and C.-P. Heisenberg, "The yolk syncytial layer in early zebrafish development.," Trends Cell Biol. **20**(10), 586–592 (2010).

31. Š. Bálint, I. Verdeny Vilanova, Á. Sandoval Álvarez, and M. Lakadamyali, "Correlative live-cell and superresolution microscopy reveals cargo transport dynamics at microtubule intersections.," Proc. Natl. Acad. Sci. U. S. A. **110**(9), 3375–3380 (2013).

32. J. Topczewski and L. Solnica-Krezel, "Cytoskeletal dynamics of the zebrafish embryo.," Methods Cell Biol. **59**, 205–226 (1999).

33. M. Marsal, M. Bernardello, E. J. Gualda, and P. Loza-Alvarez, "Multiple asters organize the yolk microtubule network during dclk2-GFP zebrafish epiboly," Sci. Rep. 12(1), 4072 (2022).

34. L. Fontenille, S. Rouquier, G. Lutfalla, and D. Giorgi, "Microtubule-associated protein 9 (Map9/Asap) is required for the early steps of zebrafish development.," Cell Cycle **13**(7), 1101–1114 (2014).

35. S. E. Webb and A. L. Miller, "Calcium signalling during zebrafish embryonic

development.," Bioessays **22**(2), 113–123 (2000).

36. L. Gelens, G. A. Anderson, and J. E. J. Ferrell, "Spatial trigger waves: positive feedback gets you a long way.," Mol. Biol. Cell **25**(22), 3486–3493 (2014).

Chapter 4: LSFM in-vivo applications on zebrafish and mouse embryos

4.1 Abstract

The ability to maintain samples alive for long periods and to observe biological processes and dynamics in real-time enables critical applications in highly relevant fields. Therefore, the adaptation of the imaging environment and the sample mounting protocols are critical in LSFM. Here two particular applications have been tested on the developed LSFM setups, developing and optimizing the specific sample mounting solutions. In the first one, the macrophages' recruitment in living zebrafish have been recorded, after the immune system reaction induced by a wound or by a bacterial infection. This study and its potential extensions toward HT workflows can provide additional information, in 3D and at high spatial-temporal resolutions, on macrophages' polarization and host-pathogen interactions in vertebrates. In the second application, efforts have been made to allow the early development of mouse embryos within the LSFM microscope and to record the related morphological and dynamical changes. This study would potentially elucidate aspects of the embryogenesis of mammalian embryos.

4.2 Macrophages imaging during wound healing and bacterial infection

4.2.1 Introduction

The study of macrophages' behavior is of utmost importance as they contribute to the control of inflammation, helping the organism to heal wounds and defending it from external pathogens such as bacteria [1]. However, macrophages can have different functions and form different subsets over a spectrum of states, changing their phenotype in relation to the environmental signals received through the so-called "polarization" process [2]. The extremes of this spectrum are the "M1" macrophages, which contribute to initiating the inflammation response, and the "M2" macrophages, which help in reducing it [1].

Although in-vitro studies are also possible, the ability to investigate these biological processes in their native environment in real-time offers more biological relevance. Moreover, the use of the zebrafish embryos and larvae as biological models permits

the generation of dedicated transgenic lines fluorescently labeling the immune cells and eventually their particular polarization state [1].

Conventionally, these studies are performed through widefield microscopy (WM), confocal microscopy (LSCM), or spinning disk microscopy [1,2]. However, as explained in the introductory chapter, when using WM the 3D information is lost. Instead, using confocal and spinning disk microscopy allows the retrieval of the 3D structures, enabling e.g. to track in 3D the paths of the macrophages. Nevertheless, this ability is severely limited over time due to the photobleaching and phototoxicity effects that these techniques induce into the sample. LSFM would instead present the needed capabilities to perform these kinds of 3D experiments, at high spatial-temporal resolutions, and over long periods.

To work on this application, I established a partnership with the "Cytokines, Evolution and Onset of Immunity" group, at the University of Montpellier (France). Particularly, the set collaboration consisted of two workflows, both implemented on the zebrafish organism. The first aimed to the recording of macrophages' recruitment during wound healing, after having applied a cut to the caudal fin of the zebrafish. The second aimed to the recording of the interaction between the macrophages and pathogens with the induction of a bacterial infection within the brain of the zebrafish. In both cases, the interest was to record the dynamics of the immune system over long periods. Through this collaboration we planned to combine our expertise in immune biology and LSFM imaging, working together and visiting the respective labs (at ICFO and the University of Montpellier). However, the outbreak of the COVID-19 pandemic and relative restrictions in travels and lab access imposed the stop of certain experiments (see future perspectives).

4.3 Macrophage recruitment during wound healing

Producing a wound to the tissue will initiate the recruitment of macrophages to the injured location, which will defend the organism from pathogens, eliminate cell debris, and participate in the healing process [2]. While M1 macrophages are recruited first, as they possess a microbicidal function and initiate the inflammatory response, M2 macrophages are present in a later stage, to resolve the inflammation and to participate in the reparation of the tissues [3].

In our experiments, we mainly used a specific zebrafish transgenic line, Tg(mfap4:mCherry-F/tnfa:GFP-F), in which all macrophages express a mCherry protein and only macrophages at the state M1 express GFP. In this way, we could monitor the recruitment of macrophages at the wound site and their activation as M1-macrophages in-vivo [2] (Fig. 4.1A). The immune response was induced by cutting the final part of the caudal fin of 3dpf zebrafish embryos through a scalpel. We then mounted the fish in the two custom-made LSFM setups described in Chapter 2, the Flexi-SPIM and the MuViSPIM, monitoring the macrophage recruitment, their phenotypes, and the healing and fin regeneration process.

Although the fin presents proprieties that are advantageous from the imaging point of view (such as being thin and optically transparent, not needing double illumination/detection schemes), the fact that the acquisition of the images has to be performed on a live sample for many hours translates into different challenges. This application, therefore, represents a perfect example of how live imaging can be insidious even if the object under investigation presents the best optical access options, highlighting the importance of the sample mounting, one of the main thematic of this thesis. In the following section, therefore, I will explain how the mounting of the delicate samples was performed to obtain the best results.

4.3.1.1 Sample mounting and imaging procedure

When using the MuViSPIM, in a first attempt we mounted the elongated zebrafish within a vertical 1.5% lmpa (low melting point agarose) cylinder, extruded from a

glass capillary. Being the object of the study only the fin of the specimen, we mounted it with the head at the top and the fin at the bottom.

Doing so, we could extrude only the first part of lmpa cylinder, in which the fin was embedded, and maintain the whole body within the glass capillary. In fact, due to the relatively large dimension and weight of the fish embryo, having the whole body hanging outside the glass capillary would cause either the detachment of the lmpa cylinder or the oscillation of the sample at every z-step while performing the translation, compromising the acquisition process.

Through this mounting, however, although appearing successful at the beginning of the session, we could not obtain data in the long-term movies because the sample was getting heavy deformations and finally was not able to survive. I believe this was because the majority of the weight of the sample (located at the head and mid part of the body) was at the top of the lmpa cylinder, weighting on the spine and tail of the fish.

Therefore, an alternative mounting method needed to be found. After trying a few different lmpa concentrations, I could gain more successful results by mounting the fish in a 0.2% lmpa solution contained in a 2x3 mm (IDxOD) FEP tube whose inner walls were coated with 3% methylcellulose, similarly to what described in [4]. This time, the head of the zebrafish was on the bottom part of the vertical cylinder, while the fin was on the upper part (Fig. 4.1B). After the insertion of the fish within the FEP tube, the bottom part needed to be closed through 1.5% lmpa, to prevent leaking of the tube content into the imaging medium. Moreover, the lmpa solution, the methylcellulose, and the E3 medium contained in the imaging chamber were all prepared with the addition of tricaine at the concentration of 160ug/ml, to anesthetize the sample. Fish were also treated with 1-phenyl 2-thiourea (PTU) during embryogenesis, which prevents pigmentation in the first days of development.

Through this mounting, we were finally able to image the macrophage recruitment and in particular the M1-macrophages for up to 5 hours (Fig. 4.1C). However, even if this solution did increase the success rate, it required from 20 to 30 minutes for the preparation of a single specimen. Although this might not seem to limit the experiment, it precludes the possibility to visualize the macrophages' recruitment in the very first minutes after provoking the wound.

In contrast, mounting the sample in the Flexi-SPIM was extremely easy. In the Hybrid Mode, the sample was simply inserted with E3 medium and tricaine into the FEP tube and transported toward the FoV of the objective by the aspiring pump (Fig. 4.1D). The specimen was inserted with the head first so that the transport along the FEP tube was mimicking the way fish swim. As a result, the fish was laying on the horizontal plane, without any constriction medium, and it could be rotated to align the fin to the LS. Moreover, by translating the sample along the tube, repeating the acquisition, and stitching the obtained images, the whole sample could be imaged, increasing the effective FoV (Fig. 4.1E). This easy and fast procedure did not affect the health of the fish in any noticeable way and resulted in an additional demonstration of the usability of the Flexi-SPIM for increased throughput..

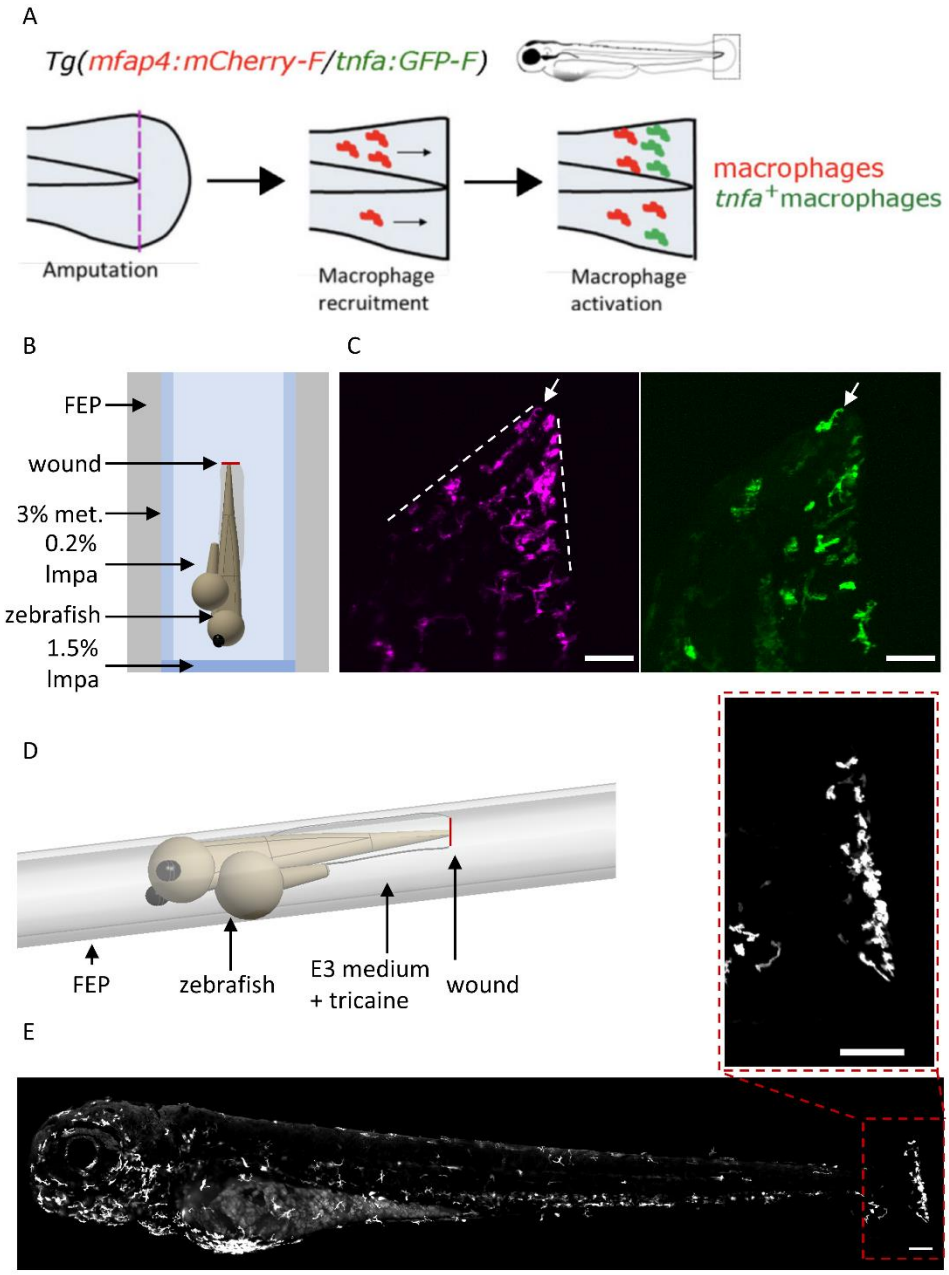

Figure 4.1: LSFM imaging of macrophages' recruitment after provoking a wound. (A) Schematic of the recruitment process: after amputation of the caudal fin, macrophages and M1-macrophages are recruited and travel toward the wound site. Image adapted from [2] *(B) Schematic of the adopted mounting solution in the MuViSPIM setup for fin imaging. (C) Examples of images showing the double amputation performed on the caudal fin (dotted lines) and the recruited macrophages. On the left, all macrophages are shown (in magenta), while on the right only the M1 macrophages subset (in green) is recorded (example highlighted by white arrows). Scale bar 50 µm. (D) Mounting the sample in the Flexi-SPIM (Hybrid LSFM mode) only needed the insertion in the fluidic circuit. (E) Images showing macrophages in an entire 3dpf zebrafish embryo. Image obtained by recording four consecutive*

sections of the embryo through translation along the FEP tube and stitching them together. In the upper panel, the zoom into the amputated fin shows a high density of macrophages at the wound site. Scale bars 50 µm.

4.3.2 Macrophage recruitment during S. Typhimurium infection

Salmonella enterica Serovar Typhimurium (S. Typhimurium) is an intracellular bacterium that evolved to survive and replicate within macrophages, therefore escaping the host's defenses [3]. It is believed that the bacteria directly interfere with the polarization process of the macrophages, reorienting them toward the M2 state [5,6], suggesting that M2 macrophages could be, due to reduced microbicidal activities, more permissive for the bacteria replication [3]. Nevertheless, even though S. Typhimurium is one of the principal causes of food poisoning in humans, the mechanisms that allow it to orient macrophages' polarization are poorly understood.

In our experiments, we imaged the macrophages' recruitment and their defensive actions during bacterial infections. Infections were induced by injecting an S. Typhimurium fluorescent strain into the hindbrain ventricle (HBV) of the zebrafish larva (operation performed by the collaboration's partner).

These experiments were performed during my secondment at the University of Montpellier, where I transferred the MuViSPIM setup to the local imaging facility for one month. This experience moreover, highlighted the usefulness of the implemented MuViSPIM setup, which can be transported to be closer to particular infrastructures, such as biological labs of different bio-hazard levels, culturing and breeding facilities, marine stations, or even for on-field experiments such as on a ship (as done in [7]).

As explained above, the advantages provided by LSFM with respect to LSCM on this application are many. First, the enhanced penetration depth that permits the excitation and collection of the signals coming from up to 100-200 µm deep. Second, the possibility to illuminate the sample from both sides permits a homogeneous illumination. Third, the acquisition speed of LSFM enables the improvement of the

volumetric temporal resolution, which in turn offers more information on the paths and speeds of the objects of study. Finally, the low photobleaching regime permitted to follow the infections for up to 24 hours, to study the evolution of the immune response.

For the same scope, the environmental control implemented in the MuViSPIM setup permits maintaining the fish alive for the whole duration of the imaging session. This is of fundamental importance, as in the case of a hostile environment (e.g. temperature too low) the sample's health might be endangered and the consequences could be confounded with the infection effects. Again, the focus of the following section consists in explaining how the mounting of the delicate samples was performed to obtain the best results.

4.3.2.1 Sample mounting and imaging procedure

In all experiments, zebrafish were treated with PTU at 12 hpf to prevent the pigmentation, and then let develop until 2 or 3dpf (depending on the actual experiment). When ready, they were anesthetized through tricaine (at the concentration of 160ug/ml), and the bacterial infection was induced through microinjection in the brain. Consequently, the samples were embedded in a 1% lmpa in E3 solution, and aspired within a glass capillary, paying attention to aspire from the tail side, so that when mounted vertically the fish would present the tail on top and the head at the bottom of the agarose cylinder.

After its solidification and insertion into the MuViSPIM, the agarose column was extruded to expose only the head of the fish (Fig. 4.2A). Both the lmpa solution and the E3 imaging medium were prepared with the addition of tricaine to maintain the fish anesthetized. Once in the FoV, the rotation stage enabled orienting the sample such that the top part of the brain, in which the injection was performed, was exposed to the single detection objective used. The image acquisition could then proceed. Typical volume scanning was performed from the head surface until 100

µm deep, with z-step varying from 0.5 µm to 1.5 µm, and performed every 1 to 5 minutes (depending on the actual experiments), typically for 8 to 24 hours.

Through these imaging sessions, we could then record the activity of the macrophages and their state. As an example, from the imaging of the whole brain one can isolate macrophages having the characteristic shape of the M2 macrophages (for which a specific transgenic line was not available) (Fig. 4.2B) and cellular division (Fig. 4.2C). In addition, thanks to a fluorescent marker conjugated with the injected S. Typhimurium bacteria, we could record over time the increasing recruitment and interaction of the macrophages with the pathogen in the whole volume of interest (Fig. 4.2D), and also the absorption of the bacteria from single macrophages (Fig. 4.2E).

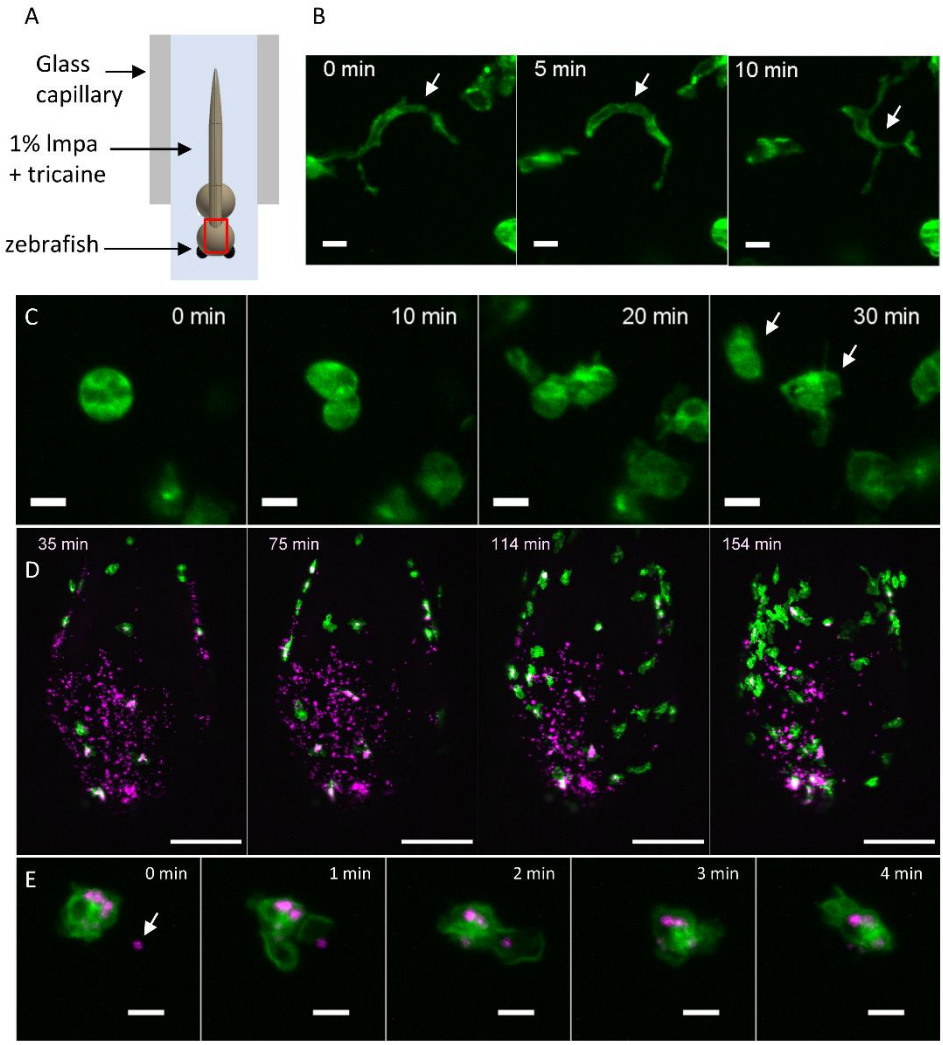

Figure 4.2: LSFM imaging of macrophages' recruitment after bacterial infection. (A) Schematics of the sample mounting within the microscope. A red rectangle highlights the region of interest for this study. (B) The passage of a macrophage showing the characteristic M2 phenotype (white arrow), Scale bar 10 µm. (C) Isolated cellular division event of a macrophage, Scale bar 10 µm. (D) Maximum intensity projection of a 100 µm volumetric dataset visualizing the brain portion interested by S. Typhimurium bacterial infection. Over time more macrophages (in green) are recruited and interact with the injected bacteria (magenta). Timestamps count from the moment of bacterial injection. Scale bar 100 µm. (E) Zoom into the process of absorption of bacteria (magenta, white arrow) by a single macrophage (green). Scale bar 10 µm.

4.4 Mouse embryo imaging

4.4.1 Introduction

Mouse embryonic development is of great interest because of its similarity with the processes happening in the human embryo [8,9]. However, as humans, mice are

mammalian vertebrates and thus embryonic development happens within the mother's uterus. Consequently, contrary to the case of the zebrafish, embryos are not directly accessible for imaging.

The study of this particular specimen in its first days of growth could be in principle done by extracting many embryos at different time points, proceeding with fixation and staining protocols, and finally image them to obtain information on the various developmental stages. However, this procedure based on embryo fixation inherently hides the dynamic processes happening within the sample. Being able instead to extract the embryos and provide them with the needed environmental conditions for their further development ex-utero within a microscope, would increase the experimental relevance [8,9]. It would in fact permit the study of the dynamical processes leading to the striking morphological changes, besides making better use of the sacrificed animal model.

Live imaging of mouse embryos has been done mainly through epi-fluorescence microscopy [8,9], but the field would benefit from LSFM technologies. In fact, mouse embryos are extremely delicate samples, and the phototoxicity and photobleaching caused by conventional confocal microscopy diminish the possibilities to image their development over a prolonged time. Altough some studies did approach this challenge through LSFM [10–12], they imaged embryos starting from the embryonic day (E) 5.5 or 6.5, which are bigger and relatively more resistant then the pre-implantation embryos I planned to visualized.

To contribute to this sector, I established a collaboration with the Mammalian Embryo and Stem Cell Group, University of Cambridge (UK). In particular, the object of our experiments was to image the dynamics underlying the morphological changes of the embryo, starting from the embryonic day (E) 4.5, and continuing ideally for 12-24 hours. This, by using embryos derived from the E-Cadherin-GFP mouse line, which allows detecting cell shapes. In the following section, therefore, I will focus on the sample mounting protocol I developed, besides the

implementations aiming to adapt the LSFM microscope to sustain mouse embryos' development.

The operations of the uterus's dissection and embryos recovering from the mother were performed following the relative guidelines and authorizations, and only from appositely trained operators (see also the ethical statement below).

4.4.2 Mounting the embryos into the LSFM microscope

As stated before, mouse embryos are extremely delicate and therefore their mounting in any microscope is particularly challenging. The sample's environment within the microscope must be under control, mimicking the conditions of the mother's uterus and ensuring their stability over a prolonged time, being the scope of the experiments the recording of the specimen's development.

With this aim, I added the needed corrections to the first version of the self-designed imaging chamber. These developments led to the implementation of the imaging chamber in 316L stainless steel (described also in Chapter 2, section 2.4.1.1) and related environmental control devices (described in detail in the following sections). The same chamber can be installed in both the Flexi-SPIM and MuViSPIM, and for this particular application, it was mounted in the MuViSPIM setup.

The main challenge I faced in this application was how to physically insert the sample into the microscope and maintain it mechanically stable during the acquisition of images. After various trials, the most promising solution found has been inserting the samples into cavities performed in a solidified 1.5% lmpa in PBS solution, contained within an FEP tube. To do that, I designed a special mechanical component that features different pillars, each of 2 mm in diameter and 10mm in height, and had it machined in aluminum (Fig. 4.3A). The particularity was that on top of each pillar, other columns were machined. These were 200 µm in diameter and 400 µm in height, and their configuration was different for each pillar, to have different mounting choices. However, for the preparation of a single experiment,

only one pillar would be used. Before the experiment, I would insert the chosen pillar, presenting a configuration of three smaller columns on top of it, into a 2x3 mm FEP tube, of about 20 mm in length (Fig. 4.3B). Then, I would introduce the liquid 1.5% lmpa solution into the other end of the tube and wait for its solidification.

After about 15 minutes, removing carefully the pillars I would obtain the FEP tube with the solidified lmpa forming three cavities of about 200x400 µm (diameter x depth), corresponding to the three columns that were on top of the pillar and that worked as negative molds (Fig. 4.3C). I would then wrap the base of the tube with parafilm, to avoid contact with the exterior environment, and leave them inside the culturing medium for hours.

Once the embryos were recovered from the mother's uterus, three of them would have been inserted into the generated agarose wells. Following, a small amount of the culturing medium would be inserted as well and on top of it, a small drop of mineral oil would prevent the evaporation of the medium (Fig. 4.3D). The operations of insertion of embryos, culturing medium, and mineral oil within the tube were performed by the collaborator. Finally, a glass capillary of 2 mm in diameter would be inserted into the FEP tube and work as connecting support between the sample and the translation stage. The FEP tube would be inserted into the imaging chamber (Fig. 4.3E), which in the meanwhile would have reached the set environmental conditions.

As described above, the FEP tube now would contain three embryos, each in a separated well. The imaging however has been performed only in one of the samples, while the other two would define the control samples. In such a way, after the imaging session, we could check the health not only of the imaged embryo but also of the other two embryos through the brightfield imaging implemented into the microscope (Fig. 4.3F). This would help in understanding if the imaged embryo was affected by the laser power and if the conditions within the chamber were adapted for the embryos' development.

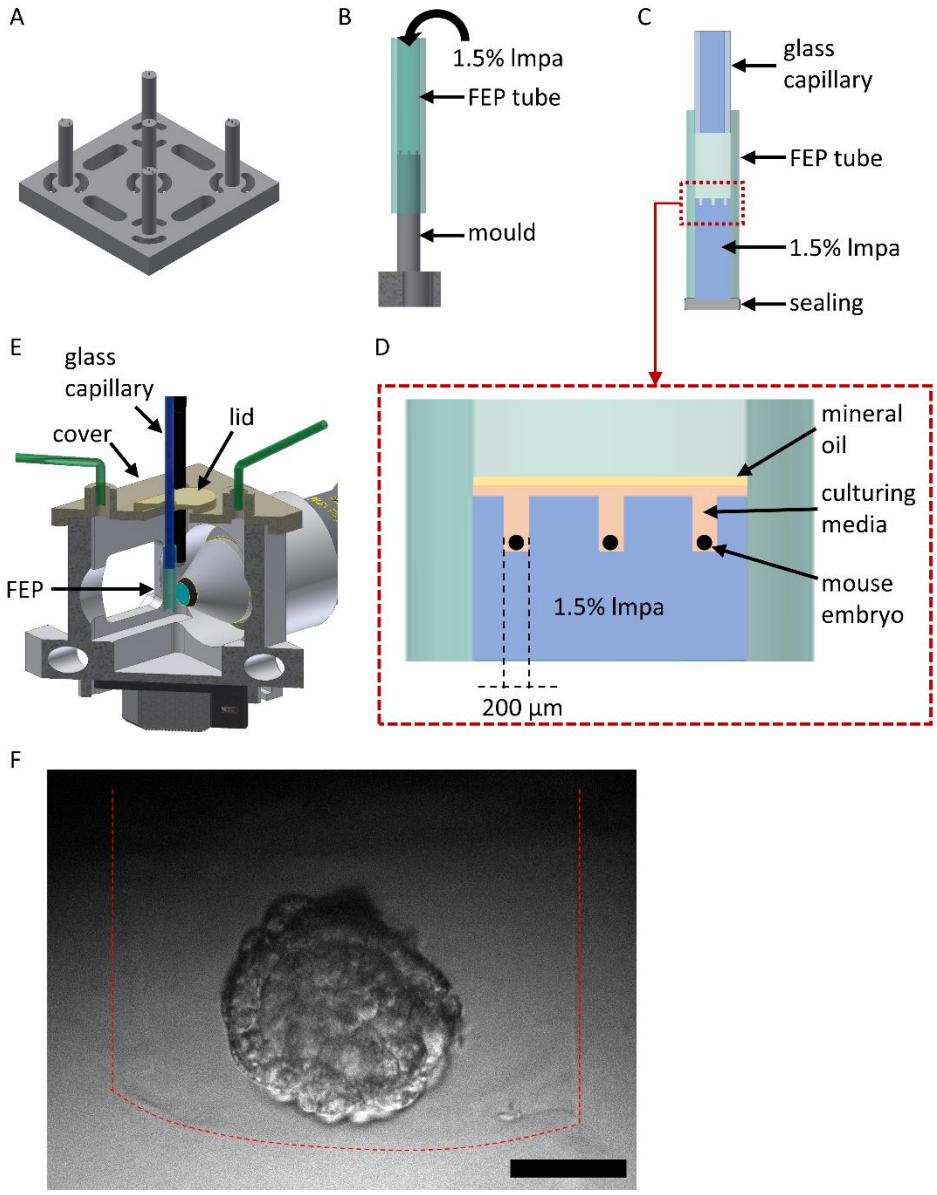

Figure 4.3: The developed mounting protocol for mouse embryo imaging. (A) The designed component consists of the different pillars and columns on top of them. (B) One of the pillars can be inserted into an FEP tube and, by adding 1.5% lmpa, work as a negative mold. (C) The agarose wells have formed, the tube has been sealed, and a glass capillary is introduced. (D) In each of the agarose wells, a mouse embryo is inserted, the culturing media is added and covered with mineral oil. (E) The glass capillary is inserted into the imaging chamber (cut view). (F) Brightfield image of one of the "control" embryos after staying for approx. 23 hours inside the imaging chamber, proving that it offers an adequate environment for the embryo's survival. The walls of the agarose wells are visible and highlighted in red. Scale bar 50 µm.

4.4.3 Environmental control and imaging

As said, the embryos need to stay in an environment in which conditions mimics the mother's uterus in term of temperature and pH, over a prolonged time. Therefore, different devices were integrated into the microscope to help the embryo's correct development (Fig. 4.4A).

First, to maintain a stable pH within the chamber, a 5% CO2 circuit was implemented that introduces the gas into a conical flask containing Milli-Q water. The gas would bubble into the water and the resulting humidified gas would be delivered toward the imaging chamber. Second, the heater at the bottom of the chamber would be set to maintain the temperature of the 18 ml of PBS medium inside the chamber constant at 37°. Third, to compensate for the evaporation of the imaging medium, which could cause temperature changes and also impede the view of the sample (as the detection objectives are water-based), a refilling system through a programmable syringe pump has been implemented. This would introduce inside the imaging chamber 45 µl every 5 minutes. This value was determined and validated experimentally to maintain the medium level approximately constant over time.

To include all the needed inlets inside the imaging chamber, I designed a cover that was machined in Teflon (i.e. sterilizable). The cover fits on the top of the chamber and it includes three circular holes for the CO2 inlet, the refilling inlet, and the medium's temperature sensor respectively (Fig. 4.4A). It also features an elongated slot, aligned with the z-direction, which is needed to permit the sample's insertion and translation. I also implemented an additional smaller lid whose aim is to cover the elongated slot. In this way, the exchange between the external environment and the conditions created within the chamber is reduced. The lid is composed of a single Teflon bar in which only a small slot (3x4 mm) needed for the sample insertion is foreseen. When imaging, in the case the glass capillary touches it during the

samples' translations, the lid can move, as it is not fixed to the cover and therefore it does not interfere with the image acquisition process.

Mouse embryos are also very sensitive to the effect induced by light illumination. Therefore, it is important to set excitation power and exposure time accurately, and the presence of two "control" embryos, which are mounted into the chamber but not illuminated by the laser, helped in separating the effects due to the chamber incubation from the phototoxicity effects. In our experiments, we tried different parameter selections and we obtained the best results using the following parameters:

- Single fluorescence channel (GFP);
- Illumination at 488 nm set at 3mW output laser power;
- Z-step of 1.5 µm;
- Exposure time 200 ms;
- Time step 10 min;
- Illumination objective Nikon 4x, NA 0.13, air;
- Detection objectives Olympus 20x, NA 0.5, water;
- Tube lens 300 mm;
- Pixel size 0.195 um (total magnification 33.3x).

Being the embryo quite transparent, and to reduce the delivered power, I opted for a single side illumination scheme. On the detection side instead, I used both objectives to capture the images relative to the front and back sides of the embryos. The views were recorded sequentially, i.e. using the rotating mirror which projected to the camera chip only one of the views (Fig. 4.4B). The controlling software was modified so that the user could select in which position of the z-stack the recorded view should change, which might not be corresponding always to the exact middle point. Finally, the entire volume can be reconstructed by merging the generated two

datasets. With these settings, we were able to image the development of mouse embryos for up to 8 hours (Fig. 4.4C).

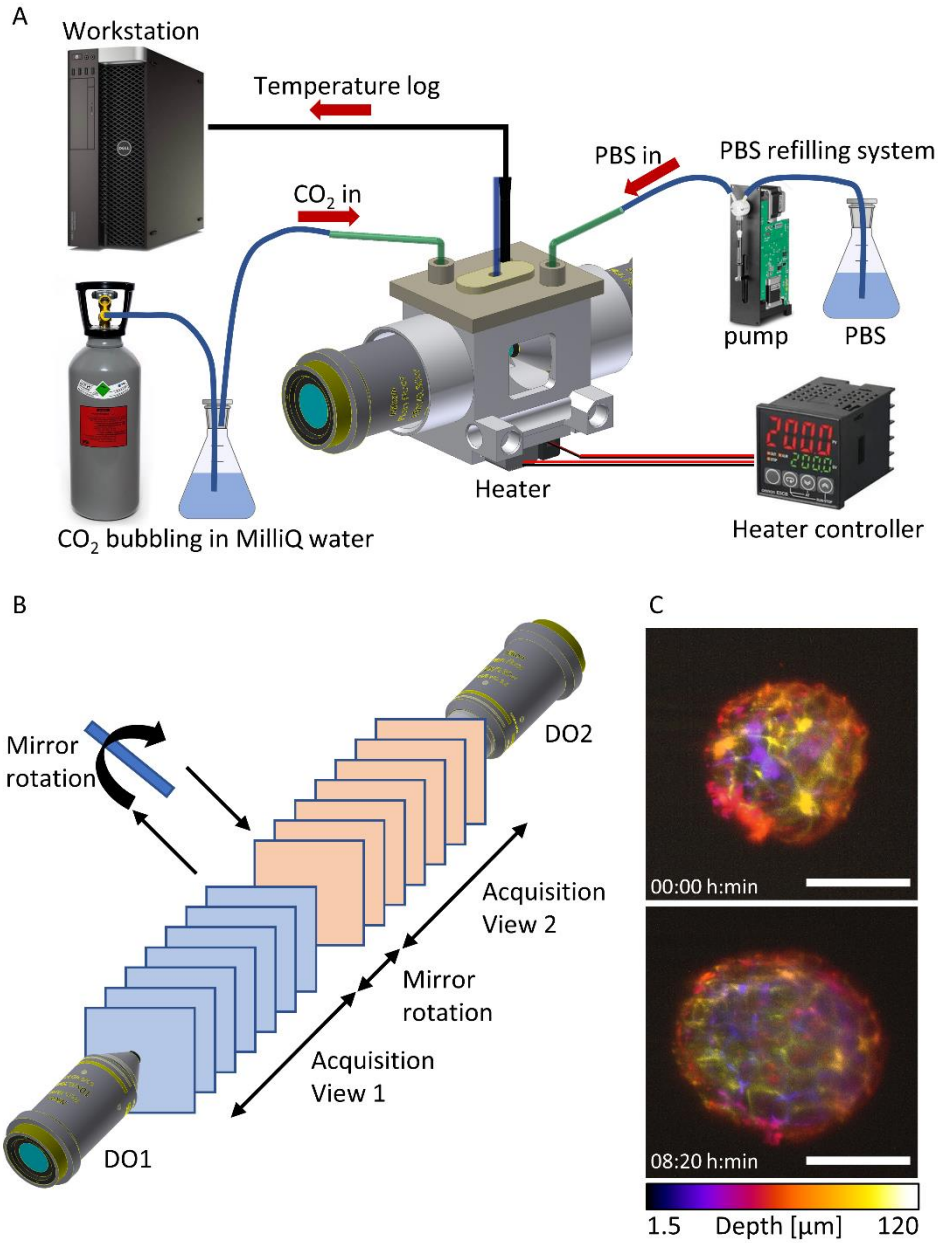

Figure 4.4: Environmental control for mouse embryos, imaging procedure, and results. (A) The stainless-steel imaging chamber features a cover through which three devices help maintain the needed conditions. The medium temperature sensor enables monitoring of the temperature inside the chamber, conditioned by the heater positioned below it. The CO_2 circuit permits maintaining the adequate pH within the chamber, and the refilling system compensates for the medium (PBS)

evaporation. (B) Through the two detection objectives (DO), the front and back views of the sample are captured sequentially thanks to the rotating mirror. (C) Depth-colored intensity projection of an E-Cadherin-GFP mouse embryo at E4.5 stage (top) that survived and developed during imaging for approx. 8 hours (bottom) thanks to the developed mounting protocol. The shown images are obtained from the fusion of the two views. Scale bars 100 µm, image adapted from [10].

The collaboration consisted of a total of 9 experiments: the first experiments were instrumental to develop the mounting devices, protocols, and selecting appropriate imaging parameters. The last two experiments were finally promising, as we were able to image a developing mouse embryo for up to 8 hours. Moreover, we could verify through brightfield images of the control embryos to verify that they also survived within the imaging chamber (Fig. 4.3F). Unfortunately, the COVID-19 pandemic forced us to interrupt the experiments and shut down this interesting and challenging application.

4.4.4 Ethical statement

All experiments involving mouse embryos were carried in compliance with protocols approved by the Comissió d'Experimentació Animal, Direcció General de Polítiques Ambientals i Medi Natural of the Departament de Territori i Sostenibilitat, Generalitat de Catalunya (Spain). "In vivo visualization of pre implantation process during mouse development through light-sheet fluorescence microscopy" (Expedient: FUE-2019-01190993; ID: XM5VTQ9BN; Project: 10758).

Animal procedures were conducted following standard ethical guidelines (European Communities Directive 2010/63/EU) and approved by the local ethical committees (Comissió d'Experimentació Animal, Direcció General de Polítiques Ambientals i Medi Natural of the Departament de Territori i Sostenibilitat, Generalitat de Catalunya (Spain)).

4.5 Future perspectives

4.5.1 Future perspectives: zebrafish’s macrophages imaging

The results of this collaboration are promising and show the various advantages of using LSFM in this specific application. Unfortunately, the COVID-19 outbreak interrupted the planned further experiments.

In particular, the planned workflow would include the integration of a laser ablation module in the Flexi-SPIM setup in the Hybrid LSFM mode. The ablation would be obtained by connecting the microscope to a Ti:Sapphire femtosecond laser available in the lab, which pulses are deviated through a dichroic mirror installed in an existing port of the detection part. The detection objective, having a high NA (0.8) therefore would not only collect the emitted photons during the LSFM imaging but would also deliver the focused near-infrared radiation and perform the localized microsurgery by two-photon ablation. The actual protocol for producing a wound foresee the manual cut through a scalpel of the caudal fin. This means that the cut is dependent on the expertise of the operator, and it is highly non-reproducible. Moreover, it can be done only in the fin, as it is the easiest part to interact with without causing the sample's death.

The laser ablation module would instead provide a platform for increasing the precision and the reproducibility of the cut. This in turn would permit to produce the cut in other parts of the fish and not only on the caudal fin. Additionally, its integration within the Flexi-SPIM, operating in the Hybrid Mode, would benefit from the peculiarities of the setup. First, the possibility to translate and rotate the sample would enable the creation of precise and arbitrary 3D patterns. Second, the imaging could start right after the microsurgery, therefore, enabling the visualization of macrophages' recruitment from its very first phases. Third, the application would profit from the enhanced throughput of the Flexi-SPIM.

As an example, let's take the case of an experiment in which the macrophage activity stimulated by a wound should be recorded for at least 12 hours on 10 samples. Using a conventional confocal microscope, this would take at least 10 days, counting only the imaging time. Moreover, as the samples examined have to be of the same age, this means that each sample comes from a different batch. Finally, the use of LSCM would probably induce photobleaching/phototoxicity effects, which could be either deleterious for the samples' health, or at least impose severe restrictions on the

time resolution. Instead, the proposed system, i.e. the Flexi-SPIM in the Hybrid Mode conjugated with a laser ablation arm, would permit to use of 10 samples from the same batch, i.e. reducing the genetic differences between the individuals. This would drastically reduce the experimental timing, as the various samples could be loaded in the FEP tube together. The microscope would be able to change the current fish under observation through the translation along the tube. In this way, the setup could acquire the volume of each fish sequentially, and then restart, building up the time-lapse movie for all the samples. Given the high speed of LSFM imaging, this would still permit reaching a good time resolution and maintain the possibility of long-term movies. Also, the induced cut would be very similar between the samples, as it can be computationally defined and it would not be dependent on the operator ability. High-throughput LSFM then would be ideal for both the applications (wound and bacterial infection) here discussed.

4.5.2 Future perspectives: mouse embryo imaging

Although we developed a successful mounting protocol and obtained promising preliminary results, the application could profit from further advances.

First, the FEP tube here used (2x3 mm) presents quite thick walls (0.5 mm). Thinner walls would be instrumental in increasing the SNR of the images and therefore in reducing eventual optical aberrations caused by the tube. Increasing the total SNR would then permit reducing the delivered excitation power or the exposure time, reducing the phototoxicity effects on the sample due to laser exposure.

Another possible improvement now that the environment within the chamber is amenable for the embryo development, would be to include the embryos here used as control into the imaging process as well. Therefore, during each experimental session, we could image three embryos instead of one, increasing the chances of successfully recording the wanted biological features. This could be accomplished by motorizing the stages controlling the lateral directions (x and y, here based on a manual stage). Through a custom-made software then, the user could select three

volumetric regions within the FEP tube to be imaged, each for a single embryo, so that for each of the time points all embryos can be imaged automatically.

4.6 References

1. M. Nguyen-Chi, B. Laplace-Builhe, J. Travnickova, P. Luz-Crawford, G. Tejedor, Q. T. Phan, I. Duroux-Richard, J.-P. Levraud, K. Kissa, G. Lutfalla, C. Jorgensen, and F. Djouad, "Identification of polarized macrophage subsets in zebrafish.," Elife **4**, e07288 (2015).

2. T. Sipka, R. Peroceschi, R. Hassan-Abdi, M. Groß, F. Ellett, C. Begon-Pescia, C. Gonzalez, G. Lutfalla, and M. Nguyen-Chi, "Damage-Induced Calcium Signaling and Reactive Oxygen Species Mediate Macrophage Activation in Zebrafish ," Front. Immunol. **12**, (2021).

3. T. Sipka, S. Tairi, M. Bernardello, E. J. Gualda, P. Loza-Alvarez, A. Blanc-Potard, G. Lutfalla, and M. Nguyen-Chi, "Dynamics of macrophage polarization during Salmonella Typhimurium infection in zebrafish," (n.d.).

4. A. Kaufmann, M. Mickoleit, M. Weber, and J. Huisken, "Multilayer mounting enables long-term imaging of zebrafish development in a light sheet microscope.," Development **139**(17), 3242–3247 (2012).

5. K. D. Gibbs, E. J. Washington, S. L. Jaslow, J. S. Bourgeois, M. W. Foster, R. Guo, R. G. Brennan, and D. C. Ko, "The Salmonella Secreted Effector SarA/SteE Mimics Cytokine Receptor Signaling to Activate STAT3.," Cell Host Microbe **27**(1), 129-139.e4 (2020).

6. I. Panagi, E. Jennings, J. Zeng, R. A. Günster, C. D. Stones, H. Mak, E. Jin, D. A. C. Stapels, N. Z. Subari, T. H. M. Pham, S. M. Brewer, S. Y. Q. Ong, D. M. Monack, S. Helaine, and T. L. M. Thurston, "Salmonella Effector SteE Converts the Mammalian Serine/Threonine Kinase GSK3 into a Tyrosine Kinase to Direct Macrophage Polarization.," Cell Host Microbe **27**(1), 41-53.e6 (2020).

7. E. Karsenti, S. G. Acinas, P. Bork, C. Bowler, C. De Vargas, J. Raes, M. Sullivan, D. Arendt, F. Benzoni, J.-M. Claverie, M. Follows, G. Gorsky, P. Hingamp, D. Iudicone, O. Jaillon, S. Kandels-Lewis, U. Krzic, F. Not, H. Ogata, S. Pesant, E. G. Reynaud, C. Sardet, M. E. Sieracki, S. Speich, D. Velayoudon, J. Weissenbach, and P. Wincker, "A holistic approach to marine eco-systems biology.," PLoS Biol. **9**(10), e1001177 (2011).

8. N. Christodoulou, A. Weberling, D. Strathdee, K. I. Anderson, P. Timpson, and M. Zernicka-Goetz, "Morphogenesis of extra-embryonic tissues directs the remodelling of the mouse embryo at implantation," Nat. Commun. **10**(1), 3557 (2019).

9. M. A. Molè, A. Weberling, and M. Zernicka-Goetz, "Chapter Four - Comparative analysis of human and mouse development: From zygote to pre-gastrulation," in *Gastrulation: From Embryonic Pattern to Form*, L. B. T.-

C. T. in D. B. Solnica-Krezel, ed. (Academic Press, 2020), **136**, pp. 113–138.

10. T. Ichikawa, K. Nakazato, P. J. Keller, H. Kajiura-Kobayashi, E. H. K. Stelzer, A. Mochizuki, and S. Nonaka, "Live imaging of whole mouse embryos during gastrulation: migration analyses of epiblast and mesodermal cells.," PLoS One **8**(7), e64506 (2013).

11. T. Ichikawa, K. Nakazato, P. J. Keller, H. Kajiura-Kobayashi, E. H. K. Stelzer, A. Mochizuki, and S. Nonaka, "Live imaging and quantitative analysis of gastrulation in mouse embryos using light-sheet microscopy and 3D tracking tools.," Nat. Protoc. **9**(3), 575–585 (2014).

12. K. McDole, L. Guignard, F. Amat, A. Berger, G. Malandain, L. A. Royer, S. C. Turaga, K. Branson, and P. J. Keller, "In Toto Imaging and Reconstruction of Post-Implantation Mouse Development at the Single-Cell Level.," Cell **175**(3), 859-876.e33 (2018).

13. M. Bernardello, E. J. Gualda, and P. Loza-Alvarez, "Modular multimodal platform for classical and high throughput light sheet microscopy.," Sci. Rep. **12**(1), 1969 (2022).

Chapter 5: Extension of single-molecule imaging to living embryos through LSFM

This chapter contains content entirely reproduced or adapted from the article [1]: Bernardello M., et al. “Analysis of intracellular protein dynamics in living zebrafish embryos using light-sheet fluorescence single-molecule microscopy.” Biomedical optics express 12 10 (2021): 6205-6227

5.1 Abstract

Single-Molecule Microscopy techniques have emerged as useful tools to image individual molecules and analyze their dynamics inside cells, but their application has mostly been restricted to cell cultures. Here, a Light-Sheet Fluorescence Microscopy setup is presented for imaging individual proteins inside living zebrafish embryos. The optical configuration makes this design accessible to many laboratories and a dedicated sample-mounting system ensures sample viability and mounting flexibility. Using this setup, we have analyzed the dynamics of individual glucocorticoid receptors, which demonstrates that this approach creates multiple possibilities for the analysis of intracellular protein dynamics in intact living organisms. This project is the result of a collaboration with the Schaaf group at University of Leiden (The Netherlands) and resumed also in [1].

5.2 Introduction

A quantitative imaging-based analysis of the biochemical processes and protein interactions inside cells requires microscopy techniques that go beyond ensemble averaging and a static molecular view [2]. Single-molecule microscopy (SMM, also known as SMLM, Single-molecule localization microscopy) has demonstrated to offer such opportunities and has enabled researchers to detect individual molecules in the variety of their conformations and associations as well as to study their dynamics with unparalleled spatial and temporal resolution. Imaging of individual proteins in living cells is enabled by fluorescent labeling of these proteins, using either genetically encoded fusion to autofluorescent proteins such as green fluorescent protein (GFP) and photoactivatable or switchable variants of these proteins, or linking of nanoparticles or organic dyes to peptide or protein tags (such as Halo-tags), that have been fused to the protein of interest [3–6].

SMM has mainly been performed using microscopy techniques such as Widefield Microscopy (WM), Total Internal Reflection Fluorescence (TIRF) microscopy, and Highly-Inclined and Laminated Optical sheet (HILO). In WM, while technically simple,

the entire sample is illuminated by the excitation beam, which creates a high background over the weak signal from the single molecules. In TIRF, an evanescent wave of excitation light at the coverslip-sample interface is created, which exponentially decays with the distance to this interface [7]. As a result, only the fluorophores present in the first 100 to 200 nm are excited, which highly reduces the background intensity, and thereby increases the sensitivity and positional accuracy. However, at the same time, TIRF limits the detection of molecules to the basal membrane of the cells mounted on the coverslip. In HILO microscopy an oblique sheet of light is used to illuminate a section of the specimen, enabling excitation of fluorophores deeper inside cells [8]. Nevertheless, since the illumination is oblique with respect to the detection focal plane, the size of the lateral Field-of-View (FoV) of the produced images is limited. Moreover, all these approaches are optimized for, and therefore limited to, coverslip-based sample mounting.

Thus far, the vast majority of SMM studies have been performed in cultured eukaryotic cells, often derived from immortalized cell lines. These cells may show artefacts, do not take into consideration the influence of cell-cell interactions, and have a limited translational value compared to studies performed in intact organisms. In addition, studies in cultured cells cannot answer questions concerning differences in protein dynamics in response to different developmental, environmental, and metabolic states that an organism might be presented with in its native habitat. Therefore, there is a need for microscopy techniques that enable in-vivo SMM analyses on biologically relevant samples, such as the living zebrafish. These techniques should provide limited background signals and large FoVs, enable maintaining the sample alive for prolonged times, and, ideally, not interfere with natural biological processes by limiting phototoxic effects or other stressors.

Previously, the Schaaf group at University of Leiden has extended SMM studies to living organisms by analyzing the dynamics of yellow fluorescent protein (YFP) fused

to the membrane anchor of the human H-Ras protein in cells inside living zebrafish embryos [9]. By using TIRF microscopy and a particular sample-mounting procedure to make the zebrafish tail adhere to the coverslip, they managed to detect individual YFP-C10H-Ras molecules in the outer membrane of the outer epithelial cells of the embryonic epidermis, and to study the mobility pattern of these proteins. However, while this approach can be used for studies on membrane protein dynamics, the implementation of the TIRF microscopy is limited by the penetration depth of the evanescent wave and is therefore not suitable for studying molecules located anywhere outside the outer membrane of the outer cell layer of the embryo.

In the present study, we have applied Light-Sheet Fluorescence Microscopy (LSFM) as an SMM technique that allows for imaging of individual non-membrane molecules inside a living organism while not being limited to the cell membrane.

The plane-based configuration typical of LSFM permits fast imaging and allows for optical sectioning at low photobleaching and phototoxicity regimes, with low background fluorescent signals. Nevertheless, the use of LSFM in SMM applications has so far been limited, mainly due to mechanical constraints imposed by the geometry of the objectives. Their orthogonality combined with their short working distances restricts the space and displacement possibilities of the sample.

This problem has often been circumvented by the use of long-working-distance air objectives for the illumination, and cuvettes containing imaging medium and sample [10–13]. This solution, however, introduces refractive index mismatches at the air-glass and glass-medium interfaces, leading to spherical aberrations. Consequently, when the cuvette translates in the illumination direction, focal shifts appear and correction strategies need to be implemented [11], increasing hardware complexity. To overcome these issues, some LSFM configurations use a modified light path, including prism-based LSFM (PCLSM) [14], and reflected LSFM (RLSFM) [15–17]. With these LSFM approaches individual, fluorescently labelled molecules have been imaged in aqueous solutions [10,12], cell nuclei of salivary glands extracted from *C.*

tentans larvae [11,13], and membranes or nuclei of cultured cells [14,15]. Interestingly, these technologies also allowed imaging of individual injected Dextran-Alexa647 molecules in Drosophila [16], and transcription factors in zebrafish embryos [17]. Custom-made illumination objectives combined with non-Gaussian excitation schemes, such as Bessel plane illumination [18] and lattice LSFM (LLSFM) [19], have been used to create a long and thin LS. These techniques have been employed in SMM studies in embryonic stem cells [20,21], membrane dynamics in cultured cells and in cells of the zebrafish eye [22], and living Drosophila [23,24]. The Light Sheet Fluorescence Single-Molecule Microscopy (LSFSMM) methods described above offer the possibility to use very high NA (from 1.0 to 1.4) detection objectives, but this is only possible at the expense of a highly increased hardware complexity of the overall system, which will limit the use of LSFSMM.

So far, single-molecule imaging has been applied to intact living organisms only in a few studies [9,17,23], which could be due to the difficulty for many biological labs in accessing the complex setups that are required. The described hardware complexity also has consequences for the sample mounting systems. In PCLSM [14], the sample is placed on a glass bottom dish over an inclined surface. Similarly, RLSFM [15,16] and LLSFM have been used for SMM in living zebrafish embryos [17,22], and in these studies the embryos were mounted on a glass bottom dish or glass coverslip and embedded in low melting agarose. In all these methods, the sample's degrees of freedom are constrained by the mounting procedure, as the specimen's movements and orientation possibilities are fixed or limited. Although this might not be a problem for cultured cells, in the case of imaging living organisms it can eventually preclude the performance of certain experiments.

In the present study, we chose an iSPIM [25] configuration to perform SMM, to have a simpler setup compared to the previously mentioned LSFM alternatives, without custom-made optical elements such as coatings [15,17] or objectives [19], thereby avoiding potential instability issues and maintaining a straightforward optical

alignment procedure. Although the collection NA achieved in our system is smaller or equal compared to the NA of PCLSM, RLSFM, or LLSFM setups, our sample mounting approach is superior in terms of sample viability and sample mounting flexibility. We believe that these are crucial factors when extending the application of SMM to intact living organisms. In addition, our design will enable the possibility to perform more complex SMM studies in-vivo, e.g. correlating macro-biological events with the intracellular dynamics at the single molecule level. The sample mounting procedure is therefore described in detail, with attention to the effects of the embedding medium on the microscope's performance.

We have utilized our LSFSMM setup using cultured cells and living zebrafish embryos as biological samples. HEK293 cells were used to perform a characterization study on the detection of single yellow fluorescent protein (YFP) molecules. Subsequently, we chose zebrafish embryos to test our capacity to image in-vivo, since it is a relevant vertebrate animal model that is commonly used in research areas, ranging from developmental biology to toxicology and drug screening [26,27]. As a protein of interest, we selected the Glucocorticoid Receptor (GR), which is a well-studied steroid receptor. Upon binding of a glucocorticoid ligand (either an endogenous hormone such as cortisol or a synthetic drug such as dexamethasone), the GR translocates to the nucleus and acts as a transcription factor, regulating gene expression by binding to specific DNA sequences and interacting with other proteins.

By using our custom-made and optimized mounting system in our LSFSMM, we demonstrate that it is possible to successfully image individual molecules in living embryos for a prolonged period of time. To image the features of interest, all experiments were performed using embryos from the *Tg(actb2:mCherry-H2A)* zebrafish line, in which a construct labeling for GR was injected. Therefore, the resulting embryos would express fluorescence marking for nuclei (through the mCherry protein) and GR (through the injected YFP construct).

To validate the robustness of our LSFSMM, we have analyzed the GR mobility pattern and characterized the sources of variation in the in-vivo results. We found that most of the variability in the results comes from imaging different areas within an individual zebrafish embryo, and to a lesser extent from imaging individual embryos on different experimental days, discarding the microscope setup as a source of variation. Overall, our data suggest that the relative simplicity of the optical design, constructed with conventional optical elements together with the described sample mounting system and protocols, will further promote in-vivo LSFSMM applications in membranes, cytoplasm, and nuclei of cells inside zebrafish and other living organisms.

5.3 The LSFSMM platform

In order to achieve in-vivo SMM on whole live organisms we have designed and built a customized LSFM platform. We took into special consideration the development of sample mounting protocols adapted to the experimental requirements and sample needs. Finally, we have characterized its optical performance and its ability to conduct SMM experiments.

5.3.1 Optical setup

Our LSFSMM implementation is built on a Nikon Eclipse body, on top of which two perpendicular objectives are mounted in iSPIM configuration [25]. Since the two objectives are positioned perpendicularly to each other, but at 45° in respect to the optical table, we define the coordinate system xyz to be the reference for the optical table and motor stages, while the coordinate system $\hat{x}\hat{y}\hat{z}$ is defined as the reference for the imaging planes, with $\hat{x}\hat{y}\hat{z}$ being the clockwise rotation of 45° around the y-axis of xyz. A schematic overview of the illumination and detection light paths and a photo of the implemented iSPIM configuration is depicted in Fig. 5.1A-B. The light sheet plane is generated by a cylindrical lens that focuses the light onto a galvo-mirror. The mirror is positioned plane-conjugate with the back focal plane (BFP) of a water dipping illumination objective by a relay lens system. This arrangement

permits to change the position in ẑ (i.e., across the sample volume) of the light sheet by electronically controlling the angle of the galvo-mirror. This capability can be used for alignment purposes and to scan different sample areas.

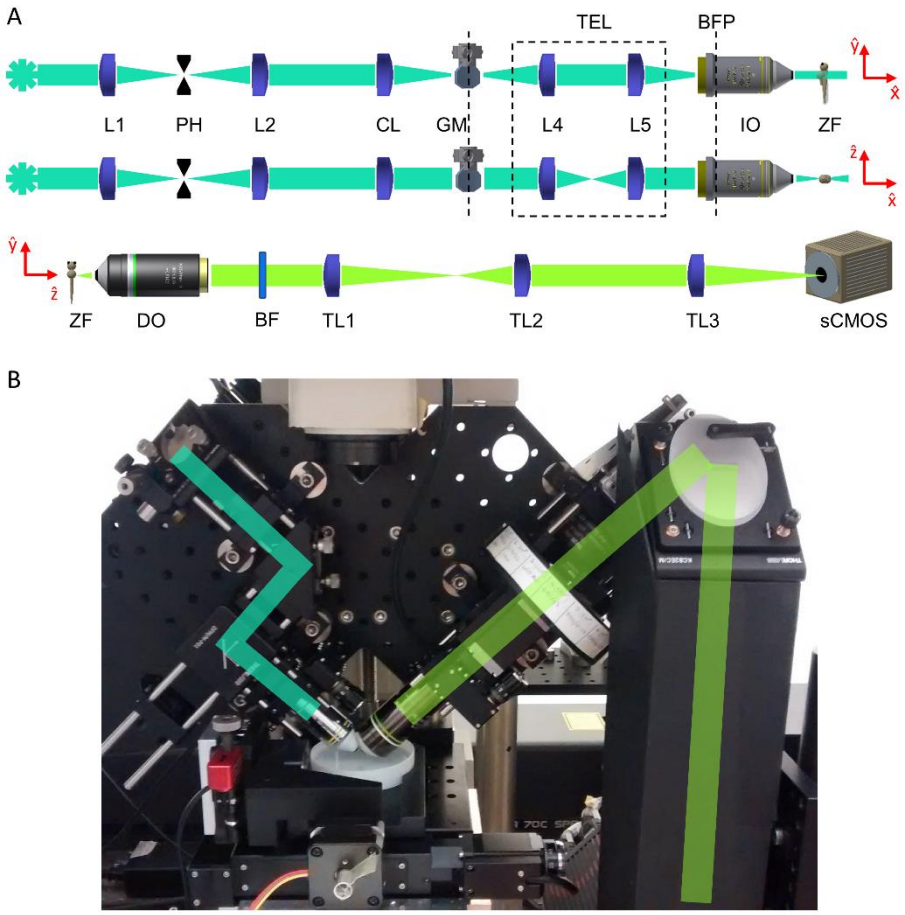

Figure 5.1: Schematic overview of the LSFM platform for in-vivo SMM imaging. (A) schematic of the optical illumination (top two) and detection (bottom one) light paths; (B) photo of the actual configuration. L= lens, PH= pinhole, CL= cylindrical lens, GM= galvo-mirror, BFP= back focal plane, TEL= telescope plane-conjugating GM to BFP, IO= Illumination objective, DO= detection objective, BF= bandpass filter, TL= tube lens, ZF= zebrafish. Figure adapted from [1].

5.3.1.1 LSFSMM setup details

In the LSFSMM setup, the light from an ArKr laser (Innova 70C Spectrum, Coherent) is first passed through an acousto-optic tunable filter (AOTFnC-400.650-TN, AAOptoelectronics) to select the needed illumination wavelengths (514.5 nm for the YFP, and 568.2 nm for the mCherry molecules). After the AOTF (see Fig. 5.1A), the

light beam is sent to a telescope (AC254-030-A-ML, AC254-250-A-ML, Thorlabs), going through a spatial filter (with a 30 µm pinhole) to produce a clean Gaussian beam. The collimated beam is then focused by a cylindrical lens (focal length of 75mm, LJ1703RM-A, Thorlabs). An additional telescope (AC254-100-A-ML, AC254-200-A-ML, Thorlabs) is then used to illuminate the back-focal plane (BFP) aperture of a water immersion illumination objective (10X Nikon CFI Plan Fluorite Objective, 0.30 NA, 3.5 mm working distance (WD)) that will finally project the light sheet at the sample plane. The illumination path also incorporates, in a conjugated plane with the BFP of the illumination objective, a galvanometric mirror (GVS002, Thorlabs) that allows scanning the light sheet across the sample volume if needed (i.e. in the depth direction). In the detection path, the fluorescent signal is collected by a water-dipping detection objective (20X Olympus XLUMPLFLN Objective, 1.00 NA, 2.0 mm WD). This is passed through a motorized filter wheel (FW103H, Thorlabs) and a 200 mm tube lens (TTL200-A, Thorlabs). A periscope formed by an additional telescope (TTL100-A and TTL200-A, Thorlabs) permits an additional 2x magnification and projects the image onto the chip of a sCMOS camera (OrcaFlash4 v.3, Hamamatsu). With this configuration (Olympus objective coupled to 200mm tube lens and 2x periscope), the total magnification is 44.4x.

5.3.2 The sample mounting system for living embryos

In the iSPIM configuration, the two objectives offer a limited volume in which the sample can be inserted. The sample mounting system is however of key importance, and it must allow simple insertion of a zebrafish embryo and provide conditions for the specimen to stay alive during the experiment, with as little stress imposed as possible. At the same time, the sample mounting system needs to avoid the introduction of unwanted optical aberrations.

I have implemented and characterized a fully motorized sample mounting stage and efficient sample mounting protocols using tailored FEP tubes and multilayer agarose mounting, as depicted in Fig. 5.2A-C. The developed sample mounting system makes

use of a FEP tube which was cut to free the top part. In this way the tube serves as a horizontal support for the relatively big and heavy sample without covering it. Its proximal and distal tips and the basis of the tube are filled with 2% low melting point agarose (lmpa). The zebrafish embryo is placed in the remaining space inside a drop of 0.5% lmpa with the addition of tricaine for anaesthesia (Fig. 5.2C). The FEP tube is suspended inside a petri-dish–like chamber by a 12 cm glass capillary (Fig. 5.2D), which is inserted into the proximal end of the FEP tube. The glass capillary is connected to a motorized rotator motor on its other end, and optimal orientation of the zebrafish embryo with respect to the LS can be obtained by rotating the capillary using simple electronic control of the motor. Finally, the incubation chamber, which is on top of an x-y-z motorized translational stage is filled with E3 medium (with the addition of tricaine), to completely immerse the zebrafish embryo and the tips of the objectives. In this way, the FEP tube containing the sample under observation results in the imaging volume between the two objectives (Fig. 5.2E).

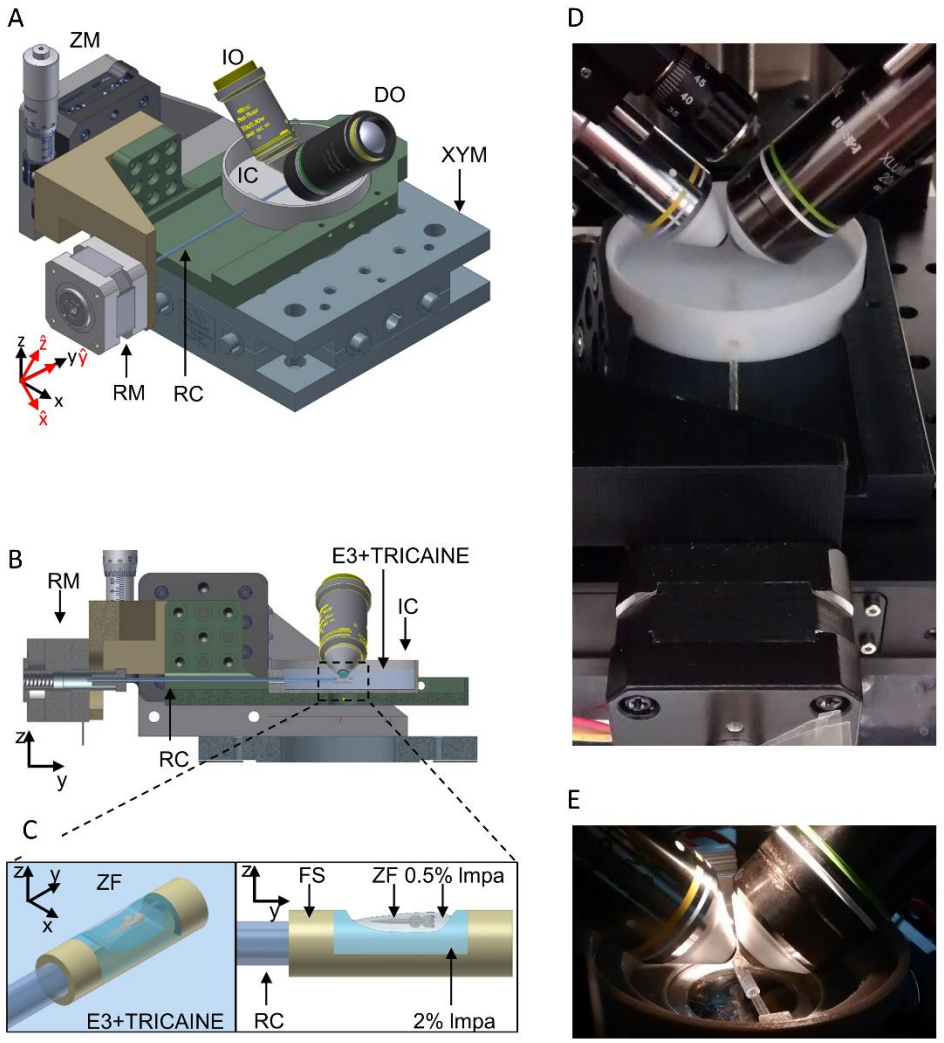

Figure 5.2: Overview of the LSFSMM sample mounting system. (A) Schematic of the sample mounting system, with (B) its lateral section view and (C) the FEP support for zebrafish mounting. IO= Illumination objective, DO= detection objective, ZF= zebrafish, RC= rotation capillary, FS= FEP support, RM= rotational motor, IC= imaging chamber, ZM= motorized stage in z, XYM= motorized stage in xy, lmpa= low melting point agarose. Figures adapted from [1] *(D) Photo of the glass capillary inserted between the two objectives and connected to a stepper motor and (E) zoom into the imaging volume where the cut FEP tube is positioned. Figure adapted from* [1].

5.3.3 Imaging performances

On the illumination side, I experimentally measured the LS thickness to be of about 2 µm at its waist (Fig. 5.3A). The illumination FoV along $\hat{x}$, i.e., the portion of the light sheet that is considered to be of homogeneous thickness, is calculated to be about 13.5 µm, in good agreement with the measured value of about 14.5 µm (Fig. 5.3A).

The total magnification of the optical system is 44.4X (See Material and Methods section), leading to an image pixel size of 146.4 nm. Considering the size along the ŷ axis of the sCMOS chip of the camera (2048 pixels), this means that the system enables the imaging of an area of about 13.5 µm x 300 µm.

On the detection side, to characterize the effect of the sample mounting protocol on the generated optical aberrations, a FEP tube filled with a 0.5% lmpa cylinder in which sub-diffraction sized fluorescent beads (100 nm in diameter) were embedded was introduced in the imaging volume. The image of a 100 nm fluorescent bead would present a theoretical FWHM of 334 nm, given by the convolution of the Gaussian PSF generated by a 1.0 NA water-objective, with the step-size profile of the bead. The images obtained from beads inserted close to the middle axis of the lmpa cylinder would instead heavily suffer from distortions, enlarging the total PSF and reducing the actual optical resolution (Fig. 5.3C-D). For beads at this location, I calculated FWHMs of 567.6 ± 59.2 nm and 536.5 ± 65.3 nm (average ± standard deviation, in x̂ and ŷ direction respectively, N=11 beads). In contrast, images from beads closer to the surface of the 0.5% lmpa cylinder did not suffer from significant distortions (Fig. 5.3E-F). For beads at this location, I calculated FWHMs of 393.0 ± 39.9 nm and 371.4 ± 34.8 nm (average ± standard deviation, in x̂ and ŷ direction respectively, N=11 beads). See also Appendix C, section C.1 for a complete description of the procedure used for measuring the mentioned values.

The position of the point source within the lmpa cylinder is therefore critical in assessing the optical resolution, which significantly differs for objects at the two locations (Fig. 5.3B). The difference between the measured values from the beads close to the surface and the theoretical one is most probably imputable to a residual aberration caused by the remaining agarose layer, and thus depending on the exact position of the single beads. The system and protocol for mounting zebrafish embryos was therefore here developed such that the living specimen was covered

by a maximally 100 µm-thick layer of 0.5% lmpa, in order to minimize optical aberrations.

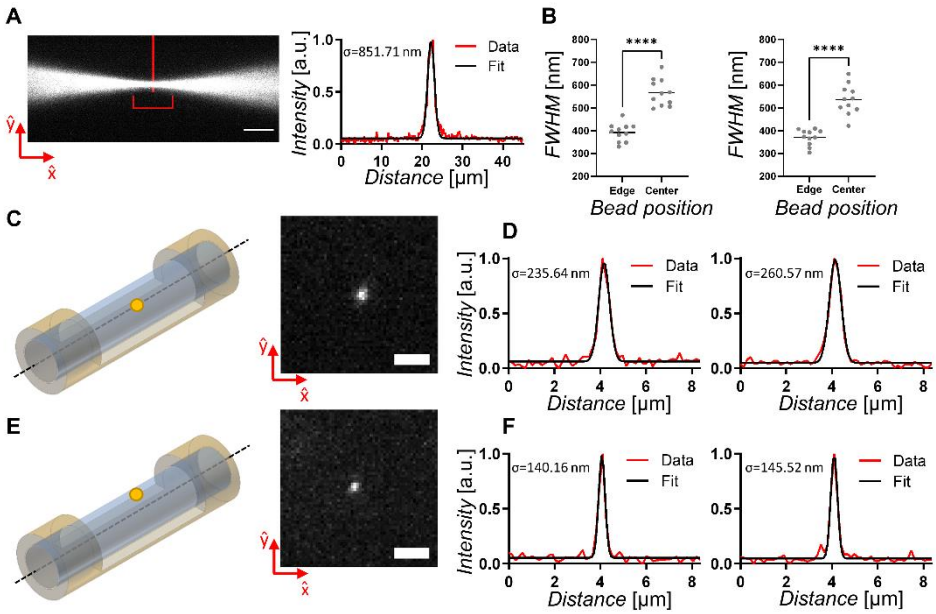

*Figure 5.3: LSFSMM system performances. (A) Illumination light beam focused by removal of the cylindrical lens. Measurement of the intensity profile through a Gaussian fit demonstrated a 2 µm diameter (FWHM) at its waist (indicated by vertical red line). The illumination FoV is also indicated (red horizontal bracket). Scale bar 10 µm. (B) Distributions and comparison of the measured FWHM of the Gaussian fits of beads close to the surface (N=11) and in the center (N=11) of the mounting lmpa cylinder. Values were measured along x̂ (left panel) and ŷ (right panel) direction. Shapiro-Wilk test was performed to check if data is normally distributed. Unpaired t-tests were then conducted to check for statistically significant difference between the two conditions and calculate two-tailed P-values. Horizontal bar represents the mean value, **** means P<0.0001. (C) Schematic of a 100 nm fluorescent bead positioned in the middle of a 0.5% lmpa cylinder and (D) normalized intensity profile measurement and Gaussian fit in x̂ (left panel) and ŷ (right panel) direction of an imaged bead. Scale bar 2 µm. (E) Schematic of a 100 nm fluorescent bead positioned close to the surface of a 0.5% lmpa cylinder and (F) normalized intensity profile measurement and Gaussian fit in x̂ (left panel) and ŷ (right panel) direction of an imaged bead. Scale bar 2 µm. For all the Gaussian fits here presented R2>0.96, and σ represents the standard deviation of the Gaussian curve. Figure reproduced from* [1].

5.4 Live embryo mounting protocol

All experiments were performed using embryos from the *Tg(actb2:mCherry-H2A)* zebrafish line, which express a fluorescent nuclei marker. A cDNA construct encoding eYFP-GR(alpha), hereafter referred to as YFP-GR, was genetically cloned into a PCS2+ zebrafish expression plasmid. The resulting PCS2+-eYFP-GR(alpha) plasmid was microinjected into zebrafish embryos at the 1-2 cell stage (30 pg per

embryo), resulting in a mosaic expression of the eYFP-GR(alpha) protein in the zebrafish embryo. To prevent embryonic pigmentation, embryos were incubated in 0.003% phenylthiourea (PTU) from 10 hpf (hours post-fertilization) onwards, and this solution was refreshed daily. See also Appendix C, sections C.2 and C.3 for the complete description of the manipulation of zebrafish embryos.

A cut FEP tube was mounted through a glass capillary inside the incubation chamber. Lmpa solutions (2% and 0.5% in E3 medium) were heated up to 70°C, and 2% lmpa was applied to the distal and proximal ends of the cut tube as well as at the basis (see also Fig. 5.1C) and left to solidify.

Naturally hatched and PTU-treated zebrafish 2dpf embryos were transferred to a petri dish containing E3 medium with tricaine (100 mg L^{-1}). Subsequently, an embryo was transferred to a glass bottom petri dish, the E3 medium was removed, and 0.5% lmpa (cooled down, with 100 mg L^{-1} tricaine) was poured onto the glass petri dish. While still liquid, a drop of 0.5% lmpa, together with the zebrafish embryo, was aspired through a glass pipette and carefully transferred into the FEP support, on top of the already present 2% lmpa layer. In this way, the zebrafish embryo was delicately laid on its side.

After waiting approximately 10 minutes for the lmpa to solidify, the incubation chamber with the FEP tube containing the zebrafish embryo was mounted into the setup, on top of a platform connected to a xyz motorized stage (8MTF from Standa for xy-translations, 8302 Picomotor Actuator from Newport, connected to LX10/M from Thorlabs, for z-translations). The glass capillary was connected, using a screw, to a stepper motor (L4018S1204-M6, Nanotec) for sample rotation. E3 medium with tricaine (100mg L^{-1}) was poured into the imaging chamber at room temperature, to completely immerse the sample and the tip of the objectives.

Using a custom-made software in LabVIEW, the position of the sample in x, y, and z was adjusted to be in the FoV of the detection objective. Rotation around the y-axis

of the specimen and the movement in $\hat{z}$ of the light sheet provided additional alignment flexibility and possibilities to change the imaged area. The position of the detection objective was manually adjusted so that its focal plane would coincide with the light sheet.

5.5 Experiments on cultured cells

Before performing experiments on live fish, we sought to prove the SMM capabilities of the LSFSMM setup on a simpler and more conventional sample, such as cultured cells. In particular, we used HEK293 cells transiently transfected with an expression vector for YFP-GR, which were first fixed and then mounted on the LSFSMM setup for imaging (see also Appendix C, section C.4 for a complete description of the protocol used).

We chose to use fixed cells in order to guarantee immobility of the fluorophores so they would not diffuse out of the FoV. In this way the sudden disappearing between two consecutive frames of an imaged molecule could be attributed to the photobleaching of the single fluorophore, therefore assuring that the signal was indeed coming from a single molecule. This approach, named “single-step photobleaching analysis”, is typically used in SMM analysis [1]. The characteristics of the YFP molecule fluorescence signal were determined by the analysis of 1241 fluorescence intensity spots that displayed single-step photobleaching behavior (Fig. 5.4A). The features obtained from the fluorescence signals of those individual YFP molecules were subsequently used to determine the threshold values for the identification of signals attributed to single YFP-GR molecules in the images acquired from living zebrafish embryos using previously developed, customized software [3,28,29]. These features are relative only to the signal intensity, which derives from the single YFP molecules that are the same used in both the cellular sample and the zebrafish sample.

To extract the information about the point-spread function (PSF) of the fluorescence from a single YFP molecule, a Gaussian function was plotted over the 2D intensity

profile (Fig. 5.4B). We determined the maximum of the Gaussian function as a measure for the intensity, and its full width at half maximum (FWHM) as a measure for the width of the PSF of a single YFP molecule. The maximum of the Gaussian function of 1241 signals from immobilized YFP-GR molecules in the fixed HEK293 cell equaled 139.8 ± 22.4 counts, which corresponds to 22.3 ± 9.7 photons. This value was calculated from the specification of the camera as:

$$N_p = \frac{(S - OL) \cdot CF}{QE}$$

Where N_p is the number of photons, S is the signal level (or counts), OL is the Offset Level specific of the camera, CF is the Conversion factor between counts and produced electrons, and QE is the Quantum Efficiency. The mean FWHM value of the Gaussian curves fitted on the single-molecule intensity profiles equaled 357.5 ± 12.6 nm. The positional accuracy of the measurements was determined by calculating the quotient of the FWHM and the square root of the number of photons detected and equaled 76 nm [30]. Signal-to-Noise Ratio (SNR), defined as the intensity of an individual fluorophore (139.8 ± 22.4 counts) divided by the standard deviation of the background signal (7.2 counts), equaled circa 20.

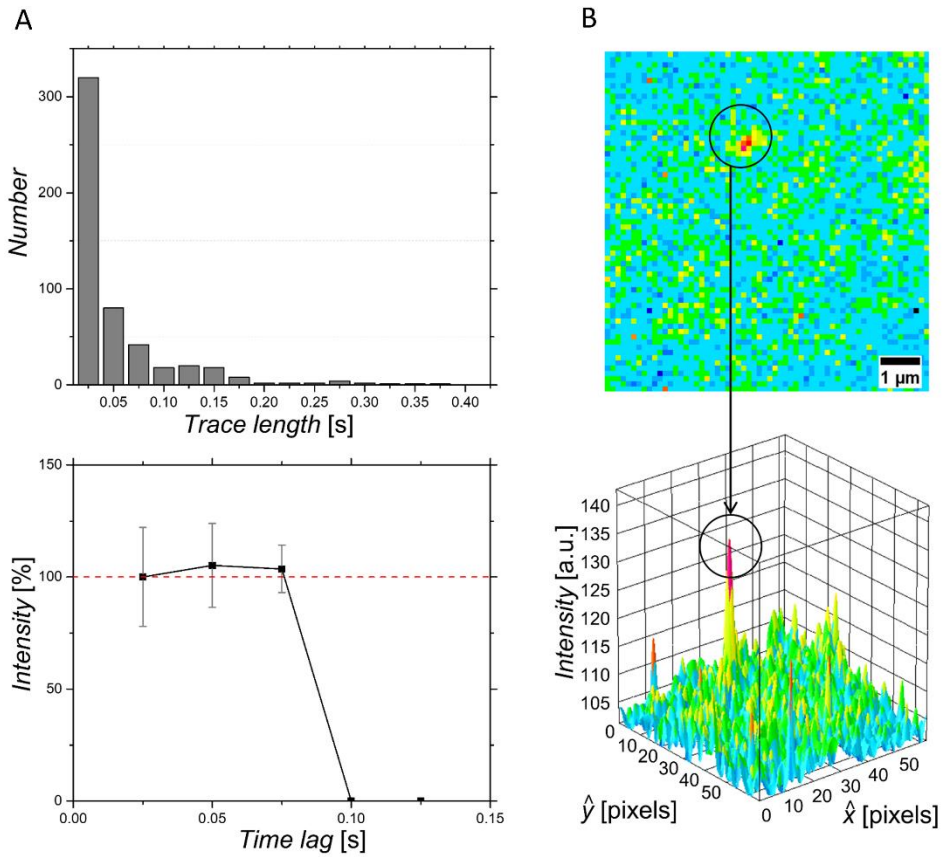

Figure 5.4: Characterization of detected fluorescence signals from individual YFP-GR molecules in fixed HEK293 cells. (A) Top: Bar graph depicting the trace length of 1241 single molecules (521 traces) identified in images of fixed HEK293 cells. The average trace lengths equaled 2.3 frames, and approximately 85% of all traces consisted of 1-3 frames. Bottom: Time trace of the relative single-molecule fluorescence signals determined for all YFP-GR molecules showing a trace length of 1-3 frames. All traces show single-step photobleaching indicating that the signals can indeed be attributed to single YFP-GR molecules. (B) Localization of a single fluorescent molecule. The circle indicates a fluorescence intensity spot that was attributed to an individual YFP molecule based on single-step photobleaching. Image adapted from [1].

5.6 Experiments on live fish

5.6.1 Live imaging using the MuViSPIM setup

To confirm the presence of the YFP-GR molecules and their localization within the nuclei of the embryonic cells, obtaining a global view on the expression levels, a PTU-treated, non-dechorionated 1 dpf (day post-fertilization) embryo was embedded in a 1.5% lmpa cylinder and immersed in the incubation chamber of the MuViSPIM setup (see Chapter 2, section 2.6).

The incubation chamber was filled with E3 medium with tricaine (400 mg L^{-1}) and its temperature was maintained at 26.5°C. Z-stack images were acquired of the embryos for both the YFP and mCherry signals every 15 minutes during 22 hours. A sequential illumination scheme was employed to illuminate both sides of the embryo. Light sheets (at 488 nm for YFP excitation and 561 nm for mCherry excitation) were generated through the coupling of cylindrical lenses (LJ1703RM-A, Thorlabs, focal length 75mm) and air objectives (4X Nikon Plan Fluorite Imaging Objective, 0.13 NA, 17.2 mm WD). The emitted photons were collected through a 10X Nikon CFI Plan Fluorite Objective (0.30 NA, 3.5 mm WD) and an sCMOS camera (OrcaFlash4 v.2, Hamamatsu).

The MuViSPIM setup allowed us to visualize, at 1.3 µm lateral resolution and extended field of view, the development of the whole embryo [31]. The resulting images showed the expression of the YFP-GR molecules and their co-localization with the H2A histone signal within the nuclei of the cells in the embryonic body (Fig. 5.5A-C).

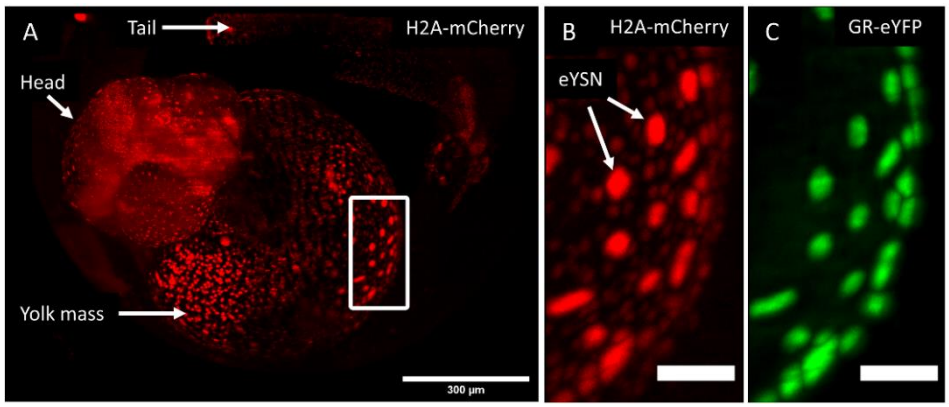

Figure 5.5: Imaging of YFP-GR in a zebrafish embryo through MuViSPIM. (A) Maximum intensity projection of a z-stack obtained using LSFM imaging of a developing 1dpf Tg(actb2:mCherry-H2A) zebrafish embryo injected with a YFP-GR expression vector (only H2A signal shown in A). Scale bar 300 µm. (B-C). Higher magnification image of the highlighted ROI showing the (B) mCherry-H2A and (C) the YFP-GR signal (maximum intensity projections, scale bars 50 µm). Imaging was performed using the MuViSPIM setup. The expression of GR is evident, as well as the localization within the eYSN. Image adapted from [1].

The YFP-GR expression was particularly evident in the external yolk syncytial nuclei (eYSN), which have migrated to cover the yolk sac during gastrulation. They are part of the yolk syncytial layer (YSL), a syncytium containing yolk syncytial nuclei (YSN) that are formed during early embryogenesis as a result of mitotic divisions without cytokinesis. It consists of internal YSN (iYSN, located between the yolk sac and the proper embryo) and eYSN that cover the yolk sac. The YSL plays an important role in meso- and endodermal differentiation, epiboly, and cardiac formation, and it plays a nutritive role during embryonic and larval stages [32–35]. These giant nuclei are transcriptionally very active and have previously been shown to display high levels of transgene expression, which may be due to high transcriptional activity or enhanced transgene replication in these nuclei [36]. We therefore chose these nuclei as the target for our SMM intranuclear analysis, as upon DNA injection their expression levels are significantly higher than those of somatic nuclei.

5.6.2 Live imaging using the LSFSMM setup

Once the selected embryo was mounted into the LSFSMM microscope and positioned in the FoV, a region of interest (ROI) was selected based on the mCherry signal (from the nuclear mCherry-H2A protein, illumination wavelength 568.2 nm, emission filter FF01-620/14-25, Semrock) to localize the nuclei (Fig. 5.6A). The YFP signal (from the YFP-GR protein, illumination wavelength 514.5 nm, emission filter FF01-535/22-25, Semrock) was chosen to check the expression of the fluorescently labeled GR. Once the ROI was so confirmed, a movie of the YFP signal was recorded using continuous illumination and a 25 ms exposure time per frame for 1000-4000 frames, therefore capturing the YFP-GR molecules (Fig. 5.6B-D).

To study the effect of GR activation, embryos were imaged in the absence and presence of the synthetic glucocorticoid dexamethasone (see Appendix C, section C.5 for the experimental design). One zebrafish embryo was selected for both vehicle- and dexamethasone-treated groups, and in each of the selected embryos, three separate areas were imaged. Images exhibited the presence of fluorescence

intensity peaks, which were then attributed to single molecules (Fig. 5.6B-D). A projection of 1000-4000 consecutive frames (depending on the actual dataset) showed the different density of fluorescence intensity peaks between the nucleus and the cytoplasm and served as a matrix for selecting the area of studying protein mobility patterns, so only localizations of nuclear GRs were taken into consideration (Fig. 5.6E). Particle Image Correlation Spectroscopy (PICS) analysis, described in the related publications [37,38], was used for the image analysis. See [1] and Appendix C, section C.6 for the procedure description, and Appendix C, Fig. C.1 for a representative image.

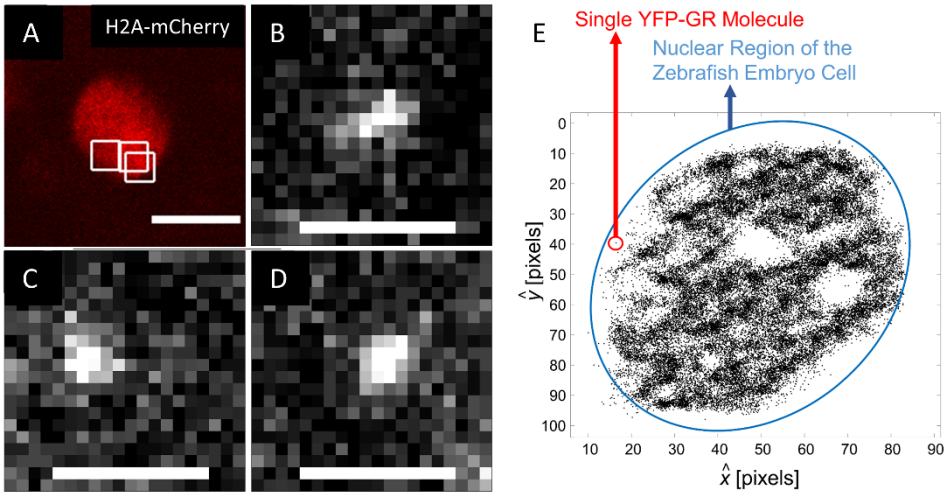

Figure 5.6: Intranuclear imaging through the LSFSMM system. (A) Image of a nuclei in the yolk from a 2dpf live zebrafish embryo obtained using the LSFSMM setup. Only H2A signal shown, scale bar 10 µm. (B-D) Three individual YFP-GR molecules imaged through the LSFSMM setup within the ROIs highlighted in D (white squares), in a 2 dpf zebrafish embryo. Scale bars 2 µm. (E) Localization of single YFP-GR molecules in a nucleus (different from the nucleus shown in A) of a living zebrafish embryo. The image depicts a representative localization of YFP-GR molecules accumulated from 3000 consecutive frames. Nucleoli are visible (white circular regions inside of the nucleus), in which YFP-GR molecules are not found. Images adapted from [1].

5.7 Discussion

5.7.1 LSFSMM setup

Here I have presented the implementation of a custom LSFM platform that permits imaging at SMM sensitivity not only in cultured cells but also in larger and more physiologically relevant biological samples, such as living zebrafish embryos. In a

previous study, TIRF microscopy was used to perform SMM in zebrafish embryos, which enabled SMM analysis in the apical membrane of the outer epidermal cell layer of the embryo [9]. Other related techniques, such as HILO microscopy, would have permitted to reach deeper structures inside these cells, e.g., the nuclei, but the FoV of these techniques is inherently limited. Using the LSFSMM setup presented in this study, we can visualize individual molecules not only at the membrane of the outer cell layers, but also inside cells, and at a relatively large FoV (13.5 x 300 µm). The developed sample mounting system allowed us to easily position specimens in the tight volume between the two objectives, permitting 3D translations and rotations in order to image the areas of interest. The FEP support and the multilayer lmpa mounting permits to sustain samples of various sizes, ranging from cultured cells to zebrafish embryos, with minimal optical aberrations.

Compared to LSFM techniques commonly used for SMM studies [14–19], the presented LSFSMM setup features a simpler optical design: in the excitation path, conventional Gaussian beams are employed, which helps also non-expert users in both alignment and experimental procedures. This illumination path also facilitates the sample mounting, as no additional components (such as a prism [14] or micro-mirrors [15–17]) are inserted. Moreover, the iSPIM configuration permits freeing the top part of the FEP support, minimizing optical aberrations. Finally, the setup is assembled from commercially available parts. Altogether, this implementation will permit other laboratories to adopt the technique as well to further expand the application of LSFM to the sub-cellular level within living organisms such as zebrafish embryos.

We demonstrated the capability of our LSFSMM platform to image individual molecules inside an intact living organism using zebrafish embryos. Our custom-designed sample support and sample-mounting procedure enabled the conduction of experiments on the same 2dpf zebrafish embryos for several hours while leaving the embryo in a healthy condition. At the same time, this procedure helped in

minimizing the optical aberrations due to the mounting medium. After the imaging sessions, we always confirmed that the samples had survived the procedure stress-free, as we were able to let them further develop without mortality or obvious malformations. Moreover, in two experiments we performed imaging on a 2dpf zebrafish embryo, kept it overnight in the microscope, and continued the experiment the next day. These quality control experiments enabled us to conclude that no phototoxicity or adverse developmental effects were induced in the embryos during the imaging session and ensured the suitability of the developed method.

5.7.2 The glucocorticoid receptor mobility patterns

Through the acquired images from the dexamethasone-treated and non-treated live fish and subsequent analysis through the customized software, the mobility pattern of the GR inside the imaged nuclei revealed that these molecules can be divided into a fast and a slow diffusing subpopulation. This subdivision has been observed previously for GR and other transcription factors [39] and has been interpreted as GRs that diffuse freely within the nucleus (fast fraction), and receptors that interact with DNA (slow fraction). Our findings show that the vast majority of the GR molecules belonged to the fast subpopulation, which constituted approximately 90% of the total GR population in the vehicle-, and 77% in the dexamethasone-treated group. However, GR molecules in either of the subpopulations did not move within the entire nuclear environment but were confined to areas with a size of around 1233 nm for the fast subpopulation and 322 nm for the slow subpopulation (which is so close to the spatial resolution of our setup that this subpopulation might as well be considered immobile).

The diffusion coefficients of the two subpopulations equaled 7.90 ± 0.53 $\mu m^2 s^{-1}$ for the fast subpopulation, and 0.78 ± 0.18 $\mu m^2 s^{-1}$ for the slow subpopulation, values that fall well within the previously published ranges [15,39,40].

Finally, the sources of variation in these experiments were analyzed. This procedure revealed that most of the existing variability in in-vivo protein mobility measurements originated from imaging different embryos as well as imaging different cell areas within an individual embryo (see Appendix C, Fig. C.2, and [1]). This suggests that the differences in values of the parameters between individual embryos might stem from an inherent genetic variation between different zebrafish batches.

5.8 Future perspectives

I believe that this implementation permits innovative SMM studies in which the mobility patterns of the single molecules are analyzed not only at a single time point but also over prolonged periods in the same living individual. It would then enable investigating the correlation between sub-cellular molecular dynamics and macro-events such as the developmental stage, metabolism, drug induction, or cell and tissue differentiation. This is thanks to the mounting system, which enables maintaining alive the sample over many hours. To perform this kind of experiment, the imaging chamber is also designed to support a temperature control system ensuring ideal environmental conditions for zebrafish development or other living organisms readily mountable using our setup.

As a practical example, the here developed sample mounting system, with its possibility for 3D translation and rotation, could be used to localize and maintain a zebrafish's eYSN in the imaging FoV during blastula and gastrula periods. At the same time, using the SMM capabilities, one could analyze the intranuclear protein dynamics at different time points, before and during its epibolic migration, studying it in its natural environment and dynamics.

After having enabled performing in-vivo single-molecule imaging using the LSFSMM setup in a plane of the nuclei of living 2dpf zebrafish embryos, it might also be possible to extend the in-vivo SMM studies towards 3D imaging at high spatial-temporal resolution. The integration of wavefront coding techniques in the actual

collection path, such as DID-LSFM (Decoupled Illumination Detection LSFM) [41], would extend the depth of focus of the detection objective, enabling the possibility for the light-sheet to optically scan the volume of interest without the need to refocus the objective. In this way, the dynamics could be observed in the whole volume of the nuclei.

5.9 Additional information

Additional information on methods and protocols used can be found in Appendix C and in [1]. Additional information on the data analysis, statistical analysis, and biological interpretation of the results can be found in [1].

5.10 References

1. M. Bernardello, R. J. Gora, P. Van Hage, G. Castro-Olvera, E. J. Gualda, M. J. M. Schaaf, and P. Loza-Alvarez, "Analysis of intracellular protein dynamics in living zebrafish embryos using light-sheet fluorescence single-molecule microscopy.," Biomed. Opt. Express **12**(10), 6205–6227 (2021).

2. H. Yokota, "Fluorescence microscopy for visualizing single-molecule protein dynamics.," Biochim. Biophys. acta. Gen. Subj. **1864**(2), 129362 (2020).

3. G. S. Harms, L. Cognet, P. H. Lommerse, G. A. Blab, and T. Schmidt, "Autofluorescent proteins in single-molecule research: applications to live cell imaging microscopy.," Biophys. J. **80**(5), 2396–2408 (2001).

4. R. Iino, I. Koyama, and A. Kusumi, "Single molecule imaging of green fluorescent proteins in living cells: E-cadherin forms oligomers on the free cell surface.," Biophys. J. **80**(6), 2667–2677 (2001).

5. F. Luo, G. Qin, T. Xia, and X. Fang, "Single-Molecule Imaging of Protein Interactions and Dynamics.," Annu. Rev. Anal. Chem. (Palo Alto. Calif). **13**(1), 337–361 (2020).

6. H. Li and J. C. Vaughan, "Switchable Fluorophores for Single-Molecule Localization Microscopy.," Chem. Rev. **118**(18), 9412–9454 (2018).

7. D. Axelrod, "Total internal reflection fluorescence microscopy in cell biology.," Traffic **2**(11), 764–774 (2001).

8. M. Tokunaga, N. Imamoto, and K. Sakata-Sogawa, "Highly inclined thin illumination enables clear single-molecule imaging in cells.," Nat. Methods **5**(2), 159–161 (2008).

9. M. J. M. Schaaf, W. J. A. Koopmans, T. Meckel, J. van Noort, B. E. Snaar-Jagalska, T. S. Schmidt, and H. P. Spaink, "Single-molecule microscopy reveals membrane microdomain organization of cells in a living vertebrate.," Biophys. J. **97**(4), 1206–1214 (2009).

10. J. G. Ritter, R. Veith, J.-P. Siebrasse, and U. Kubitscheck, "High-contrast single-particle tracking by selective focal plane illumination microscopy.," Opt. Express **16**(10), 7142–7152 (2008).

11. J.-H. Spille, T. Kaminski, H.-P. Königshoven, and U. Kubitscheck, "Dynamic three-dimensional tracking of single fluorescent nanoparticles deep inside living tissue.," Opt. Express **20**(18), 19697–19707 (2012).

12. B. Yu, J. Yu, W. Li, B. Cao, H. Li, D. Chen, and H. Niu, "Nanoscale three-dimensional single particle tracking by light-sheet-based double-helix point spread function microscopy.," Appl. Opt. **55**(3), 449–453 (2016).

13. J. G. Ritter, R. Veith, A. Veenendaal, J. P. Siebrasse, and U. Kubitscheck, "Light sheet microscopy for single molecule tracking in living tissue.," PLoS One **5**(7), e11639 (2010).

14. Y. Li, Y. Hu, and H. Cang, "Light sheet microscopy for tracking single molecules on the apical surface of living cells.," J. Phys. Chem. B **117**(49), 15503–15511 (2013).

15. J. C. M. Gebhardt, D. M. Suter, R. Roy, Z. W. Zhao, A. R. Chapman, S. Basu, T. Maniatis, and X. S. Xie, "Single-molecule imaging of transcription factor binding to DNA in live mammalian cells.," Nat. Methods **10**(5), 421–426 (2013).

16. F. Greiss, M. Deligiannaki, C. Jung, U. Gaul, and D. Braun, "Single-Molecule Imaging in Living Drosophila Embryos with Reflected Light-Sheet Microscopy.," Biophys. J. **110**(4), 939–946 (2016).

17. M. Reisser, A. Palmer, A. P. Popp, C. Jahn, G. Weidinger, and J. C. M. Gebhardt, "Single-molecule imaging correlates decreasing nuclear volume with increasing TF-chromatin associations during zebrafish development.," Nat. Commun. **9**(1), 5218 (2018).

18. L. Gao, L. Shao, C. D. Higgins, J. S. Poulton, M. Peifer, M. W. Davidson, X. Wu, B. Goldstein, and E. Betzig, "Noninvasive imaging beyond the diffraction limit of 3D dynamics in thickly fluorescent specimens.," Cell **151**(6), 1370–1385 (2012).

19. B.-C. Chen, W. R. Legant, K. Wang, L. Shao, D. E. Milkie, M. W. Davidson, C. Janetopoulos, X. S. Wu, J. A. 3rd Hammer, Z. Liu, B. P. English, Y. Mimori-Kiyosue, D. P. Romero, A. T. Ritter, J. Lippincott-Schwartz, L. Fritz-Laylin, R. D. Mullins, D. M. Mitchell, J. N. Bembenek, A.-C. Reymann, R. Böhme, S. W. Grill, J. T. Wang, G. Seydoux, U. S. Tulu, D. P. Kiehart, and E. Betzig, "Lattice light-sheet microscopy: imaging molecules to embryos at high spatiotemporal resolution.," Science **346**(6208), 1257998 (2014).

20. J. Chen, Z. Zhang, L. Li, B.-C. Chen, A. Revyakin, B. Hajj, W. Legant, M. Dahan, T. Lionnet, E. Betzig, R. Tjian, and Z. Liu, "Single-molecule dynamics of enhanceosome assembly in embryonic stem cells.," Cell **156**(6), 1274–1285 (2014).

21. Z. Liu, W. R. Legant, B.-C. Chen, L. Li, J. B. Grimm, L. D. Lavis, E. Betzig, and R. Tjian, "3D imaging of Sox2 enhancer clusters in embryonic stem cells.," Elife **3**, e04236 (2014).

22. F. Aguet, S. Upadhyayula, R. Gaudin, Y.-Y. Chou, E. Cocucci, K. He, B.-C. Chen, K. Mosaliganti, M. Pasham, W. Skillern, W. R. Legant, T.-L. Liu, G. Findlay, E. Marino, G. Danuser, S. Megason, E. Betzig, and T. Kirchhausen,

"Membrane dynamics of dividing cells imaged by lattice light-sheet microscopy.," Mol. Biol. Cell **27**(22), 3418–3435 (2016).

23. M. Mir, A. Reimer, J. E. Haines, X.-Y. Li, M. Stadler, H. Garcia, M. B. Eisen, and X. Darzacq, "Dense Bicoid hubs accentuate binding along the morphogen gradient.," Genes Dev. **31**(17), 1784–1794 (2017).

24. M. Mir, A. Reimer, M. Stadler, A. Tangara, A. S. Hansen, D. Hockemeyer, M. B. Eisen, H. Garcia, and X. Darzacq, "Single Molecule Imaging in Live Embryos Using Lattice Light-Sheet Microscopy.," Methods Mol. Biol. **1814**, 541–559 (2018).

25. Y. Wu, A. Ghitani, R. Christensen, A. Santella, Z. Du, G. Rondeau, Z. Bao, D. Colón-Ramos, and H. Shroff, "Inverted selective plane illumination microscopy (iSPIM) enables coupled cell identity lineaging and neurodevelopmental imaging in Caenorhabditis elegans.," Proc. Natl. Acad. Sci. U. S. A. **108**(43), 17708–17713 (2011).

26. H. W. 3rd Detrich, M. Westerfield, and L. I. Zon, "Overview of the Zebrafish system.," Methods Cell Biol. **59**, 3–10 (1999).

27. D. Y. Stainier, B. Fouquet, J. N. Chen, K. S. Warren, B. M. Weinstein, S. E. Meiler, M. A. Mohideen, S. C. Neuhauss, L. Solnica-Krezel, A. F. Schier, F. Zwartkruis, D. L. Stemple, J. Malicki, W. Driever, and M. C. Fishman, "Mutations affecting the formation and function of the cardiovascular system in the zebrafish embryo.," Development **123**, 285–292 (1996).

28. T. Schmidt, G. J. Schütz, W. Baumgartner, H. J. Gruber, and H. Schindler, "Imaging of single molecule diffusion.," Proc. Natl. Acad. Sci. U. S. A. **93**(7), 2926–2929 (1996).

29. P. H. M. Lommerse, G. A. Blab, L. Cognet, G. S. Harms, B. E. Snaar-Jagalska, H. P. Spaink, and T. Schmidt, "Single-molecule imaging of the H-ras membrane-anchor reveals domains in the cytoplasmic leaflet of the cell membrane.," Biophys. J. **86**(1 Pt 1), 609–616 (2004).

30. N. Bobroff, "Position measurement with a resolution and noise-limited instrument," Rev. Sci. Instrum. **57**(6), 1152–1157 (1986).

31. U. Krzic, S. Gunther, T. E. Saunders, S. J. Streichan, and L. Hufnagel, "Multiview light-sheet microscope for rapid in toto imaging.," Nat. Methods **9**(7), 730–733 (2012).

32. C. B. Kimmel and R. D. Law, "Cell lineage of zebrafish blastomeres. II. Formation of the yolk syncytial layer.," Dev. Biol. **108**(1), 86–93 (1985).

33. C. B. Kimmel, W. W. Ballard, S. R. Kimmel, B. Ullmann, and T. F. Schilling,

"Stages of embryonic development of the zebrafish.," Dev. Dyn. an Off. Publ. Am. Assoc. Anat. **203**(3), 253–310 (1995).

34. L. Carvalho and C.-P. Heisenberg, "The yolk syncytial layer in early zebrafish development.," Trends Cell Biol. **20**(10), 586–592 (2010).

35. L.-T. Chu, S. H. Fong, I. Kondrychyn, S. L. Loh, Z. Ye, and V. Korzh, "Yolk syncytial layer formation is a failure of cytokinesis mediated by Rock1 function in the early zebrafish embryo.," Biol. Open **1**(8), 747–753 (2012).

36. D. W. Williams, F. Müller, F. L. Lavender, L. Orbán, and N. Maclean, "High transgene activity in the yolk syncytial layer affects quantitative transient expression assays in zebrafish Danio rerio) embryos.," Transgenic Res. **5**(6), 433–442 (1996).

37. S. Semrau and T. Schmidt, "Particle image correlation spectroscopy (PICS): retrieving nanometer-scale correlations from high-density single-molecule position data.," Biophys. J. **92**(2), 613–621 (2007).

38. G. J. Schütz, H. Schindler, and T. Schmidt, "Single-molecule microscopy on model membranes reveals anomalous diffusion.," Biophys. J. **73**(2), 1073–1080 (1997).

39. F. L. Groeneweg, M. E. van Royen, S. Fenz, V. I. P. Keizer, B. Geverts, J. Prins, E. R. de Kloet, A. B. Houtsmuller, T. S. Schmidt, and M. J. M. Schaaf, "Quantitation of glucocorticoid receptor DNA-binding dynamics by single-molecule microscopy and FRAP.," PLoS One **9**(3), e90532 (2014).

40. V. I. P. Keizer, S. Coppola, A. B. Houtsmuller, B. Geverts, M. E. van Royen, T. Schmidt, and M. J. M. Schaaf, "Repetitive switching between DNA-binding modes enables target finding by the glucocorticoid receptor.," J. Cell Sci. **132**(5), (2019).

41. O. E. Olarte, J. Andilla, D. Artigas, and P. Loza-Alvarez, "Decoupled illumination detection in light sheet microscopy for fast volumetric imaging," Optica **2**(8), 702–705 (2015).

Chapter 6: Impact of the conducted studies and future perspectives

In this interdisciplinary thesis, I developed and implemented three different LSFM systems and applied them to a variety of biological samples. The performed studies span spatial-temporal scales from volumetric imaging to high-throughput screenings, until single molecules, contributing to the understanding of specific phenomena and novel applications.

The design and implementation of a multimodal LSFM microscope have been described (see Chapter 2), which allows the use of a single setup for different experimental needs. This is thanks to a modular approach and to the integration of a fluidic circuit within the microscope that enables samples to be mounted easily and without the need of an embedding medium, effectively increasing the imaging throughput. The setup, called Flexi-SPIM [1], can then be used for applications varying from long-term imaging of developing samples, to high-speed recording, until screenings of multiple samples also with the possibility of sample rotation and translation. All imaging modalities profit from the intrinsic advantages of LSFM, such as low photobleaching, high speed, and 3D sectioning capability.

I believe that the described design and the resulting Flexi-SPIM setup can produce an impact on various fields. As an example, HT studies are necessary for different sectors and are mainly performed through widefield microscopy or confocal microscopy. However, these microscopy techniques show their limits when imaging 3D samples, such as embryos or organoids, which are nowadays valuable specimens as they better represent the native biological environment if compared to 2D cellular cultures. These samples are however thick and can be highly scattering. For these reasons, the quality of their imaging would benefit from the intrinsic advantages that LSFM can offer. Though, an HT-LSFM platform that could deal with relatively big samples bringing together flexibility, repeatability, and simple sample mounting was so far missing.

The design implemented through the Flexi-SPIM setup is meant to be the paradigm conjugating LSFM with these HT needs. I believe therefore that its imaging capabilities, especially in the *Hybrid LSFM* mode, could highly benefit fields such as toxicology, drug screening, and personalized medicine. The plate reader offers the needed hardware for interfacing with the commonly used 96-multiwell plate and it can also offer the possibility to automatically administer the drugs to test to the samples. The usage of a fluidic circuit enables easy and fast sample mounting, opening up the possibility of HT screenings. The rotation of the sample allows the imaging of particular features of interest for different samples with the same conditions and repeating it in time keeping the same orientations. The enhanced penetration depth of LSFM offers the possibility of optical access to the inner parts of scattering samples, such as embryos and organoids, enabling their 3D reconstruction. Moreover, through this system and thanks to the possibility of repeating the imaging over time producing time-lapse movies, the development of many living samples can also be monitored over time, through which developmental characterization (such as cell fates) can be performed over various embryos, retrieving the common developmental milestones.

Additionally, I foresee a possible further implementation that would benefit even more the multimodality of the setup. The implemented detection path, when using the *Hybrid LSFM* mode, offers an access port in which a dichroic mirror can be inserted. Through this port, pulsed laser radiation in the near-infrared spectrum could be delivered, which would allow the coupling of LSFM imaging with two-photon laser ablation on the sample under observation. For this scope, a high NA detection objective would be needed to produce the ablation effect. In turn, this implementation would enable continuing the studies presented in this thesis with the possibility of interaction with the sample, even at high-throughput regimes.

From the Flexi-SPIM design, an additional LSFM has been implemented (Chapter 2, section 2.6), which reproduces the *Classic LSFM* modality and focuses on long-term

imaging sessions, making use of an imaging chamber adapted to assure the needed environmental conditions for the development of delicate embryos. These two setups, Flexi-SPIM and MuViSPIM, have been then applied for various biological questions.

Firstly, the microtubules networks (MTN) of the zebrafish's yolk have been studied (see Chapter 3). In the first hours of development, I showed how the external MTN (eMTN) undergoes a progressive and periodic reorganization through a wave-like process that I called Microtubules Organizational Wave (MOW) [3]. I have studied this particular feature by interfering with the cell cycle, and through a custom-made software I developed I could define a global approach, to my knowledge for the first time, to show how MOWs progressively travel from the blastoderm margin toward the vegetal pole. Moreover, an additional internal microtubule network (iMTN) has been identified and visualized over the development of the embryo.

This study, therefore, impacts the related literature by updating the current view on the microtubules network organization and dynamics in the zebrafish embryo. The microtubule network was usually visualized either in fixed samples, in a limited FoV, or for limited time windows. Instead, this application highlights the importance of using an imaging approach, such as LSFM, that enables a global view of live samples to better describe the nature of the microtubule network. In the future, the chemical- or phase-wave nature and the interaction between mitotic waves and MOWs should be further investigated. Particularly interesting would be the application of a temperature gradient to attempt the de-synchronization of the two sides of the embryo, as described in [4] for the frog embryo and proposed for zebrafish in the relative chapter of this thesis. In this way, the cross-talking between different microtubules branches could also be assessed. Finally, the nucleation points of the iMTN should be investigated as well by isolation of the yolk cell from the animal cap and staining for microtubules' organizing centers.

In addition, through the enhanced throughput of the Flexi-SPIM setup, we could also characterize a particular feature, called YCL asters, appearing during the epiboly of embryos from the dclk2-GFP transgenic line (see Chapter 3, section 3.3.6, and [5]). This study showed the applicability of the Flexi-SPIM setup to the characterization of many samples and also define a novel model where it would be possible to study the interaction between microtubules' asters. How microtubules organize and interact in large environments is currently a field of broad interest, which studies are performed in in-vitro systems [5]. This project, instead, provides a valuable in-vivo system on a well-established biological model to which in the future many experimental procedures can be executed to interact with the microtubules asters.

Besides approaching the physical, technical, and biological challenges expressed within the SLN group, this thesis also sought to test the developed microscopy designs on other fields of biology, profiting from the secondments and collaborations established within the ImageInLife network.

Firstly, I applied LSFM to the study of macrophages' recruitment in the zebrafish either after provoking a wound or a bacterial infection [6] (see Chapter 4, section 4.2). This application highlights again the various experimental possibilities and the additional information that can be retrieved by using LSFM instead of LSCM or WM. As a future prospect, the implementation of ablation capabilities on the Flexi-SPIM setup would also benefit this particular application. The wound on the caudal fin here performed manually to examine the macrophages' recruitment could be done through laser microsurgery. In this way, the wound pattern could be computationally defined, on different regions, and highly repeatable. Therefore, high-throughput studies would then be possible on a large number of samples coming from the same batch, i.e. sharing similar genetic backgrounds.

Secondly, I established a specific protocol to insert and maintain alive mouse embryos within the LSFM setup, that allowed to monitor their development for up to 8 hours (see Chapter 4, section 4.4). This was the first critical step to enable the

LSFM imaging in the instruments I developed of such delicate samples. The application is particularly challenging but also offers a highly valuable perspective. The in-vivo recording of the early stages in the mouse embryo development would lead to clarify and eventually confirm the actual theories on the dynamics underlying the striking morphological changes and growth of mammalian specimens. The results obtained so far were promising but unfortunately, the outbreak of the COVID-19 pandemic and related restrictions posed an end to these experiments. Therefore, in the future, those experiments should continue until enabling the recording of three mouse embryos per imaging session, through the developed agarose-wells mounting.

Finally, a third LSFM system was implemented and the designed mounting protocol enabled the imaging of single molecules within the nucleus of 2 dpf zebrafish embryos [7] (see Chapter 5). This study opens up the valuable possibility to extend the application of SMM from the classical cultured cells, to living organisms, i.e. to examine the cell machinery within the native environment. Moreover, the developed protocol and sample mounting system allows for keeping alive for many hours the zebrafish embryo under observation. This in turn enables a possible and interesting new application by correlating macro-events (such as sample development, drug interaction…) with the events happening at the sub-cellular level, through SMM imaging in a time-lapse fashion. The sample mounting system would also enable the translation and rotation of the specimen to follow the FoV of interest during eventual morphological changes.

To produce the work described in this thesis, a total of about 25 TB of raw images have been generated. The large amount of data produced, as described in Chapter 1, is a particular aspect of LSFM and it should be managed carefully. Currently, within the SLN lab, efforts are being made to automatize the saving of a big amount of data and to convert existing images into file formats enabling easy access and visualization in 3D, such as HDF5 and Zarr. Therefore, in the next future, all the raw

images generated here will also be included in this workflow and uploaded to a dedicated data-management platform.

Concluding, from this thesis three different LSFM designs and related setups have been developed. In all those systems particular attention has been put on the sample management, to enable straightforward sample mounting and to maintain alive the specimen over a long period. These designs and the related sample management have enabled the recording and analysis of phenomena not previously described with a global view (such as the MOWs and the YCL asters), to put the basis for LSFM imaging of macrophage recruitment in zebrafish and mouse embryo development, and to extend SMM studies from the cultured cells to living organisms.

6.1 References

1. M. Bernardello, E. J. Gualda, and P. Loza-Alvarez, "Modular multimodal platform for classical and high throughput light sheet microscopy.," Sci. Rep. **12**(1), 1969 (2022).

2. P. J. Keller, A. D. Schmidt, J. Wittbrodt, and E. H. K. Stelzer, "Reconstruction of zebrafish early embryonic development by scanned light sheet microscopy.," Science **322**(5904), 1065–1069 (2008).

3. M. Bernardello, M. Marsal, E. J. Gualda, and P. Loza-Alvarez, "Light-sheet fluorescence microscopy for the in vivo study of microtubule dynamics in the zebrafish embryo," Biomed. Opt. Express **12**(10), 6237–6254 (2021).

4. G. A. Anderson, L. Gelens, J. C. Baker, and J. E. J. Ferrell, "Desynchronizing Embryonic Cell Division Waves Reveals the Robustness of Xenopus laevis Development.," Cell Rep. **21**(1), 37–46 (2017).

5. M. Marsal, M. Bernardello, E. J. Gualda, and P. Loza-Alvarez, "Multiple asters organize the yolk microtubule network during dclk2-GFP zebrafish epiboly," Sci. Rep. 12(1), 4072 (2022).

6. T. Sipka, S. Tairi, M. Bernardello, E. J. Gualda, P. Loza-Alvarez, A. Blanc-Potard, G. Lutfalla, and M. Nguyen-Chi, "Dynamics of macrophage polarization during Salmonella Typhimurium infection in zebrafish," (n.d.).

7. M. Bernardello, R. J. Gora, P. Van Hage, G. Castro-Olvera, E. J. Gualda, M. J. M. Schaaf, and P. Loza-Alvarez, "Analysis of intracellular protein dynamics in living zebrafish embryos using light-sheet fluorescence single-molecule microscopy.," Biomed. Opt. Express **12**(10), 6205–6227 (2021).

Acknowledgments

The work presented in this thesis has been the result of the efforts I have done in the last years, but it would not have been possible without the presence and support of many other people.

Firstly, I would like to thank my supervisor Pablo, for giving me the opportunity to pursue my PhD in such an interdisciplinary lab and for building up a research group made of wonderful people. Besides that, I would like to thank Pablo also for his great flexibility and positive approach, and for guiding me through this scientific path and its ups and down. Another big acknowledgment for help and guidance goes to my co-supervisor Emilio, which taught me from the very beginning the lab life and everything I know about microscopy. Although not officially mentoring me, Maria has guided me in all the biology-related discussions and taught me all wet-lab procedures I know, and I am grateful to her for being tireless, and for her continuous help and support. I would also like to thank Jordi for his assistance on multiple occasions and topics such as hardware management and software programming. Gustavo has been an incredibly valuable lab mate, always available and ready to help in all optics-related doubts and setup adjustments. I would also like to thank Marina for her incredible work in the last years, initially managing many aspects of the lab and now for her example as an unrestrainable researcher. Finally, I would like to thank all SLN lab members, past and present, for the fruitful discussions and for maintaining a great environment within the lab.

Outside the SLN lab, I would like to thank all ICFO's infrastructures and especially the personnel of the biolab, the electronics, and mechanical facilities, that have been essential for providing all the services, instrumentations, and devices needed for this thesis.

Being part of the ImageInLife EU project (imageinlife.eu), I had the opportunity to meet many interesting people such as my peers ESRs and their respective mentors.

This by participating in conferences and training, hosting collaborators at ICFO, and traveling to perform the planned secondments.

A special thank goes to Prof. Georges Lutfalla (University of Montpellier) for taking care of the coordination of the whole project and for being so approachable and available to all of us ESRs. My thank goes also for hosting me in his lab together with Dr. Mai Eva Nguyen Chi (University of Montpellier), who was always very helpful in organizing the secondment and planning the experiments on macrophage recruitment. Prof. Marcel Schaaf (Leiden University) has also been very supportive during our collaboration and my secondment in his group, sharing his scientific expertise and closely following the LSFSMM experiments and subsequent paper preparation. Moreover, I would like to thank the ImageInLife project manager Veronika Peciarova (University of Montpellier) for making it easier for us ESRs to participate in all the training and conferences organized.

In addition, a special thank goes to Svetlana, Radek, Tamara, Valerio, and all the ESRs with whom I shared this path, getting to know each other and sharing ideas, doubts, and mutual support. I would also like to thank Stefano, Estefano, Francesco, Giuseppe, and Laura for the laughs and friendship.

Finally, outside the lab but always firmly present, I deeply thank Federica, my parents, my grandparents, my brother, and my sisters for their continuous support.

Appendix A: Solutions for multimodal LSFM in-vivo imaging

This chapter contains content entirely reproduced or adapted from the article: Bernardello, M., Gualda, E.J. & Loza-Alvarez, P. Modular multimodal platform for classical and high throughput light sheet microscopy. Sci Rep 12, 1969 (2022). https://doi.org/10.1038/s41598-022-05940-2

A.1 Flexi-SPIM: Illumination path

Four CW lasers with excitation wavelengths of 405, 488, 561 and 637 nm (Cobolt, MLD 50 mW, MLD 50 mW, DPL 100 mW and MLD 150 mW, respectively) are used for excitation. In its basic implementation (single side excitation), the illumination arm uses a telescope system composed of two achromatic doublets (Thorlabs, AC254-050-A-ML, f=50 mm, and AC254-200-A-ML, f=200 mm) to expand the beams. Subsequently, the air-objective (either Nikon 4x PlanFluor NA 0.13, or Nikon 10x PlanFluor NA 0.3) is mounted on a manual translation mount (Thorlabs, SM1Z), allowing fine positioning of the beam waist. At the back focal plane of the objective, a circular slit is added in order to adjust the illuminating numerical aperture and thus, the light-sheet thickness along the camera FoV. Double side illumination is achieved by duplicating the above-described elements and adding a 50/50 beam-splitter cube (Thorlabs, CCM1-BS013) and a relay lens set with two achromatic lenses (Thorlabs, AC254-075-A-ML, f=75 mm) at the entering of the illumination arms. An Arduino controlled servo motor inserted in each illumination arm works as shutter, allowing the selection of the illumination side.

The system can work in SPIM or DSLM configurations. In SPIM configuration, a 150 mm round achromatic cylindrical lens (ACY254-150-A) is mounted on each illumination arm in a cage rotational mount (CRM1). Additionally, an adjustable slit (Thorlabs, VA100C) will allow adjusting the light sheet height at the illuminated plane. In DSLM configuration (Fig. A.1) the light sheet is created by a pair of galvanometric mirrors (Thorlabs, GVSM002). The two galvanometric mirrors are mounted independently, so perfect conjugation of optical planes will be achieved. Two achromatic doublets (Thorlabs, AC254-030-A-ML, f= 30 mm) projects the pivoting beam from the first onto the second galvanometric mirror. Two identical achromatic doublets perform the same operation between the second galvanometric mirror and the centre of the 50:50 beam splitter cube, which in turn results conjugated with the back focal aperture of the illumination objectives. The DSLM module could be easily attached to the SPIM illumination block using four rod

adapters (Thorlabs, ERSCA). The whole block is supported with a mounting post (Thorlabs, P200) and a clamp system (CH1530/M), ensuring stability and modularity. All deflections of the illumination beams are performed through elliptical mirrors (Thorlabs PFE10-G01) mounted in right-angle cage mounts (Thorlabs, KCB1E).

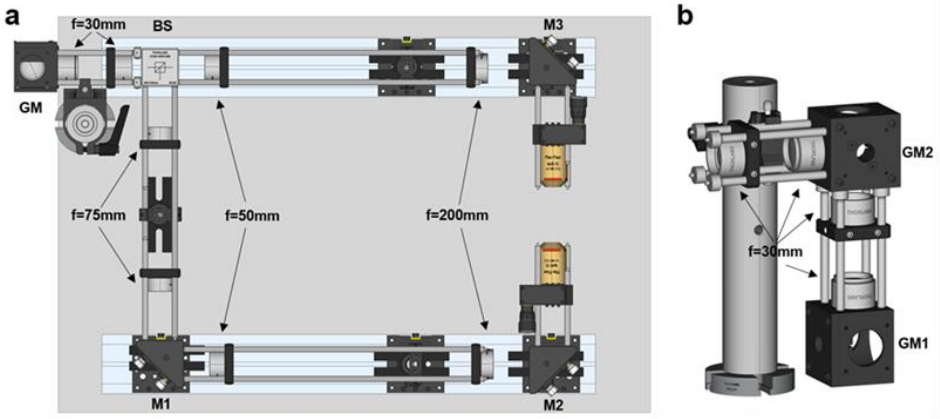

Figure A.1: Description of the illumination path and DSLM module. (a) Detailed scheme of the illumination arms with double side illumination. M=Mirror, BS=Beam splitter, GM=Galvanometric scanning module. (b) DSLM attachment integrated by two conjugated galvanometric mirrors (GM), through four achromatic lenses (f=30 mm). GM1 is conjugated with GM2, and this one with the center of the beam splitter (BS). Figure adapted from [1].

A.2 Flexi-SPIM: Light-sheet thickness and illumination FoV measurements

The light-sheet thickness was determined by measuring the waist diameter from an image of a focused beam, at different aperture diameters (R1 to R5) which modulate the illuminating NA. The values are reported in Fig. A.2, and they were obtained as follow. The Gaussian beam appears propagating along the horizontal direction of the image and the intensity profile at its waist (perpendicularly to the propagation direction) was extracted through FIJI, and Gaussian fitted. The FWHM diameter, representing the LS thickness, was calculated from the standard deviation of the Gaussian fit as $d_{waist} = FWHM_{waist} = 2.355\ \sigma$. From this value, the diameter of the beam at the Rayleigh range was calculated as $d_{rayleigh} = \sqrt{2} \cdot d_{waist}$. Through a custom-made FIJI macro, the intensity profile of each column of the image was extracted and sent to the FIJI built-in Gaussian fit, retrieving for each column the FWHM of the Gaussian peak as described above. The code for this macro is available

upon request. This array of values represents the FWHM beam diameter as function of the propagating distance. The number of columns presenting values smaller than $d_{rayleigh}$ were counted and converted from pixel to micrometers (pixel size is 0.65 µm), delivering the illumination FoV.

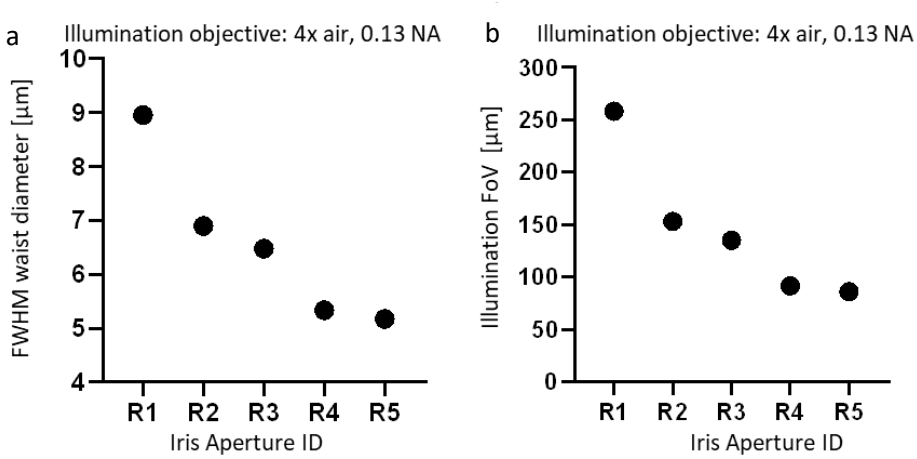

Figure A.2: (a) The FWHM waist diameter of the illumination beam (i.e. the thickness of the light sheet) as a function of the iris aperture, defined by the index R1 (the smallest) to R5 (the largest). (b) The illumination FoV (i.e. the double of the Rayleigh range of a Gaussian beam) as a function of the iris aperture, defined by the index R1 (the smallest) to R5 (the largest). Image adapted from [1].

A.3 Flexi-SPIM: Detection path

Different detection objectives are compatible with our design, both water dipping (Olympus UMPLFLN10XW NA 0.3, UMPLFLN20XW NA 0.5, or Nikon 10x 0.3) or air objective (Nikon 10x 0.3). On each detection arm an achromatic doublet (AC508-200-A-ML, f=200 mm, or AC508-180-A-ML, f=180 mm depending on the objective brand, and AC254-200-A-ML, f=200 mm for Hybrid Mode arm, from Thorlabs) is used as tube lens. In the path selector component, implemented through a cage cube (C6W, Thorlabs), the element inserted is either a knife-edge prism (MRAK25-P01, Thorlabs), a rotating mirror (PFR10-P01 Thorlabs on a Nanotec, L4018S1204-M6 stepper motor), or no elements. After the path selection, the collected radiation is passing through the emission filter (either 520/15, 590/50, 638LP, from Chroma and Semrock) inserted into a motorized filter wheel (FW102C, Thorlabs).

Subsequently, the images form onto the chip of a Hamamatsu Orca Flash4.0 sCMOS camera. For the Raman module a tunable filter was used (Semrock, TBP01-790/12) mounted on an Arduino controlled stepper motor (Nanotec, L4018S1204-M6). All deflections of the collected beams are performed through elliptical mirrors (Thorlabs PFE10-G01) mounted in right-angle cage mounts (Thorlabs, KCB1E).

A.4 Resolution measurements

Lateral and axial resolutions obtained from two different detection objectives (Nikon 10x, 0.3 NA and Olympus 20x, 0.5 NA, leading to a pixel size of 433 nm and 195 nm respectively) were measured in two different mounting condition (Fig. A.3). In the first condition, sub-diffraction fluorescent beads (180 nm in diameter) were embedded in a 1.5% lmpa (low melting point agarose) cylinder, which is the usual mounting for the *Classic LSFM* configuration, and scanned across the light-sheet with a 100 nm z-step. In the second condition, in order to mimic the mounting used for the *Flow LSFM* and *Hybrid LSFM*, the same beads were inserted into a FEP tube (1.6 mm OD x 1 mm ID, the same used for the experiments on embryos). However, while in the real application no agarose is present in the FEP tube to constraint the sample, to maintain the beads steady during z-stack acquisition I embedded them into a low agarose concentration (0.5% lmpa) inside the FEP tube. For each condition, 10 different beads were considered. The lateral resolutions were measured by retrieving the intensity profiles in both lateral directions (x and y) and by fitting them through a Gaussian function. The FWHMs, corresponding to the actual resolutions, were calculated as $R_{lateral} = \mathrm{FWHM}_{lateral} = 2.355\,\sigma$, were σ is the variance of the Gaussian fit. After reslicing in z the images of the same beads, the same procedure was applied to the z-axis profile, obtaining the axial resolutions as FWHM of the Gaussian fit.

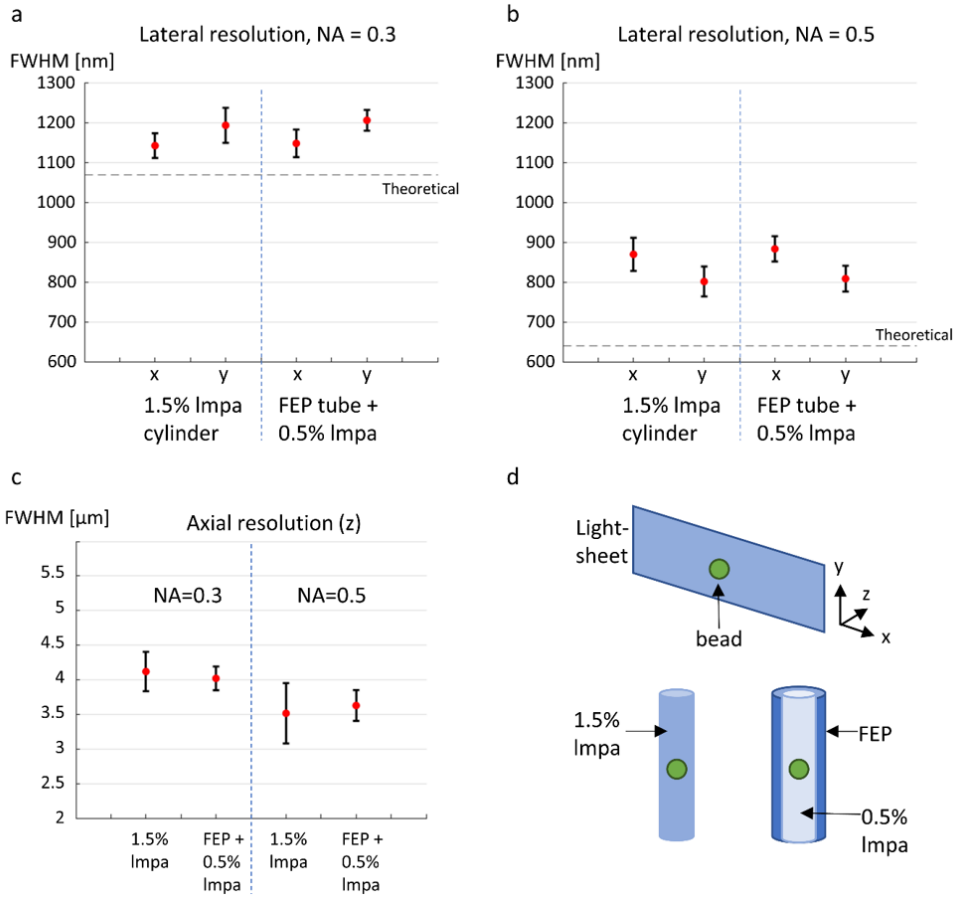

Figure A.3: Resolution measurements with different mounting configurations. (a) The lateral resolution measured along (x) and perpendicularly (y) to the light-sheet propagation direction through a 0.3 NA objective (pixel size = 433 nm). FWHM values are obtained by imaging of sub-diffraction beads embedded in a 1.5% lmpa (low melting point agarose) cylinder (left) and in 0.5% lmpa within a 1.6mm OD x 1mm ID FEP tube. The dotted line represents the theoretical resolution, which equals 1067.5 nm. (b) The lateral resolution measured through a 0.5 NA objective (pixel size = 195 nm) with the same conditions as (a). The dotted line represents the theoretical resolution, which equals 640.5 nm. (c) Axial FWHM values obtained for the same conditions as in (a), for 0.3 and 0.5 NA objectives. The shown values are the average FWHMs, error bars represent ± standard deviations, N=10 beads for each condition. (d) Schematic of the coordinate system and of the mounting solutions of the beads for these measurements. Note that in the real application, when using the FEP tube mounting, no agarose embedding is needed. However, in order to maintain the beads steady during imaging, they were embedded in 0.5% lmpa. As shown, the introduction of the embedding medium between the objective and the sample (either lmpa or FEP tube) slightly degrade the resolutions with respect to the theoretical ones, but do not interfere with the capability of imaging at cellular levels. Image reproduced from [1].

A.5 Flexi-SPIM: Sample scanning

Depending on the chosen modality (*Classic LSFM, Flow LSFM, Hybrid LSFM*), sample scanning is performed differently. When samples are mounted in the *Classic LSFM*

configuration, the embedding cylinder is attached to a linear stepper motor stage (Thorlabs, LNR25ZFS) for sample translation across the light-sheet plane, and an Arduino controlled stepper motor (Nanotec, L4018S1204-M6) for sample rotation. When the *Flow LSFM* mode is used, samples are loaded into the FEP tube (Adtech Polymer Engineering Ltd.) circuit and flowed through the light sheet using a syringe pump (Tecan, Cavro Centris). The used specialized and programmable syringe pump permits to set the needed flow rate, from 5ml/sec until 5 nl/sec, and the quantity of liquid displaced with a resolution of 1.4 nl (derived from the datasheet). In the *Flow LSFM* mode, the sample is continuously moving along the tube at the programmed flow rate, but this movement is slow enough in respect to the exposure time to avoid image blurring. In both *Classic* and *Flow LSFM* the light-sheet is created perpendicular to the optical table. In the *Hybrid LSFM* mode the scanning of the sample is performed by translation of the whole chamber containing the sample with a motor (PI M-501.1DG) through a fixed horizontal light sheet plane. Alternatively, the sample is kept static while the light sheet is scanned vertically and it is synchronized with the vertical movement of the detection objective, mounted on a piezo motor (PiezoConcept PiFoc). The imaging chamber includes a blue LED to permit brightfield imaging, and it enables the automatic detection of the passage of the sample under the FoV of the collection objective. Two Arduino controlled stepper motors (Nanotec, L4018S1204-M6) connected to the “imaging tube” permit the rotation of the sample. The entire HT chamber is placed at 45 degrees respect to the illumination objectives.

A.6 Arduino-based controller

The Flexi-SPIM setup features different hardware components that, thanks to a single LabVIEW-based homemade software, work in synergy. In order to interact with these components, we use an Arduino UNO board, which is connected via USB to our workstation, and is integrated in the LabVIEW software through the LIFA (LabVIEW Interface for Arduino) interface, provided by National Instrument (Fig. A.4a).

In order to control the four stepper motors (2 for the imaging chamber, and 2 for the MPR), the controller includes four Big Easy Drivers and two power supplies at +12V DC, 3.3 A. The controller also includes one power source at +5V DC, which supply the needed power for all the servomotors (MPR and shutters) and the LED included in the imaging chamber.

A principle schematic of the connections is shown in Fig. A.4a. The front panel layout of the controller is divided in 4 different areas, respect to the specific function and devices to be controlled, as shown in Fig. A.4b. These devices are:

- 1x stepper motor for sample rotation for Classic LSFM mode (or tunable filter)
- 1x stepper motor for the alternate detection in Classic LSFM mode
- 2x servomotors used as shutters for the alternate-illumination configuration.
- 2x stepper motors and 1x LED of HT Chamber for Hybrid LSFM mode.
- 2x stepper motors, 1x servomotor and 2x switches that act as contact sensors for the multi-well plate reader platform.

The Arduino UNO board is the central part of the controller. Through its I/O pins, it provides the digital control of the devices. For a general stepper motor however, an additional driver is required, as the Arduino Board cannot provide the needed power supply. We choose the Big Easy Driver v1.2 (Fig. A.4c) from by Brian Schmalz (Schmalz Haus LLC).

The two motors relative to the HT Chamber share the same Arduino pins for ENABLE, STEP, and DIR. This assures that the two motors receive the same signal at the same time, moving synchronously. However, the connections between the two coils of the motors and the A and B pairs of pins of the drivers are inverted between each other. In this way, the two motors move in opposite directions, as needed for the HT Chamber. The stepper motor drivers relative to the XYZ platform only share the ENABLE pin, as they supply two independent motors. During our experiment we

always used the 1/16 micro-step resolution, which permits a smoother movement of the motor.

While the servomotors signal pins are directly connected to the output pins of the Arduino board, the LED is connected to a potentiometer and a MOSFET. Through the potentiometer (10 KΩ) we can regulate the correct intensity of the LED, while the transistor closes the circuit, and then powers the LED, when the GATE pin is triggered, through a digital output pin of the Arduino. Two Arduino digital pins are also used as input pins, to detect the status change of the switches implemented in the XYZ Platform, which indicate the Home position of the Platform. A resuming table of the Arduino pins needed is shown in Fig. A.4e. Additionally, some pins of the Arduino are left free, which could be further used for future development and integration (e.g. temperature sensor).

Thanks to the LIFA (LabVIEW Interface For Arduino) code, developed by National Instruments, we can communicate with the Arduino board through LabVIEW and dedicated VIs (Virtual Instruments). In our application we need only digital signals, thus we need to use some analogue pins of the Arduino board as digital pins. Although this is possible when programming the Arduino through its own text-based code, in LabVIEW we need to modify a default setting of the “Check For Pin Out Of Range” VI of the LIFA interface. In the “Uno, Default” case, “Digital” sub-case, changing the Num Pins constant to a value of 20 will let the usual analogue pins work as digital, as shown in Fig. A.4f.

a

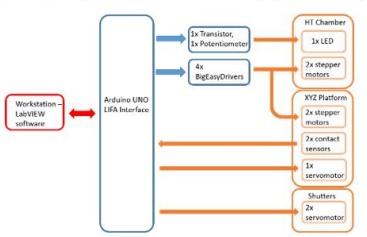

b

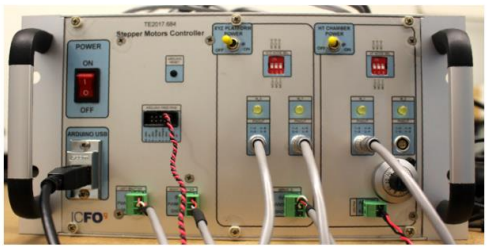

c

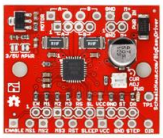

d

MS1	MS2	MS3	Micro-step Resolution
0	0	0	1 Step
1	0	0	½ Step
0	1	0	¼ Step
1	1	0	1/8 Step
1	1	1	1/16 Step

e

Hardware	Arduino Pin	Setting
SHUTTERS		
RIGHT SHUTTER	6	OUTPUT
LEFT SHUTTER	5	OUTPUT
XYZ PLATFORM		
XY ENABLE	14	OUTPUT
X STEP	13	OUTPUT
X DIR	12	OUTPUT
X SWITCH	9	INPUT
Y STEP	7	OUTPUT
Y DIR	8	OUTPUT
Y SWITCH	10	INPUT
HT CHAMBER		
HT ENABLE	17	OUTPUT
HT STEP	15	OUTPUT
HT DIR	16	OUTPUT
HT LED	11	OUTPUT

f

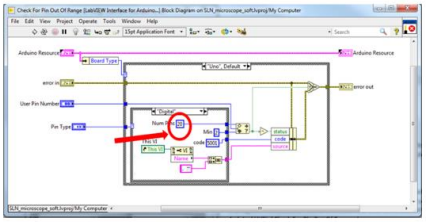

Figure A.4: Arduino based controller. (a) Principle schematic of the Arduino-controller application. (b) Front panel of the Arduino-controller. (c) Upper view of the Big Easy Driver (d) Micro-stepping resolution for given values of MS1, MS2, MS3. (e) Arduino-controller pinout. (f) How to modify the default setting of the "Check For Pin Out Of Range" VI of the LIFA interface. Image reproduced from [1].

A.7 Flexi-SPIM: Multiwell plate reader (MPR)

We implemented a multiwell plate reader (MPR) system (Fig. A.5), in order to automatize the loading procedure in the *Flow LSFM* and *Hybrid LSFM* modes. These imaging modalities, instead of using low melting point agarose, permits to bring the sample under the imaged field of view along a FEP tube, connected to a programmable syringe pump. The MPR system was adapted from an open-source project called XY Table developed by Geir Andersen (https://www.robotshop.com/letsmakerobots/xy-table).

The main aim of the MPR is to automatize the loading process, thus increasing the number of samples imaged, for high-throughput application. It consists of 3D printed components connected through metallic rails. Two stepper motors provide the possibility to move the translational part in the horizontal (xy) plane, while a servomotor displaces in the vertical direction (z) the tip of the FEP tube. On the base

of the platform, a 96-multiwell plate, commonly used in biological laboratories, is placed and fixed. The MPR is connected to the Arduino-based controller, which provides the power and signals to the motors, reads the two switches that sense the "home" position of the platform, and permits the customization and automation of the protocols. A custom-made LabVIEW interface allows easy control of all the elements of the MPR, as well the automation of complex protocols. In this way, the MPR is able to move the loading head above the multiwell plate in order to reach the well of interest, place the tip of the FEP tube into the selected well, and let the pump aspire the sample. Additionally, a webcam is placed under the transparent platform base, in order to detect if the loading of the sample has been successful. If not, force the MPR to repeat the sample loading protocol.

The MPR can also be used to implement more complex or diversified protocols, like loading and, after imaging, sorting of the sample in specific well, or even direct and automated drug delivery to specific wells.

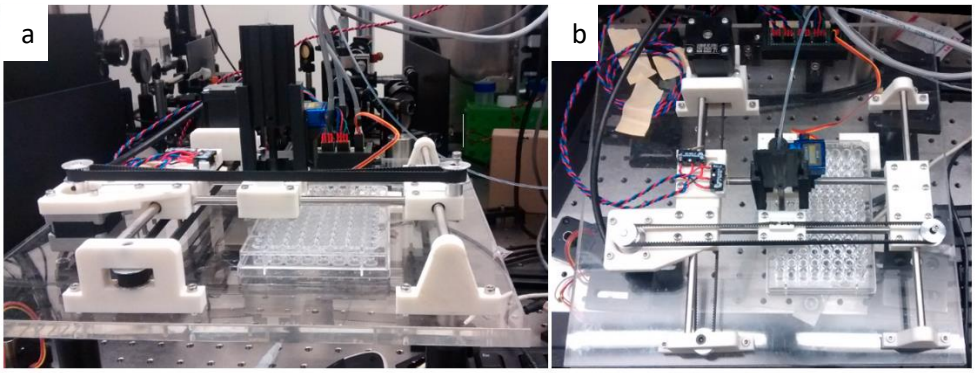

Figure A.5: Multiwell Plate Reader (MPR). (a) Lateral view of the MPR and (b) Top view of the MPR. Image reproduced from [1].

A.8 HT screenings

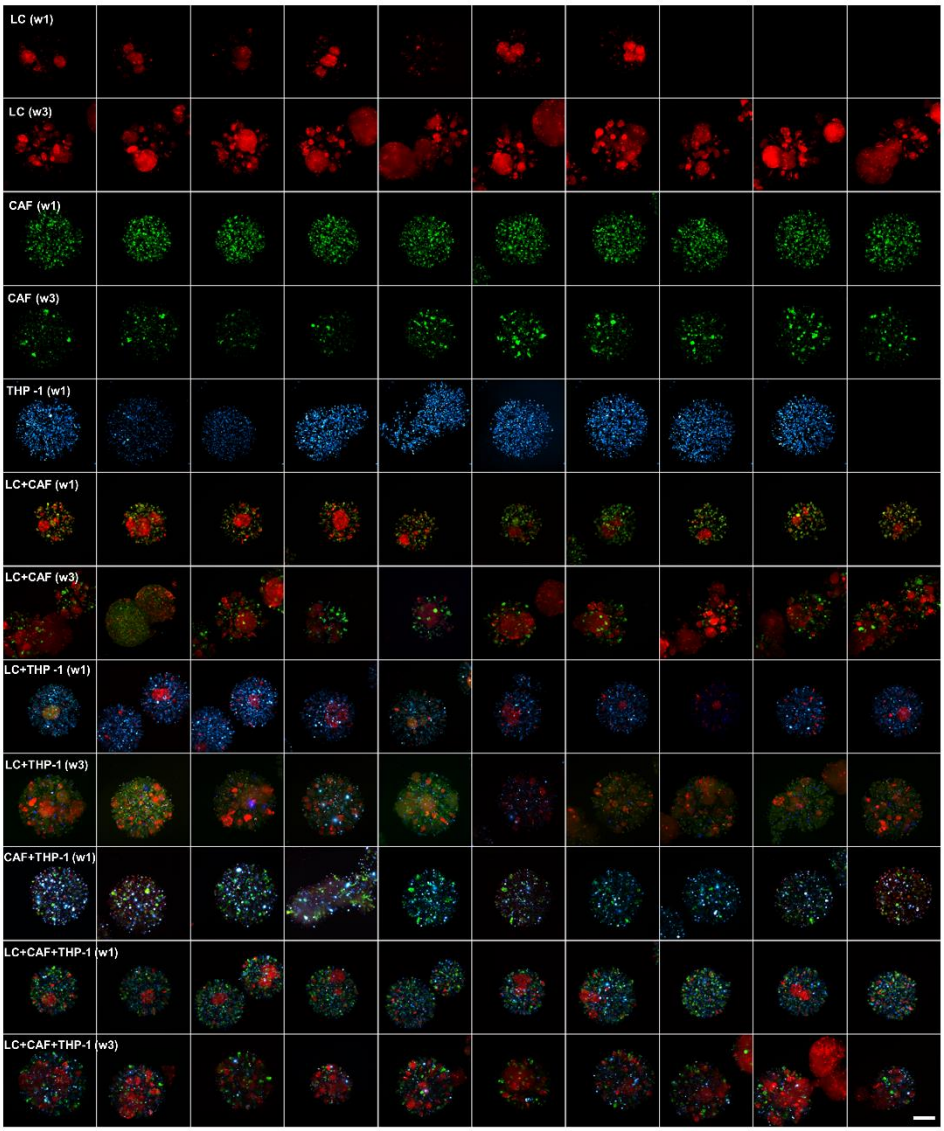

Figure A.6: HT analysis of co-cultured 3D samples. Different complex 3D culture models were evaluated in a semi-automatic manner using the Hybrid LSFM mode. During the experiment we image different 3D mono (rows 1-5), different 2 co-culture (rows 6-10) and 3 co-culture models (rows 11-12) including tumour cell spheroids of non-small cell lung carcinoma (LC) (tdTomato, red), cancer associated fibroblasts (CAF) (GFP, green) and a monocytic cell line (THP-1) (Cell tracker™, blue) on embedded on alginate capsules. For each group, except for monoculture of THP-1 (row 5) and co-culture of CAF-THP-1 (row 8), first row display results at week #1, while second row correspond to week #3. Scale bar 300 µm. Image reproduced from [1].

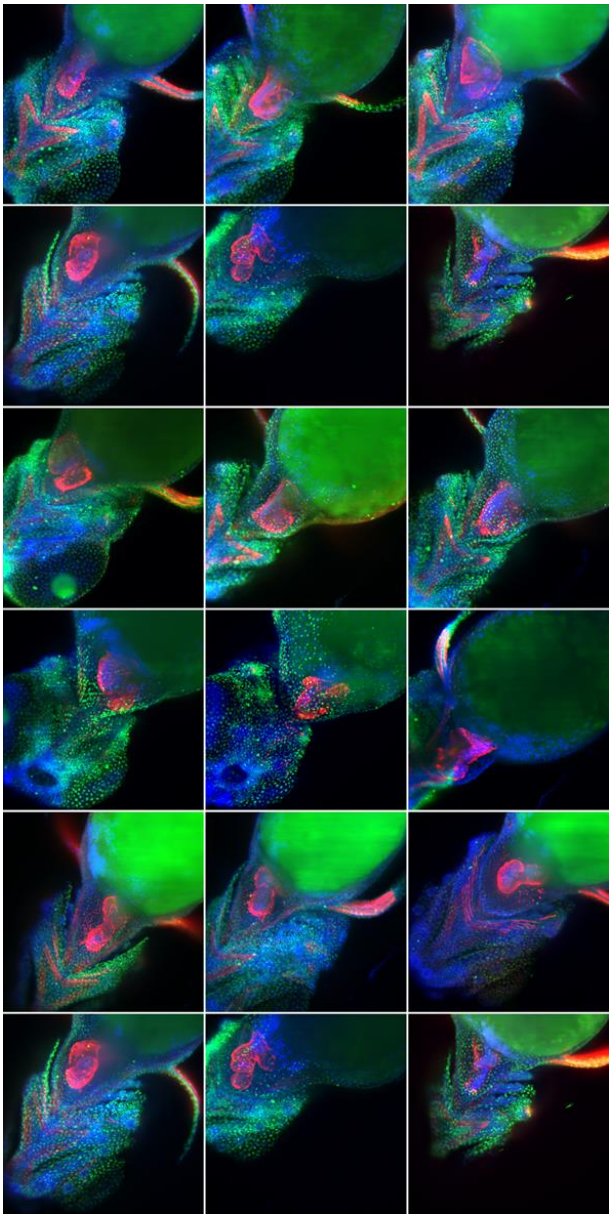

Figure A.7: High-Throughput screen of fixed immunostained zebrafish larvae. Multicolor maximum projection of eighteen 72hpf zebrafish larvae measured with the Hybrid LSFM mode with a 20x water dipping objective. Nuclei were stained with DAPI (blue), while myosin light chain (myl7) was conjugated with Alexa fluor 488 (red) and histone 3 acetylated in lysine 9 (H3K9Ac) was conjugated with Alexa Fluor 568 (green). Larvae pigmentation has been removed with 6% H202. Zebrafish heart was reoriented towards the detection objective using the High-Throughput Imaging Chamber with rotation capability. Scale bar 100 µm. Image reproduced from [1].

A.9 Flexi-SPIM: Computer hardware and software

The Flexi-SPIM microscope features a custom-made software based on LabVIEW (National Instruments). This software permits the user to have access to the settings of the various devices, on a single graphic interface. The controller, and in consequence the settings and the regulation of imaging chamber, MPR, and shutters, have been integrated in this software. Experiments were run on a Dell Precision T7810 workstation, with 64 GB of RAM and equipped with a frame grabber (Active Silicon) for the sCMOS camera and digital-analogue card (National Instruments, PCIe-6363) providing up to 4 analogue outputs (two for the galvo and one for the piezo motor).

A.10 Zebrafish

All experiments involving zebrafish were carried in compliance with protocols approved by ICFO and by Comissió d'Experimentació Animal, Direcció General de Polítiques Ambientals i Medi Natural of the Departament de Territori i Sostenibilitat, Generalitat de Catalunya (Spain). "Neural activity recording in zebrafish larvae" (Expedient: FUE-2019-01161091; ID: PD8GZTVV7; Project: 10716).

A.11 3D cell cultures

Complex 3D culture models embedded on alginate capsules including different combinations of tumour cell spheroids of non-small cell lung carcinoma (LC), cancer associated fibroblasts (CAF) and a monocytic cell line (THP-1) were generated from the collaborators following protocols described in [2].

A.12 Videos

All videos are available at https://www.nature.com/articles/s41598-022-05940-2#Sec22

A.12.1 Video A.1

Zebrafish embryo development during epiboly visualized through the Classic LSFM mode. Microtubules are labels through dclk:GFP transgenic line. The four views correspond to the maximum intensity projections for the double illumination/double detection scheme.

A.12.2 Video A.2

Development of a zebrafish embryo expressing GFP:actin visualized through the Classic LSFM. (a) Both sides of the sample are acquired simultaneously with a single camera, after the two detection views are fused into a single image in the knife-edge mirror. In this example, illumination is performed simultaneously from both sides. (b) The two detected views can be easily fused into a single dataset that preserve the more relevant information of each view. (c) Colour depth map representation of the previous fused dataset.

A.12.3 Video A.3

Maximum intensity projection of a GFP:Myosin zebrafish embryo development (gray), with injected mCherry:Myosin bleb cells (orange). Images were acquired with the Classic LSFM mode, with simultaneous dual side illumination and dual side detection, allowing to visualize the whole embryo sphere. The total movie consists of 150 time points every 2 minutes.

A.12.4 Video A.4

Using the Flow LSFM mode, an entire Fli-GFP zebrafish embryo can be visualized as it flows through the system. The front view (top panel) and the back view (middle panel) are simultaneously registered on the same camera chip. The two views can be subsequently fused together (bottom panel).

A.12.5 Video A.5

Maximum intensity projection of macrophage migration on the zebrafish head. The sample was monitored using the Hybrid LSFM mode, including sequential dual side illumination and two channel acquisitions, autofluorescence (green filter) and macrophage expressing arg2:mCherry (red filter) (upper panel). For each time point, four different 100 images stacks were acquired at 10 fps (100 ms exposure time) over a range of 300 microns (zstep=3 microns). In the lower panel only macrophages are displayed. The total movie consists of 50 time points every 10 minutes.

A.12.6 Video A.6

Maximum intensity projection of the zebrafish caudal fin expressing arg2:mCherry after provoking a wound at the tail. Macrophages were monitored with the Hybrid LSFM mode with sequential dual side illumination and two channel acquisitions at high speed (0.5 vol/sec, with piezo refocusing). The total movie consist in 134 time points every 2 minutes. For each time point, four different 100 images stacks were acquired at 50 fps (20 ms exposure time) over a range of 200 microns (zstep=2 microns). Here only red channel is displayed.

A.12.7 Video A.7

Zebrafish brain activity monitored in 6 days post-fertilization larvae expressing GCamP6s pan-neuronally with the Hybrid LSFM mode and piezo refocusing at 1 vol/sec, using a triangular wave. In this movie we only display one direction of the scanned wave, i.e. recorded at 0.5 vol/sec: slow motion visualization of the brain volume; a single plane time-lapse (one image every 2 second); the maximum intensity projection time-lapse; depth colour coded maximum intensity projection. For each time point, 50 images stacks were acquired at 100 fps (10 ms exposure time) over a range of 300 microns (zstep=6 microns).

A.13 Acknowledgments

The work described has profited financial support from the Spanish Ministerio de Economía y Competitividad (MINECO) through the “Severo Ochoa” program for Centres of Excellence in R&D (CEX2019-000910-S), MINECO/FEDER Ramón y Cajal program (RYC-2015-17935); Laserlab-Europe EU-H2020 GA no. 871124, Fundació Privada Cellex, Fundación Mig-Puig and from Generalitat de Catalunya through the CERCA program; European Union’s Horizon 2020 Framework Programme (H2020 Marie Skłodowska-Curie Innovative Training Networks ImageInLife N. 721537). Verena Ruprecht (CRG-Center of Genomic Regulation, Barcelona), Paz Herráez (Universidad de León), Ester Antón-Galindo and Noelia Fernández-Castillo (Universitat de Barcelona), Marymar Becerra (Universidad Nacional Autónoma de México), Georges Lutfalla, Mai Nguyen Chi, and Tamara Sipka (Université de

Montpellier), Catarina Brito (ITQB/IBEQ, Lisbon), Antonia Weberling and Magdalena Zernicka-Goetz (University of Cambridge), and Corinne Lorenzo (ITAV – CNRS, Toulouse) are acknowledged for providing some of the shown samples.

A.14 References

1. M. Bernardello, E. J. Gualda, and P. Loza-Alvarez, "Modular multimodal platform for classical and high throughput light sheet microscopy.," Sci. Rep. **12**(1), 1969 (2022).

2. S. P. Rebelo, C. Pinto, T. R. Martins, N. Harrer, M. F. Estrada, P. Loza-Alvarez, J. Cabeçadas, P. M. Alves, E. J. Gualda, W. Sommergruber, and C. Brito, "3D-3-culture: A tool to unveil macrophage plasticity in the tumour microenvironment.," Biomaterials **163**, 185–197 (2018).

Appendix B: Yolk's microtubule dynamics in the early zebrafish embryo

This chapter contains content entirely reproduced or adapted from the article [1]: M. Bernardello, M. Marsal, E. J. Gualda, and P. Loza-Alvarez, "Light-sheet fluorescence microscopy for the in vivo study of microtubule dynamics in the zebrafish embryo," Biomed. Opt. Express 12, 6237-6254 (2021).

B.1 Zebrafish breeding, sample mounting, and imaging procedures

Tg(XlEef1a1:dclk2-GFP) [2] (noted as dclk2-GFP) females were crossed with AB WT males and the embryos collected and maintained in E3 medium, and staged as in [3]. Embryos were then imaged by means of two different LSFM setups: the MuViSPIM and the FlexiSPIM in the *Hybrid LSFM* modality (see Chapter 2).

In order to be mounted in the MuViSPIM setup (shown in Fig. B.1A-B), one embryo was transferred to a petri-dish and left in a small drop of water. A 1.5% low melting agarose solution in E3, previously heated up to 70°, was left to cool down until approx. 40°. While still liquid, the lmpa solution was poured in the petri-dish to completely cover the embryo. The lmpa solution and the embryo were aspired within a glass capillary through a plunger. After solidification, the lmpa cylinder was extruded and cut until approximately 1 mm from the embryo position. Other 5 mm, in which the embryo was placed, were extruded from the glass capillary. The microscope xyz stage permits the insertion and fixation of the glass capillary in such a way that the extruded agarose falls within the FoV of the objective. Note that the embryo was not dechorionated, i.e. no mechanical constriction was induced by the 1.5% lmpa cylinder. The incubation chamber was filled with 17 ml of E3 medium.

In the FlexiSPIM setup, in the *Hybrid LSFM* mode (shown in Fig. B.1C-D), a fluidic circuit (1.5 m long) composed of a FEP tube filled with E3 medium crosses the incubation chamber at 45° with respect to the illumination objectives, on the horizontal plane. On one side of the FEP tube (1mm ID) the zebrafish embryo can be inserted, and the programmable syringe pump connected to the opposite end of the tube is used to flow the specimen until it reaches the FoV of the vertically positioned detection objective. Once here, the scanning through the horizontal light sheet(s) is performed by the motorized vertical translation of the entire imaging chamber. The chamber is also filled with E3 medium. Note that the embryo is not dechorionated and that there is no use of agarose. The pump blocks the flow and prevents the sample from moving during the acquisition of the images. The embryo is mounted

only by its insertion in the fluidic circuit, without the need to wait for agarose solidification, which facilitates the entire procedure and greatly reduces the time required. The sample can be also easily retrieved from the setup.

In both setups, the excitation light is provided by a laser at 488 nm. Being the zebrafish embryo a large organism of roughly 700 µm in diameter, two illumination air objectives (Nikon 4x, 0.13NA, placed one on each side of the embryo) were used in an alternated excitation scheme to sequentially irradiate the sample from both sides and improve image quality, while one detection water objective (either Nikon 10x, 0.3NA or Olympus 20x, 0.5NA) was used to collect the emitted fluorescence photons.

In each of the illumination arms, a shutter is present to alternatively block or allow the passage of the light, and to obtain the sequential illumination of both sides of the specimen (Fig. B.1). 3D z-stacks were acquired by sample scanning with z-step ranging from 1 to 2 µm, and typically 60 to 90 seconds between two consecutive volume acquisitions. Imaging sessions started during cleavage and blastula stages of the embryos, typically between 32 to 128 cell stages.

The double illumination scheme produces for each embryo two set of images stacks, which maximum intensity projections and 3D stacks images were fused together either using the FIJI [4] plugin "Pairwise Stitching" [5] or a custom-made FIJI macro. Through this macro, the user manually selects the in-focus portion of the image for both the left- and right-illuminated stacks. After that, the software generates a new stack in which on each of the images the selected left and right portions are pasted, to form the complete picture. The code of this macro is available upon request. Image analysis was performed through dedicated workflows (see following sections) on the produced data without image intensity treatment. Only the images of one embryo (showed in the main text in Fig. 3.1A, Fig. 3.2, and Video B.2) were treated with the FIJI plugin "Bleach Correction" through an exponential fit to account for photobleaching through time before the analysis.

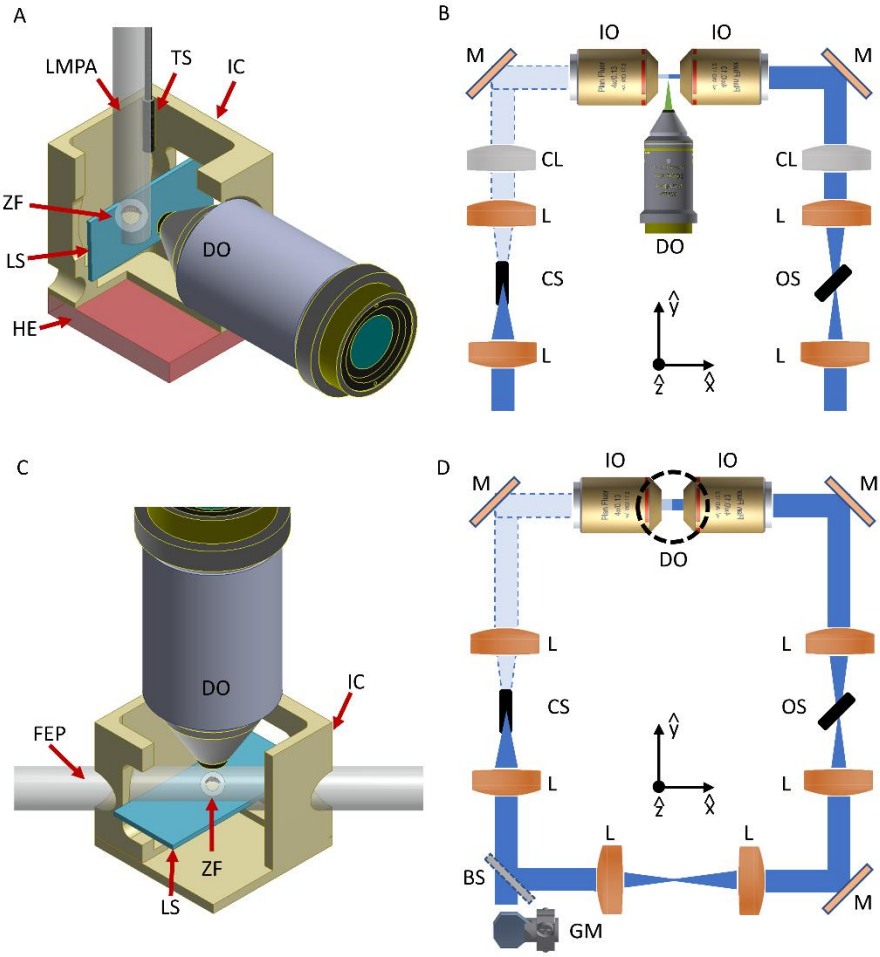

Figure B.1: Schematic of the LSFM mounting and scanning methods used. (A) The zebrafish embryo (ZF), within its chorion, is embedded inside a lmpa cylinder hanging from the top of the imaging chamber (IC) and connected to a translation-rotational stage, to enable the scan through the vertical light-sheet (LS). The emitted photons are collected by the detection objective (DO). A heating element (HE) is integrated below the chamber, while a temperature sensor (TS) is immersed in the imaging medium to monitor the temperature for the whole experiment. (B) Schematic of the illumination optical path for the MuViSPIM setup. Each of the two illumination arms contains two lenses (L) and a cylindrical lens (CL) for the LS formation. After reflection on a mirror (M), the illumination objective (IO) generates the vertical LS in the sample plane. The illumination paths also contain two shutters (CS= closed shutter, OS= open shutter), that are employed to block the light from one of the two arms, generating the alternate illumination scheme. (C) A FEP tube crosses at 45^o the imaging chamber, creating a fluidic circuit through which the embryo is loaded and then positioned in the FoV of the detection objective. Once here, the entire chamber (and the attached FEP tube) is displaced vertically to scan the sample across the horizontal LS. The imaging chamber models are here sectioned to ease visualization of the interior part. (D) Schematic of the illumination optical path for the FlexiSPIM setup. A galvanometric mirror (GM) generates the LS that through a beam-splitter (BS) is sent to each illumination objective, to create the horizontal LS at the sample plane. The dotted circumference denotes the position of the vertical detection objective. Shutters are again used to implement the double alternate excitation scheme. $\hat{x}$ and $\hat{y}$ denote the horizontal plane, while $\hat{z}$ denotes the vertical axis. Figure reproduced from [1].

B.2 Local analysis

Being the embryos mounted within their chorion, they are not constricted by any mounting medium, and can move. Particularly, the dividing cells can change position. Therefore, the FIJI plugin "Manual Tracking with Trackmate" [6] was used to manually track the moving cells/YSNs associated with a particular microtubule branch of the yolk cell, and a region of the branch itself. The obtained mean intensity graphs vs time calculated over the adopted ROIs (as shown in the main text Fig. 3.2J and Fig. 3.2K), contain the information related to the cell cycle and to yolk's MT density. The analysis was performed on the maximum intensity projections of the z-stack over time. The diameter of the tracking ROIs was equivalent to 52 µm, and the tracks with the mean intensities were exported to CSV files.

B.3 Blastoderm margin analysis

A threshold was applied to the maximum intensity projection over time, to obtain the blastoderm shape in white over a black background. This allows the measurement to be independent of the cell's intensity variation over time. Perpendicular to the AV axis, a line ROI was drawn with FIJI and the intensity profile over time (showed in Fig. 3.2L) exported as CSV file.

B.4 Global analysis

Custom-made MATLAB scripts were developed to analyze the mean intensity of a 50 µm ROI traveling over the surface of a sphere modeling the embryo's yolk. From the acquired 3D images, the lateral and depth positions of the center of the yolk and of the vegetal pole were retrieved, and given as input to the software. Connecting those points, the direction of the animal-vegetal axis (AV axis) and the diameter of the yolk were calculated.

The 3D coordinate system of the images (x as width, y as height, z as depth) was translated in the center of the sphere and rotated so that the z-axis lays on the AV axis. Based on this, the spherical coordinates of the sphere's meridians (defined by having the same azimuth coordinate) and parallels (defined by having the same

elevation coordinate) were calculated and back-projected onto the 2D coordinate system of the images' maximum intensity projection. Next, a 50 µm ROI was allowed to travel over the meridians, at the different elevation angles, to follow the path of the MOWs, i.e. from the blastoderm margin towards the vegetal pole, over the yolk's surface. For every position and movie's frame, the mean intensity of the ROI was calculated. By plotting as kymograph, the normalized intensities over time at the different elevation angles of the same meridian, the signal's valleys marking the passage and propagation of the MOW are visible, and their speed is calculated from the images in degree/min by linear fitting.

This was done for all the calculated meridians. From the angular speed in degree/min (denoted as w), linear velocities in µm/min (denoted as v) were calculated using the formula $v = r \cdot (w \cdot \pi) / 180$, where r is the yolk radius calculated for the specific embryo under examination. The kymograph obtained from the normalized intensities over time at the different azimuth angles of the same parallel, permits to analyze the symmetry with respect to the AV axis of the MOWs' passage at the given latitude. This was done for each calculated parallel. The same algorithm has been used to model the blastoderm as a (hemi)sphere, and visualize the cells' division waves from the animal pole to the blastoderm margin.

The MATLAB package with the developed code can be shared upon request to the author of this thesis or to the supervisor. To load the images into the MATLAB console and for some graphical representation, ready MATLAB functions were downloaded from the MATLAB Central File Exchange [7–9].

B.5 Last MOW and last YSN division analysis

To evaluate the possibility that the last YSN division coincides temporally with the last MOW initiation, we used the "Manual Tracking with Trackmate" FIJI plugin in the 3D stack over time of the embryo under analysis to track the eYSN cycle. The eYSN were tracked over time in the 3D stacks and not in the maximum intensity projections since, in those images, with the onset of epiboly, the blastoderm would

cover the YSL and block our view on the eYSN. The mean intensity of the tracks reflects the cycle of the eYSN, enabling the last divisions to be detected and permitting the post-mitotic nuclei to be followed for an additional time to ensure that no further division occurs. Only embryos for which the movie was long enough to ensure that the last YSN division was visible were taken into consideration and at least 3 YSNs/embryo were tracked. The tracking ROI had a diameter of 19 µm and the tracks with the intensity profiles were exported to a CSV file. The temporal information regarding the last MOW initiation was obtained either by detecting the mean intensity over time (through the FIJI z-profiler) of a ROI of 19 µm over the maximum intensity projection image of a microtubule branch, or from the previous local analysis. Its intensity profile was exported to a CSV file. The analysis was performed in six different embryos, following three YSNs per embryo, for at least 60 minutes after the last detected division.

B.6 Intensities plots

All the outputs generated from the different analysis containing the mean intensities either as text or CSV files, were imported to MATLAB, normalized, and plotted. Conclusions on the timing of the cell/YSNs divisions and MOW passages (correctness of the peak/valley position) were also checked by visual inspection of the related images.

B.7 Statistical analysis

To evaluate statistical significance, the software GraphPad Prism 9 was used. To compare the measures of cell/YSN mitosis periodicities between the three groups (defined by the experimental temperature) a Kruskal-Wallis test was performed, and p-values were evaluated with Dunn's multiple comparison test. The same approach was used to compare the measures of MOWs' initiation periodicities between the three groups. Two tailed p-values between the periodicities of cell/YSN divisions and MOWs' initiations at the same experimental temperature were evaluated through Mann-Whitney tests.

B.8 Immunostaining of WT embryos

Fixation and immunostaining procedures were obtained through an adaptation of the protocol described in [10]. Wild Type (WT) embryos were dechorionated and fixed in MT assembly buffer (80 mM KPIPES (pH 6.5), 5 mM EGTA, 1 mM MgCl2, 3.7% formaldehyde, 0.25% glutaraldehyde, 0.5 uM taxol, and 0.2% TritonX-100) for 6 hours at room temperature. After that, they were dehydrated and kept in methanol for different days at -20°C. Re-hydration was achieved through several washing in PBS with 0.1% NP40. After incubation in 100mM NaBH4 in PBS for up to 16 hours at room temperature, embryos were washed in tris buffered saline (TBS), and subsequently the blocking solution (2% BSA in TBS) was applied at room temperature for 30 minutes. Following, incubation of the embryos with β-tubulin primary antibody in blocking solution was performed at 4ºC, overnight. Embryos were then washed 5 times in TBS and incubated at room temperature with secondary antibody in blocking solution for 3 hours. Subsequently, after 4 washes in TBS, they were ready to be imaged. The mouse anti-β-tubulin antibody (E7, Developmental Studies Hybridoma Bank, DSHB) was used at 1:200, while the secondary antibody was in-house conjugated [11] to the Abberior STAR 635P fluorophore (Sigma) and used at 8ug/ml.

B.9 Photobleaching analysis

Visually, the images of all embryos except one did not presented relevant photobleaching, and the analysis here developed to detect the microtubule dynamics was performed on the raw data, i.e. without applying intensity correction strategies. The images of the only embryo affected by non-negligible photobleaching were corrected through the FIJI plugin "Bleach Correction" through an exponential fit. This photobleaching was caused by an imperfection present in the detection arm, which was later noticed and corrected.

Through FIJI, I also examined the mean intensity of a ROI positioned over the yolk region covered by microtubules in the maximum intensity projection, over time for

the various embryos. After retrieving the mean intensity traces, I performed an exponential fitting. From the fits that showed an $R^2 > 0.75$ (meaning they are a good representation of the photobleaching decay), the decay constant λ was extrapolated, which represents the speed of the signal's loss. Its reciprocal, called "time constant" $\tau = 1/\lambda$, represents the time needed for the signal to show a decay of $1/e \approx 37\%$ from the initial value. The smaller the time constant, the higher the photobleaching effect.

I only detected a high photobleaching effect (τ =2.3 hours) for the previously mentioned embryo, that was later computationally corrected. Another trace showed a higher time constant (τ=6.2 hours), while all the other traces showed τ > 40 hours, i.e. the photobleaching was negligible for the duration of the imaging here discussed (ranging from a minimum of 1 to a maximum of 12 hours).

B.10 Supplementary figures

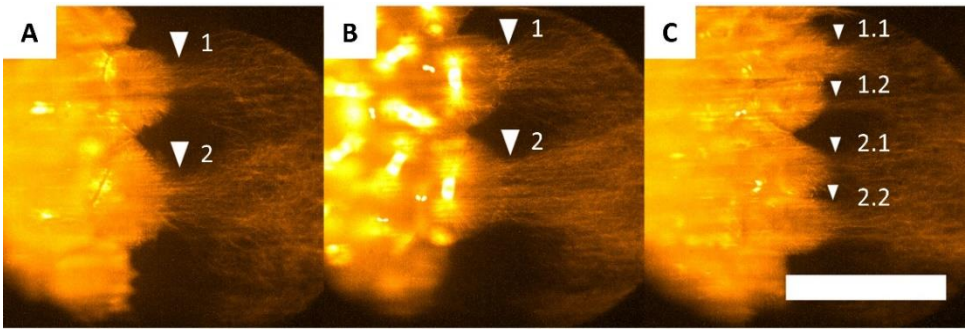

Figure B.2: Branching nature of the eMTN visualized in live dclk2-GFP. (A) Two branches emerge from the blastomeres (arrowheads) and (B) upon mitosis, (C) they divide into two sub-branches each (arrowheads). Scale bar 50 µm. Figure reproduced from [1].

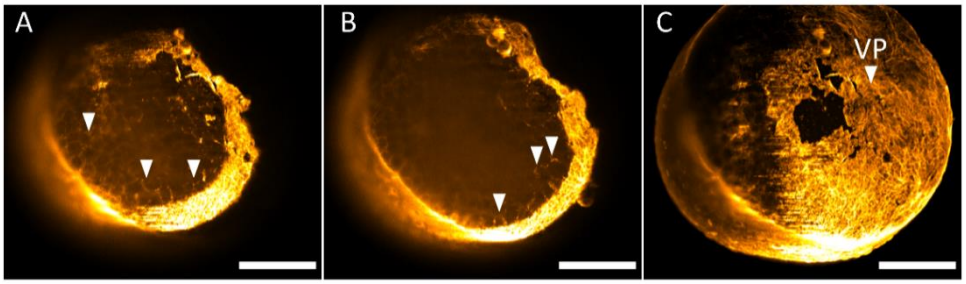

Figure B.3: Immunostaining of iMTN. (A-B) Maximum intensity projection performed on two set of slices relative to the interior part of the yolk for a WT fixed and immunostained (β-tubulin) embryo. Fluorescent signal appears from the iMTN below the YCL, surrounding the lipid yolk granules (arrowheads). (C) Maximum intensity projection of all the slices to show the entire imaged volume as reference, with approximated position of the vegetal pole (VP and arrowhead). The yolk in (C) appears slightly damaged, possibly due to mechanical rupture after the immunostaining protocol. Scale bars 200 µm. Figure reproduced from [1].

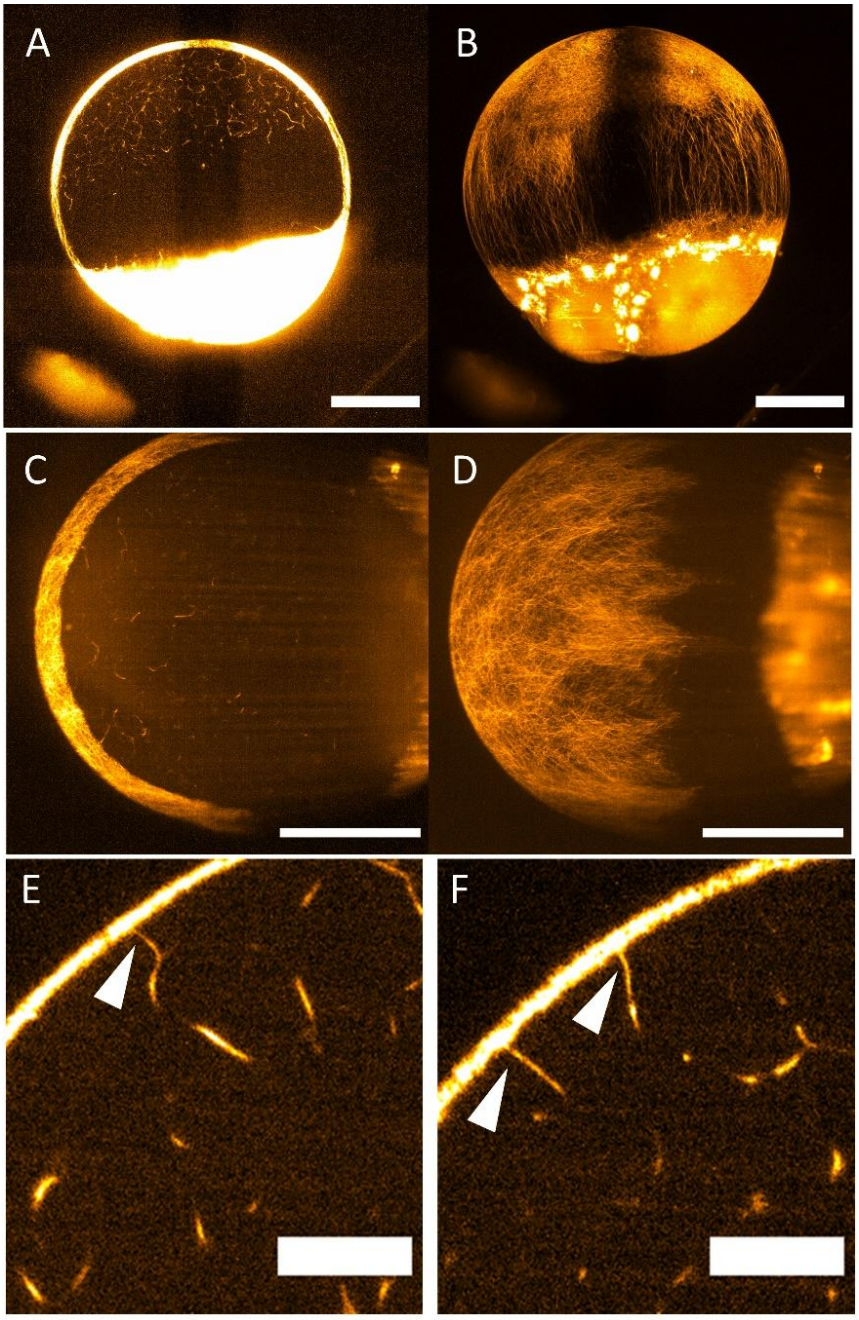

Figure B.4: Details on the iMTN. The maximum intensity projection performed on a sub-set of images relative to the interior part of the yolk for a non-fertilized egg (A) and an embryo at cleavage stage (C) reveals the presence of the iMTN. The eMTN visualized through the maximum intensity projection performed on the whole z-stack for the same eggs is also provided (B, D). Scale bars 200 µm. (E-F) Single slice images showing in live dclk2-GFP the connections between the eMTN and the iMTN (arrowheads) before (E) and after (F) a MOW passage. The displayed area is the same as that shown in Figure 6B-D. Scale bars 50 µm. All images relative to dclk2-GFP eggs. Figure reproduced from [1].

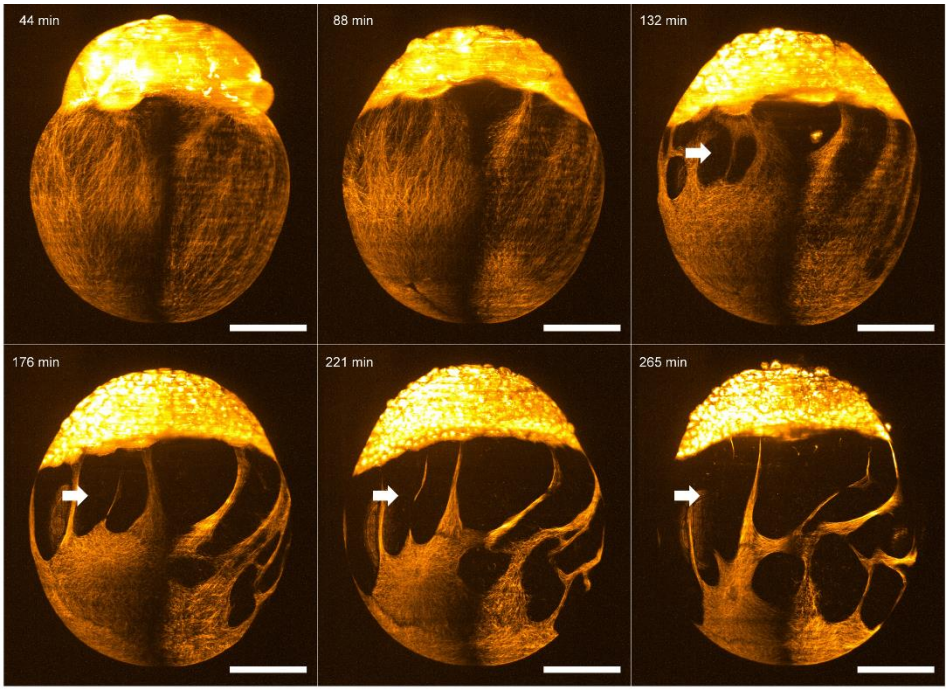

Figure B.5: Effects of dinaciclib on the eMTN. Time lapse images of a dclk2-GFP embryo to which dinaciclib was applied at a concentration of 200 µMol/L and imaged at 28°. Dinaciclib stops the development of the embryo, but also heavily affects the morphology of the eMTN (white arrows). Other experiments with different doses of dinaciclib were performed, but presenting the same consequences on the microtubule network. Scalebar 200 µm.

B.11 Supplementary videos

B.11.1 Video B.1:

https://opticapublishing.figshare.com/articles/media/SupplementaryVideo1_mp4/15116931

LSFM imaging of a dclk2-GFP embryo (Vegetal view). Two MOWs are crossing the yolk over the YCL in a belt-like fashion, bundling the eMTN, and closing concentrically at the vegetal pole. Scale bar 100 µm. Central black region is due to the LS bending caused by the curvature of the sample.

B.11.2 Video B.2:

https://opticapublishing.figshare.com/articles/media/SupplementaryVideo2_mp4/15116943

LSFM imaging of a dclk2-GFP embryo at blastula stages (Lateral view). Multiple MOWs are passing over the YCL from the blastoderm margin toward the vegetal pole, bundling the eMTN. Animal pole at top right, vegetal pole at bottom left. Scale bar 200 µm.

B.11.3 Video B.3:

https://opticapublishing.figshare.com/articles/media/SupplementaryVideo3_compressed_mp4/15116934

LSFM imaging of a dclk2-GFP embryo from cleavage until bud stages (Lateral view). Several MOWs are shown, but no MOWs are visible during epiboly. Animal pole at top right, vegetal pole at bottom left. Scale bar 200 µm.

B.11.4 Video B.4:

https://opticapublishing.figshare.com/articles/media/SupplementaryVideo4_mp4/15116940

Video formed by three movies on the same area of a dclk2-GFP embryo. The z-stack (from 00:00 to 00:19) starts from the interior of the yolk and continues towards the surface, where an eYSN is placed. It shows an internal MT bundle (arrowhead) connected to the eYSN. A 3D rotating projection of the same area (from 00:20 to 00:23) shows the extension of the same MT bundle towards the interior of the yolk, and again its connection to the eYSN (arrowhead). A resliced view (YZ) of the same area (from 00:24 to 00:30) shows the evolution of the connection between the internal MT bundle and the eYSN versus time. The connections (arrowheads) are lost upon eYSN mitosis and reform with the resulting nuclei. Orange HOT colormap is used to ease visualization of the internal MT bundle. Time stamp in minutes : seconds. Scale bar 50 µm.

B.11.5 Video B.5:

https://opticapublishing.figshare.com/articles/media/SupplementaryVideo5_mp4/15116946

Video formed by three movies in the same area of a dclk2-GFP embryo. The z-stack (from 00:00 to 00:09) shows another internal MT bundle (arrowhead) connected to an eYSN. A 3D rotating projection of the same area (from 00:10 to 00:12) shows the extension of the same MT bundle toward the interior of the yolk, and again its connection to the eYSN (arrowhead). The same area (from 00:13 to 00:18), visualized through a maximum intensity projection over 20 µm in depth, shows the evolution of the connection between the internal MT bundles and the eYSN versus time. The connections (arrowheads) are lost upon eYSN mitosis and reform with the resulting nuclei. Orange HOT colormap is used to ease visualization of the internal MT bundle. Time stamp in minutes : seconds. Scale bar 50 µm.

B.11.6 Video B.6:

https://opticapublishing.figshare.com/articles/media/SupplementaryVideo6_compressed_mp4/15116937

Maximum intensity projection over 30 µm showing the section of the interior of the yolk. LSFM imaging of the dclk2-GFP embryo was performed from about sphere until bud stages. The iMTN is visible in the whole yolk and it is present also during epiboly. The embryo moves as it is not constricted by the mounting medium. Animal pole at top/top-right, vegetal pole at bottom/bottom-left. Time stamp in minutes : seconds. Scale bar 200 µm.

B.11.7 Video B.7:

https://opticapublishing.figshare.com/articles/media/SupplementaryVideo7_mp4/15116949/1

Maximum intensity projection over 40 µm showing the section of the interior of the yolk, from LSFM imaging of a dclk2-GFP embryo (from 00:00 to 00:07). The connections between eMTN and iMTN are lost upon MOW passage, and reform afterwards. Scale bar 200 µm. A ROI is highlighted (from 00:08 to 00:12) to better visualize the connections' dynamics (arrowheads). Scale bar 50 µm. Orange HOT colormap is used to ease visualization of the iMTN.

B.12 References

1. M. Bernardello, M. Marsal, E. J. Gualda, and P. Loza-Alvarez, "Light-sheet fluorescence microscopy for the in vivo study of microtubule dynamics in the zebrafish embryo," Biomed. Opt. Express **12**(10), 6237–6254 (2021).

2. L. D. Tran, H. Hino, H. Quach, S. Lim, A. Shindo, Y. Mimori-Kiyosue, M. Mione, N. Ueno, C. Winkler, M. Hibi, and K. Sampath, "Dynamic microtubules at the vegetal cortex predict the embryonic axis in zebrafish.," Development **139**(19), 3644–3652 (2012).

3. C. B. Kimmel, W. W. Ballard, S. R. Kimmel, B. Ullmann, and T. F. Schilling, "Stages of embryonic development of the zebrafish.," Dev. Dyn. an Off. Publ. Am. Assoc. Anat. **203**(3), 253–310 (1995).

4. J. Schindelin, I. Arganda-Carreras, E. Frise, V. Kaynig, M. Longair, T. Pietzsch, S. Preibisch, C. Rueden, S. Saalfeld, B. Schmid, J.-Y. Tinevez, D. J. White, V. Hartenstein, K. Eliceiri, P. Tomancak, and A. Cardona, "Fiji: an open-source platform for biological-image analysis.," Nat. Methods **9**(7), 676–682 (2012).

5. S. Preibisch, S. Saalfeld, and P. Tomancak, "Globally optimal stitching of tiled 3D microscopic image acquisitions.," Bioinformatics **25**(11), 1463–1465 (2009).

6. J.-Y. Tinevez, N. Perry, J. Schindelin, G. M. Hoopes, G. D. Reynolds, E. Laplantine, S. Y. Bednarek, S. L. Shorte, and K. W. Eliceiri, "TrackMate: An open and extensible platform for single-particle tracking.," Methods **115**, 80–90 (2017).

7. Y. Tak, "Multipage TIFF stack," https://www.mathworks.com/matlabcentral/fileexchange/35684-multipage-tiff-stack.

8. D. Helmick, "varycolor," https://www.mathworks.com/matlabcentral/fileexchange/21050-varycolor.

9. T. Davis, "Arrow3," https://www.mathworks.com/matlabcentral/fileexchange/14056-arrow3.

10. J. Topczewski and L. Solnica-Krezel, "Cytoskeletal dynamics of the zebrafish embryo.," Methods Cell Biol. **59**, 205–226 (1999).

11. Š. Bálint, I. Verdeny Vilanova, Á. Sandoval Álvarez, and M. Lakadamyali, "Correlative live-cell and superresolution microscopy reveals cargo transport dynamics at microtubule intersections.," Proc. Natl. Acad. Sci. U. S. A. **110**(9), 3375–3380 (2013).

Appendix C: Extension of single-molecule imaging to living embryos through LSFM

This appendix contains content entirely reproduced or adapted from the article: Bernardello M., et al. “Analysis of intracellular protein dynamics in living zebrafish embryos using light-sheet fluorescence single-molecule microscopy.” Biomedical optics express 12 10 (2021): 6205-6227

C.1 Determination of imaging parameters

To measure the thickness of the light sheet, the cylindrical lens was removed from the optical path, and the beam that was focused through a fluorescent solution by the illumination objective was imaged. Using FIJI software [1], the intensity line profile at the beam waist was generated and Gaussian-fitted (Fig. 5.3A). The standard deviation σ of the Gaussian fit was used to calculate the full width at half maximum (FWHM) of the intensity line profile as $FWHM = 2\sigma \cdot \sqrt{(2 \cdot \ln 2)} \approx 2.355\sigma$, which represents the light sheet thickness waist diameter, and equaled 2 µm. The illumination field of view (FoV) was calculated as in Olarte *et al*. [2], i.e., $FoV = 1.78 \cdot n \cdot \frac{\lambda}{(NA)^2}$, where *n* is the medium refractive index (water), λ is the illumination wavelength, and *NA* is the illumination objective's numerical aperture, and equaled 13.5 µm. The illumination FoV, considered as the double of the Rayleigh range, was also measured on the imaged beam profile and found to be 14.5 µm, in good agreement with the theoretical value.

To obtain the excitation power density, the optical losses introduced by the illumination path were first determined. These were about 69%, due to the overfilling of the back-focal plane of the objective, to ensure homogeneous illumination. By setting the power at the input port of the microscope at 66 mW, the power at the sample plane resulted in 20.25 mW. Being the illumination focal plane area defined by the thickness (2 µm) and height (1.2 mm) of the light sheet, the resulting power density equaled ~0.85 kW cm^{-2}.

To measure the optical resolution of the system, sub-diffraction fluorescent beads (100 nm in diameter) were embedded in 0.5% low melting point agarose (lmpa) and placed as sample in the microscope using a Fluorinated Ethylene Propylene (FEP) support. Images were taken for beads close to the middle axis and near the surface of the produced agarose cylinder (Fig. 5.3C and Fig. 5.3E respectively). The intensity profiles in $\hat{x}$ and $\hat{y}$ were measured, Gaussian fitted, and their FWHMs calculated (Fig. 5.3D and Fig. 5.3F). Shapiro-Wilk tests were performed to confirm the normal

distribution of the FWHMs values. Unpaired t-tests were then conducted to check for statistically significant difference between the values obtained for beads close to the middle axis (N=11 beads) and near the surface (N=11 beads), in both lateral directions (Fig. 5.3B).

C.2 Zebrafish

Zebrafish (*Danio rerio*) were grown, maintained and handled in compliance with the directives of the local animal welfare body. They were exposed to a 14h light and 10h dark diurnal cycle at 28°C. Fertilization was performed by natural spawning at the beginning of the light period, and the fertilized eggs were collected and maintained in E3 medium (5 mM NaCl, 0.17 mM KCl, 0.33 mM $CaCl_2$, 0.33 mM $MgSO_4$) at 28°C. All experiments were performed using embryos from the *Tg(actb2:mCherry-H2A)* zebrafish line.

C.3 Microinjection and treatment of embryos

A cDNA construct encoding eYFP-GR(alpha), hereafter referred to as YFP-GR, was genetically cloned into a PCS2+ zebrafish expression plasmid. The resulting PCS2+-eYFP-GR(alpha) plasmid was microinjected into zebrafish embryos at the 1-2 cell stage (30 pg per embryo), resulting in a mosaic expression of the eYFP-GR(alpha) protein in the zebrafish embryo. Microinjections were done under a stereomicroscope (Leica S8AP0), using a microinjector (Pneumatic Pico Pump PV820, WPI) and a micromanipulator with pulled microcapillary pipettes (model GC100F-15 from Harvard Apparatus, pulled with P-97 Micropipette Puller from Sutter Instrument). Injected eggs were left to develop in an incubator at 28°C. Viability and development of the eggs after microinjections were checked on a daily basis using a fluorescence stereomicroscope (Nikon SMZ1000 C-DSD230). To prevent embryonic pigmentation, embryos were incubated in 0.003% phenylthiourea (PTU) from 10 hpf (hours post-fertilization) onwards, and this solution was refreshed daily. For treatment with the synthetic glucocorticoid dexamethasone, a 10 mM stock solution in DMSO was prepared. The zebrafish

embryos were incubated in dexamethasone (final concentration of 25 μM) in egg water for 3 hours, at 28°C, prior to the microscopy imaging. As a control, a group of zebrafish embryos was incubated in a vehicle solution of 0.01% DMSO.

C.4 Cultured cells fixation, mounting, and LSFSMM imaging

To determine the characteristics of the detection of a single YFP molecule in the LSFSMM setup, HEK293 cells were transfected with the plasmid PCS2+-eYFP-GR(alpha) for expression of YFP-GR. For transfection, cells were cultured in DMEM (Dulbecco's Modified Eagle Medium, Invitrogen, Waltham, MA, USA) supplemented with penicillin and streptomycin (10 μg ml^{-1}, Invitrogen), Glutamax (10 μg ml^{-1}, Invitrogen) and 10% fetal calf serum (Invitrogen) at 37°C in humidified atmosphere containing 5% of CO2. Before transfection, cells were transferred onto a sterile glass coverslip (diameter 25 mm, Marienfeld, Germany) and placed in a well of a 6-well plate. At a confluence level of 20-30%, cells were transfected with 1 μg of DNA per well, using FuGENE 6 (Roche Molecular Biochemicals, Indianapolis, USA). The transfection efficiency, determined by fluorescence microscopy screening at 48h after transfection, was approximately 20%. Two days post-transfection cells were fixed with 4% PFA. Fixed cells were then immersed in 0.5% lmpa, transferred into a cut FEP support tube, and mounted in the LSFSMM system. Movies were taken using continuous illumination and a 25 ms exposure time per frame for 1000-4000 frames.

C.5 Experimental Design

On three experimental days, one zebrafish embryo was selected for the LSFSMM imaging per experimental (vehicle- and dexamethasone-treated) group, and in each of the selected embryos, three separate areas were imaged, yielding three independent movies of 1000-4000 consecutive frames. All movies were analyzed individually, resulting in a value per movie for α (mobile fraction size), r_1^2 (mean square displacement of the mobile fraction) and r_2^2 (mean square displacement of the immobile fraction) for each time lag.

C.6 Data Analysis

To study the mobility of proteins, Particle Image Correlation Spectroscopy (PICS) analysis was used, described in detail previously [5,6]. In PICS analysis, individual molecules are not tracked, but all possible correlations between the locations of molecules in two image frames are determined. See also [7] for a complete description of the data analysis procedure.

C.7 Supplementary Figures

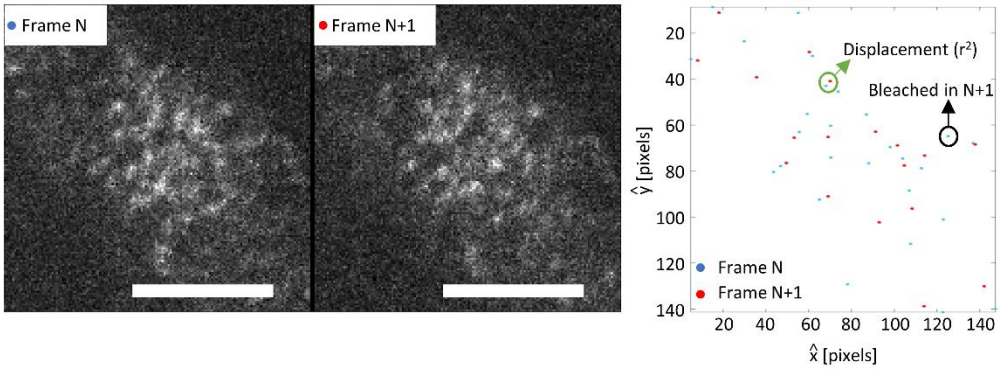

Figure C.1: Representative image of a displacement analysis based on a single image pair (Frames N and N+1). Not every molecule is positionally correlated due to the photobleaching. The average number of peaks per image here equals 23.0. This image pair is a part of a 3000-image movie. For the entire movie, the total number of displacements found in the 2999 image pairs equals to 35467. Image reproduced from [7]. *Scalebars 10 µm.*

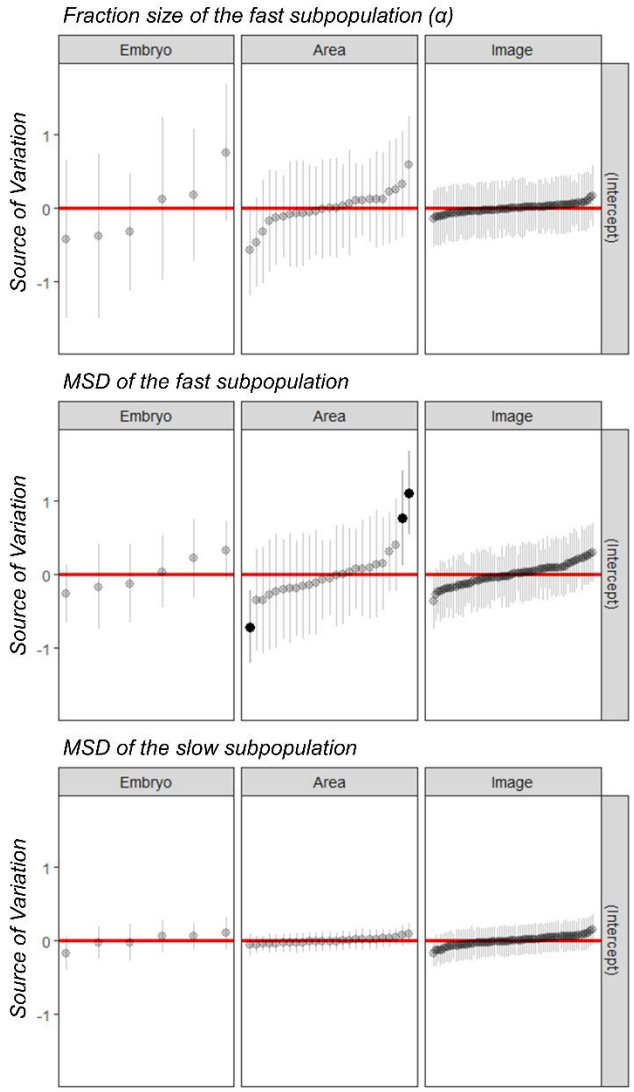

Figure C.2: Results of the mixed linear model analysis reveal potential sources of the data variability. To establish effect ranges, data were logit-transformed and presented on a logit scale. Caterpillar plots present the effect from random components as the deviation of the group intercepts from the global mean of the data. The effect range represents the deviation between different embryos, different areas within an embryo, and different images of the same area within an embryo, that are parts of the total measurement error in the mobile fraction size, α (A), MSD (Mean Square Displacement) of the mobile fraction (B), and MSD of the immobile fraction (C). Red lines indicate the global mean of the data, while black dots signify significant deviations from the global mean among embryos, areas, and images. The data points are sorted from the ones most negatively deviating from the global average to the ones that deviate most positively. Image reproduced from [7].

C.8 References

1. J. Schindelin, I. Arganda-Carreras, E. Frise, V. Kaynig, M. Longair, T. Pietzsch, S. Preibisch, C. Rueden, S. Saalfeld, B. Schmid, J.-Y. Tinevez, D. J. White, V. Hartenstein, K. Eliceiri, P. Tomancak, and A. Cardona, "Fiji: an open-source platform for biological-image analysis.," Nat. Methods **9**(7), 676–682 (2012).

2. O. E. Olarte, J. Andilla, E. J. Gualda, and P. Loza-Alvarez, "Light-sheet microscopy: a tutorial," Adv. Opt. Photonics **10**(1), 111–179 (2018).

3. G. S. Harms, L. Cognet, P. H. Lommerse, G. A. Blab, and T. Schmidt, "Autofluorescent proteins in single-molecule research: applications to live cell imaging microscopy.," Biophys. J. **80**(5), 2396–2408 (2001).

4. T. Schmidt, G. J. Schütz, W. Baumgartner, H. J. Gruber, and H. Schindler, "Imaging of single molecule diffusion.," Proc. Natl. Acad. Sci. U. S. A. **93**(7), 2926–2929 (1996).

5. S. Semrau and T. Schmidt, "Particle image correlation spectroscopy (PICS): retrieving nanometer-scale correlations from high-density single-molecule position data.," Biophys. J. **92**(2), 613–621 (2007).

6. G. J. Schütz, H. Schindler, and T. Schmidt, "Single-molecule microscopy on model membranes reveals anomalous diffusion.," Biophys. J. **73**(2), 1073–1080 (1997).

7. M. Bernardello, R. J. Gora, P. Van Hage, G. Castro-Olvera, E. J. Gualda, M. J. M. Schaaf, and P. Loza-Alvarez, "Analysis of intracellular protein dynamics in living zebrafish embryos using light-sheet fluorescence single-molecule microscopy.," Biomed. Opt. Express **12**(10), 6205–6227 (2021).

Appendix D: Results dissemination and scientific training

D.1 Scientific publications

1. M. Bernardello, M. Marsal, E. J. Gualda, and P. Loza-Alvarez, "Light-sheet fluorescence microscopy for the in vivo study of microtubule dynamics in the zebrafish embryo," Biomed. Opt. Express 12(10), 6237–6254 (2021).
2. M. Bernardello, R. J. Gora, P. Van Hage, G. Castro-Olvera, E. J. Gualda, M. J. M. Schaaf, and P. Loza-Alvarez, "Analysis of intracellular protein dynamics in living zebrafish embryos using light-sheet fluorescence single-molecule microscopy.," Biomed. Opt. Express 12(10), 6205–6227 (2021).
3. M. Bernardello, E. J. Gualda, and P. Loza-Alvarez, "Modular multimodal platform for classical and high throughput light sheet microscopy.," Sci. Rep. 12(1), 1969 (2022).
4. M. Marsal, M. Bernardello, E. J. Gualda, and P. Loza-Alvarez, "Multiple asters organize the yolk microtubule network during dclk2-GFP zebrafish epiboly," Sci. Rep. 12(1), 4072 (2022).

D.2 Manuscripts in preparation

1. T. Sipka, S. Tairi, M. Bernardello, E. Gualda, P. Loza, A. Blanc-Potard, G. Lutfalla, and M. Nguyen-Chi, "Dynamics of macrophage polarization during Salmonella Typhimurium infection in zebrafish," in preparation

D.3 Contributions to scientific meetings

Selected talks:

Photonics meets Biology (19-22/09/2017) Tarragona, Spain
Talk: Flexi-spim: a modular multimodal platform for classical and high-throughput light-sheet microscopy

SPAOM2018 (23-26/10/2018) Granada, Spain
Talk: Yolk microtubules organization's dynamics in zebrafish embryonic development visualized through Light-Sheet Microscopy

Organized Workshops:

MiFoBio 2018 (5-12/10/2018) Seignosse, France
Workshop: Sample's environment control in LSFM: mechanics, electronics, 3D printing, and programming for biological questions.

SPAOM2018 (23-26/10/2018) Granada, Spain
Workshop: Arduino based open-source hardware for light-sheet microscope control

Posters:

Frontiers of Light Summer School (03-06/07/2017) @ICFO, Castelldefels, Spain

Poster: Flexi-SPIM: a modular multimodal platform for classical and high-throughput light-sheet microscopy

TOPIM TECH 2017 Summer school (10-15/07/2017) Chania, Crete, Greece
Poster: Flexi-SPIM: a modular multimodal platform for classical and high-throughput light-sheet microscopy

Photonics meets Biology (19-22/09/2017) Tarragona, Spain
Poster: Flexi-SPIM: a modular multimodal platform for classical and high-throughput light-sheet microscopy

ICFO internal meeting (20/10/2017) @ICFO, Castelldefels, Spain
Poster: Flexi-SPIM: a modular multimodal platform for classical and high-throughput light-sheet microscopy

ELMI 2018 (5-8/06/2018) Dublin, Ireland
Poster: Dynamics of zebrafish microtubule organization during embryonic development using light-sheet microscopy

10th Anniversary Light Sheet Fluorescence Microscopy Conference (12-15/08/2018) Dresden, Germany
Poster: Light-sheet microscopy: studying zebrafish microtubules during embryonic development

MiFoBio 2018 (5-12/10/2018) Seignosse, France
Poster: Light-sheet microscopy for the study of microtubule organization's dynamics during the development of zebrafish embryos

D.4 Outreach activities

Radio interview for German-speaking Slovak radio-station (made in Bratislava, 19.02.2019) http://dersi.rtvs.sk/clanky/189967/die-slowakei-hautnah-magazin-uber-die-slowakei-in-deutscher-sprache-11-3-2019
Audience: general public

Outreach conference about the project and ImageInLife network, at Comenius University (Bratislava, Slovakia, 19.02.2019).
Audience:
French ambassador in Slovakia
Professors, researchers, and students from Bratislava's universities

Contribution (creation of the page and of the fundamental content) to the Italian-Wikipedia page about Light sheet Fluorescence Microscopy.
Audience – open access https://it.wikipedia.org/wiki/Microscopia_a_foglio_di_luce

Researcher's night at EMBL Heidelberg (27.09.2019), presenting the LEGOLISH setup (LSFM made out of LEGO pieces) and the ImageInLife network.
Audience: kids, families, researchers

Two YouTube videos (10 minutes each) about fundamental of microscopy and confocal microscopy included also in a MOOC (Massive Open Online Courses) course.
Audience: general public and Bachelor/Master students
https://youtu.be/ckblwEO50RY
https://youtu.be/BmiWwBMj6cY
https://www.fun-mooc.fr/en/courses/imageinlife-imaging-vertebrate-embryo/

Various labtours at the imaging facility
Audience: Masters students

D.5 Courses

1. Laser Safety Course (3 hours)
2. LabVIEW Introductory course (12 hours, 06/2017)
3. Molecular Biology Course (12 hours, 03-04/2018)
4. Cell Biology Course (12 hours, 05/2018)

D.6 Secondments performed

1. At University of Leiden, The Netherlands. Duration: 1 month.
   Aim: Extending single-molecule microscopy to living zebrafish embryos through LSFM
2. At University of Montpellier, France. Duration: 1 month.
   Aim: imaging macrophage recruitment

D.7 Secondments and visits hosted at ICFO

1. 1 ESR from University of Montpellier, France. Duration: 2 weeks.
   Aim: imaging macrophage recruitment
2. 1 ESR from CNRS, France. Duration: 1 month.
   Aim: Imaging the development of the early zebrafish embryo
3. 1 ESR from University of Leiden, The Netherlands. Duration: 4 months.
   Aim: Extending single-molecule microscopy to living zebrafish embryos through LSFM
4. 1 ESR from CNRS, France. Duration: 1 week.
   Aim: Imaging of the zebrafish pectoral fin development
5. 1 ESR from University of Cambridge, UK. Duration: 1 month.
   Aim: Imaging of the pre-implantation mouse embryo development